2013

Novel strategies for depositing nanoelectrode materials using dip-pen nanolithography of liquid inks

Cathal D. O'Connell
University of Wollongong

Novel Strategies for Depositing Nanoelectrode Materials using Dip-Pen Nanolithography of Liquid Inks

A thesis submitted in fulfilment of the requirements for the award of the degree of

DOCTOR OF PHILISOPHY

from the

UNIVERSITY OF WOLLONGONG

by

CATHAL D. O'CONNELL, B.A.

SCHOOL OF CHEMISTRY

(2013)

Certification

I, Cathal D. O'Connell, declare that this thesis, submitted in fulfilment of the requirements for the award of Doctor of Philosophy, in the School of Chemistry, University of Wollongong, is wholly my own work unless otherwise referenced or acknowledged. The document has not been submitted for qualifications at any other academic institution.

Cathal D. O'Connell

31 May, 2013

Table of Contents

List of Figures

List of Tables

Acknowledgements

In his book *The Design of Experiments* RA Fisher said that science is nothing but the rational collection of experience. I have been fortunate enough to be surrounded by people who, by freely sharing their own experience and expertise, gave me a huge head-start on this adventure.

I am deeply grateful for all of the work, time and brain cells my supervisors have contributed to this work. A special thank you to Michael Higgins, for showing me the ropes, not just of AFM instrumentation but of research itself. Thank you for the long after-hours chats, for your enthusiasm, your creativity and your friendship. Thank you to Simon Moulton for your support and welcome, especially in the early days of the project when I was timid and shy in a new country far from home. Thank you for your general good advice and for making key suggestions that got us over some tough obstacles along the way. Thank you to Gordon Wallace for overseeing the project, for always shining new light on a problem and for the occasional (and justified) kick-up-the-arse. Your infectious drive and buoyancy showcase how it is not only the result which matters; you have to enjoy the journey too.

To the researchers and students at the Intelligent Polymer Research Institute, thank you for all the countless questions answered and for all the help given. There are simply too many people to name. It is a wonderful, thriving community and I will miss you all. A special thank you goes to those who helped me outside of the lab environment, especially Andrew Nattestad and Brianna Thompson. Thank you to the late, great Leon Kane-Maguire, who will always remain a true inspiration.

To my family back home in Ireland, thank you for all of your support throughout my education. I will always work to make you proud. Thank you to the extended McNamara family, in particular Peter Sn and Nellie, and Peter Jr and Jacinta, for adopting me as one of your own. You have saved the day on many occasions, from moving my stuff across town, to providing

a roof over my head. It is down to you that Australia has come to feel like home.

Finally, thank you to Monika Fekete for your love and for taking care of me during the write-up. Everything before you was just prologue. I can't wait to see how our story will unfold.

List of publications

1. O'Connell, C.D., Higgins, M.J., Nakashima, H., Moulton, S.E. & Wallace, G.G. Vapor phase polymerization of EDOT from submicrometer scale oxidant patterned by dip-pen nanolithography. *Langmuir : the ACS journal of surfaces and colloids* 28, 9953–60 (2012).

Author contribution: I designed and carried out experiments, analysed results and wrote the manuscript. Chapter 3 includes and expands on this work.

2. Nakashima, H., Higgins, M.J., **O'Connell, C.,** Torimitsu, K. & Wallace, G.G.* Liquid deposition patterning of conducting polymer ink onto hard and soft flexible substrates via dip-pen nanolithography. *Langmuir : the ACS journal of surfaces and colloids* 28, 804–11 (2012).

Author contribution: I assisted with the ink development strategy, design of experiments, and interpretation of results.

3. Higgins M.J., **O'Connell C.D.,** Gelmi A. and Wallace G.G. Characterization and Fabrication Tools for Emerging Nanobionics. *Journal of Imaging and Microscopy* (2012).

Author contribution: I contributed ideas and wrote part of the manuscript. Chapters 1 and 2 include ideas from this work.

4. Wagner M., **O'Connell C.D.,** Harman D.G., Ivaska A., Higgins M.J. and Wallace G.G. Synthesis and optimisation of PEDOT:PSS based ink for printing nanoarrays using dip-pen nanolithography. (*Submitted*, May 2013)

Author contribution: I assisted with ink development strategy and performed some experiments.

5. O'Connell, C.D., Higgins, M. J., Marusic, D., Moulton, S. E. & Wallace, G. G. Liquid ink deposition from an atomic force microscope tip: deposition

monitoring and control of feature size. *Langmuir* (2014). doi:10.1021/la402936z

Author contribution: I designed and carried out experiments, analysed results and wrote the manuscript. Chapter 5 includes and expands upon this work.

6. O'Connell C.D., Sullivan R., Higgins M.J., Moulton S.E. and Wallace G.G. Variation in feature size due to ink-on-tip hydrodynamics in dip-pen nanolithography of liquid inks. (*Under review*, March 2014)

Author contribution: I designed and carried out experiments, analysed results and wrote the manuscript. Chapter 6 includes and expands upon this work.

7. O'Connell C.D., Sullivan R., Higgins M.J., Moulton S.E. and Wallace G.G. Nanoscale platinum printing on insulating substrates. *Nanotechnology* **24,** 505301 (2013).

Author contribution: I designed and carried out experiments, analysed results and wrote the manuscript. Chapter 4 includes and expands upon this work.

8. O'Connell C.D., Higgins M.J., Moulton S.E. and Wallace G.G. The development of dip-pen nanolithography for fabricating nanobionic interfaces. (S*ubmitted,* June 2013)

Author contribution: I performed the literature review and wrote the manuscript. Chapters 1, 2 and 7 form the basis of this review manuscript.

Abstract

Medical bionic devices restore human function by interfacing electrical technology with the body. The emerging field of nanobionics is borne from advances in our ability to control the structure of materials on finer and finer length-scales, coupled with an increased appreciation of the sensitivity of living cells to nanoscale topographical, chemical and mechanical cues. As we envisage and prototype nanostructured bionic devices there is a crucial need to understand how cells feel and respond to nanoscale materials, particularly as material properties (surface energy, conductivity etc.) can be very different at the nanoscale than at bulk. However, the patterning of bionic materials of interest is often not achievable using conventional fabrication techniques, especially on soft, biocompatible substrates. Nonconventional nanofabrication strategies are required.

Dip-pen nanolithography (DPN) is a nanofabrication technique which uses the nanoscale tip of an atomic force microscope to direct-write functional materials. This thesis contributes to the development of the DPN technique in two main aspects. The first aspect is the development of two novel methods of patterning electro-materials at submicron- to nano resolution. The second is a contribution to the understanding of ink transport in liquid ink DPN.

A novel oxidant ink was developed for *in situ* synthesis of the conducting polymer poly(3,4-ethylenedioxythiophene) (PEDOT) via vapour phase polymerisation. DPN patterning of the oxidant ink was facilitated by the incorporation of an amphiphilic block copolymer thickener, an additive that also assisted with stabilization of the oxidant. When exposed to EDOT monomer in a VPP chamber, each deposited feature localized the synthesis of conducting PEDOT structures of several micro-meters down to 250 nm in width, at a scale (picogram) which is much smaller than any previously reported.

A strategy was developed to DPN print a platinum precursor (H_2PtCl_6) based liquid ink onto insulating substrates with nanoscale resolution. The ink formulation was printable on Si, glass, ITO, Ge, PDMS, Parylene C and even a human hair. A mild plasma treatment effected reduction of the precursor patterns *in situ* without subjugating the substrate to destructively high temperatures. Feature size was controlled via dwell time and degree of ink loading, and platinum features with 50 nm dimensions could be routinely achieved on silanized Si. We confirmed the electrical conductivity of printed platinum by two point probe measurements and we characterized electrochemical activity using Scanning Electrochemical Microscopy (SECM). A modified method enabled deposition of micron scale Pt snowflakes. By tuning the substrate hydrophobicity using functionalization with a long chain alkane group the spreading of the precursor ink was tempered, and growth of a fractal-like crystal proceeded via a diffusion limited aggregation mechanism. Reduction of the precursor crystal by plasma treatment resulted in a 2D dendritic structure composed of <20 nm Pt nanoparticles. This combined top-down/bottom-up approach enabled the arbitrary placement of Pt fractal-like structures on Si or glass.

Model ink-substrate systems, which exhibiting a range of viscosities and wettabilities, were used to explore various methods of controlling feature size in liquid ink DPN. The ink-transfer mechanism was investigated using AFM force measurements acquired during ink deposition. This data was used to elucidate the shape of the meniscus during deposition and illustrate a method to monitor the volume of deposition *in-situ*. However, the deposition rate was found to change dramatically over the course of an experiment due to a dependence of deposition rate on the changing volume of ink on the pen.

The effect of depleting ink volume on deposition rate over a long term experiment was investigated. A hierarchy of phenomena were uncovered which were related to ink movement and reorganisation along the

cantilever. These ‘ink-on-tip hydrodynamics’ were suggested to arise from (I) changes in ink volume on cantilever, (II) ‘rest-time’ between grids and (III) travel time between individual dots. In light of our conclusions, we posed critical questions of reservoir-on-tip liquid ink DPN as a nanofabrication technique and discuss the various parameters which need to be controlled in order to achieve uniformity of feature size.

The novel electro-material printing strategies developed in this thesis may have applications in the fabrication of nanoelectronic and nanobionic platforms, particularly on flexible, polymeric substrates. The insights gained into the dynamics of liquid ink transport may have implications in the rational design of DPN inks and probes.

Notes on usage

1. The term ‘lithography’ (from *lithos* ‘stone’ and graphein ‘to write’) was originally coined in the late 18th Century to describe a new technique of reproducing images on paper using a flat stone and an etched coating of wax or grease. In modern usage, lithography can refer to almost any method of reproducing or transferring a pattern between media (thus photo-*lithography*, electron beam *lithography*), but especially those involving an etching step.

In the science community, this broadening of the definition of ‘lithography’ has led to coinage of the bulky terms ‘destructive’ and ‘constructive’ lithography to differentiate between processes that involve etching, and those that involve deposition of material. Thus, a hierarchal transposition has occurred. In the 19th Century, lithography was considered a form of printing; in the 21st Century, printing is considered a form of lithography. The new terms can be oxymoronic and confusing.

Herein, we shall make a simple distinction. Wherever possible, ‘lithography’ will refer to a patterning process that involves an etching step. ‘Printing’ will refer to a patterning process involving the deposition of material (i.e. of ‘ink’). Thus Dip-Pen Nanolithography (DPN) will be considered a printing technique. The verb ‘to print’ will be used in descriptions of the DPN process.

2. Personals pronouns are used in the plural form (‘we’ and ‘our’ rather than ‘I’ and ‘my’) as a stylistic preference throughout the thesis.

Chapter 1: General introduction

1.1 Towards nanobionics: the nanofabricational challenge

Medical bionic devices restore human function by interfacing electrical technology with the body.[1] Proven treatments include the Cochlear Implant (or "bionic ear") which has restored useful hearing to hundreds of thousands of patients with profound deafness,[2] and the deep brain stimulator, which has provided significant relief to sufferers of Parkinson's disease and chronic pain.[3] Many other devices are currently in development, such as implants to restore vision,[4] to restore limb movement[5] and as a means to control epileptic seizures.[6] In recent years, the use of electrical stimuli to encourage and direct regrowth of damaged tissue has also been explored.[7-10] The functional interface between any bionic device and the body is at the electrode which locally stimulates electroactive tissue.[11]

Current bionic devices use electrodes with geometrical areas of ~mm^2, where each electrode addresses thousands of cells. The performance of many bionic devices, particularly those designed to restore sensory function, could be greatly improved by fabricating arrays of many smaller electrodes, with each electrode targeting fewer cells.[12] Figure 1-1 compares a conventional cochlear implant with macro-scale platinum ring electrodes with a high density array implant as fabricated by Allitt et al., 2011. The high density array resulted in less activity at nonspecific

frequency regions in rat brains and produced significantly lower thresholds and larger dynamic ranges than the platinum ring electrode array.[12]

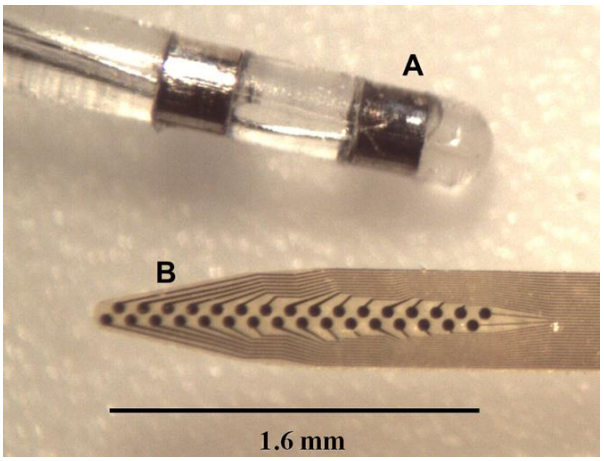

Figure 1-1: (A) The electrode array of a conventional cochlear implant consists of a platinum ring electrodes around a polydimethylsiloxane (PDMS) shank. (The figure shows a model fabricated for implantation into a rat.) (B) High density electrode array (HDA) of 32 iridium activated stimulation sites along a polyimide shank. The HDA resulted in less activity at nonspecific frequency regions of the inferior colliculus than the platinum ring array. The HDA also produced significantly lower thresholds and larger dynamic ranges.[12] [Reprinted from Hearing Research, 287, Allitt B.J. et al. 30-42, copyright (2012), with permission from Elsevier]

Microelectrode arrays of 100 μm diameter have been used to monitor neuronal cell activity *in vitro* for over thirty years.[13] Ideally, however, electrodes would interface with individual cells (cell body <30 μm diameter), or even individual axons and dendrites (cross-section <500 nm). This goal of electrode miniaturization presents new challenges on several levels. On one hand, the choice of material must be informed by the scaling of relevant properties as electrode area is decreased. For example, as a gold or platinum electrode is shrunk down, the poor charge injection capacity of noble metals becomes a limiting factor.[14] On the contrary, novel materials may show improved performance at smaller scales; shrinking a conducting polymer electrode can increase the surface/volume ratio resulting in a relative increase in redox switching speeds.[15] On the biological side, the interaction of cells with micron- and nanoscale features

must be understood. Research over the past decade has confirmed that living cells feel and respond to topographical and chemical patterns with dimensions on the order of tens of nanometres.[16,17] An inability to create structures of novel materials at nanometre length-scales will ultimately hamper development in both materials and understanding of the cell-material interface. The design of bionic devices with structure on the nanoscale constitutes the merging of bionics with nanotechnology, heralding the advent of 'nanobionics'.[18,19]

In the first instance, there is a need to fabricate model *in vitro* platforms with controlled nanodimensional architectures to address questions such as: how do living cells respond to an electrical stimulus from nanodimensional electrodes? Can enhanced performance of bionic devices be achieved by shrinking electrodes so as to address single cells? Can the growth of individual axons be directed using stimulation from electrodes of the same dimension (~500 nm) as they are? Can favourable scaling behaviours as electrodes are miniaturized (e.g., decreased switching time for conducting polymers) be usefully exploited?

Before beginning to answer these questions, we must have the capability to fabricate electrodes in predesigned, nanodimensional architectures, and on biocompatible substrates.[20] Soft, flexible, organic materials may not be compatible with conventional fabrication strategies, especially where definition of nanodimensional structure is a requisite.[21] This thesis aims to address this nanofabricational challenge by exploring the deposition of biocompatible electronic conductors on relevant substrates at submicron- to nanoscales.

1.2 Nanofabrication Techniques

The fabrication of nanostructured bionic devices poses a number of unique challenges. Recent work has highlighted how an artificial biomaterial must be as soft as the tissue with which it is integrated.[22] A nanostructure which

emulates the extra-cellular matrix is also desireable.[23] Additionally, the device may be loaded with drugs for the controlled release of anti-inflammatories or growth factors.[24,25] Future devices can be envisaged which will be laced with chemo-attractants to encourage interface with specific cell types. Fabrication of such devices will require structure on a hierarchy of scales from macro-, to micro- to nano-. It is unlikely that any one fabrication strategy will meet all of these requirements. We focus here on the fabrication of nanoscale elements only.

Nanofabrication has been defined as the process of making functional structures with arbitrary patterns having minimum feature size less than 100 nm in at least two spatial dimensions.[21] Recent reviews of the latest developments in nanofabrication can be found in the literature.[21,26,27]

An overview of some of the most important nanofabrication techniques is shown in Table 1-1. We will consider the strengths and weaknesses of each technique in terms of six main attributes: (i) Resolution (minimum feature size). Though this is the most obvious attribute for a nanofabrication technique, it is rarely the only consideration. The ultimate resolution of atom-by-atom placement was achieved using scanning tunnelling microscopy (STM) in 1990,[28] but other drawbacks prevent STM from becoming a viable nanofabrication platform. (ii) Pattern fidelity. The fabricated structure must be faithful to the original design. Each fabrication technique has its own idiosyncratic sources of defects. (iii) Registry. Where multiple step processing is required, it is imperative that sequential steps are performed in a precise overlay. Nanofabrication techniques often use high-quality piezo-electric positioning systems to achieve sub-nanometre precision in registration. (iv) Versatility (in both processible materials and in definable patterns). Some nanofabrication techniques are highly specialised in the materials they can process. Other techniques are limited in terms of the range patterns they can reliably achieve (directed self-assembly). (v) Throughput. This can be measured in

terms of the number of replications per hour. (vi) Cost. Both capital cost and operating cost must be considered.

Technique	*Materials*	*Advantages*	*Issues*	*Example bio applications*
Photo-lithography (PL)	Semi-conductors Metals	**Resolution Fidelity Registry** Multi-step processing	**Cost** Versatility Diffraction limit Req. mask	Neural interface devices (conventional materials)[29,30] Hi res stimulators (conventional materials)[31] Recording devices (organic conductors)[32-34]
Scanning beam lithography (SBL)	Speciality resist Polymers (PMMA)	**Resolution Fidelity Registry** Direct write	**Through-put** Cost	Niche device fabrication[35]
Nanoimprint lithography (NIL)	Polymers Prepolymers	Resolution	Lifetime of mould	Biomolecule patterning[36]
Contact printing (nCP, μCP)	SAMs, biomolecules nanoparticles	**Low cost**	Fidelity	Workhorse of research lithography Patterning cellular adhesion[37]
Self-assembly (SA)	Block copolymers Polymer blends	Simplicity Cost	Non-arbitrary pattern design	Nanoscale protein arrays[38,39]
Jet printing (JP)	Biomolecules Conducting polymers Living cells	Versatility	Resolution	Cell printing[40,41] Organic conductor tracks (micro-scale)[42]
Dip-pen nanolithography	SAMs, biomolecule, nanoparticle, liquids, polymers metals	Versatility Multi-plexing	Pattern fidelity (esp. liquids)	Biomolecule nanoarrays[43] Nanopatterned model substrates[44-46]

Table 1-1: An overview of selected nanofabrication strategies.
***Resolution: the minimum achievable feature-size.**
****Fidelity: the reproduction of a predefined pattern without defects.**
*****Registry: the precise overlay of successive patterns.**

1.2.1 Photolithography

The micro-processor has been described as the most complex device ever manufactured.[47] The drive to keep pace with Moore's law of periodically doubling transistor density has fuelled investment in ever more highly sophisticated photolithography systems over six decades.[48] As a result, photolithography is the most advanced lithography technology in operation.

The basic procedure of photolithography involves: (1) Coating of a planar substrate with a thin layer of photoresist, an organic material that undergoes a chemical change when exposed to UV light. (2) Exposure of the photoresist to UV light through a patterned mask. (3) Immersion in basic solution selectively dissolves the photoresist; a positive tone resist becomes soluble in developer, a negative tone resist becomes insoluble. The freshly exposed substrate is now amenable to further processing steps, such as deposition of metal contacts. (4) After processing, the remaining photoresist is removed by further chemical treatment.

The diffraction limit of light ($\lambda/4$, where λ is the wavelength of the light) seems to impose a fundamental limit on the feature size which is definable by photolithography. In order to beat the diffraction limit, a number of sophisticated resolution enhancement strategies have been developed, such as immersion lithography,[49] optical proximity correction[50] and others. The switch to ever shorter wavelengths of light also increases resolution, though requires considerable investment in equipment and in new resist materials.[51] The resolution of the most advanced photolithography facilities is currently less than 20 nm. Sub-nanoscale registry enabled by high-end alignment and manipulation systems.[52] Defects can arise from contamination with airborne particles and so commercial lithography systems are housed in class 10 cleanrooms. Throughput for a single process step is on the order of hundreds of wafers per hour.[47]

The main limitation of high-end photolithography is its prohibitive expense for most applications. High powered excimer lasers and precision optical elements are required, and can cost tens of millions of dollars. Huge operational cost is also associated with maintaining the clean-room environment. Semi-conductor fabrication is very expensive, but there are different levels of photolithography. Many research institutions are also home to photolithography systems as standard fabrication equipment. Research scale photolithography is relatively unsophisticated and rarely achieves resolution to beat the diffraction limit. At its most basic,

transparency films patterned with an office printer can be used as photomasks for >50 μm features, though resolution can be greatly improved by projection through an optical microscope.[53]

Photolithography has been used to fabricate high-resolution semiconductor devices for investigating the electrode interface at a single cell level. The Fromherz group at the Max Planck Institute for Biochemistry in Munich have been pioneers in this field.[54] For example, Figure 1-2 (A) shows a hippocampal neuron cell cultured on an electrolyte-oxide-silicon (EOS) field-effect transistor, and (B) shows a schematic cross section of the neuron on transistor with blow-up of the contact area.[29] Signal transduction occurs via current in the cell membrane (flowing during an action potential) creating an extracellular voltage in the cleft and thus modulating the source–drain current. Another group has used photolithography to fabricate arrays of individually addressable 2 μm diameter electrodes for the localized stimulation of neurons with sub-cellular resolution. Figure 1-2 (C) shows a scanning electron micrograph of a primary hippocampal neuron (3DIV) on top of such a micro-electrode array chip.[31]

Although highly successful for fabricating devices from metals and crystalline semiconductors, photolithography processes are usually tailored to specific materials and harsh developer solutions may be incompatible with the non-conventional materials (such as soft, organic conductors) ear-marked for bionic applications.[19] Novel processes are being developed to extend photolithography to organic materials. For example, the Malliaras group at Cornell University (now at the Ecole des Mines de Saint Etienne) has shown how organic electronic devices can be fabricated through a parylene lift-off approach.[55] The group have fabricated a range of devices to interface with living cells, in particular organic electrochemical transistors capable of detecting neurotransmitter release from single neurons[32] and flexible, highly conformal devices for *in vivo* recording.[34] Figure 1-2 (D) shows a high density array of 64 organic electrochemical transistors (OECTs) fabricated by the Malliaras group. The transistors were

composed of a 6 μm long poly(3,4-ethylenedioxythiophene):poly(styrene sulfonate) channel contacted by gold electrodes.[56] (E) The inset shows a magnified view of an individual OECT in the array, and (F) shows a schematic of the photolithography process. Although organic electronic devices have been successfully fabricated in this manner, feature size is presently limited by the lift-off process to >1 μm.[55]

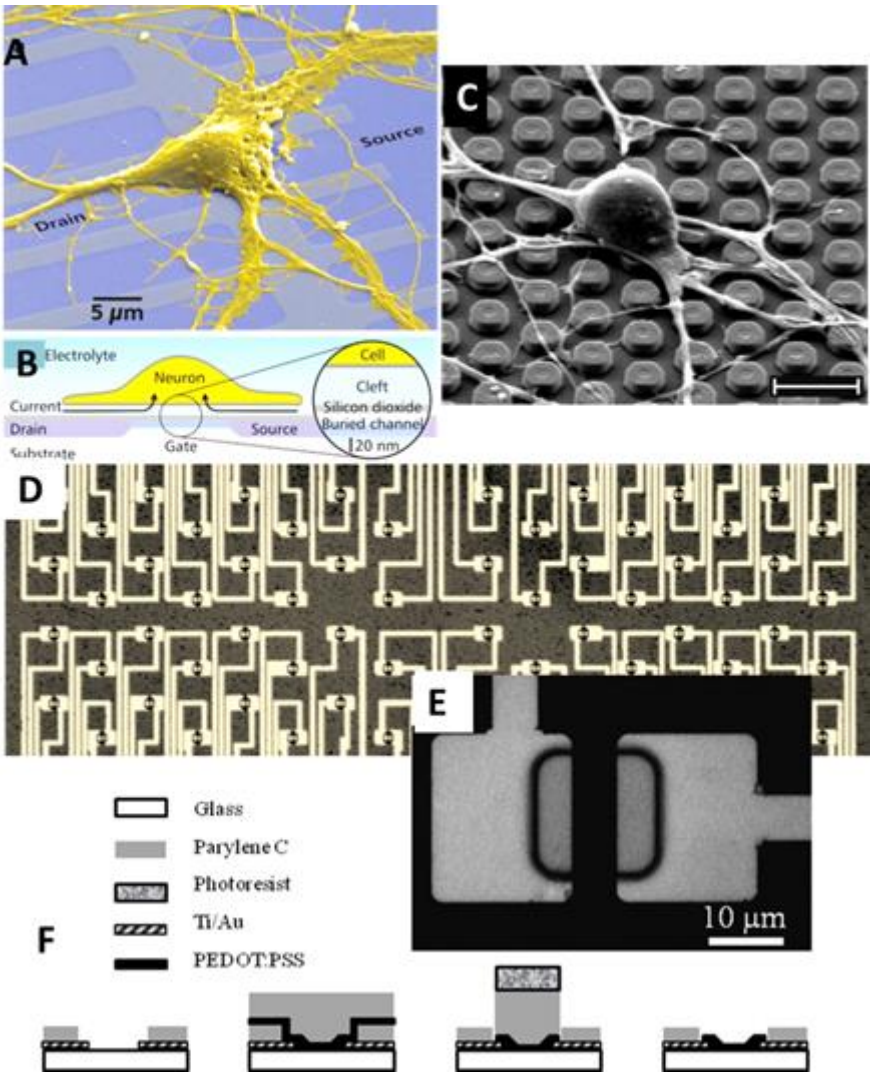

Figure 1-2: High density electrode arrays fabricated by photolithography. (A) Scanning electron micrograph (colorized) of a hippocampal neuron cultured on an electrolyte-oxide-silicon (EOS) field-effect transistor. (B) Schematic cross section of a neuron on a buried-channel field-effect transistor with blow-up of the contact area. [(A-B) reproduced from Small 1, 206–10 copyright 2005 with permission from Wiley & Sons.][29] (C) Scanning electron micrograph of a primary hippocampal neuron (3DIV) on top of a

micro-electrode array chip (TiN coated tungsten electrodes in SiO_2). Scale bar 5 μm. Reprinted from Biosensors and Bioelectronics 26, 1474-7 copyright 2010 with permission from Elsevier.[31] (D) A high density array of 64 organic electrochemical transistors (OECTs). The transistors were composed of a 6 μm long poly(3,4-ethylenedioxythiophene):poly(styrene sulfonate) channel contacted by gold electrodes.[56] (E) The inset shows a magnified view of an individual OECT in the array, and (F) shows a schematic of the photolithography process. [(D-F) reprinted with permission from Khodagholy et al. Applied Physics Letters 99, 163304 copyright 2011 AIP Publishing LLC.[56]]

1.2.2 Scanning beam lithography

Scanning beam lithography (SBL) is a direct-write technique where a spot of a tightly focused beam is used to generate a pattern by either the selective removal of material or the selective deposition of a species. The pattern can be generated on a resist for further processing (such as etching), or on the substrate directly. SBL is very slow (requiring up to 24 hours per cm^2 for 20 nm scale features)[21] but its high resolution and pattern fidelity make it a critical technology for the fabrication of masks for photolithography.

The main classes of SBL include scanned laser beams, electron beams (EBL) and focused ion beams (FIB). Laser beams are relatively cheap, but feature sizes are limited to ~250 nm and above. EBL and FIB systems can achieve <10 nm resolution, but are more expensive to purchase and maintain. Throughput is often not a large concern in research, and SBL is widely used for generating arbitrary patterns for niche applications and for the fabrication of device prototypes. Figure 1-3 (A) shows an array of nanowire transistors fabricated by the Lieber group at Harvard for their pioneering work in interfacing with neuron cells. The group succeeded in interfacing a single axon with a linear array of 50 SBL fabricated nanowire devices and thus monitor the propagation of an action potential.[35]

1.2.3 Micro- and nano contact printing

The contact printing technique uses a patterned elastomeric stamp (typically PDMS) to transfer molecules to a substrate, typically via the formation of covalent bonds (e.g. self-assembled alkanethiolates on gold).[57,58] The flexibility of the stamp is advantageous for achieving conformal contact over large areas or on curved surfaces.[21] Resolution is determined by the feature size of the stamp. Although typically used to generate micron-scale features, sub 100 nm resolution has been demonstrated.[59] Limitations to feature size arise from the fidelity of the molding process used to create the stamp, the properties of the stamp material (e.g. ability to retain nanoscale features), distortion of the stamp while in contact with the surface and the substrate grain size.[21] Additional defects can also arise from the contamination of the substrate with PDMS molecules from the stamp during printing.[60,61]

The major advantage of contact printing is its low cost. Once a master mold is fabricated, PDMS stamps can be so cheap as to be considered a disposable reagent.[26] The technique has been widely adopted by the biomedical research community for applications such as; patterning ECM proteins for controlling cellular adhesion,[62] fabricating model substrates to study cellular biomechanics[63] and for creating bio-molecular gradients.[64] Figure 1-3 (B) shows a biomolecule array generated by μCP for an in vitro study of cellular spreading as a function of ECM geometry. B16 (murine myeloma) cells were cultured on substrata patterned with different geometrical arrangements of the cell adhesion protein fibronectin. The degree of spreading was found to be dependent on spacing of the fibronectin features.[65]

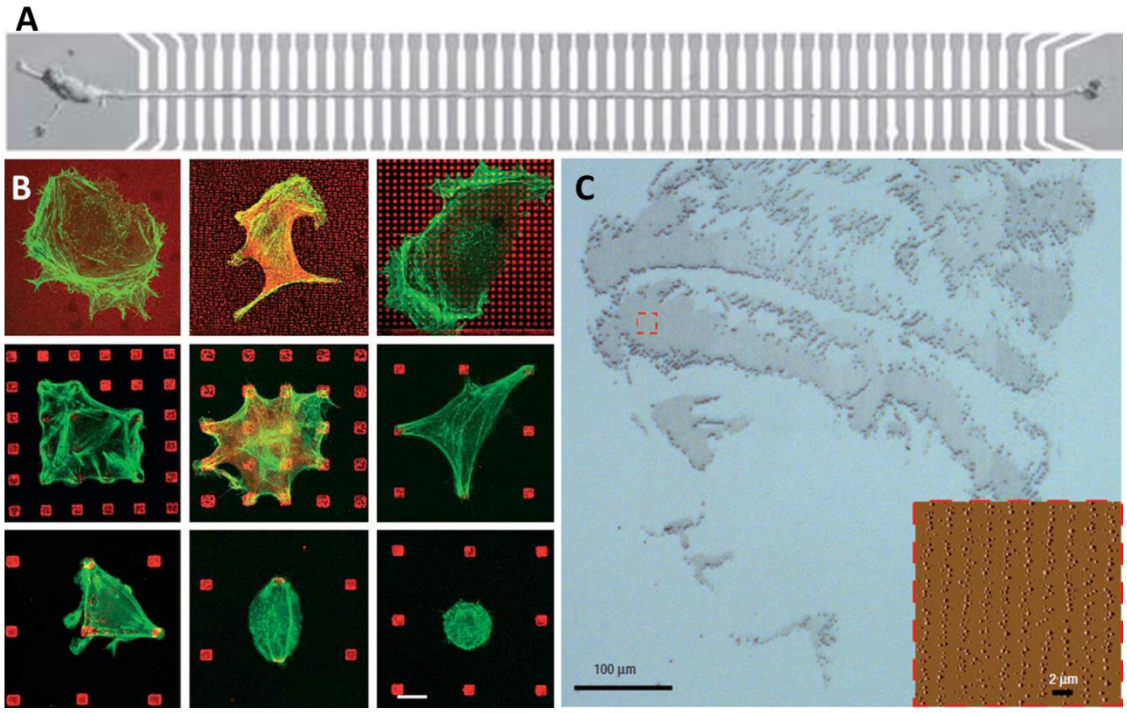

Figure 1-3: Fabrication by scanning beam lithography (SBL), micro-contact printing (µCP) and electrohydrodynamic jet (e-jet) printing. (A) SBL was used to fabricate a linear array of fifty nanowire (NW) transistors. Axon growth was direct along the NW junctions by patterning poly-L-lysine. The array of transistors used to follow the propagation of an action potential along the axon. [From Patolsky, F. et al. Science (New York, N.Y.) 313, 1100-4 (2006). Reprinted with permission from AAAS.[35]] (B) The images show B16 (murine myeloma) cells cultured on fibronectin substrata as patterned by µCP and labelled for fibronectin (red) and actin (green). The degree of spreading was found to be dependent on spacing of the fibronectin features.[Adapted with permission from the Journal of Cell Science (2004)[65]] (C) High resolution liquid deposition by e-jet printing. Optical micrograph of a portrait of the ancient scholar, Hypatia, printed using a polyurethane ink and a 500-nm-internal-diameter nozzle. The inset shows an AFM image of the printed dots.[Reprinted by permission from Macmillan Publishers Ltd: Nature materials 6, 782-9 copyright (2007)[66].]

1.2.4 Nanoimprint lithography

Nanoimprint lithography (NIL) involves using a patterned master to 'imprint' a structured topography into a deformable substrate.[67,68] In some variants the substrate polymer is made deformable on contact by the application of heat, and cooled again before removal of the master. In

other variants, a liquid precursor is placed in contact with the master and then cured by heat or UV light. Quartz molds, in particular, allow for alignment on optical markings and for UV exposure to photo-crosslink the molded prepolymer.[69] Minimum feature sizes of 5 nm have been demonstrated by NIL,[70] and the technique may be compatible with a roller for extremely high throughput manufacture.[71] Its maturation as a potential technique in the semiconductor fabrication industry is evidenced by its recent incorporation in the International Technology Roadmap for Semiconductors.[48]

One major issue with NIL is associated with the release of contact. A non-adhesive release layer, often a fluorinated silane, must be used to allow for removal of the master without distortion of the substrate pattern. Despite the release layers, NIL masters usually have a limited lifetime,[21] and defects can accumulate after repeated usage of the same stamp.[48]

NIL is versatile in material compatibility and has been used to pattern organic conductors, DNA and proteins at a <100 nm resolution.[36,72,73] In terms of biomolecule printing, it remains to be seen whether NIL can provide additional capabilities over the simpler nCP technique.

1.2.5 Jet printing

Although ink-jet printing (IJP) was initially developed for the publishing industry, it has been adopted as an important and versatile technique for direct-write deposition of many functional materials.[74] One unique prospect of IJP is incorporation of living cells within the ink, leading to the possibility of 'bio-fabricating' structures composed of both material and living components.[40,41] IJP is ostensibly a micro-scale fabrication technique, with a lower limit of droplet size in the picolitre range. Nevertheless, clever wetting/de-wetting strategies can be used to fabricate devices with nanoscale resolution using IJP.[75-77] A technique related to IJP, known as electrohydrodynamic jet printing (e-JP) has been recently devised which

can jet femtolitre and even attolitre volumes, corresponding to droplets with diameter on the ~200 nm scale.[66,78] Resolution is dependent on liquid properties, substrate wettability and the diameter of the jet nozzle. e-JP is promising… however it is limited in that a conductive substrate must be used. Figure 1-3 (C) shows a pattern e-jet printed using a polyurethane ink and a 500-nm-internal-diameter nozzle. Individual dots have a diameter of ~490 nm. The inset shows an AFM image of the printed dots.[66]

1.2.6 Self-assembly

Self-assembly (SA) is the spontaneous organization of components into a desired structure. SA can achieve molecular scale resolution as it is properties inherent in the molecular interaction cause them to into a locally defined, ordered arrangement. SA is useful for the patterning of block-copolymers, self-assembled monolayers or nanoparticles. SA structures are prone to defects, however, and only a limited number of different ordered arrangements are possible. Block copolymer lithography, a form of SA, has been used to generate model substrates with periodic arrays of cell adhesion proteins.[39]

The directed self-assembly (DSA) method is a modified SA technique where a block copolymer or polymer blend is deposited on a substrate, and then annealed in such a way as to "direct" it to form ordered structures, such as periodic lines.[79] DSA is being actively pursued as a potential method to generate sub 10 nm features in semi-conductor industry and has been included in the most recent ITRS report.[48] A major disadvantage, however, is that neither SA nor DSA can generate arbitrary patterns. Further processing is required in order to fabricate complex structures.

1.3 Dip-pen nanolithography

Dip-pen nanolithography (DPN) is one further candidate technology for fabricating novel substrates tailored at the nanometre scale. DPN is an

additive lithography technique which uses an atomic force microscope (AFM) tip to deposit molecules or materials in a direct-write fashion.[80] Many of the essential ingredients of prospective nanobionic devices can be printed by DPN including metals,[81–85] insulators[86] and conducting polymers.[87–89] DPN also enables the nanoscale patterning of biomolecule cues through the deposition of DNA and proteins.[90,91] The capability to 'multiplex' many different biomolecules within a subcellular area allows for the creation of complex substrates tailored with biomolecules on the nanometre scale, with huge implications for both fundamental and applied cell biology.[92] The non-destructive nature of DPN means it is compatible with many substrates including soft, flexible polymers[93] and even biological tissue.[94] Although AFM based lithography has traditionally been regarded as a serial, and therefore slow fabrication technique, great strides have been made in parallelization of DPN; first to "massively parallel" 55000 cantilever arrays,[95] and more recently using polymer pen lithography (PPL) arrays capable of simultaneously printing up to 11 million patterns over cm^2 areas.[96] DPN is already finding use as a tool for fabricating novel nanopatterned cell-growth platforms for fundamental cell-biology studies.[44–46,97,98]

Particularly unique is the ability of DPN to manipulate minute quantities of liquids.[85,91,93,99] Liquid inks are interesting in the biomedical field for their ability to operate as 'universal' carrier matrices for biomolecules.[91] The patterning of hydrogels is fascinating as it may also provide a novel means to tailor a heterogeneous soft material interface at the nanoscale.[99] Liquid deposition patterning is usually not substrate specific and so is versatile enough for printing on a variety of hard and soft substrates.[93] The development of liquid ink DPN may also by accelerated by the adaption of many hundreds of strategies already developed for other liquid printing techniques, such as ink jet printing.[74]

In order to take advantage of liquid ink DPN for bionic applications, a number of limitations must be overcome. In particular, the ink transport

mechanism is poorly understood and techniques to enable a more stringent control of feature size are required. In addition, strategies for the deposition of functional materials on biocompatible substrates are lacking.

The scope of this thesis is limited to the development and characterisation of liquid ink DPN as a nanofabrication strategy for electrode materials.

1.4 Thesis aims

The broad aims of the thesis are to:

1. Develop strategies for the deposition of biocompatible electrode materials on biocompatible substrates and at nanoscale resolution using liquid ink DPN.

2. Develop an understanding of the mechanism of liquid ink DPN deposition using a model ink system.

3. Characterise and develop methods to overcome the limitations of liquid ink DPN in terms of pattern fidelity and resolution.

1.5 Thesis content

Chapter 2 is a review chapter. We chart the development of the DPN technique in terms of instrumentation, ink development and applications. Background is provided to the theory of ink transport for both molecular and liquid inks. The deficiencies in current understanding of liquid ink DPN are also outlined.

In **Chapter 3**, we describe the development of an oxidant ink for the vapour phase polymerisation of the conducting polymer poly(3,4-ethylenedioxythiophene) (PEDOT) via in situ vapour phase polymerisation. DPN patterning of the oxidant ink was facilitated by the incorporation of an amphiphilic block copolymer thickener, an additive that also assists with

stabilization of the oxidant. When exposed to EDOT monomer in a VPP chamber, each deposited feature localized the synthesis of conducting PEDOT structures of several micrometres down to 250 nm in width. PEDOT patterns are characterized by atomic force microscopy (AFM), conductive AFM, two probe electrical measurement, and micro-Raman spectroscopy, evidencing in situ vapor phase synthesis of conducting polymer at a scale (picogram) which is much smaller than that previously reported. Although the process of VPP on this scale was achieved, we highlight some of the challenges that need to be overcome to make this approach feasible in an applied setting.

In **Chapter 4** we describe the development of a platinum precursor (H_2PtCl_6) based liquid ink to DPN print onto hard and soft, flexible substrates with nanoscale resolution. The ink formulation could be printed on Si, glass, ITO, Ge, PDMS, Parylene C and even a human hair. A mild plasma treatment effected reduction of the precursor patterns *in situ* without subjugating the substrate to destructively high temperatures. Feature size was controlled via dwell time and degree of ink loading, and platinum features with 50 nm dimensions could be routinely achieved on Si. A modified method enabled deposition of micron scale Pt snowflakes. By tuning the substrate hydrophobicity using functionalization with a long chain alkane group we can temper spreading of the precursor solution and effect fractal-like crystal growth via a diffusion limited mechanism. Reduction of the precursor crystal by plasma treatment results in a 2D dendritic structure composed of ~5 nm Pt nanoparticles. This combined top-down, bottom-up approach enables the arbitrary placement of Pt fractal-like structures on Si or glass. We characterized morphology by optical microscopy, SEM and AFM. We confirm the electrical conductivity of printed platinum by two point probe measurements and we characterize electrochemical activity using Scanning Electrochemical Microscopy (SECM).

In **Chapter 5** we use model ink-substrate systems (exhibiting a range of viscosities and wettabilities) to explore various methods of controlling

feature size in liquid ink DPN. The ink-transfer mechanism is investigated using AFM force measurements acquired during ink deposition. We use the information as a means to elucidate the shape of the meniscus during deposition and illustrate a method to monitor the volume of deposition *in-situ*. However, the deposition rate is found to change dramatically over the course of an experiment. Thus, the instantaneous volume of ink on the pen is found to be a critical factor in determining deposition rate.

In **Chapter 6** we examine the effect of depleting ink volume on deposition rate over a long term experiment and uncover a hierarchy of phenomena related to ink movement and reorganisation along the cantilever. These 'ink-on-tip hydrodynamics' are elucidated to arise from (I) changes in ink volume on cantilever, (II) 'rest-time' between grids and (III) travel time between individual dots. In light of our conclusions, we pose critical questions of reservoir-on-tip liquid ink DPN as a nanofabrication technique and discuss the various parameters which need to be controlled in order to achieve uniformity of feature size.

In **Chapter 7** we outline the main conclusions of the thesis, including the main advantages and fundamental limitations of liquid ink DPN. We also discuss the future development of the technique in light of the recent closure of the Nanoink company.

1.6 References

1. Wallace, G. G., Moulton, S. E., Kapsa, R. M. I. & Higgins, M. J. *Organic Bionics*. (Wiley-VCH Verlag GmbH & Co. KGaA: Weinheim, Germany, 2012).doi:10.1002/9783527646029

2. Clark, G. M. The multiple-channel cochlear implant: the interface between sound and the central nervous system for hearing, speech, and language in deaf people-a personal perspective. *Philosophical transactions of the Royal Society of London. Series B, Biological sciences* **361**, 791–810 (2006).

3. Perlmutter, J. S. & Mink, J. W. Deep brain stimulation. *Annual review of neuroscience* **29**, 229–57 (2006).

4. Ong, J. M. & Da Cruz, L. The bionic eye: a review. *Clinical & experimental ophthalmology* **40**, 6–17 (2012).

5. *Neural prostheses for restoration of sensory and motor function. Vol 4.* (CRC Press: 2010).

6. Velasco, A. L. *et al*. Electrical stimulation of the hippocampal epileptic foci for seizure control: a double-blind, long-term follow-up study. *Epilepsia* **48**, 1895–903 (2007).

7. Al-majed, A. A., Neumann, C. M., Brushart, T. M. & Gordon, T. Brief Electrical Stimulation Promotes the Speed and Accuracy of Motor Axonal Regeneration. **20**, 2602–2608 (2000).

8. Brushart, T. M. *et al*. Electrical Stimulation Promotes Motoneuron Regeneration without Increasing Its Speed or Conditioning the Neuron. **22**, 6631–6638 (2002).

9. Flaibani, M. *et al*. Muscle differentiation and myotubes alignment is influenced by micropatterned surfaces and exogenous electrical stimulation. *Tissue engineering. Part A* **15**, 2447–57 (2009).

10. Tandon, N. *et al*. Electrical stimulation systems for cardiac tissue engineering. *Nature protocols* **4**, 155–73 (2009).

11. Wallace, G. G., Moulton, S. E. & Clark, G. M. Electrode-Cellular Interface. *Science* **324**, 185–186 (2009).

12. Allitt, B. J. *et al*. Midbrain responses to micro-stimulation of the cochlea using high density thin-film arrays. *Hearing research* **287**, 30–42 (2012).

13. Gross, G. W., Rieske, E., Kreutzberg, G. W. & Meyer, A. A new fixed-array multi-microelectrode system designed for long-term monitoring of extracellular single unit neuronal activity in vitro. *Neuroscience Letters* **6**, 101–105 (1977).

14. Cogan, S. F. Neural stimulation and recording electrodes. *Annual review of biomedical engineering* **10**, 275–309 (2008).

15. Higgins, M. J., Mcgovern, S. T. & Wallace, G. G. Visualizing Dynamic Actuation of Ultrathin Polypyrrole Films. *Microscopy* 3627–3633 (2009).

16. Stevens, M. M. & George, J. H. Exploring and engineering the cell surface interface. *Science (New York, N.Y.)* **310**, 1135–8 (2005).

17. Yim, E. K. F. & Leong, K. W. Significance of synthetic nanostructures in dictating cellular response. *Scanning Electron Microscopy* **1**, 10 – 21 (2005).

18. Moulton, S. E. & Wallace, G. G. An introduction to nanobionics. *Materials Australia* 22–23 (2008).

19. Moulton, S. E., Higgins, M. J., Kapsa, R. M. I. & Wallace, G. G. Organic Bionics: A New Dimension in Neural Communications. *Advanced Functional Materials* **22**, 2003–2014 (2012).

20. Pan, T. & Wang, W. From cleanroom to desktop: emerging micro-nanofabrication technology for biomedical applications. *Annals of biomedical engineering* **39**, 600–20 (2011).

21. Gates, B. D. *et al.* New approaches to nanofabrication: molding, printing, and other techniques. *Chemical reviews* **105**, 1171–96 (2005).

22. Discher, D. E., Janmey, P. & Wang, Y. Tissue Cells Feel and Respond to the Stiffness of Their Substrate. *Science* **1139**, (2009).

23. Dvir, T., Timko, B. P., Kohane, D. S. & Langer, R. Nanotechnological strategies for engineering complex tissues. *Nature nanotechnology* **6**, 13–22 (2011).

24. Langer, R. Biomaterials in Drug Delivery and Tissue Engineering : One Laboratory ' s Experience. *Accounts of Chemical Research* **33**, 94–101 (2000).

25. Green, R. A., Lovell, N. H., Wallace, G. G. & Poole-warren, L. A. Biomaterials Conducting polymers for neural interfaces : Challenges

in developing an effective long-term implant q. *Hearing Research* **29**, 3393–3399 (2008).

26. Geissler, M. & Xia, Y. Patterning: Principles and Some New Developments. *Advanced Materials* **16**, 1249–1269 (2004).

27. Wang, Y., Mirkin, C. A. & Park, S. Nanofabrication beyond Electronics. **3**, 1049–1056 (2009).

28. Eigler, D. M. & Schweizer, E. K. Positioning single atoms with a scanning tunnelling microscope. *Nature* **344**, 524–526 (1990).

29. Voelker, M. & Fromherz, P. Signal transmission from individual mammalian nerve cell to field-effect transistor. *Small (Weinheim an der Bergstrasse, Germany)* **1**, 206–10 (2005).

30. Eversmann, B. *et al*. A Neural Tissue Interfacing Chip for In-Vitro Applications with 32k Recording / Stimulation Channels on an Active Area of 2 . 6 mm 2. 211–214 (2011).

31. Braeken, D. *et al*. Localized electrical stimulation of in vitro neurons using an array of sub-cellular sized electrodes. *Biosensors & bioelectronics* **26**, 1474–7 (2010).

32. Yang, S. Y. *et al*. Detection of Transmitter Release from Single Living Cells Using Conducting Polymer Microelectrodes. 1–5 (2011).doi:10.1002/adma.201100035

33. Khodagholy, D. *et al*. Highly conformable conducting polymer electrodes for in vivo recordings. *Advanced materials (Deerfield Beach, Fla.)* **23**, H268–72 (2011).

34. Khodagholy, D. *et al*. In vivo recordings of brain activity using organic transistors. *Nature Communications* **4**, 1575 (2013).

35. Patolsky, F. *et al*. Detection, stimulation, and inhibition of neuronal signals with high-density nanowire transistor arrays. *Science (New York, N.Y.)* **313**, 1100–4 (2006).

36. Ohtake, T., Nakamatsu, K., Matsui, S., Tabata, H. & Kawai, T. DNA nanopatterning with self-organization by using nanoimprint. *Journal of Vacuum Science & Technology B: Microelectronics and Nanometre Structures* **22**, 3275 (2004).

37. Mrksich, M. *et al*. Controlling cell attachment on contoured surfaces with self-assembled monolayers of alkanethiolates on gold. **93**, 10775–10778 (1996).

38. Malmström, J. *et al*. Large area protein patterning reveals nanoscale control of focal adhesion development. *Nano letters* **10**, 686–94 (2010).

39. Spatz, J. P. & Geiger, B. Molecular engineering of cellular environments: cell adhesion to nanodigital surfaces. *Methods in cell biology* **83**, 89–111 (2007).

40. Calvert, P. Printing cells. *Science (New York, N.Y.)* **318**, 208–9 (2007).

41. Ferris, C. J. *et al*. Bio-ink for on-demand printing of living cells. *Biomaterials Science* **1**, 224 (2013).

42. Weng, B., Liu, X., Higgins, M. J., Shepherd, R. & Wallace, G. Fabrication and characterization of cytocompatible polypyrrole films inkjet printed from nanoformulations cytocompatible, inkjet-printed polypyrrole films. *Small (Weinheim an der Bergstrasse, Germany)* **7**, 3434–8 (2011).

43. Lee, K.-B., Kim, E.-Y., Mirkin, C. a. & Wolinsky, S. M. The Use of Nanoarrays for Highly Sensitive and Selective Detection of Human Immunodeficiency Virus Type 1 in Plasma. *Nano Letters* **4**, 1869–1872 (2004).

44. Curran, J. M. *et al*. Nanoscale definition of substrate materials to direct human adult stem cells towards tissue specific populations. *Journal of materials science. Materials in medicine* **21**, 1021–9 (2010).

45. Hoover, D. K., Chan, E. W. L. & Yousaf, M. N. Asymmetric peptide nanoarray surfaces for studies of single cell polarization. *Journal of the American Chemical Society* **130**, 3280–1 (2008).

46. Hoover, D. K., Lee, E., Chan, E. W. L. & Yousaf, M. N. Electroactive nanoarrays for biospecific ligand mediated studies of cell adhesion. *Chembiochem : a European journal of chemical biology* **8**, 1920–3 (2007).

47. Intel From sand to circuits: How Intel makes integrated circuit chips. (2008).

48. *International Technology Roadmap for Semiconductors*. (Semicoductor Industry Association: 2012).at <http://www.itrs.net/Links/2012ITRS/2012Chapters/2012Overview.pdf>

49. Switkes, M. & Rothschild, M. Immersion lithography at 157 nm. *Journal of Vacuum Science & Technology B: Microelectronics and Nanometre Structures* **19**, 2353 (2001).

50. Huang, L.-D. & Wong, M. D. F. Optical proximity correction (OPC). *Proceedings of the 41st annual conference on Design automation - DAC '04* 186 (2004).doi:10.1145/996566.996622

51. Rothschild, M. *et al*. Recent Trends Optical Lithography. *Lincoln Laboratory Journal* **14**, 221–236 (2003).

52. Corporation, I. From Sand to Silicon " Making of a Chip " Illustrations 32nm High-K / Metal Gate – Version. 1–16 (2011).

53. Love, J. C., Wolfe, D. B., Jacobs, H. O. & Whitesides, G. M. Microscope Projection Photolithography for Rapid Prototyping of Masters with Micron-Scale Features for Use in Soft Lithography. *Langmuir* **17**, 6005–6012 (2001).

54. Fromherz, P. Electrical interfacing of nerve cells and semiconductor chips. *Chemphyschem : a European journal of chemical physics and physical chemistry* **3**, 276–84 (2002).

55. Defranco, J. A., Schmidt, B. S., Lipson, M. & Malliaras, G. G. Photolithographic patterning of organic electronic materials. *Organic Electronics* **7**, 22–28 (2006).

56. Khodagholy, D. *et al*. High speed and high density organic electrochemical transistor arrays. *Applied Physics Letters* **99**, 163304 (2011).

57. Kumar, A., Biebuyck, H. a. & Whitesides, G. M. Patterning Self-Assembled Monolayers: Applications in Materials Science. *Langmuir* **10**, 1498–1511 (1994).

58. Monolayers, S., Wilbur, B. J. L., Kumar, A., Kim, E. & Whitesides, G. M. Microfabrication by Microcontact Printing of Self-Assembled Monolayers **. 600–604 (1994).

59. Li, H., Muir, B. V. O., Fichet, G. & Huck, W. T. S. Nanocontact Printing: A Route to Sub-50-nm-Scale Chemical and Biological Patterning. *Langmuir* **19**, 1963–1965 (2003).

60. Hale, P. S. *et al*. Minimizing silicone transfer during micro-contact printing. *Applied Surface Science* **253**, 3746–3750 (2007).

61. Thibault, C., Séverac, C., Mingotaud, A.-F., Vieu, C. & Mauzac, M. Poly(dimethylsiloxane) contamination in microcontact printing and its

influence on patterning oligonucleotides. *Langmuir : the ACS journal of surfaces and colloids* **23**, 10706–14 (2007).

62. Ostuni, E., Whitesides, G. M., Ingber, D. E. & Chen, C. S. Using self-assembled monolayers to pattern ECM proteins and cells on substrates. *Methods in molecular biology (Clifton, N.J.)* **522**, 183–94 (2009).

63. Tan, J. L. *et al*. Cells lying on a bed of microneedles : An approach to isolate mechanical force. **2002**, (2002).

64. Weibel, D. B., Diluzio, W. R. & Whitesides, G. M. Microfabrication meets microbiology. *Nature reviews. Microbiology* **5**, 209–18 (2007).

65. Lehnert, D. *et al*. Cell behaviour on micropatterned substrata: limits of extracellular matrix geometry for spreading and adhesion. *Journal of cell science* **117**, 41–52 (2004).

66. Park, J.-U. *et al*. High-resolution electrohydrodynamic jet printing. *Nature materials* **6**, 782–9 (2007).

67. Chou, S. Y. Nanoimprint lithography. *Journal of Vacuum Science & Technology B: Microelectronics and Nanometre Structures* **14**, 4129 (1996).

68. Guo, L. J. Nanoimprint Lithography: Methods and Material Requirements. *Advanced Materials* **19**, 495–513 (2007).

69. Colburn, M. *et al*. Step and flash imprint lithography: a new approach to high-resolution patterning. *Proc. SPIE 3676, Emerging Lithographic Technologies III* 379–389 (1999).doi:10.1117/12.351155

70. Austin, M. D. *et al*. Fabrication of 5 nm linewidth and 14 nm pitch features by nanoimprint lithography. *Applied Physics Letters* **84**, 5299 (2004).

71. Tan, H. Roller nanoimprint lithography. *Journal of Vacuum Science & Technology B: Microelectronics and Nanometre Structures* **16**, 3926 (1998).

72. Leising, G. *et al*. Nanoimprinted devices for integrated organic electronics. *Microelectronic Engineering* **83**, 831–838 (2006).

73. Hoff, J. D., Cheng, L.-J., Meyhöfer, E., Guo, L. J. & Hunt, A. J. Nanoscale Protein Patterning by Imprint Lithography. *Nano Letters* **4**, 853–857 (2004).

74. Calvert, P. Inkjet Printing for Materials and Devices. *Chemistry of Materials* **13**, 3299–3305 (2001).

75. Sirringhaus, H. High-Resolution Inkjet Printing of All-Polymer Transistor Circuits. *Science* **290**, 2123–2126 (2000).

76. Wang, J. Z., Zheng, Z. H., Li, H. W., Huck, W. T. S. & Sirringhaus, H. Dewetting of conducting polymer inkjet droplets on patterned surfaces. *Nature materials* **3**, 171–6 (2004).

77. Caironi, M., Gili, E., Sakanoue, T., Cheng, X. & Sirringhaus, H. High yield, single droplet electrode arrays for nanoscale printed electronics. *ACS nano* **4**, 1451–6 (2010).

78. Rogers, J. a & Paik, U. Nanofabrication: Nanoscale printing simplified. *Nature nanotechnology* **5**, 385–6 (2010).

79. Farrell, R. A. *et al*. Large-scale parallel arrays of silicon nanowires via block copolymer directed self-assembly. *Nanoscale* **4**, 3228–36 (2012).

80. Piner, R. D., Zhu, J., Xu, F., Hong, S. & Mirkin, C. A. "Dip-Pen" Nanolithography. *Science* **283**, 661–663 (1999).

81. Li, Y., Maynor, B. W. & Liu, J. Electrochemical AFM "Dip-Pen" Nanolithography. *Journal of the American Chemical Society* **123**, 2105–2106 (2001).

82. Nelson, B. a., King, W. P., Laracuente, a. R., Sheehan, P. E. & Whitman, L. J. Direct deposition of continuous metal nanostructures by thermal dip-pen nanolithography. *Applied Physics Letters* **88**, 033104 (2006).

83. Weinberger, D. A., Hong, S., Mirkin, C. A., Wessels, B. W. & Higgins, T. B. Combinatorial Generation and Analysis of Nanometre- and Micrometer-Scale Silicon Features via "Dip-Pen" Nanolithography and Wet Chemical Etching. *Advanced Materials* **12**, 1600–1603 (2000).

84. Wang, H. *et al*. Toward conductive traces : Dip Pen Nanolithography ® of silver nanoparticle-based inks. *Applied Physics Letters* 143105 (2008).doi:10.1063/1.2995859

85. Hung, S. *et al*. Dip Pen Nanolithography of Conductive Silver Traces. *The Journal of Physical Chemistry C* 9672–9677 (2010).

86. Hernandez-Santana, A., Irvine, E., Faulds, K. & Graham, D. Rapid prototyping of poly(dimethoxysiloxane) dot arrays by dip-pen nanolithography. *Chemical Science* **2**, 211 (2011).

87. Maynor, B. W., Filocamo, S. F., Grinstaff, M. W. & Liu, J. Direct-Writing of Polymer Nanostructures: Poly(thiophene) Nanowires on Semiconducting and Insulating Surfaces. *Journal of the American Chemical Society* **124**, 522–523 (2002).

88. Su, M., Aslam, M., Fu, L., Wu, N. & Dravid, V. P. Dip-pen nanopatterning of photosensitive conducting polymer using a monomer ink. *Applied Physics Letters* **84**, 4200 (2004).

89. Lim, J.-H. & Mirkin, C. A. Electrostatically Driven Dip-Pen Nanolithography of Conducting Polymers. *Advanced Materials* **14**, 1474–1477 (2002).

90. Lim, J.-H. *et al*. Direct-write dip-pen nanolithography of proteins on modified silicon oxide surfaces. *Angewandte Chemie (International ed. in English)* **42**, 2309–12 (2003).

91. Senesi, A. J., Rozkiewicz, D. I., Reinhoudt, D. N. & Mirkin, C. A. Agarose-assisted dip-pen nanolithography of oligonucleotides and proteins. *ACS nano* **3**, 2394–402 (2009).

92. Jang, J.-W., Smetana, A. & Stiles, P. Multi-ink pattern generation by dip-pen nanolithography. *Scanning* **32**, 24–9 (2010).

93. Nakashima, H., Higgins, M. J., O'Connell, C., Torimitsu, K. & Wallace, G. G. Liquid deposition patterning of conducting polymer ink onto hard and soft flexible substrates via dip-pen nanolithography. *Langmuir : the ACS journal of surfaces and colloids* **28**, 804–11 (2012).

94. Sistiabudi, R. & Ivanisevic, A. Dip-Pen Nanolithography of Bioactive Peptides on Collagen-Terminated Retinal Membrane. *Advanced Materials* **20**, 3678–3681 (2008).

95. Salaita, K. *et al*. Massively parallel dip-pen nanolithography with 55 000-pen two-dimensional arrays. *Angewandte Chemie (International ed. in English)* **45**, 7220–3 (2006).

96. Huo, F. *et al*. Polymer pen lithography. *Science (New York, N.Y.)* **321**, 1658–60 (2008).

97. Curran, J. M. *et al*. Introducing dip pen nanolithography as a tool for controlling stem cell behaviour: unlocking the potential of the next generation of smart materials in regenerative medicine. *Lab on a chip* **10**, 1662–70 (2010).

98. Giam, L. R. *et al*. Scanning probe-enabled nanocombinatorics define the relationship between fibronectin feature size and stem cell fate.

Proceedings of the National Academy of Sciences of the United States of America 1–6 (2012).doi:10.1073/pnas.1201086109

99. Stiles, P. L. Direct deposition of micro- and nanoscale hydrogels using Dip Pen Nanolithography (DPN). *Nature Publishing Group* **7**, i–ii (2010).

Chapter 2: The development of dip-pen nanolithography

2.1 Introduction

Dip-pen nanolithography (DPN) is an additive lithography technique which uses an atomic force microscope (AFM) tip to "direct-write" self-assembled-monolayers (SAMs),[1] biological molecules[2,3] and functional materials.[4-6] A key advantage of DPN is the excellent resolution achievable using a variety of different material 'inks'. Many of the essential ingredients of prospective nanobionic devices can be printed by DPN including metals,[5,7-10] conducting polymers[6,11,12] and proteins.[13,14] DPN also has the unique capability to 'multiplex' several different inks at nanometre resolution within a subcellular area.[15] In this chapter we will chart the evolution of the technique, in terms of instrumentation, theory and applications.

The basic hardware of a DPN system is an adapted Atomic Force Microscope (AFM). In section 2.2 we will begin by briefly reviewing the origins of AFM, and discuss the instrumental components which give AFM unique capabilities. We will see how these capabilities enabled the evolution of AFM from a tool of visualisation to a tool of fabrication. A host of different AFM lithography approaches have been demonstrated, all utilising the tip to pattern a substrate by the application of either a controlled force or a local electric field. The advent of DPN, however, represents a new take on AFM lithography as it involves the controlled deposition of material, opening

new doors in versatility (range of ink-substrate choices) and upscalability (simplicity of parallelization). We will analyse the inherent differences between DPN and other forms of AFM lithography as well as its unique potential to overcome the limitations of throughput and cost which have prevented other AFM lithography techniques from leaving the research lab and becoming commercially viable.

In section 2.3 we will chart the development of DPN itself. We will present a timeline of landmark DPN developments, including the diversification of ink formulations and the continued progress in parallelization. We will thus trace the evolution of DPN from a niche demonstration of controlled SAM formation, into a unique tool which is helping laboratories around the world answer previously unanswerable questions.

In section 0 we will delve into the physics behind molecular ink DPN, reviewing of the considerable body of work gone into understanding the transport of the paradigmic alkanethiol ink from tip to substrate.

In section 2.5 we will focus on the development and theory behind liquid ink DPN, exploring some of the unique advantages of this approach yet highlighting that understanding of the ink transfer mechanism is still in its infancy.

Finally, section 2.6 will conclude with an outlook to the future of DPN development.

2.2 SPM Lithography

Scanning probe microscopes (SPMs) have been described as the 'picks and shovels' of nanotechnology. The SPM provides the capability to 'see' (visualize), 'feel' (measure force) and manipulate materials at the nanoscale. In order to provide some perspective for the invention of DPN, we will now briefly chart the development of SPM technology from tools of visualisation to tools of fabrication.

2.2.1 The evolution of Atomic Force Microscopy

Binnig and Rohrer were awarded the Nobel prize in 1986 for the invention of Scanning Tunnelling Microscopy (STM). STM enabled the direct visualisation of electrically conducting materials down to single atom resolution.[16] By 1990, the STM had been used to manipulate single Xenon atoms to spell the acronym 'IBM', thereby creating a celebrated image, often regarded as heralding the beginning of the age of nanotechnology.[17] However, it was the same group's later invention, the Atomic Force Microscope (AFM),[18] invented as a tool for high resolution imaging of insulators in an ambient environment, which has had an arguably more widespread impact on the field of nanotechnology. As of February 2013, the 1982 publication heralding the birth of STM has 3900 citations, whereas the 1986 AFM publication has been cited over 10700 times.

The key components of the AFM are (Figure 2-1):

(1) The tip, which contacts the surface. The sharpness of the tip (typically 10-20 nm) affects the ultimate lateral resolution of the instrument. To increase resolution, tips using single molecules (carbon nanotubes), and even down to single atom sharpness have been fabricated.

(2) The cantilever. The tip is located on the end of a cantilever with typical length ~100 μm or less. The dimensions (length, width, height) and the elastic modulus of the material determine the cantilever stiffness. (i.e. the force required to bend the cantilever. Knowledge of the stiffness and the deflection can be translated to force using Hooke's law (spring).

(3) The optics. A system to measure minute changes in cantilever bending based on measuring the deflection of a laser (or other highly coherent light source) spot reflected from the back of the cantilever. Sub-Angstrom height resolution has been demonstrated, and the sensitivity of force measurements is typically in the piconewton range.

(4) Piezoelectric motors manipulate the cantilever (or the substrate beneath the cantilever) with nanometre or sub nanometre registry. For basic topographical imaging, the tip is 'raster-scanned' in the x and y directions over the sample, and the z-piezo is operated by a feedback system designed to keep the cantilever deflection value at a nominal set-point value. A three dimensional topographical image is then generated by plotting the z-height at every x,y position. The x- and y- piezoelectric motors have a typical range of ~100 μm. The z-motor has a typical range of ~15 μm.

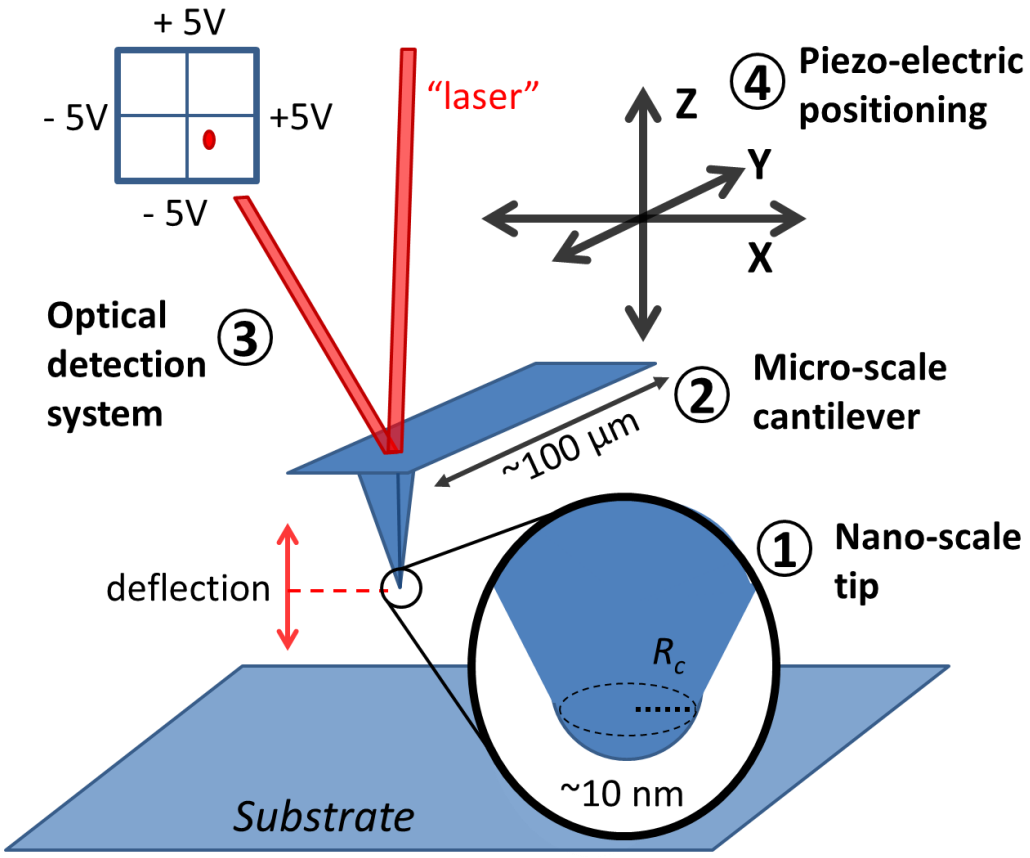

Figure 2-1: Schematic illustrating the four basic components of an atomic force microscope. In basic contact mode, the AFM cantilever is brought into contact with the substrate and raster scanned across the substrate using the piezo-electric motors. As the tip follows the nanoscale topography of the surface, the deflection of the cantilever is detected by means of a laser (or LED). A feedback loop operates between

the photodetection system and the piezo-electrics to maintain the cantilever at a predefined 'setpoint' deflection value. The applied z-piezo voltage at each raster scanned position (x,y) is used to reconstruct a 3D topographical image of the surface.

Basic AFM operation is purely physical, and so the technique can be used to image any material (the only limitation being the substrate must be relatively flat). Soft materials can be imaged using appropriately soft cantilevers. Importantly, the instrument can run at room temperature and pressure. This last point is especially salient for two reasons; (1) it obviates the need for sophisticated cooling and/or vacuum systems, thereby reducing the cost dramatically compared with other high resolution imaging platforms, and (2) significantly reducing sample preparation requirements.

The subsequent development of AFM in solution has allowed for a further revolution, this time in biology (or nanobiology). The ability to image and manipulate biological molecules such as DNA, proteins and even living organisms (bacteria, cells, tissue) in a physiologically relevant environment has resulted in a further explosion of new science since the 1990s.[19]

After its commercialisation and rapid adoption by the scientific community, it soon became apparent that AFM was more than just an imaging tool. The instrument evolved from its original purpose to encompass a wide range of characterisation capabilities, including the measurement of mechanical forces of adhesion and indentation,[20] the measurement of surface forces including forces between colloids,[21] the probing of individual molecular interactions via chemical force microscopy (by controlling the chemical species being presented at the tip)[22] as well as the characterisation of local electric and magnetic properties.[23] The staggering diversity of possible measurements has led to AFM being described as the 'lab on a tip'.[24]

2.2.2 AFM Lithography

During its continued evolution, the applications of AFM have extended beyond the field of characterisation altogether. Concomitant with the

ability to *measure* tiny forces, is the ability to *apply* a controlled force. The same capabilities which made for its success as an imaging tool (tip, registry, force control, ambient environment) also made for a tool capable of building up individual nanostructures for the first time. Promising early results in fabricating nanometre scale, single-electron transistors led to speculation by one of the original inventors of the AFM that scanning probe lithography (SPL) could be the technology to enable transistor fabrication beyond the reach of optical lithography.[25] AFM lithography was also the basis of a new high density data storage device pioneered by Binnig's IBM group in the early 2000's.[26] Although the device did not make it to market, the impressive technological achievements may feed back into other AFM lithography systems still under development.

Several reviews of AFM based lithography exist.[27-31] An overview of the most important AFM lithography techniques is shown in Table 2-1. All AFM lithography techniques are capable of superb resolution, however their material specificity and/or serial nature mean that most variations are suitable only for niche research applications. We can place AFM lithography into three broad categories: Force-assisted, bias-assisted and material deposition (printing). As an illustration of the diversity of possibilities, we will briefly highlight some example of each of these sub-categories.

Description	Lith	Sub	Special requirements	Up-scale	Res
Indentation/ Plowing Use of AFM tip to physically modify substrate	Force	Mainly soft polymers. Metallic coatings.	Tip durability (diamond)	Serial	~tip
Thermo-mechanical lithography Localised heating and force to physically modify substrate	Force (therm -al)	Heat sensitive soft polymers (e.g. PMMA)	Local heating to tip (laser, resistive)	64x64 tips Addressable	40 nm
Nanoshaving/ Nanografting Tip shaves pattern in SAM (Grafting) other molecule/material adsorbs in place	Force	SAMs. (e.g. Thiols on gold)	Tip durability (diamond)	Serial	15 nm
Local oxidation lithography Spatial confinement of oxidation reaction under AFM tip	Bias, redox	Metals. Semi-conductors. SAMs.	Applied bias (conductive substrate) Water meniscus	Serial and linear arrays of up to 50 cantilevers	30 nm
Dip-pen nanolithography Transfer of ink from AFM tip to substrate.	Deposi tion	Ink dependent. Almost any flat substrate	Ink-substrate affinity, covalent attachment preferred	Serial and up to 55,000 pen array	15 nm
Polymer pen lithography Transfer of ink to substrate from AFM manipulated polymer pen array.	Deposi tion	Ink dependent. Almost any flat substrate	Simple, cheap stamp fabrication.	Up to 1 million pen array	50 nm
Nanofountain pen Transfer of ink through nanochannel etched through AFM tip to substrate.	Deposi tion	Ink dependent. Almost any flat substrate	Liquid inks. Pen fabrication expensive.	Serial. Limited pen arrays.	100 nm
Nano-electrodeposition Use of electric-field to induce ink transfer between AFM tip and substrate	Deposi tion	Electrically conducting flat substrates	Requires ink supply to cantilever.	Serial.	100 nm

Table 2-1: An overview of selected AFM lithography techniques.

Force-assisted lithography

In force-assisted AFM lithography, a pre-existing substrate is patterned or modified by the application of controlled force via the AFM tip. The category incorporates several distinct techniques including; AFM nanoindentation, nanoploughing, nanoshaving/nanografting, and thermal/thermo-mechanical lithography.

1. Mechanical indentation/ploughing

Probably the simplest form of AFM lithography is to use the AFM tip literally as a nanoscale 'pick' or 'shovel' to scratch or cut into a substrate. A key concept is the control of force, thereby controlling the depth of penetration. Tips made from the most durable possible material (e.g. diamond) are required in order to avoid tip wear. The technique has been demonstrated on several hard materials. For example, it has been used to 'nanomachine' gold nanowires,[32] and to create electronic devices from semiconductors such as gallium arsinide.[33] However, its application on polymers is most promising where ploughing can even be achieved in tapping mode.[34] PMMA in particular has been patterned to form templates for the directed growth of patterned nanostructures.[35] The mechanical patterning of a soft conducting polymer has also been demonstrated, with the intriguing capability of reversible shape memory after actuation via electrochemical oxidation and reduction.[36]

2. Thermal/thermo-mechanical AFM lithography

Many polymers, such as PMMA, become softer at temperatures above their glass transition temperature. In thermo-mechanical AFM lithography the AFM tip is heated in order to reduce the force required to indent the sample.

The key advantage of this approach is the possibility of using localised heating to switch a pen 'on' or 'off' during writing. The result is a multiplication of the potential complexity of the resulting pattern by many

orders of magnitude. A thorough exploration of the potential of such a device was performed by Binnig and colleagues at IBM Zurich.[26,37-39] Their approach was based on the thermo-mechanical writing of a thin layer of PMMA. They first developed a method of resistive heating of the tip and characterised the critical threshold temperature for indentation; a tip heated to 400°C would indent the sample, but a tip heated to lower temperature would not. They developed a method whereby the same tip used to 'write' the features could also be used to 'read' them (the reading mechanism was based on inferring the presence or absence of an indentation via localised heat dissipation). In the binary system, an indentation constituted a 'one' and the absence of indentation constituted a 'zero'. Importantly, the data could be erased by heating the whole chip to 150 C, and data could be rewritten again.

Following on from the proofs of concept using a single tip device, the group developed the 'Millipede' design (see Figure 2-2) of one-thousand cantilevers in an array. Each cantilever wrote and read in its own 100 μm^2 area. They also developed a relatively simple method of addressing individual cantilevers by addressing each row and column in a coordinate system.[26] The array is manipulated by one piezo-electric system, and although all cantilevers touch the surface with the same force, only some of them are heated to the necessary temperature to indent.

Due to the rapid advances in cheap 'flash' memory, the Millipede technology is no longer being pursued as a memory device. Nevertheless the technology is a landmark development and case study in the field AFM lithography. The IBM group have demonstrated how arrays of thousands of addressable cantilevers could be fabricated and individually addressed to write, read, erase and rewrite complex patterns.

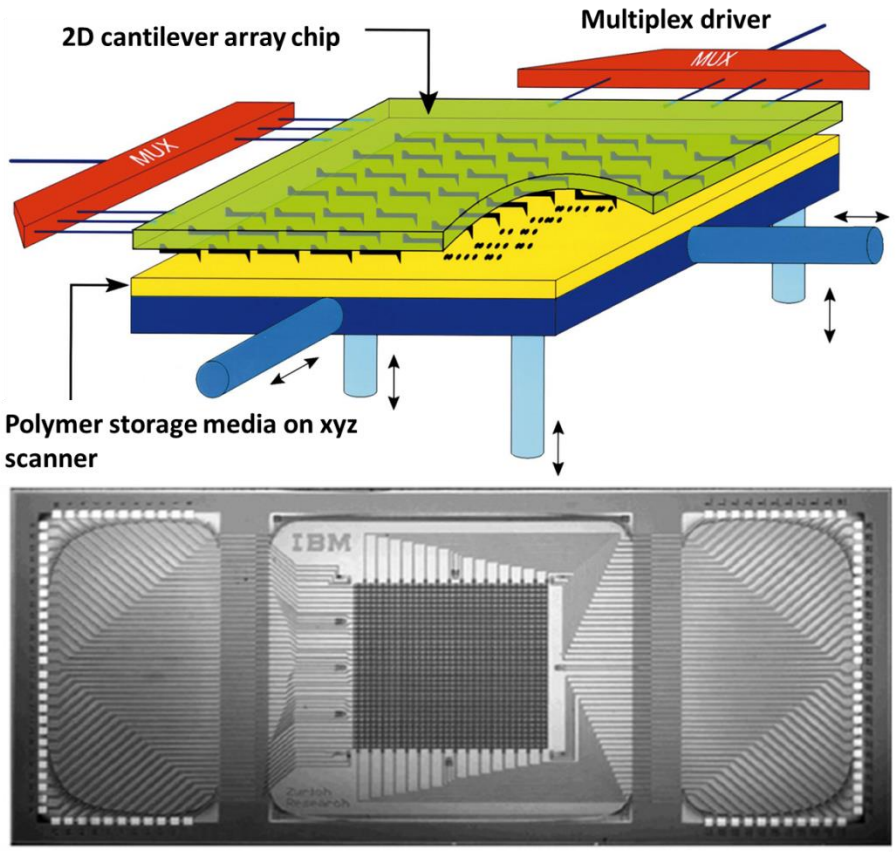

Figure 2-2: (Top) Schematic showing the configuration of the AFM probe arrays; (Bottom) Photograph of fabricated chip with the 32 x 32 cantilever array located at the centre. [©1999 IEEE. Reprinted, with permission, from IEEE Int. MEMS 99 Conf. Twelfth IEEE Int. Conf. Micro Electro Mech. Syst.[26]]

3. AFM Nanoshaving and Nanografting

There has been great progress in the last three decades in tailoring the surfaces of metals and oxide with self-assembled organic molecules.[40] Of particular importance are the systems of alkanethiols on metals,[41,42] and organosilanes on oxides.[43] AFM nanoshaving involves the selective removal of nanoscale regions of a self-assembled organic layer by the application of a controlled force from an AFM tip. The advantage of this technique is that resolution approaching the sharpness of the AFM tip (~10 nm) can be achieved. However, tip wear is an issue, and diamond coated probes are often used to prolong probe lifetime. AFM nanografting is a variation performed in solution whereby a second molecule adsorbs in place of the

first.[44] Besides secondary SAM molecules, both proteins[45] and nanoparticles[46] have been nanografted. Figure 2-3 (A) shows a basic illustration of both nanoshaving and nanografting techniques.

3. AFM nanoscopic manipulation

Whilst manipulation is not a form of lithography (in that it does not seek to reproduce multiple copies of an image), it is an important, non-characterization, niche application of AFM. Carbon nanotubes, in particular, have been manipulated into electrical devices, and 'cut' or 'nicked' by an AFM tip to study their electrical transport properties. Nanoparticles, nanocrystals and biological molecules such as DNA have also been manipulated. In one particularly creative example, a nanoscale mechanical latch was fabricated by cutting and pushing MoO_3 nanocrystals on a MoS_2 surface.[47] The ultimate example, single atom manipulation, has also been achieved; Sn adatoms were laterally manipulated on a Ge (111) substrate at room temperature.[48]

Bias-assisted AFM lithography

Bias-assisted AFM lithography involves the application of an electrical bias between tip and sample. The technique can be used to effect chemical changes of a substrate, such as with local oxidation and electrochemical lithography. It may also exploit the huge voltage gradient set up across micro-scale distances, even with a modest bias, to enact surprising effects such as dielectric breakdown or electrohydrodynamic instabilities. Other niche variants include piezoresponse force lithography.

1. Local Oxidation AFM Lithography

In local oxidation nanolithography (LON) the applied field induces ionic dissociation of the water meniscus between tip and sample; the oxidative OH^- anions react with the substrate to form localised oxide structures. Figure 2-3 (B) shows, at left, a generic schematic of the LON technique.[29] The technique has been used to push the fabrication limits of devices such

as metal-oxide-semiconductors via nanoscale definition of the local oxide growth.[49,50] Figure 2-3 (B) also shows a nanoscale oxide structure fabricated by LON for fundamental quantum mechanical experiments in ring geometries.[51]

It was the rapid advances being made in LON in the mid 1990's which prompted speculation by C.F. Quate, one of the original inventors of the AFM, that scanning probe lithography may be the means to continue the miniaturization of transistors below the photolithographic diffraction limit.[25] Although this prediction has not been realised, LON has developed as a versatile technique for modification of diverse materials surfaces and organic SAMs.[52,53] Some efforts at upscaling the technique have been made, for example the Quate group at Stanford have used arrays of up to 50 cantilevers to effect centimetre scale lithography.[54]

2. Exotic forms of bias induced lithography

More exotic forms of bias induced lithography exploit the huge voltage-gradient set-up between an AFM tip positioned a few microns or less above a substrate, even at modest applied voltage. The 'nanoexplosion' resulting from electrical discharge in a nanoscale air/water gap has been used to create crater-like circular deposits extending up to 4 μm around a central structure.[55] In AFM electrostatic nanolithography a bias applied to the tip locally heats polymer substrate, which is then polarised and attracted to the tip pulling a dimple-like structure up from the substrate.[56] A similar lithography method has also been demonstrated which exploits locally induced electrohydrodynamic instability in thin polymer films; in this case the patterned structures are nanoscale Taylor cones pulled up from the PMMA or polystyrene substrate beneath the AFM tip.[57,58]

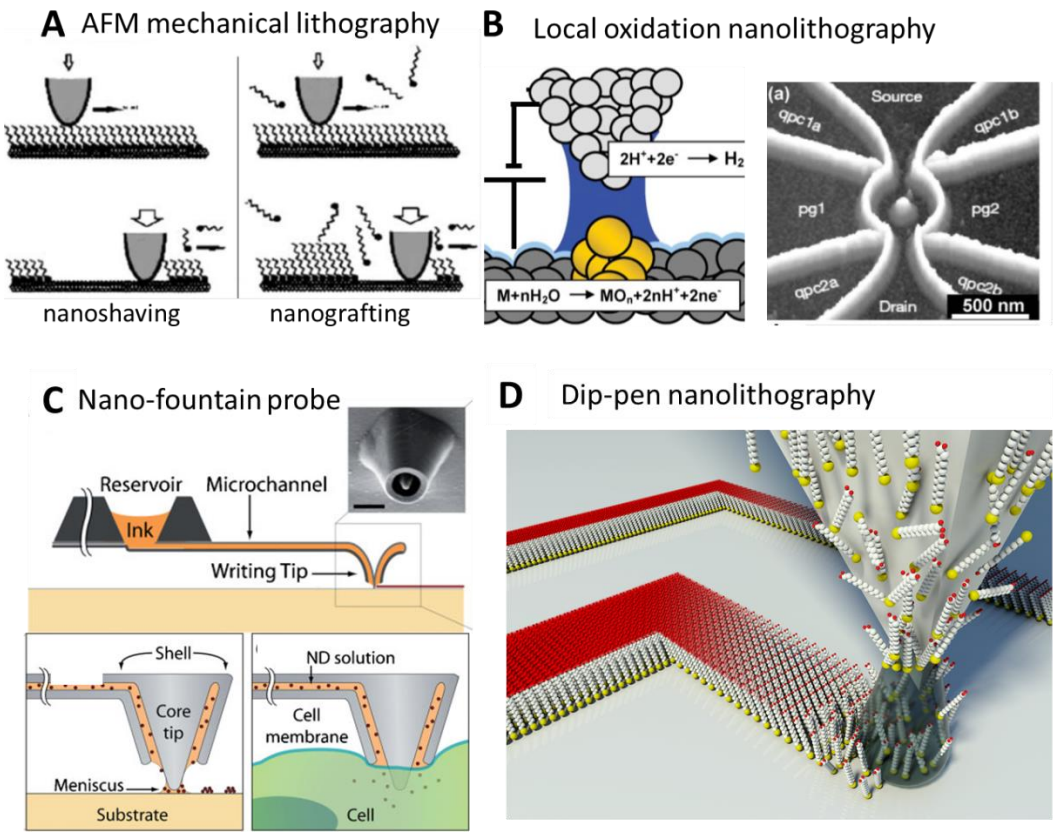

Figure 2-3: Selected AFM lithography strategies: (A) AFM nanoshaving involves the selective removal of an organic SAM from a metal or oxide surface using mechanical force applied by an AFM tip. When nanoshaving is performed in a solution of secondary SAM molecules, the shaved regions are 'nanografted' with the secondary SAM. [Adapted with permission from Liu et al, Accounts of Chemical Research 33, 457-466. Copyright (2000) American Chemical Society.][27] (B) In local oxidation nanolithography (LON), the applied field induces ionic dissociation of the water meniscus between tip and sample and the oxidative OH^- anions migrate to the substrate and react with it to form localised oxide structures. [Schematic reproduced Ref 29 with permission of The Royal Society of Chemistry.][29] LON has been used to create novel nanoelectronic architectures by patterning local oxide on semiconductors [Reprinted by permission from Macmillan Publishers Ltd: Nature 413, 822-5, copyright (2001).][51] (C) The nanofountain probe (NFP) incorporates microfluidic channels inside the cantilever to deliver liquid or molecular ink from a reservoir to the writing tip. The design allows for not only deposition of ink on substrates, but also the injection of ink (in this case a nanoparticle solution) into living cells. [Copyright © 2009 Wiley-VCH Verlag GmbH & Co. KGaA, Weinheim. Reproduced with permission,][59] (D) Dip-pen nanolithography (DPN) involves the direct deposition of ink from a coated AFM tip to the substrate.

Constructive AFM lithography (AFM printing)

The AFM lithography techniques described above generate a pattern by delivering a force, heat or electrical bias (i.e. forms of *energy*) to selectively remove or modify a pre-existing substrate. The idea to use an AFM tip to deliver *material* opened up totally new possibilities for AFM lithography.[60] Ink deposition incorporates DPN (and its extensions including polymer pen lithography and electrochemical DPN) and Nano Fountain Pen (NFP) techniques. We will discuss the development of DPN itself in section 2.3 below.

1. Nanofountain probe

In 1999 (the same year as the invention of DPN), a group at the Hebrew University of Jerusalem reported the use of an AFM tip to deliver small quantities of liquid reagent to enact a localized chemical reaction.[61] The group set up a system to deliver etchant to the probe using a micropipette and demonstrated controlled etching of a chromium thin film with resolution down to 100 nm line width.

The "Nanofountain probe" concept was revisited several years later by the Espinosa group at Northwestern University.[62,63] Their 'volcano' probe was designed to overcome the ink supply limitation of DPN by incorporating a microfluidic channel within the cantilever which linked to a large ink reservoir. Figure 2-3 (C) includes a schematic of the basic design. In contrast to the focused ion beam method (discussed below) the volcano tips are fabricated using only conventional photolithography and may be up-scalable to massively parallel arrays.[64] The group have since demonstrated the suitability for the probes for printing gold colloids,[65] and DNA[66], though an electric field between tip and substrate was required to induce deposition of proteins.[67] The design has allowed for some unique

applications, for example, the injection of single cells with nanoparticles (Figure 2-3 (C)).[59]

In 2004, the fabrication of a liquid nanodispensing (NADIS) AFM probe was accomplished using focused ion beam (FIB) to drill a nanoscale channel through the tip.[68] The Ondarcuhu group in Toulouse have studied the deposition from such a device extensively, concluding that control of droplet size is mainly a function of tip and substrate hydrophobicity as well as the diameter of the nanochannel aperture.[69–71] They have used the device to deposit individual femto-liter droplets of glycerol onto a nanomechanical mass sensor to measure evaporation rate on the nanoscale.[72] While the NADIS design is useful for depositing uniform droplets of pure liquids, the nanochannel is prone to clogging which limit its versatility to more complex fluids. Also, the FIB fabrication step is prohibitively laborious for manufacture of multiple-probe arrays.

2. Exotic AFM deposition techniques

Several conventional fabrication techniques have been adapted to the nanoscale using AFM, and these could be categorized as exotic forms of AFM based deposition. A nanoscale analogue of evaporative coating was demonstrated as early as 1995.[73] In that work, an applied bias to a gold coated AFM tip in high vacuum induced field evaporation of gold to form nanometre sized gold dots on a SiOx/Si substrate. Nanoelectrospinning from a single AFM tip has also been reported, though the authors demonstrated only limited control in defining a pattern with the fabricated polyethelene oxide nanofibres.[74]

2.3 The development of dip-pen nanolithography

Jaschke and Butt first reported the direct deposition of material from an AFM tip in 1995.[75] They observed the formation of aggregates of crystalline octadecanethiol (ODT) on mica while scanning with a tip coated in the

alkanethiol. The deposition was unreliable, however, and highly tip-dependent. Deposition could not be achieved on gold and 'direct write' pattern formation was not attempted.

In 1997, Piner and Mirkin reported the deposition of water on mica from an AFM tip, using the technique to lithographically define sub-micron letters.[76] In 1999 they reported the invention of dip pen nanolithography, a new lithography technique based on the controlled deposition of alkanethiol self-assembled monolayers using an AFM tip.[1] (See Figure 2-3 (D) for an illustration). The first DPN paper, published in *Science,* reported dots and lines could be drawn with a feature-size of down to 30 nm, and they noted that deposition rate seemed to depend on relative humidity. Two further *Science* papers followed over the next eighteen months. They demonstrated multi-ink capability, superb registration (5 nm pitch) between different inks printed sequentially, an improved ultimate resolution (15 nm) when monocrystalline gold and ultra-sharp tips were used.[77] Importantly, they also demonstrated the potential up-scalability of the technique using an array of 8 cantilvers.[78] As DPN printing was not force dependent, an array of 8 cantilevers could be used to print identical patterns simultaneously with only one of them engaged in active AFM feedback. These studies laid out the unique capabilities of DPN and bolstered the argument that DPN represented the invention of a new and significant lithography technology.

As no specialized equipment (other than an AFM) is required, DPN was quickly adopted by many labs for many diverse applications. By 2004, dozens of laboratories around the world were using DPN,[79] and by 2007 the number was over 200.[60] We chart the evolution of DPN in Table 2-2 via a timeline of influential studies in the field. The timeline shows ~40 key publications from 1999-2013, from a total of over 400. We categorise these DPN studies into one of three domains; ink development, instrumentation or application.

Year	Development	Lab	Journal	Type
1995	First deposition of organics material by SPM.[75]	Butt	Langmuir	Inst, ink
1999	Fountain pen nanochemistry.[61]	Lewis	APL	Inst
	'Invention' of DPN.[1]	Mirkin	Science	Inst
	First multi-ink.[77]	Mirkin	Science	Ink/inst
2000	8 cantilever passive pen array.[78]	Mirkin	Science	Inst
	DPN patterns as etch resists.[8]	Mirkin	Adv Mat	App
2001	Electrochemical AFM DPN.[5]	Maynor. L. Liu	JACS	Inst,Ink
	First protein printing (collagen)[80]	Mirkin	PNAS	Ink
2002	Protein nanoarray cell adhesion.[3]	Mirkin	Science	App
	First DPN solid state features.[4]	Mirkin	JACS	Ink
	First conducting polymer ink.[12]	Mirkin	Adv Mat	Ink
	First oligonucleotide ink.[2]	Mirkin	Science	Ink
	32 cantilever pen-array.[81]	C. Liu, Mirkin	Nanotech	Inst
	Nanoink inc. founded	Mirkin	---	Inst
2003	Proteins on glass.[13]	Mirkin	Ang Chem	Ink
	First printing of alkoxysilanes on glass.[82]	Collier	JACS	Ink
	DPN feeding monomer to live polymerisation of polymer brushes.[83]	Mirkin	Ang Chem	App
	Assembly of modified virus capsids on DPN patterns.[84]	Mrksich, Mirkin	Nano Lett	App
	Release of NSCRIPTOR, first commercial DPN system.	Nanoink	---	Inst
2004	Nanofountain pen for liquid nanodispensing. [68]	Heinzel-mann	APL	Inst.
	Individually addressable active pens.[85]	C. Liu, Mirkin	APL	Inst
	Fabrication of HIV assay.[86]	Mirkin, Wolinsky	Nano Lett	App
2005	Nanoarrays of single virus particles.[87]	Mirkin	Ang Chem	App
	Controlled evolution of a polymer single crystal.[88]	Mirkin	Science	App
2006	Thermal DPN of metal nanostructures.[7]	King, Whitman	APL	Inst/ink
	'Massively-parallel' 55,000 cantilever array.[89]	C. Liu, Mirkin	Ang Chem	Inst
	Control of CNT shape and orientation with DPN fabricated templates.[90]	Schatz, Mirkin	PNAS	App
2007	Living cell infectivity from virus nanoarrays.[91]	Mirkin	Small	App
	Phospholipid ink.[92]	Fuchs, Mirkin	Small	Ink
2008	First biological substrate. Bioactive peptides on retinal membrane.[93]	Ivanisevic	Adv Mat	App
	Invention of polymer pen lithography.[94]	Mirkin	Science	Inst
2009	Multi-protein inking of PPL stamp.[95]	Mirkin	Ang Chem	Inst
2010	DPN nanopatterns direct stems cell differentiation.[96]	Curran	Lab Chip	App
	Beam pen lithography.[97]	Mirkin	Nat Nano	Inst
	Scanning probe block copolymer lithography.[98]	Mirkin	PNAS	Ink
2011	Hard-tip, soft-spring lithography.[99]	Mirkin	Nature	Inst
	Single molecule protein arrays.[100]	Mirkin	PNAS	Ink
2012	First bacterial 'ink'.[101]	Lim	JACS	Ink
	PPL fibronectin arrays for in vitro stem cell biology.[102]	Mirkin	PNAS	App

Table 2-2: Timeline of influential DPN advances. In the right-most column 'Inst' (blue) refers to an advance in instrumentation, 'Ink' (red) refers to ink development and 'App' (green) denotes the use of DPN in an applied study. Journal acronyms are as follows: APL= Applied Physics Letters, Adv Mat= Advanced Materials, JACS= Journal of the American Chemical Society, Ang Chem= Angewandte Chemie (International Edition), PNAS= Proceedings of the National Academy of Sciences.

2.3.1 Ink development

Although much of the early interest in DPN centred on manipulating the alkanethiol/gold system, it was soon realised that other materials could be printed too, as long as the ink-substrate affinity was strong enough to drive transport. Key developments include the printing of solid-state metal oxides,[4] conducting polymers,[6,12] and metals.[5]

The huge potential of DPN in the biomedical field also began to generate excitement. As the technique can operate in an ambient environment, and with little or no post-treatment, fragile biological structures such as DNA[2] and proteins[80] could also be printed at nanoscale resolution while retaining their native structure. A biomolecule carrier ink has been developed for versatile printing of proteins or oligonucleotides with consistent deposition rates.[14] The possibility of patterning hydrogels and lipids at nanoscale dimensions also has numerous potential applications in the patterning of a soft localised cellular nanoenvironment.[15] DPN has also been used to pattern virus particles,[87] and even a bacterial 'ink' has been developed.[101]

More recently, block-copolymer lithography was married with DPN to produce arrays of single gold nanoparticles of ~4 nm diameter, reflecting a feature size much smaller than the tip-s used to print them.[98] These arrays of individually positioned gold nanoparticles present a binding area of similar dimensions to that of a single protein. The Mirkin group has taken advantage of this methodology to generate single-molecule protein arrays.[100]

The early work of DPN ink development was comprehensively reviewed in 2004,[79] and again in 2007.[60] Since then the number of methodologies and applications has grown so as to require more specialised treatments. The fabrication of metal and semi-conductor structures by DPN was reviewed in 2009[103]. The dozens of methods to DPN print biomolecules, by both direct and indirect methods, were reviewed in 2011.[104]

We will present more in depth discussions of the methods previously used to pattern conducting polymers in **Chapter 3** and metals in **Chapter 4**.

2.3.2 Instrumentation development

The continued developments in DPN instrumentation over the past decade have targeted various obstacles preventing it from becoming a mainstream lithography technique.

Upscaling DPN

Early DPN experiments were considered very low through-put as they used only single pen or limited linear pen-arrays. The limitation of upscalability has been addressed by successive examples of increased parallelization;[105] the 32 cantilever linear pen array was introduced in 2002,[81] and the 55,000 cantilever 2D 'massively parallel' pen array in 2006 (though whole wafers of 1.3 million pens were also fabricated as proof of concept).[89] Although they were commercialised, the pen arrays were fragile, expensive to fabricate and required a labour intensive levelling process.[106]

Invention of polymer pen lithography

The efforts toward parallelization culminated in 2008 with the invention of polymer pen lithography (PPL).[94] PPL presented an elegant 'cantilever-free' solution to the problem of increasing pen density array using a PDMS stamp of thousands of nanosharp pyramidal tips. The PDMS stamp could fabricated using a Si mould, greatly simplifying the pen fabrication process, and reducing the material cost per 'stamp' to just $1. PPL represented the

convergence of large area but pattern specific soft-lithography with small area, direct write DPN.[107]

In the past five years, significant advances have been made in improving the practicality of PPL. A clever solution to the multi-plexed inking of PPL stamps was found in using the silicon master (used to fabricate the stamp) as the ink-wells. Ink-jet printing was used to fill different 'ink wells' with different proteins.[95] A method of levelling the stamp with the potential of automation was developed which uses the force applied by a non-levelled stamp on the substrate as the basis for a feedback loop.[108]

An additional parameter to be considered with PPL is that, in contrast with DPN, feature size is force dependent.[94] This can be advantageous as feature size can be controlled without relying on environmentally sensitive diffusion processes.[109] However, the deformation of the PDMS tips does place a resolution threshold on the technique. The contamination of printed features with molecules of PDMS (a problem in soft-lithography) is also left open. A recent development, dubbed 'hard-tip soft-spring' lithography, addresses these issues by using a PDMS stamp capped in silicon oxide.[99]

An intriguing spin-off technology from PPL, dubbed 'beam-pen lithography' (BPL), has enabled a maskless, direct-write parallelization of photolithography.[97] In BPL, 400 nm light is passed through nanoscopic apertures in the polymer pen tips, to generate thousands of sub-wavelength (100 nm) spots. Piezo-electric manipulation of the polymer pen allows for generation of arbitrary photolithographic patterns.

The progress in up-scaling the DPN technology over the past decade has been impressive. For example the printing time to deposit 1 billion features has decreased 5 orders of magnitude over three generations of DPN systems (Figure 2-4).[107]

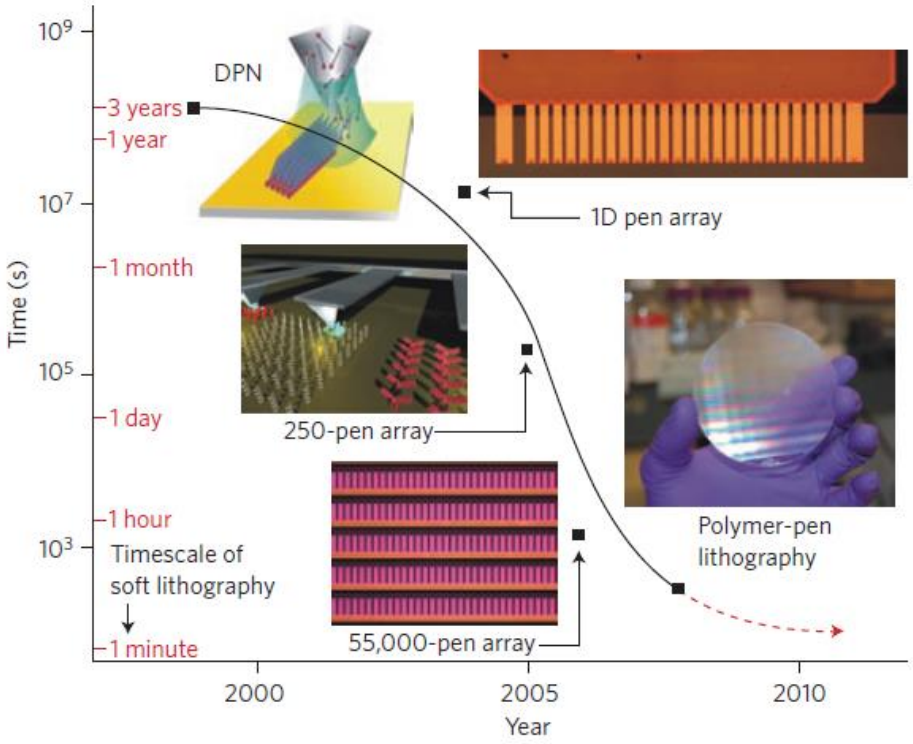

Figure 2-4: The logarithmic decrease in printing time for 1 billion features highlights increased parallelization over several generations of DPN systems. [Reprinted by permission from Macmillan Publishers Ltd: Nature Chemistry 1, 353-8, copyright (2009).[107]]

'Active' probe arrays

Besides up-scalability, some limitations to DPN do remain. In particular, the major advances in parallelisation have utilized passive pen arrays. Although millions of tips over multi cm^2 areas can engage in printing simultaneously, a passive pen array can only generate duplicates of a single design. A vast increase in the possible pattern complexity would be achieved if each tip could be actuated individually. In 2004, Bullen et al., in collaboration with the Mirkin group, demonstrated 'active' parallel probe arrays consisting of individually addressable cantilevers.[85] The design used thermo-mechanical actuation to switch each pen 'on' or 'off'. The group demonstrated the simultaneous printing of the letters 0-9 by moving ten tips in a figure 8 and using the actuation to raise and lower each of the pens as required. The technology was later commercialised by Nanoink Inc. However, the system was expensive and plagued with a number of issues;

in particular, the array was affected by thermal cross-talk between cantilevers and deposition from heated cantilevers was affected by the temperature dependence of the ink diffusion rate. A later design, using electrostatic rather than thermo-mechanical actuation, resolved some of these issues.[110] No active probe system for a 2D DPN probe array has been reported. However, IBM Zurich did demonstrate the actuation of individual cantilevers in a massively parallel arrangement during the development of their 'Millipede' memory storage device.[26]

2.3.3 Applications of DPN

The advances described above are all 'inward-looking' improvements in the DPN system itself. The ultimate challenge for a new research technique is to answer previously unanswerable questions. We now present a brief summary of some research applications where DPN has provided a novel capability. Figure 2-5 illustrates some key advances.

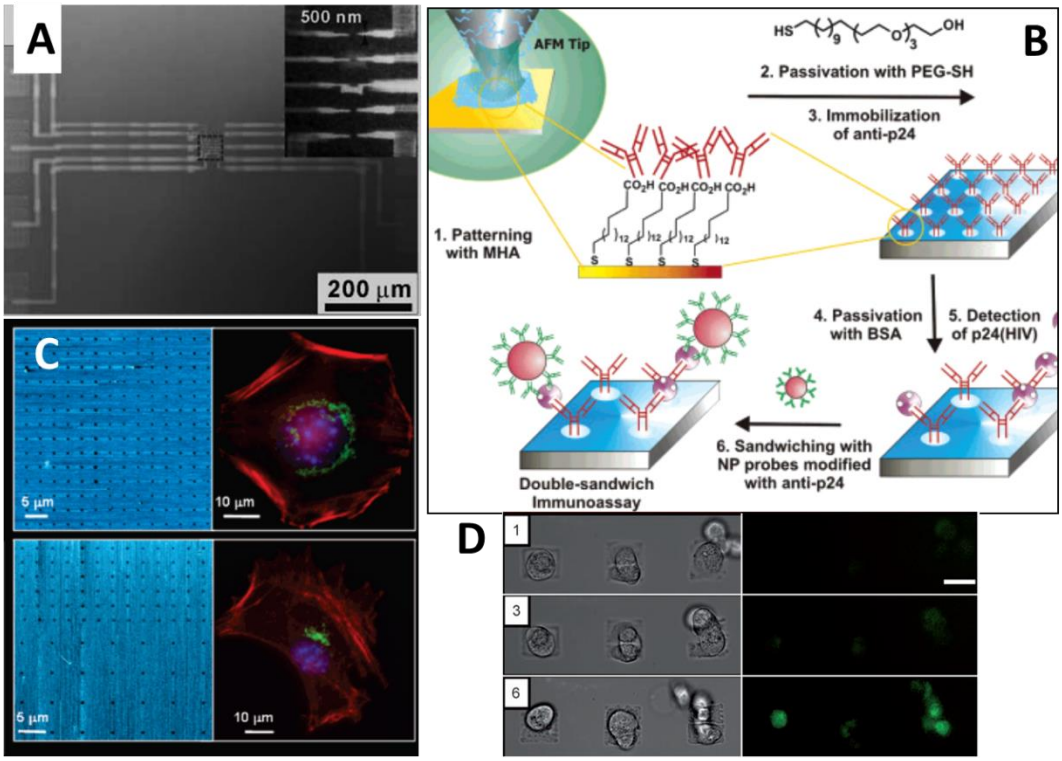

Figure 2-5: Selected applications of DPN and PPL: (A) An optical microscope image of a multidimensional gold circuit fabricated using PPL to pattern an alkanthiol etch resist on gold. Both micro-scale and nanoscale electrodes were defined by PPL. The inset shows a magnified SEM image of the circuit center. [From Science 321, 1658-60 (2008). Reprinted with permission from AAAS.][94] (B) Schematic of the immunoassay format used to detect HIV-1 p24 antigen with anti-p24 antibody nanoarray. The anti-p24 antiobody was immobilized on DPN printed MHA patterns by an electrostatic interaction. Binding of the p24 antigen produced an increase in height of the nanoarray as monitored by AFM. The increased height signal could be amp Nano Lett. 4, 1869-1872 (2004). lified using anti-p24 modified gold nanoparticles. [Adapted with permission from Nano Lett. 4, 1869-1872. Copyright (2004) American Chemical Society.][86] (C) 3T3 mouse fibroblast cells adhering to symmetric (top) and asymmetric (bottom) nanoarrays of immobilized RGD linear peptide. The diffuse distribution of the Golgi surrounding the nucleus indicates that the cell on the symmetric nanoarray is not polarized. [Adapted with permission from J. Am. Chem. Soc. 130, 3280-1. Copyright (2008) American Chemical Society.][111] (D) CV1 monkey kidney cells adhering to nanoarrays of rSV5-EGFP virus engineered to express green fluorescent protein (GFP). Infection of the cells by the virus could be monitored by the increased GFP fluorescence over time. [Copyright © 2007 WILEY-VCH Verlag GmbH & Co. KGaA, Weinheim. Adapted with permission.][91]

Nanoelectronics

The first application-orientated DPN study exploited patterned alkanethiols as etch resists to form gold and silicon nanostructures, highlighting the potential of DPN in the fabrication of nanoelectronics.[8] DPN has significant advantages for this purpose over methods developed by the Whitesides group using micro- and nanocontact printing[41] as it achieves increased resolution (<20 nm) and arbitrary pattern design. The methodology has been successfully upscaled to polymer pen lithography, as shown in Figure 2-5 (A).[94] In working devices, nanoscale electrodes are often addressed by macro-scale electrodes made using conventional photolithography. Some methods for achieving registry between DPN and micro-fabricated structures have been described,[112] however a facile and reliable protocol is still lacking.

Rather than fabrication the electrodes directly, DPN has also been used to fabricate masks for high-resolution photolithography.[113] Another potential application which has been cited is the inspection and repair of defects in prefabricated photomasks[105] and in integrated circuits.[10]

Biomolecule nanoarrays

The applications for which DPN seems most immediately suited are in the generation of biomolecule nanoarrays for high through-put screening assays in proteomics, genomics and drug development.[60] The powerful potential of nanoarrays in biomedicine is illustrated by an example outlined by Mirkin:[105] A DNA array capable of identifying any known sequence would require 4^{17} features and so a micro-array with 50 μm features would be approximately the size of a tennis court. A nanoarray with 50 nm features would be only ~1 cm^2, making such a chip practical in real world applications.

The first proof of concept of a DPN printed nanoarray used for diagnostic purposes was demonstrated by the Mirkin group in 2004 (Figure 2-5 (B)).[86] Nanoarrays of antibodies against the HIV-1 p24 antigen (anti-p24) were

created by electrostatic binding to MHA nanopatterns. HIV-1 p24 antigen in plasma obtained from HIV-1-infected human patients was hybridized to the antibody array in situ. Detection of the hybridization was via height change (from 6.4 nm to 8.7 nm) as measured by AFM. A gold antibody-functionalized nanoparticle probe was also used for signal enhancement (height change 20 nm). Although a slow and laborious process in this form, the assay achieved a limit of detection of 0.025 pg per ml, exceeding that of conventional enzyme-linked immunosorbent assay (ELISA)- based immunoassays.

Nanoarrays are also important as models for fundamental studies of biomolecular interactions, and have huge potential when coupled with strategies of AFM force measurements. DPN printed nanoarrays of $\alpha_v\beta_3$ integrins or BSA were probed by an AFM tip functionalised with vitronectin.[114] Increased adhesion forces arising from specific interactions could distinguish integrin from BSA. Although still in its infancy, this methodology may lead to a robust model system of studying the interaction force of pairs of biomolecules as a function of solution condition (pH, ionic strength) and conformation, especially with the advent of strategies to generate single-molecule protein arrays.[100]

Although the first DPN printed nanoarrays of proteins and oligonucleiotides were achieved over a decade ago,[2,3] the full potential of nanoarray technology can only be unlocked by a reliable method of generating patterns of thousands (millions, billions…) of different biomolecules. Although some promising advances in multi-plexed patterning have recently been reported,[95] truly revolutionary advances will require orders of magnitude increases in the number of simultaneously printed biomolecules.

Nanopatterned model substrates for fundamental in vitro cell studies

An understanding of the processes of adhesion, migration, differentiation in artificial environments is crucial to the development of novel approaches to

medicine such as tissue engineering[115] and medical bionics.[116] Model substrates presenting well defined patterns allow for the systematic study of the cell-material interface and have been important for elucidating the spatial and temporal mechanisms of these processes.[117]

Since the 1990s SAMs of alkanethiolates on gold have been a prominent model substrate for fundamental *in vitro* cell studies.[118] Key to their success as a model substrate is the simplicity of their preparation, and the diversity in choice of the presented groups. The ability to pattern these SAMs on the scale of single-cells using micro-contact printing[41] lead to some seminal work in the control of cell-fate by purely geometric means.[119] A generic protocol has become the method of choice for patterning cells:[120] hydrophobic alkanethiols are generated on gold via micro-contact printing and remainder of the substrate is rendered biologically inert by immersion in a solution containing oligo(ethylene glycol) terminated alkanethiol. Hydrophobic alkanethiols permit the adsorption of ECM proteins, and cells only adhere to the patterned areas.

Living cells are sensitive to nanoscale topographic and biomolecular patterns,[121] though the mechanisms by which cells transduce signals from their microenvironment is poorly understood. DPN has allowed for the fabrication of model substrates at the nanodomain, allowing the study of geometric effects at a much finer scale than previously possible, that of individual focal adhesions. The Curran group at the University of Liverpool in collaboration with researchers at Nanoink Inc., recently used DPN generated alkanethiolate nanopatterns to reproducibly control the differentiation of human mesenchymal stem-cells (MSC) differentiation without the use of differentiation media.[96,122] The size of nanospots was optimized at 70 nm diameter corresponding to the diameter of cellular focal adhesion structures. MSC adhesion and phenotype was dependent on both the terminal functionality (amino, methyl, hydroxyl or carboxyl) and the pitch (140 to 1000 nm) of the nanopatterns. The nanopatterns were shown to influence the formation of focal adhesions through controlling

specific integrin clustering, which can then be used to direct cellular response.

Besides nanopatterning of surface chemistry, the capability of DPN to generate biomolecule nanoarrays is enabling the systematic study of biospecific interactions at the nanoscale.[117] In 2002, the Mirkin group reported the adhesion of living cells to nanoarrays of the cell-adhesion protein retronectin, illustrating the potential of DPN as a new tool to study the fundamental processes of cellular adhesion.[3]

The Yousaf group at the University of North Carolina have studied the adhesion of 3T3 mouse fibroblast cells on DPN generate nanoarrays of both linear and cyclic RGD cell adhesion peptides.[123] Cells were found to develop eight times more focal adhesions on the cyclic rather than the linear RGD patterns. Cell adhesion was also dependent on spot-size and pitch of the nanoarrays. In a later work, the group explored this effect further, studying how nanoarray geometry influences cell polarity orientation (Figure 2-5 (C)).[111] They found that 3T3 cells were polarized on asymmetric arrays, but not on symmetric arrays, of linear RGD peptide.

Lenhert and Fuchs have DPN printed lipids with the goal of generating biomimetic membrane patterns as model substrates for cell culture.[124] They demonstrated the multi-plexed printing of lipids with lateral resolution down to 100 nm. By binding functional proteins to lipids containing either a nickel chelating headgroup or a biotinylated headgroup, they could demonstrate the selective adhesion and activation of T-cells. In a related development, the Salaita group used patterns of a cationic polyelectrolyte to impede lipid diffusion and therefore control spatial organization of ligands in membranes and cells.[125]

Recently, the Mirkin group studied the influence of fibronectin feature size on the adhesion and differentiation of human mesenchymal stem cells (MSCs). The group used a deliberately tilted PPL stamp to rapidly generate millions of MHA spots on gold over ~cm^2 areas with feature sizes from nano

to micro-scales.[102] They passivated the surrounding gold with an oligo(ethylene glycol) terminating alkanethiolate, then immobilized fibronectin on the MHA patterns. The large area nanoarray enabled a rapid and systematic screening of MSC adhesion as a function of fibronectin feature size. MSCs cultured on optimised nanopatterns of fibronectin differentiated towards osteogenic fates when compared to nonpatterned fibronectin substrates, even without media containing osteogenic-inducing chemical cues.

Infectivity studies

The Mirkin group demonstrated the capability of DPN to generate arrays of single virus particles in an active state.[87] The immobilized virus particles were capable of infecting living cells cultured on the arrays.[91] Through the use of green fluorescent protein expressing virus particles, an assay was developed to follow the infectivity process on nanoarrays by fluorescence (Figure 2-5 (D)). Thus the systematic examination of single-cell infectivity with control of the density and spatial distribution of virus particles has been made possible.

The direct write patterning of bacterial cells by DPN was also recently demonstrated, opening the door to similar infectivity studies at the bacterial level as well as possible applications in drug-delivery, biofilms and molecular motors.[101]

2.4 Theory: Molecular ink transport

In section 2.3 above we charted the development of DPN in three domains; instrumentation, ink development and application. The fourth domain of DPN research has been the endeavour to understand the essential mechanisms of ink transport and the parameters which affect transport rate. Dozens of studies have been performed on the influence of individual factors and, recently, the first study purporting a complete model for

predicting feature size was reported.[126] Table 2-3 shows an overview of selected literature studies of parameters affecting deposition rate in DPN of molecular inks. A brief description of each experiment and its main conclusions are shown. These studies are extensively referenced in the following description of the mechanism of molecular ink DPN.

Param	Experiment	Conclusions	Ref	Year
	1. Tip/substrate condition			
r_c (Tip) R_q (Sub)	Tip sharpness, gold crystallinity	Highest resolution (15 nm) obtained for sharpest tips on monocrystalline gold.	77	1999
r_c (Tip)	Tip sharpness (Deliberate blunt tip)	Meniscus size dependent on tip radius Rate ink transport dependent on tip radius	127	2007
Tip treatment	Plasma treatment	Plasma treatment necessary?	128	2004
R_q (Sub)	Simulation of surface roughness	Diffusion rate inversely dependent on R_q (Sub).	129	2011
	2. Tip loading			
Conc (Tip)	Vapour and dip coating.	Deposition rate largely irreproducible regardless of coating method	130	2002
Conc (Tip)	Decrease in ink loading with time	Long term exponential decay in printing rate	128	2004
Conc (Tip)	Control tip loading by IJP	Ink dissolution is rate limiting step	131	2009
Conc (Tip)	Complete ink transfer model	Quantifying ink loading is key to predicting feature size.	126	2010
	3. Contact meniscus			
RH%	Meniscus observation, by environmental SEM	Meniscus size dependent on RH% Meniscus larger than theory predicts	132	2005
RH%	Environmental SEM monitors dynamics of meniscus growth	Meniscus growth as rate limiting step?	133	2006
meniscus	Minimum meniscus size	Theory, limit imposed by thermal fluctuation at RT		
RH%	Kinetics of molecular dissolution	Transport rate (MHA) dependent on RH%	134	2002
RH%	Dwell time, Humidity	Transport rate (ODT) not dependent on RH% Printing at 0% RH	130, 135	2002
RH%, T	Solubility in meniscus, Temperature, humidity	Transport rate MHA, ODT vs RH% T dependence on RH%	136	2003
RH% (organic)	Effects of organic vapor on alkanethiol deposition	Molecular reorganisation on tip affects deposition rate	137	2010
	4. Molecular Transport			
solubility	Annular diffusion	Amphiphilic molecules' affinity for air interface causes 'ring' deposition.	138	2006
T	Temperature of tip, kinetics of deattachment from tip	Kinetics of dissolution & reattachment at tip is rate limiting.	139	2011
	5. Surface Diffusion			
Dwell time	Dot-size dwell time relationship	2D point source model (const flux)	140	2001
Hydro-philicity	Substrate hydrophilicity, lateral diffusion	Transport rate?? Double dip DPN	141	2005
Dwell time	Dot-size dwell time relationship	Const. conc model	135	2002
Ink-sub binding	Ink-sub interaction	Weak ink-sub binding can lead to fractal like growth	142	2003
Dwell time	Feature size at very long dwell times	Deposition rate slows at long DT	143	2005
Sub attach	Simulation	Moleculess from tip may displace bound molecules	144	2006

Table 2-3: Selected studies of the various parameters affecting deposition rate in DPN of molecular inks.

It must be noted that studies of molecular ink transport are usually limited to the model system of alkanethiols on gold. The factors affecting transport may be totally different for different classes of ink. For example, DPN of lipids exhibits a growth of feature height (due to stacking) with increasing dwell time[92]. This behaviour is totally absent from the alkanethiol/gold system as the growth of a single molecular layer is

generally assumed. The deposition of salts, nanoparticles, oligonucleiotides or proteins may also show esoteric behaviours. Distinct models for the deposition of each ink class may have to be derived.

2.4.1 Stages of alkanethiol deposition

The basic mechanism of molecular-ink deposition is the diffusion of molecules from tip to substrate via the condensed water meniscus (or otherwise). Many different intrinsic (i.e. inherent to the ink or substrate) and extrinsic (related to particular experimental conditions) parameters have been shown to affect ink transfer. The alkanethiol printing process can be broken down into five main stages, as illustrated in Figure 2-6:

1. Tip/substrate pre-treatment.
2. Inking of tip.
3. Contact with surface. (Formation of water meniscus.)
4. Ink transport to substrate.
5. Lateral diffusion and covalent attachment (SAM formation)

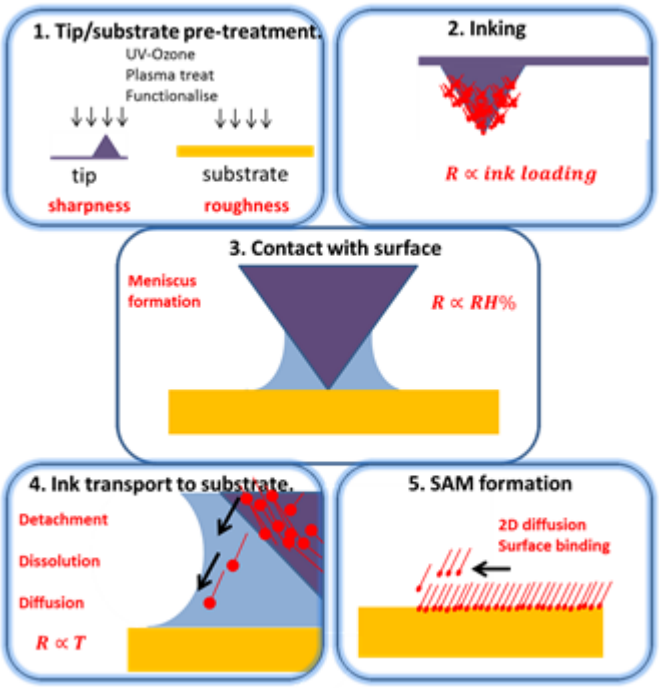

Figure 2-6: The five-step process of molecular ink transport. [Reprinted with permission from Liquid ink deposition from an atomic force microscope tip: deposition monitoring and control of feature size, O'Connell, C.D. et al., Langmuir, copyright 2014). American Chemical Society.]

Step 1: Tip, substrate condition

From some of the earliest work on molecular ink DPN it was clear that the minimum achievable feature size was dependent on the sharpness (radius of curvature) of the AFM tip used as a pen, as well as the quality of the gold substrate.[77] Further work by Nanoink inc., upon the release of the first dedicated DPN system (NScriptor), confirmed these findings.[145] The Nanoink results confirmed that the printing resolution was limited by the quality of the consumable tool (the AFM tip), and not by the precision of the piezo-actuator positioning system. The effects of tip and substrate have since been studied in isolation. An explicit DPN study using deliberately blunted tips showed that the size of water meniscus, and thus patterning resolution, is dependent on tip sharpness.[127] The effect of substrate roughness on molecular diffusion from a DPN tip has also been simulated using molecular dynamics.[129]

Step 2: Ink loading

The original method of loading a DPN pen with molecular inks (from which the moniker "dip-pen" nanolithography originates) was to dip the whole cantilever chip into a dilute alkanethiol solution, and then to dry off excess solvent in a stream of inert gas.[1] This method suffers from an unreliability in ink loading,[135] however, and several other methods have been described for more uniform ink-loading, such as vapour phase deposition.[130] The Mirkin group have used ink-jet printing as a method of controlling MHA loading onto a DPN tip, and so quantified the effect of ink loading on deposition rate.[131] They concluded that the effect of ink loading on deposition rate derived from the (ink on tip) surface-area dependent dissolution of MHA into the water meniscus.[131] Several studies have stressed the accurate knowledge of degree of inking as imperative for the accurate prediction of feature size.[126,128] If deposition rate is dependent on the loading of the tip, then a uniform deposition rate can only be achieved with a constant ink loading. As DPN deposition of molecules necessitates their removal from the tip (therefore decreasing loading), a constant deposition rate may not be possible. The depletion of ink from the tip over the course of an experiment has been shown to result in an exponential decay in printing rate.[128,146]

Step 3: Contact meniscus (Relative humidity)

When an AFM tip contacts a surface in ambient conditions a water meniscus will form by capillary condensation.[147] Transport of molecules through the meniscus was the original mechanism proposed to explain DPN printing.[1] The tool of environmental scanning electron microscopy (E-SEM) has provided unprecedented insight into the process of meniscus formation.[132] The E-SEM experiments found that the meniscus could be much larger than predicted by theory, although this anomalous result may be explainable by a charging effect caused by the electron flux. In a later E-SEM study, the 'rate of growth' of the meniscus was found to correlate with DPN

deposition rate, suggesting that the rate of meniscus formation itself may play a role in defining the dwell-time/feature size relationship.[133]

The necessity of a meniscus to effect DPN has been questioned however. DPN of the hydrophobic alkanethiol octadecanethiol (ODT) is not humidity sensitive, and printing in high vacuum has been achieved.[135] One salient conclusion is that the dependence on relative humidity varies with ink choice.[130,136] Thus, some molecules (such as MHA) may transfer through the water meniscus, and others (such as ODT) may transfer from tip to substrate via direct molecular diffusion (reactive spreading).

Most DPN experiments are conducted under conditions of controlled humidity, however this often necessitates a chamber equilibration time of an hour or more. A technique to control RH% via local delivery of water through a micropipette has been demonstrated.[148] In this study, the size of the water meniscus was probed as a function of local water delivery using AFM force curves. The increased meniscus size was correlated with increased deposition rate.

In the early days of DPN, the rapid development of understanding led to the suggestion that resolution would continue to increase; that deposition of single molecules may be possible, and that the ultimate limitation would then be in detecting the deposition by AFM.[134] Recent theoretical work has proposed a minimum stable water meniscus (~1.5 nm), the limit imposed by thermal fluctuation at room temperature.[149]

Step 4: Ink transport to surface

The transport of ink molecules through the water meniscus has been revealed to be a rich problem in physical chemistry involving several intermediate steps. Through measurements of the temperature dependence of the transport rate, the journey of an alkanethiol from tip to substrate has been found to depend on several factors, including; rate of detachment from the tip,[134,150] and solubility in the water meniscus[131,136]. In

one further twist, it was found that conventional Fickian diffusion through the meniscus cannot always be assumed. The phenomenon of 'annular diffusion', whereby an amphiphilic molecule (e.g. MHA) is preferentially transported along the meniscus water-air interface, was used to explain the printing of ring rather than dot features.[138]

Step 5: Lateral diffusion and substrate binding

Once the ink molecule reaches the substrate it must either bind to the surface or, if there are no binding sites available, diffuse laterally until it finds one. In the ideal case, the resulting feature will be a perfect circle of closed packed SAM. The first and simplest theoretical description of the dwell time dependent growth of feature size used a two dimensional model of constant flux from a point source.[140] Later, a constant concentration model was found to be a better fit to DPN dwell-time dependence data.[135]

Understanding this lateral diffusion and surface binding is crucial to avoiding imperfections in the resulting features, such as a diffuse cloud of molecules surrounding the main feature. The influence of lateral diffusivity has previously been highlighted in the case of micro-contact printing, where the achievable pattern definition was found to be critically dependent on alkanethiol chain length.[151] SAM formation beneath the tip can slow the lateral diffusion of further molecules, resulting in a decrease in deposition rate for very long dwell times.[143] In the case of a relatively weak ink-substrate binding, 2D diffusion can be dominated by the interaction between ink molecules, leading to random sprouting of preferential crystalline domains and 'anomalous' fractal-like growth.[142] Input from molecular simulation studies has added additional layers of complexity to the mechanism of lateral diffusion. For example, the growth of features may involve the displacement of substrate-bound molecules by molecules diffusing from the tip.[144]

2.5 Liquid ink DPN

The description of molecular ink DPN described above is essential for a comprehensive review of the technique. However, we must emphasize that DPN printing of liquid inks represents a very different problem; with different parameters to be considered and optimized. For example, a key issue with minute volumes of liquid is their rapid evaporation. Even a relatively non-volatile liquid, glycerol, will evaporate completely in a matter of minutes when droplet volume is in the femtolitre regime.[72]

2.5.1 DPN liquid ink development

Although DPN research was initially focused on developing molecular based inks, liquid inks are required for certain applications as not all materials can be transported by molecular diffusion of through a water meniscus. As the liquid itself functions as its own carrier, liquid inks are more versatile and can be deposited on a range of substrates. The advantages of using a liquid or gel based 'carrier matrix' have been described by the Mirkin group. In particular, ink-transport rates for the agarose matrix ink were consistent regardless of the protein or oligonucleotide being transported.[14]

A wide variety of liquid inks have been printed by DPN. A silver nanoparticle based liquid ink was developed for potential applications such as circuit repair.[9,10] In order to achieve longer ink lifetime glycerol was added to the aqueous based NP solution at a 10% v/v concentration. An aqueous based catalyst was DPN printed for the site-specific growth of carbon nanotubes (CNTs).[152] Circular deposits of catalyst around the perimeter of the printed dot were sometimes observed. The authors did not give an explanation. (We observe a similar effect in **Chapter 4** and attribute it to the 'coffee-drop' drying effect.) The native solution was diluted with high boiling point solvents (e.g. dimethylformamide (DMF) or glycerol) to reduce volatility of the ink. Polydimethylsiloxane (PDMS) patterns have been printed onto SiO_2 substrates.[153] (Though a similar result

had been achieved nine years before before by the Chaudhury group.[154]) The printed micron-scale spherical caps were used as templates to generate stamps. Recently our group demonstrated the deposition of liquid conducting polymer dispersion on a variety of hard and soft substrates.[155]

The Mirkin group have used DPN generated patterns of polyethylene glycol (PEG) as a gold etch resist.[113,156] Spherical cap structures of PEG were deposited on hexamethylsilazane (HDMS) functionalised silicon, with both the dot height and diameter growing with dwell time. Despite the three dimensional nature of the printed features, the ink transport was described in terms of the molecular 'diffusion coefficient' of the PEG on the substrate. DPN printed PEG droplets were also used as nanoscale lenses for sub-wavelength photolithography.[157] Nanoink Inc. has also promoted several liquid ink formulations including functional hydrogels based on a cross-linkable polyethylene glycol (PEG),[15,158] protein and DNA ink carriers, and an acrylic polymer based UV-curable ink.

2.5.2 The ink meniscus

Key to understanding the mechanism of DPN liquid ink deposition is the meniscus formed between tip and substrate upon contact. This 'liquid ink meniscus' differs from the water meniscus formed due to capillary condensation, as discussed in section 2.4 above.

The contact meniscus formed between nanoscale surfaces by ambient water condensation and/or adsorbed lubricant is of fundamental importance for understanding the origin of adhesion, friction, wear and lubrication.[159] The drive to improve magnetic-storage devices drove extensive work to understand the formation of nanoscale menisci.[159–161] The AFM and other proximal probe techniques have been vital to the developing science of nanotribology, by providing a 'model asperity' with which to compare theory and experiment.[159] Understanding meniscus formation has been important to the development of the AFM technique itself, as the

water meniscus can result in unwanted effects in AFM contact mode measurements, including snap-in and adhesion.[147]

Probing the ink meniscus by AFM

AFM measurements of adhesion forces have previously been used to probe the formation of liquid menisci between the tip and substrate. Malotky and Chaudhury coated an AFM tip with liquid PDMS (M_W=3700) and investigated the capillary forces acting on the tip when retracting from hydrophilic and hydrophobic surfaces.[154] On hydrophilic surfaces, they found the PDMS drained completely from the tip over the surface and no meniscus was distended during retraction. On hydrophobic surfaces, however, a liquid meniscus was distended and a droplet deposited upon breakage. The PDMS meniscus was stable enough that the tip could be retracted and advanced without breaking it. The group were primarily interested in modeling the capillary forces, and so control of the deposited droplet size was not investigated.

The Ondarçuhu group in Toulouse have published extensively on the use of a "liquid nanodispenser" (NADIS) to deposited atto-litre volumes of liquid in a controlled manner.[69-72] They have performed a dedicated study of the control of glycerol dot-size on APTES functionalised Si/SiOx, finding that the hydrophlicity of the tip and substrate, as well as the width of the nanochannel aperture were the dominant factors in determining feature size.[69] The found that, in contrast to DPN of molecular inks, liquid ink deposition was a non-diffusive process and dot-size reached 'saturation' after a dwell time of about 10 s. They attributed the saturation of the dwell time-dot size dependence to the attainment of equilibrium; the meniscus fulfilling the relationship between equilibrium contact angles (on tip and substrate) with the Laplace pressure of the liquid reservoir sitting on the cantilever. In a later study, the group used AFM force curves to measure the capillary forces at play during the deposition event, using 'Surface Evolver' to model the results.[71] (The Surface Evolver software

package minimizes the surface energy of a liquid with a given volume at a defined model geometry, yielding the equilibrium shape of the meniscus.)[162] Capillary forces calculated from the software model reproduced those measured from AFM force curves during deposition, however the model did contain multiple adjustable parameters.

Recently, the King group at UIUC in Illinois have used a heated AFM tip to deposit molten polyethylene in a form of thermal DPN (tDPN).[163] They could deposit both lines and dots, with stable flow achieved at >200°C. The group explored the qualitative scaling of various forces affecting deposition in order to deduce which were dominant in their system. They identified four forces acting on the growing edge of the polymer meniscus: the shear force (F_{shear}) acting when tip is moving relative to the substrate for line deposition, the line forces (F_{line}) arising from Marangoni effects due to the gradient in liquid surface tension across the temperature difference between heated tip and sample, as well as surface wetting), the Laplace force (F_{Lap}) arising due to the pressure gradient within the meniscus, and the resisting force to flow (F_{visc}) from polymer viscosity. Through estimating the magnitude of forces, they concluded that both thermal Marangoni and Laplace forces were likely to drive deposition during tDPN.

2.5.3 Mechanism of Liquid Ink deposition

In section 2.4.1 we described the mechanism of alkanethiol transport in DPN, a process which is at root diffusive in nature. Liquid ink deposition occurs due to very different mechanism.

Briefly, the DPN pen is usually 'inked' by dipping the tip in a microfluidic inkwell; ink flows onto the cantilever and forms a local reservoir of printable ink around the tip. When the pen is brought in contact with the substrate, the ink forms a liquid meniscus between tip and substrate. This meniscus grows with time. When the tip is retracted, it distends a meniscus bridge. Dot deposition occurs when the meniscus bridge breaks. The

deposited dot feature assumes the equilibrium shape of a spherical cap. The deposition process can again be broken down into five stages, as illustrated in Figure 2-7:

1. Tip/substrate pre-treatment.
2. Inking of tip.
3. Contact with surface (formation of ink meniscus.)
4. Tip retraction (distension of meniscus bridge).
5. Breaking of meniscus and final droplet deposition.

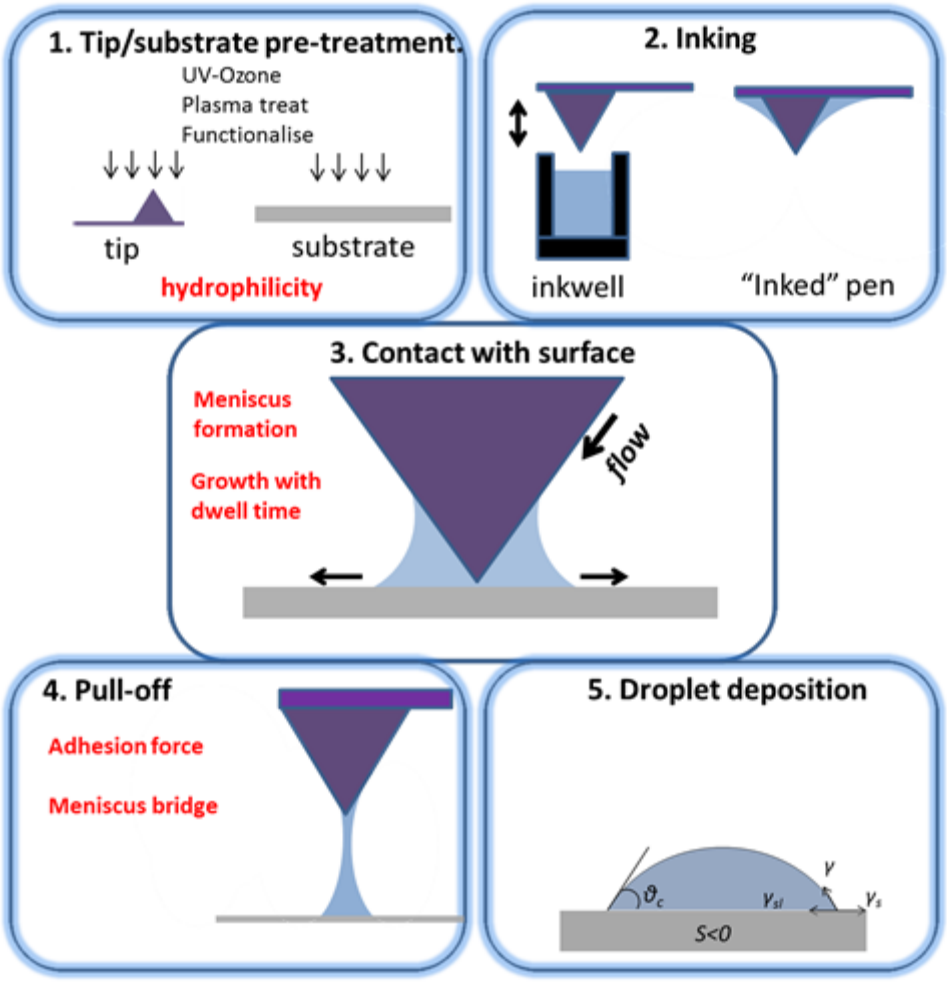

Figure 2-7: Stages of liquid ink DPN deposition. [Reprinted with permission from Liquid ink deposition from an atomic force microscope tip: deposition monitoring and control of feature size, O'Connell, C.D. et al., Langmuir, copyright 2014). American Chemical Society.]

Stage 1: Tip, substrate pretreatment

In the first instance, the ink must stick to the tip, and so a pre-treatment to control hydrophobicity may be performed. For example, for polar inks a UV or plasma treatment can be used to render the cantilever hydrophilic.[152] On the other hand, too-strong an affinity can cause the ink to diffuse over the back of the cantilever and reduce printing lifetime (see **Chapter 4**).

Tip-pretreatment can also satisfy esoteric needs of a particular ink formulation. For example, by functionalizing the tip with polyethyelene glycol, the Mirkin group were able to maintain proteins in a hydrated state and therefore maintain native structure and activity during direct write deposition.[13]

The substrate may also be modified to promote a covalent affinity for the ink. For example, the Mirkin group have used a N-hydroxysuccinimide-ester (NHS) activated surface for binding amine modified proteins via amide linkages.[14]

Stage 2: Inking of tip

In 2005 and 2006, Nanoink introduced microfluidic ink-wells specifically tailored for loading DPN pens with liquid inks.[164,165] These ink-wells also enable the multi-plexed inking of several different liquid inks on the same pen array, a capability especially interesting for patterning arrays of multiple different biological molecules.[15] Nanoink have also commercialized a linear cantilever array, the M-type probe, for use in liquid ink DPN. The M-type probe has an ink reservoir etched into the underside of the cantilever to hold the ink in place to feed the tip and to increase printing lifetime.

In **Chapter 6** we will demonstrate a method of monitoring the degree of inking using the resonance frequency of the cantilever.

Stage 3: Contact with substrate, meniscus formation

The ink coating a DPN tip will assume a shape minimizing its surface energy according to the Young-Laplace equation. Most of the ink volume is held at the base of the pyramid, but a very thin layer of liquid will coat the whole tip pyramid down to the apex. The thickness of this coating at the apex can be measured by its effect on the 'snap in' distance of a probe approaching a substrate. The liquid PDMS layer coating an inked AFM tip was measured at ~5 nm in this way.[154]

When the tip touches down, the thin ink coating forms a liquid meniscus between tip and substrate. The shape of this meniscus is again determined by the Young-Laplace equation and also the contact angles of the ink with the tip and substrate respectively. The dwell time dependence of liquid ink deposition provides evidence that the volume of this liquid meniscus grows with time. A full description of the growth of meniscus volume is currently lacking. In relation to the increased static adhesion between rough substrates with time, Bhushan et al. derived a time-dependent expression for the growth of a meniscus around a nanoscale aperture.[160] They predicted exponential growth dynamics up to a maximum volume. However, their system consisted of the wicking of a liquid thin film onto a nanoscale aperture, not the flow of liquid down the tip to a substrate.

We will explore this topic further in **Chapter 5**. We will find that the size of the deposited droplet is critically dependent on the volume of the contact meniscus. We will also see how the volume of ink located around the tip can increase and decrease over the course of a printing experiment due to ink-on-tip hydrodynamics. These changes in local volume can have a significant impact upon deposition rate.

Step 4: Pull off, distension of meniscus bridge

When the cantilever is retracted, the adhesive force of the ink meniscus will initially pin the tip to the substrate. These meniscus forces are well understood and are primarily composed of the capillary force arising from

the ink surface tension and the Laplace force arising from the negative Laplace pressure within a meniscus of negative curvature.[147,154,166] When the tip does pull-off the substrate, the ink is pulled into a meniscus bridge between tip and substrate. The meniscus bridge 'necks' during retraction until it breaks.

Step 5: Breaking of meniscus bridge, deposition

Upon breaking of the meniscus bridge, a liquid droplet is deposited on the substrate. In their study of the NADIS technique, the Ondarcuhu group found the 'extension length' (height at which the meniscus breaks) was related in a non-linear fashion to the resulting dot radius.[71]

In **Chapter 5** we will show how, in the case of DPN, the height at meniscus break is directly related to the size of the deposited droplet. We will describe how geometrical arguments can be used to directly calculate the deposited dot volume from extension length alone. We will also investigate the spherical cap shape of the droplets on hydrophilic and hydrophobic surfaces, finding that the dynamics of deposition can cause droplets to deviate from their equilibrium contact angle.

2.6 Summary and outlook

In a 2003 George Whitesides (Harvard University) argued that the impact of DPN technology would be limited because no problem had yet been found for which DPN was the only answer.[167] In the decade since then, DPN has become increasingly recognized by the research community as a powerful tool for creating designer substrates using nanoscale, molecular building blocks. The huge versatility afforded by the availability of hundreds of demonstrated ink-substrate systems has piqued the interest of researchers from a wide range of disciplines. However, whether the technique will transition from being a useful tool in the research setting, to being a successful lithography technique in its own right, remains to be seen.

The impact of DPN on the biological sciences has grown. In recent years, several important breakthroughs in understanding stem cell differentiation have been made possible using DPN nanoarrays. However, much of DPN's potential is as yet untapped. In particular, the recent advances demonstrating multi-ink protein patterning over large areas have yet to be utilized to address long standing questions in fundamental cell biology, such as the complexities of how cell phenotype is influenced by multiple signaling proteins arrayed on a surface.

Major advances have been made in addressing the limitations of DPN. throughput. In particular, the invention of polymer pen lithography has enabled the high resolution printing of DPN to be up-scaled to millions of simultaneous patterns in a cost-effective manner. Multi-plexed inking strategies have also been developed, but pattern complexity still remains restricted by limitations imposed by the passive probe design. The greatest potential of DPN/PPL technology will be only unlocked when multi-inking strategies are married with individually addressable, massively parallel active pen arrays. A good understanding of the parameters affecting molecular ink transport has been built up. However, much further work is required to achieve a similar level of understanding for liquid ink deposition.

2.7 References

1. Piner, R. D. "Dip-Pen" Nanolithography. *Science (80-.).* **283,** 661–663 (1999).

2. Demers, L. M. *et al.* Direct patterning of modified oligonucleotides on metals and insulators by dip-pen nanolithography. *Science* **296,** 1836–8 (2002).

3. Lee, K.-B., Park, S.-J., Mirkin, C. a, Smith, J. C. & Mrksich, M. Protein nanoarrays generated by dip-pen nanolithography. *Science* **295,** 1702–5 (2002).

4. Su, M., Liu, X., Li, S.-Y., Dravid, V. P. & Mirkin, C. a. Moving beyond molecules: patterning solid-state features via dip-pen nanolithography with sol-based inks. *J. Am. Chem. Soc.* **124,** 1560–1 (2002).

5. Li, Y., Maynor, B. W. & Liu, J. Electrochemical AFM "Dip-Pen" Nanolithography. *J. Am. Chem. Soc.* **123,** 2105–2106 (2001).

6. Maynor, B. W., Filocamo, S. F., Grinstaff, M. W. & Liu, J. Direct-Writing of Polymer Nanostructures: Poly(thiophene) Nanowires on Semiconducting and Insulating Surfaces. *J. Am. Chem. Soc.* **124,** 522–523 (2002).

7. Nelson, B. a., King, W. P., Laracuente, a. R., Sheehan, P. E. & Whitman, L. J. Direct deposition of continuous metal nanostructures by thermal dip-pen nanolithography. *Appl. Phys. Lett.* **88,** 033104 (2006).

8. Weinberger, D. A., Hong, S., Mirkin, C. A., Wessels, B. W. & Higgins, T. B. Combinatorial Generation and Analysis of Nanometer- and Micrometer-Scale Silicon Features via "Dip-Pen" Nanolithography and Wet Chemical Etching. *Adv. Mater.* **12,** 1600–1603 (2000).

9. Wang, H. *et al.* Toward conductive traces: Dip Pen Nanolithography® of silver nanoparticle-based inks. *Appl. Phys. Lett.* **93,** 143105 (2008).

10. Hung, S. *et al.* Dip Pen Nanolithography of Conductive Silver Traces. *J. Phys. Chem. C* **114,** 9672–9677 (2010).

11. Su, M., Aslam, M., Fu, L., Wu, N. & Dravid, V. P. Dip-pen nanopatterning of photosensitive conducting polymer using a monomer ink. *Appl. Phys. Lett.* **84,** 4200 (2004).

12. Lim, J.-H. & Mirkin, C. A. Electrostatically Driven Dip-Pen Nanolithography of Conducting Polymers. *Adv. Mater.* **14,** 1474–1477 (2002).

13. Lim, J.-H. *et al.* Direct-write dip-pen nanolithography of proteins on modified silicon oxide surfaces. *Angew. Chem. Int. Ed. Engl.* **42,** 2309–12 (2003).

14. Senesi, A. J., Rozkiewicz, D. I., Reinhoudt, D. N. & Mirkin, C. A. Agarose-assisted dip-pen nanolithography of oligonucleotides and proteins. *ACS Nano* **3,** 2394–402 (2009).

15. Jang, J.-W., Smetana, A. & Stiles, P. Multi-ink pattern generation by dip-pen nanolithography. *Scanning* **32,** 24–9 (2010).

16. Binnig, G., Rohrer, H., Gerber, C. & Weibel, E. Surface Studies by Scanning Tunneling Microscopy. *Phys. Rev. Lett.* **49,** 57–61 (1982).

17. Eigler, D. M. & Schweizer, E. K. Positioning single atoms with a scanning tunnelling microscope. *Nature* **344,** 524–526 (1990).

18. Binnig, G. & Quate, C. F. Atomic Force Microscope. *Phys. Rev. Lett.* **56,** 930–933 (1986).

19. Müller, D. J. & Dufrêne, Y. F. Atomic force microscopy as a multifunctional molecular toolbox in nanobiotechnology. *Nat. Nanotechnol.* **3,** 261–9 (2008).

20. Bhushan, B. & Koinkar, V. N. Nanoindentation hardness measurements using atomic force microscopy. *Appl. Phys. Lett.* **64,** 1653 (1994).

21. Heim, L. *et al.* Adhesion and Friction Forces between Spherical Micrometer-Sized Particles. 16–19 (1999).

22. Noy, A., Vezenov, D. V. & Lieber, C. M. Chemical Force Microscopy. *Annu. Rev. Mater. Sci.* **27,** 381–421 (1997).

23. Sáenz, J. J. *et al.* Observation of magnetic forces by the atomic force microscope. *J. Appl. Phys.* **62,** 4293 (1987).

24. Meyer, E., Hug, H. J. & Bennewitz, R. *Scanning probe microscopy: the lab on a tip*. (Springer, 2003).

25. Quate, C. F. Scanning probes as a lithography tool for nanostructures. *Surf. Sci.* **386,** 259–264 (1997).

26. Vettiger, P. *et al.* The "Millipede"—More than thousand tips for future AFM storage. *IBM J. Res. Dev.* **44,** 323–340 (2000).

27. Liu, G.-Y., Xu, S. & Qian, Y. Nanofabrication of Self-Assembled Monolayers Using Scanning Probe Lithography. *Acc. Chem. Res.* **33,** 457–466 (2000).

28. Xie, X. N., Chung, H. J., Sow, C. H. & Wee, a. T. S. Nanoscale materials patterning and engineering by atomic force microscopy nanolithography. *Mater. Sci. Eng. R Reports* **54,** 1–48 (2006).

29. Garcia, R., Martinez, R. V & Martinez, J. Nano-chemistry and scanning probe nanolithographies. *Chem. Soc. Rev.* **35,** 29–38 (2006).

30. Liu, X. & Zhang, H. in *Mod. Res. Educ. Top. Microsc.* 770–778 (2007).

31. Rosa, L. G. & Liang, J. Atomic force microscope nanolithography : tapping mode , electrochemical and thermal nanolithography. **483001,** (2009).

32. Li, X., Nardi, P., Baek, C.-W., Kim, J.-M. & Kim, Y.-K. Direct nanomechanical machining of gold nanowires using a nanoindenter and an atomic force microscope. *J. Micromechanics Microengineering* **15,** 551–556 (2005).

33. Schumacher, H. W., Keyser, U. F., Zeitler, U., Haug, R. J. & Eberl, K. Nanomachining of mesoscopic electronic devices using an atomic force microscope. *Appl. Phys. Lett.* **75,** 1107 (1999).

34. Cappella, B. & Sturm, H. Comparison between dynamic plowing lithography and nanoindentation methods. *J. Appl. Phys.* **91,** 506 (2002).

35. Chen, J.-M., Liao, S.-W. & Tsai, Y.-C. Electrochemical synthesis of polypyrrole within PMMA nanochannels produced by AFM mechanical lithography. *Synth. Met.* **155,** 11–17 (2005).

36. Higgins, M. J., Grosse, W., Wagner, K., Molino, P. J. & Wallace, G. G. Reversible shape memory of nanoscale deformations in inherently conducting polymers without reprogramming. *J. Phys. Chem. B* **115,** 3371–8 (2011).

37. Binnig, G. *et al.* Ultrahigh-density atomic force microscopy data storage with erase capability. *Appl. Phys. Lett.* **74,** 1329 (1999).

38. Lutwyche, M. I. *et al.* Highly parallel data storage system based on scanning probe arrays. *Appl. Phys. Lett.* **77,** 3299 (2000).

39. King, W. P. *et al.* Atomic force microscope cantilevers for combined thermomechanical data writing and reading. *Appl. Phys. Lett.* **78,** 1300 (2001).

40. Ulman, A. Formation and Structure of Self-Assembled Monolayers. *Chem. Rev.* **96,** 1533–1554 (1996).

41. Kumar, A., Biebuyck, H. a. & Whitesides, G. M. Patterning Self-Assembled Monolayers: Applications in Materials Science. *Langmuir* **10,** 1498–1511 (1994).

42. Love, J. C., Estroff, L. a, Kriebel, J. K., Nuzzo, R. G. & Whitesides, G. M. Self-assembled monolayers of thiolates on metals as a form of nanotechnology. *Chem. Rev.* **105,** 1103–69 (2005).

43. Navarre, S. *et al.* Structural Characterization of Self-Assembled Monolayers of Organosilanes Chemically Bonded onto Silica Wafers by Dynamical Force Microscopy. *Society* 4961–4967 (2001).

44. Xu, S. & Liu, G. Nanometer-Scale Fabrication by Simultaneous Nanoshaving and Molecular Self-Assembly. *Langmuir* **13,** 127–129 (1997).

45. Staii, C., Wood, D. W. & Scoles, G. Verification of biochemical activity for proteins nanografted on gold surfaces. *J. Am. Chem. Soc.* **130,** 640–6 (2008).

46. Garno, J. C. *et al.* Precise Positioning of Nanoparticles on Surfaces Using Scanning Probe Lithography. *Nano Lett.* **3,** 389–395 (2003).

47. Sheehan, P. & Lieber, C. Nanotribology and Nanofabrication of MoO3 Structures by Atomic Force Microscopy. *Science* **272,** 1158–61 (1996).

48. Sugimoto, Y. *et al.* Atom inlays performed at room temperature using atomic force microscopy. *Nat. Mater.* **4,** 156–9 (2005).

49. Campbell, P. M., Snow, E. S. & McMarr, P. J. Fabrication of nanometer-scale side-gated silicon field effect transistors with an atomic force microscope. *Appl. Phys. Lett.* **66,** 1388 (1995).

50. Snow, E. S. & Campbell, P. M. Fabrication of Si nanostructures with an atomic force microscope. *Appl. Phys. Lett.* **64,** 1932 (1994).

51. Fuhrer, A. *et al.* Energy spectra of quantum rings. *Nature* **413,** 822–5 (2001).

52. Qin, G. & Cai, C. Sub-10-nm patterning of oligo(ethylene glycol) monolayers on silicon surfaces via local oxidation using a conductive atomic force microscope. *Nanotechnology* **20,** 355306 (2009).

53. Meroni, D., Ardizzone, S., Schubert, U. S. & Hoeppener, S. Probe-Based Electro-Oxidative Lithography of OTS SAMs Deposited onto Transparent ITO Substrates. *Adv. Funct. Mater.* **22,** 4376–4382 (2012).

54. Minne, S. C. *et al.* Centimeter scale atomic force microscope imaging and lithography. *Appl. Phys. Lett.* **73,** 1742 (1998).

55. Xie, X. N., Chung, H. J., Sow, C. H., Adamiak, K. & Wee, A. T. S. Electrical discharge in a nanometer-sized air/water gap observed by atomic force microscopy. *J. Am. Chem. Soc.* **127,** 15562–7 (2005).

56. Lyuksyutov, S. F. *et al.* Electrostatic nanolithography in polymers using atomic force microscopy. *Nat. Mater.* **2,** 468–72 (2003).

57. Chung, H. J., Xie, X. N., Sow, C. H., Bettiol, A. A. & Wee, A. T. S. Polymeric conical structure formation by probe-induced electrohydrodynamical nanofluidic motion. *Appl. Phys. Lett.* **88,** 023116 (2006).

58. Xie, X. N. *et al.* Micro/nanoscopic patterning of polymeric materials by atomic force microscope assisted electrohydrodynamic nanolithography. *J. Appl. Phys.* **103,** 024307 (2008).

59. Loh, O. *et al.* Nanofountain-probe-based high-resolution patterning and single-cell injection of functionalized nanodiamonds. *Small* **5,** 1667–74 (2009).

60. Salaita, K., Wang, Y. & Mirkin, C. A. Applications of dip-pen nanolithography. *Nat. Nanotechnol.* **2,** 145–55 (2007).

61. Lewis, A. *et al.* Fountain pen nanochemistry: Atomic force control of chrome etching. *Appl. Phys. Lett.* **75,** 2689 (1999).

62. Kim, K., Moldovan, N. & Espinosa, H. D. Patterning techniques A Nanofountain Probe with Sub-100 nm Molecular Writing Resolution**. 632–635 (2005). doi:10.1002/smll.200500027

63. Moldovan, N., Kim, K. & Espinosa, H. D. Design and Fabrication of a Novel Microfluidic Nanoprobe. **15,** 204–213 (2006).

64. Kim, K. & Ke, C. Massively parallel multi-tip nanoscale writer with fluidic capabilities–fountain pen nanolithography (FPN). … *MEMS* … **60208,** 235–238 (2003).

65. Wu, B., Ho, A., Moldovan, N. & Espinosa, H. D. Direct deposition and assembly of gold colloidal particles using a nanofountain probe. *Langmuir* **23,** 9120–3 (2007).

66. Kim, K.-H. *et al*. Direct Delivery and Submicrometer Patterning of DNA by a Nanofountain Probe. *Adv. Mater.* **20,** 330–334 (2008).

67. Loh, O. Y. *et al*. Electric field-induced direct delivery of proteins by a nanofountain probe. *Proc. Natl. Acad. Sci. U. S. A.* **105,** 16438–43 (2008).

68. Meister, a., Liley, M., Brugger, J., Pugin, R. & Heinzelmann, H. Nanodispenser for attoliter volume deposition using atomic force microscopy probes modified by focused-ion-beam milling. *Appl. Phys. Lett.* **85,** 6260 (2004).

69. Fang, A., Dujardin, E. & Ondarçuhu, T. Control of droplet size in liquid nanodispensing. *Nano Lett.* **6,** 2368–74 (2006).

70. Ondarçuhu, T. *et al*. Controlled deposition of nanodroplets on a surface by liquid nanodispensing: Application to the study of the evaporation of femtoliter sessile droplets. *Eur. Phys. J. Spec. Top.* **166,** 15–20 (2009).

71. Fabié, L., Durou, H. & Ondarçuhu, T. Capillary forces during liquid nanodispensing. *Langmuir* **26,** 1870–8 (2010).

72. Arcamone, J., Dujardin, E., Rius, G., Pérez-Murano, F. & Ondarçuhu, T. Evaporation of femtoliter sessile droplets monitored with nanomechanical mass sensors. *J. Phys. Chem. B* **111,** 13020–7 (2007).

73. Hosaka, S. *et al*. Fabrication of nanostructures using scanning probe microscopes. *J. Vac. Sci. Technol. B Microelectron. Nanom. Struct.* **13,** 2813 (1995).

74. Wu, Y., Johannes, M. S. & Clark, R. L. AFM-based voltage assisted nanoelectrospinning. **62,** 699–702 (2008).

75. Jaschke, M. & Butt, H.-J. Deposition of Organic Material by the Tip of a Scanning Force Microscope. *Langmuir* **11,** 1061–1064 (1995).

76. Piner, R. D. & Mirkin, C. A. Effect of Water on Lateral Force Microscopy in Air. **49,** 6864–6868 (1997).

77. Hong, S. Multiple Ink Nanolithography: Toward a Multiple-Pen Nano-Plotter. *Science (80-.).* **286,** 523–525 (1999).

78. Hong, S. & Mirkin, C. A nanoplotter with both parallel and serial writing capabilities. *Science* **288,** 1808–11 (2000).

79. Ginger, D. S., Zhang, H. & Mirkin, C. A. The Evolution of Dip-Pen Nanolithography Angewandte. 30–45 (2004). doi:10.1002/anie.200300608

80. Wilson, D. L. *et al*. Surface organization and nanopatterning of collagen by dip-pen nanolithography. *Proc. Natl. Acad. Sci. U. S. A.* **98,** 13660–4 (2001).

81. Zhang, M. *et al*. A MEMS nanoplotter with high-density parallel dip-pen nanolithography probe arrays. *Nanotechnology* **13,** 212–217 (2002).

82. Jung, H., Kulkarni, R. & Collier, C. P. Dip-pen nanolithography of reactive alkoxysilanes on glass. *J. Am. Chem. Soc.* **125,** 12096–7 (2003).

83. Liu, X., Guo, S. & Mirkin, C. a. Surface and site-specific ring-opening metathesis polymerization initiated by dip-pen nanolithography. *Angew. Chem. Int. Ed. Engl.* **42,** 4785–9 (2003).

84. Smith, J. C. *et al.* Nanopatterning the Chemospecific Immobilization of Cowpea Mosaic Virus Capsid. *Nano Lett.* **3,** 883–886 (2003).

85. Bullen, D. *et al.* Parallel dip-pen nanolithography with arrays of individually addressable cantilevers. *Appl. Phys. Lett.* **84,** 789 (2004).

86. Lee, K.-B., Kim, E.-Y., Mirkin, C. a. & Wolinsky, S. M. The Use of Nanoarrays for Highly Sensitive and Selective Detection of Human Immunodeficiency Virus Type 1 in Plasma. *Nano Lett.* **4,** 1869–1872 (2004).

87. Vega, R. a, Maspoch, D., Salaita, K. & Mirkin, C. a. Nanoarrays of single virus particles. *Angew. Chem. Int. Ed. Engl.* **44,** 6013–5 (2005).

88. Liu, X. *et al.* The controlled evolution of a polymer single crystal. *Science* **307,** 1763–6 (2005).

89. Salaita, K. *et al.* Massively parallel dip-pen nanolithography with 55 000-pen two-dimensional arrays. *Angew. Chem. Int. Ed. Engl.* **45,** 7220–3 (2006).

90. Wang, Y. *et al.* Controlling the shape, orientation, and linkage of carbon nanotube features with nano affinity templates. *Proc. Natl. Acad. Sci. U. S. A.* **103,** 2026–31 (2006).

91. Vega, R. a *et al.* Monitoring single-cell infectivity from virus-particle nanoarrays fabricated by parallel dip-pen nanolithography. *Small* **3,** 1482–5 (2007).

92. Lenhert, S., Sun, P., Wang, Y., Fuchs, H. & Mirkin, C. a. Massively parallel dip-pen nanolithography of heterogeneous supported phospholipid multilayer patterns. *Small* **3,** 71–5 (2007).

93. Sistiabudi, R. & Ivanisevic, A. Dip-Pen Nanolithography of Bioactive Peptides on Collagen-Terminated Retinal Membrane. *Adv. Mater.* **20,** 3678–3681 (2008).

94. Huo, F. *et al.* Polymer pen lithography. *Science* **321,** 1658–60 (2008).

95. Zheng, Z. *et al.* Multiplexed Protein Arrays Enabled by Polymer Pen Lithography: Addressing the Inking Challenge. *Angew. Chemie* **121,** 7762–7765 (2009).

96. Curran, J. M. *et al.* Introducing dip pen nanolithography as a tool for controlling stem cell behaviour: unlocking the potential of the next generation of smart materials in regenerative medicine. *Lab Chip* **10,** 1662–70 (2010).

97. Huo, F. *et al.* Beam pen lithography. *Nat. Nanotechnol.* **5,** 637–40 (2010).

98. Chai, J. *et al.* Scanning probe block copolymer lithography. *Proc. Natl. Acad. Sci. U. S. A.* **107,** 20202–6 (2010).

99. Shim, W. *et al*. Hard-tip, soft-spring lithography. *Nature* **469,** 516–20 (2011).

100. Chai, J., Wong, L. S., Giam, L. & Mirkin, C. a. Single-molecule protein arrays enabled by scanning probe block copolymer lithography. *Proc. Natl. Acad. Sci. U. S. A.* **108,** 19521–5 (2011).

101. Kim, J. *et al*. Direct-write patterning of bacterial cells by dip-pen nanolithography. *J. Am. Chem. Soc.* **134,** 16500–3 (2012).

102. Giam, L. R. *et al*. Scanning probe-enabled nanocombinatorics define the relationship between fibronectin feature size and stem cell fate. *Proc. Natl. Acad. Sci. U. S. A.* 1–6 (2012). doi:10.1073/pnas.1201086109

103. Basnar, B. & Willner, I. Dip-pen-nanolithographic patterning of metallic, semiconductor, and metal oxide nanostructures on surfaces. *Small* **5,** 28–44 (2009).

104. Wu, C.-C., Reinhoudt, D. N., Otto, C., Subramaniam, V. & Velders, A. H. Strategies for patterning biomolecules with dip-pen nanolithography. *Small* **7,** 989–1002 (2011).

105. Mirkin, C. A. The power of the pen: development of massively parallel dip-pen nanolithography. *ACS Nano* **1,** 79–83 (2007).

106. Haaheim, J. R., Tevaarwerk, E. R., Fragala, J. & Shile, R. Commercially available high-throughput dip pen nanolithography. in (George, T. & Cheng, Z.) **6959,** 69590I–69590I–11 (2008).

107. Braunschweig, A. B., Huo, F. & Mirkin, C. a. Molecular printing. *Nat. Chem.* **1,** 353–8 (2009).

108. Liao, X., Braunschweig, A. B. & Mirkin, C. a. "Force-feedback" leveling of massively parallel arrays in polymer pen lithography. *Nano Lett.* **10,** 1335–40 (2010).

109. Liao, X., Braunschweig, A. B., Zheng, Z. & Mirkin, C. a. Force- and time-dependent feature size and shape control in molecular printing via polymer-pen lithography. *Small* **6,** 1082–6 (2010).

110. Bullen, D. & Liu, C. Electrostatically actuated dip pen nanolithography probe arrays. *Sensors Actuators A Phys.* **125,** 504–511 (2006).

111. Hoover, D. K., Chan, E. W. L. & Yousaf, M. N. Asymmetric peptide nanoarray surfaces for studies of single cell polarization. *J. Am. Chem. Soc.* **130,** 3280–1 (2008).

112. Pena, D. J., Raphael, M. P. & Byers, J. M. " Dip-Pen " Nanolithography in Registry with Photolithography for Biosensor Development. *Society* 9028–9032 (2003).

113. Jang, J.-W. *et al*. Generation of metal photomasks by dip-pen nanolithography. *Small* **5,** 1850–3 (2009).

114. Lee, M. *et al*. Measurement of interaction force between nanoarrayed integrin alphavbeta3 and immobilized vitronectin on the cantilever tip. *Biochem. Biophys. Res. Commun.* **362,** 935–9 (2007).

115. Vacanti, J. P. & Langer, R. Tissue engineering: the design and fabrication of living replacement devices for surgical reconstruction and transplantation. *Lancet* **354,** S32–S34 (1999).

116. Moulton, S. E., Higgins, M. J., Kapsa, R. M. I. & Wallace, G. G. Organic Bionics: A New Dimension in Neural Communications. *Adv. Funct. Mater.* **22,** 2003–2014 (2012).

117. Yousaf, M. N. Model substrates for studies of cell mobility. *Curr. Opin. Chem. Biol.* **13,** 697–704 (2009).

118. Mrksich, M. A surface chemistry approach to studying cell adhesion. *Chem. Soc. Rev.* **29,** 267–273 (2000).

119. Chen, C. S., Mrksich, M., Huang, S., Whitesides, G. M. & Ingber, D. E. Geometric Control of Cell Life and Death. *Science (80-.).* **276,** 1425–1428 (1997).

120. Ostuni, E., Whitesides, G. M., Ingber, D. E. & Chen, C. S. Using self-assembled monolayers to pattern ECM proteins and cells on substrates. *Methods Mol. Biol.* **522,** 183–94 (2009).

121. Stevens, M. M. & George, J. H. Exploring and engineering the cell surface interface. *Science* **310,** 1135–8 (2005).

122. Curran, J. M. *et al.* Nanoscale definition of substrate materials to direct human adult stem cells towards tissue specific populations. *J. Mater. Sci. Mater. Med.* **21,** 1021–9 (2010).

123. Hoover, D. K., Lee, E., Chan, E. W. L. & Yousaf, M. N. Electroactive nanoarrays for biospecific ligand mediated studies of cell adhesion. *Chembiochem* **8,** 1920–3 (2007).

124. Sekula, S. *et al.* Multiplexed lipid dip-pen nanolithography on subcellular scales for the templating of functional proteins and cell culture. *Small* **4,** 1785–93 (2008).

125. Narui, Y. & Salaita, K. S. Dip-pen nanolithography of optically transparent cationic polymers to manipulate spatial organization of proteolipid membranes. *Chem. Sci.* **3,** 794 (2012).

126. Saha, S. K. & Culpepper, M. L. An Ink Transport Model for Prediction of Feature Size in Dip Pen Nanolithography. *Small* 15364–15369 (2010).

127. John, N. S. & Kulkarni, G. U. Dip-Pen Lithography Using Pens of Different Thicknesses. *J. Nanosci. Nanotechnol.* **7,** 977–981 (2007).

128. Peterson, E. J., Weeks, B. L., Yoreo, J. J. De & Schwartz, P. V. Effect of Environmental Conditions on Dip Pen Nanolithography of Mercaptohexadecanoic Acid. 15206–15210 (2004).

129. Wu, C.-D. & Fang, T.-H. Simulation of deposition of ink molecules on rough substrates in dip-pen nanolithography. *Model. Simul. Mater. Sci. Eng.* **19,** 065008 (2011).

130. Schwartz, P. V. Molecular Transport from an Atomic Force Microscope Tip: A Comparative Study of Dip-Pen Nanolithography. *Langmuir* **18,** 4041–4046 (2002).

131. Giam, L. R., Wang, Y. & Mirkin, C. A. Nanoscale molecular transport: the case of dip-pen nanolithography. *J. Phys. Chem. A* **113,** 3779–82 (2009).

132. Weeks, B. L., Vaughn, M. W. & Deyoreo, J. J. Direct imaging of meniscus formation in atomic force microscopy using environmental scanning electron microscopy. *Langmuir* **21,** 8096–8 (2005).

133. Weeks, B. L. & DeYoreo, J. J. Dynamic meniscus growth at a scanning probe tip in contact with a gold substrate. *J. Phys. Chem. B* **110,** 10231–3 (2006).

134. Weeks, B., Noy, A., Miller, A. & De Yoreo, J. Effect of Dissolution Kinetics on Feature Size in Dip-Pen Nanolithography. *Phys. Rev. Lett.* **88,** 1–4 (2002).

135. Sheehan, P. & Whitman, L. Thiol Diffusion and the Role of Humidity in "Dip Pen Nanolithography."*Phys. Rev. Lett.* **88,** 156104 (2002).

136. Rozhok, S., Piner, R. & Mirkin, C. a. Dip-Pen Nanolithography: What Controls Ink Transport? *J. Phys. Chem. B* **107,** 751–757 (2003).

137. Salaita, K., Amarnath, A., Higgins, T. B. & Mirkin, C. A. The effects of organic vapor on alkanethiol deposition via dip-pen nanolithography. *Scanning* **32,** 9–14 (2010).

138. Nafday, O. A., Vaughn, M. W. & Weeks, B. L. Evidence of meniscus interface transport in dip-pen nanolithography : An annular diffusion model Evidence of meniscus interface transport in dip-pen nanolithography : An annular diffusion model. **144703,** (2006).

139. Chung, S., Felts, J. R., Wang, D., King, W. P. & De Yoreo, J. J. Temperature-dependence of ink transport during thermal dip-pen nanolithography. *Appl. Phys. Lett.* **99,** 193101 (2011).

140. Jang, J., Hong, S., Schatz, G. C. & Ratner, M. a. Self-assembly of ink molecules in dip-pen nanolithography: A diffusion model. *J. Chem. Phys.* **115,** 2721 (2001).

141. Hampton, J. R., Dameron, A. A. & Weiss, P. S. Double-ink dip-pen nanolithography studies elucidate molecular transport. *J. Am. Chem. Soc.* **128,** 1648–53 (2006).

142. Manandhar, P., Jang, J., Schatz, G. C., Ratner, M. A. & Hong, S. Anomalous Surface Diffusion in Nanoscale Direct Deposition Processes. **1,** 1–4 (2003).

143. Hampton, J. R., Dameron, A. A. & Weiss, P. S. Transport rates vary with deposition time in dip-pen nanolithography. *J. Phys. Chem. B* **109,** 23118–20 (2005).

144. Ahn, Y., Hong, S. & Jang, J. Growth dynamics of self-assembled monolayers in dip-pen nanolithography. *J. Phys. Chem. B* **110,** 4270–3 (2006).

145. Haaheim, J. *et al.* Dip Pen Nanolithography (DPN): process and instrument performance with NanoInk's NSCRIPTOR system. *Ultramicroscopy* **103,** 117–32 (2005).

146. Wu, T.-H., Lu, H.-H. & Lin, C.-W. Dependence of transport rate on area of lithography and pretreatment of tip in dip-pen nanolithography. *Langmuir* **28,** 14509–13 (2012).

147. Butt, H.-J. & Kappl, M. Normal capillary forces. *Adv. Colloid Interface Sci.* **146,** 48–60 (2009).

148. Su, M., Pan, Z., Dravid, V. P. & Thundat, T. Locally enhanced relative humidity for scanning probe nanolithography. *Langmuir* **21,** 10902–6 (2005).

149. Jang, J., Schatz, G. & Ratner, M. How Narrow Can a Meniscus Be? *Phys. Rev. Lett.* **92,** 085504 (2004).

150. Hsiao, Y.-S. *et al.* Manipulating location, polarity, and outgrowth length of neuron-like pheochromocytoma (PC-12) cells on patterned organic electrode arrays. *Lab Chip* **11,** 3674–80 (2011).

151. Delamarche, E. *et al.* Transport Mechanisms of Alkanethiols during Microcontact Printing on Gold. *J. Phys. Chem. B* **102,** 3324–3334 (1998).

152. Kuljanishvili, I., Dikin, D. A., Rozhok, S., Mayle, S. & Chandrasekhar, V. Controllable patterning and CVD growth of isolated carbon nanotubes with direct parallel writing of catalyst using dip-pen nanolithography. *Small* **5,** 2523–7 (2009).

153. Hernandez-Santana, A., Irvine, E., Faulds, K. & Graham, D. Rapid prototyping of poly(dimethoxysiloxane) dot arrays by dip-pen nanolithography. *Chem. Sci.* **2,** 211 (2011).

154. Malotky, D. L. & Chaudhury, M. K. Investigation of Capillary Forces Using Atomic Force Microscopy. *Langmuir* **17,** 7823–7829 (2001).

155. Nakashima, H., Higgins, M. J., O'Connell, C., Torimitsu, K. & Wallace, G. G. Liquid deposition patterning of conducting polymer ink onto hard and soft flexible substrates via dip-pen nanolithography. *Langmuir* **28,** 804–11 (2012).

156. Sanedrin, R. G., Huang, L., Jang, J.-W., Kakkassery, J. & Mirkin, C. A. Polyethylene Glycol as a Novel Resist and Sacrificial Material for Generating Positive and Negative Nanostructures**. 920–924 (2008). doi:10.1002/smll.200701089

157. Jang, J., Zheng, Z., Lee, O., Shim, W. & Zheng, G. Array of nanoscale lenses for subwavelength optical lithography.

158. Stiles, P. L. Direct deposition of micro- and nanoscale hydrogels using Dip Pen Nanolithography (DPN). *Nat. Publ. Gr.* **7,** i–ii (2010).

159. Bhushan, B., Israelachvili, J. N. & Landman, U. Nanotribology: friction, wear and lubrication at the atomic scale. *Nature* **374,** 607–616 (1995).

160. Gao, C. & Bhushan, B. Tribological performance of magnetic thin-film glass disks: its relation to surface roughness and lubricant structure and its thickness. *Wear* **190,** 60–75 (1995).

161. Chilamakuri, S. K. & Bhushan, B. A comprehensive kinetic meniscus model for prediction of long-term static friction. *J. Appl. Phys.* **86,** 4649 (1999).

162. Brakke, K. a. The Surface Evolver and the Stability of Liquid Surfaces. *Philos. Trans. R. Soc. A Math. Phys. Eng. Sci.* **354,** 2143–2157 (1996).

163. Felts, J. R., Somnath, S., Ewoldt, R. H. & King, W. P. Nanometer-scale flow of molten polyethylene from a heated atomic force microscope tip. *Nanotechnology* **23,** 215301 (2012).

164. Banerjee, D. & Cos, D. Investigation of Volume of Fluids (VOF) Method and System Models for Design of Microfluidic Ink Delivery Apparatus for Dip Pen Nanolithography (DPN). **1,** 680–683 (2005).

165. Rosner, B. *et al.* Functional extensions of Dip Pen Nanolithography TM : active probes and microfluidic ink delivery. *Smart Mater. Struct.* **15,** S124–S130 (2006).

166. Yang, S. H., Nosonovsky, M., Zhang, H. & Chung, K.-H. Nanoscale water capillary bridges under deeply negative pressure. *Chem. Phys. Lett.* **451,** 88–92 (2008).

167. Gould, P. Lithography: rewriting the rules. *Mater. Today* **6,** 34–39 (2003).

Chapter 3: Vapor phase polymerization of EDOT from submicron scale oxidant*

**Part of this chapter, including all figures, is reprinted with permission from* O'Connell, C. D., Higgins, M. J., Nakashima, H., Moulton, S. E. & Wallace, G. G. Vapor phase polymerization of EDOT from submicrometer scale oxidant patterned by dip-pen nanolithography. *Langmuir : the ACS journal of surfaces and colloids* 28, 9953–60, copyright (2012) American Chemical Society.

3.1 Introduction

At the core of several emerging fields, including flexible electronics[1] and organic bioelectronics,[2] is the rapid development of organic conductors. Organic conducting polymers (CPs) possess a combination of physical and chemical properties which make them unique electronic conductors, including their soft structure, flexibility, transparency and tunable functionality.[3] The manufacture of complex devices requires the manipulation of electromaterials into predesigned architectures. Recent advances, such as particles-replication in solvent-resistant templating,[4] and advanced ink-jet methods exploiting wetting/dewetting strategies,[5,6] have demonstrated the patterning of conducting polymers at resolution approaching the nanoscale. These innovations highlight the burgeoning potential for cost-effective organic electronic devices.

One of the most intensely studied CPs is currently poly(3,4-ethylenedioxythiophene) (PEDOT) due to its stability over a large pH range, high conductivity and interesting optoelectronic properties.[7,8] Much of the most exciting recent progress in PEDOT synthesis has centred around the in-situ vapor phase polymerization approach.[9–17] VPP is a relatively rapid and simple method for producing homogenous CP layers and the highest conductivities for PEDOT generated via the VPP method (currently >3000 S/cm)[16] are generally higher than those reported for other forms of PEDOT, such as PEDOT:polystyrene sulfonate (PEDOT:PSS), even after solvent annealing.[18] Most of the PEDOT VPP studies to date have been thin-film studies where an oxidant solution is first spin-coated onto a substrate before being introduced to the VPP chamber. If the attractive properties of PEDOT formed by VPP are to be fully exploited, however, technologies for the high-resolution patterning of the polymer must be developed.

One patterning strategy is the *in situ* VPP of PEDOT in pre-designated patterns of oxidant solution. In particular, *in situ* VPP approaches have been demonstrated using ink-jet printing.[19,20] However, the *in situ* synthesis of CPs by VPP at nanoscales has not been demonstrated. Challenges in scaling down the deposition of liquids to sub-micron and nanoscales still remain as many liquid dispensing techniques (e.g. extrusion printing, inkjet printing, micro-contact printing and micro-plotting) operate within the limit of micron resolution. One avenue to address this challenge has been the use of Atomic Force Microscope (AFM)-based probe designs with integrated reservoirs and channels to dispense subpicolitre volumes of liquid.[21,22]

The capability of dip pen nanolithography (DPN) to print nanoscale patterns of chemical reagents is enabling novel strategies in synthesis via confined chemical reactions at the nanoscale.[23] The range of feature size resolution of DPN (from tens of nanometres up to several microns), ability to simultaneously pattern multiple inks,[24] upscalability[25] and versatility in non-destructive lithography on substrates including semiconductors,

plastics, biomaterials and even biological tissue,[26] mean DPN is a promising tool for the nanostructuring of future nanoelectronic devices.

DPN of conducting polymers has been achieved by several methods including; electrostatically driven transport,[27] electrochemical DPN,[28] in situ polymerization[29] and direct writing of soluble CP.[30] The approaches are outlined in Table 3-1. Although nanoscale resolution was achieved in several cases, none of the approaches exploit the high quality CP generated by VPP.

Poly-mer	*Sub*	*Method*	*Res (nm)*		*σ (S/cm)*	*Adhes -ion*	*Ref*	*Year*
			Dot	*Line*				
Ppy, SPAN	Si, Au	Electrostatic driven transport	130	290	-	e-static	27	2002
PEDOT	SiO_2	Electrochemical DPN	-	50	(echem)	Not discussed	28	2002
Ppy	SiO_2	In situ polymerization of monomer ink	500	200	-	Not discussed, vdW	29	2004
PEDOT :PSS	Si/SiOx, SiO2, PDMS, PET	Meniscus transport of soluble CP	-	300	(NO gas sensor)	e-static	30	2009
PEDOT :PSS		Liquid ink deposition	800	-	Con-firmed	Physio-adsorption	31	2012

Table 3-1: Selected DPN conducting polymer printing studies.

In the interest of developing a complementary high-resolution printing method which may take advantage of the attractive properties of conducting polymer synthesized by VPP, we report on the development of an oxidant ink which is optimized for deposition and patterning via DPN. In addition to the ability to pattern the oxidant on sub-micron lengthscales, the use of DPN to deposit attolitre volumes of the oxidant ink enables us to explore the feasibility of the VPP of conducting polymer (PEDOT) at significantly reduced dimensions.

3.2 Experimental

3.2.1 Materials

The amphiphilic block-copolymer Poly(ethylene glycol)-ran-poly(propylene glycol) MW 12,000 (hereafter PEG-PPG), and 3,4-ethylenedioxythiophene (EDOT) monomer (97%) were obtained from Sigma-Aldrich. Baytron C-B 40 (40 wt% iron(III) para-toluenesulfonate in butanol) was obtained from H.C. Stark. All reagents were used without further purification.

Substrate preparation: Silicon oxide and gold substrates were cleaned by water bath sonication for 10 min each in methanol, acetone, and Milli-Q water. Substrates were cleaned by O2 plasma (Harrick) for 10 minutes at 1000 mTorr immediately prior to patterning. Gold substrates were fabricated by depositing gold/chromium (30 nm/10 nm) on glass or silicon wafer using a laboratory-built metal evaporator.

3.2.2 Patterning methodology

DPN patterning was performed using an Nscriptor system (NanoInk, Skokie, IL) in an environment controlled at 60% relative humidity and 25°C temperature. The oxidant ink (formulation discussed in results section) was wetted onto a single tip (hereafter 'DPN-tip') of NanoInk M-Type probes (NanoInk part # PEN-0300-03, material Si3N4, length 107 μm, width 22 μm, spring constant 0.6N/m) by dipping for five seconds into the microwell of a NanoInk Universal Inkwell (part # IWL-0009-03). The tip was bled of excess ink in a method similar to that previously reported for DPN of liquid inks[21,22] by bringing it in contact with the substrate in several (typically 4-5) locations, until deposition of large ~10 μm 'bleed-spots' ceased. One further test array (25 dots of 5s dwell time) was deposited in order to ensure the system entered a regime of reproducible submicron-scale patterning. Consistent patterning continued for at least 30 minutes

before ink properties began to be modified due to evaporation of the solvent. All patterns were generated using the InkCAD software (v 2.7.1) provided with the Nscriptor system. Patterned substrates were withdrawn from the DPN system, without delay, for immediate VPP.

3.2.3 Vapor Phase Polymerization

The vapor phase chamber consisted of a large desiccator jar connected to a vacuum pump and placed on a hotplate set at 70 °C.[12] The chamber was saturated in 3,4 ethylenedioxythiophene (EDOT) monomer and held at a humidity of 30% +/- 5%. The oxidant-patterned samples were placed on a shelf in the middle the chamber, where the temperature was 30-32 °C, and the vacuum switched on. VPP was allowed to proceed under vacuum for 20 min. The sample was placed in an oven or on a hotplate at 70 °C for 20 min to anneal the PEDOT patterns (this helps prevent stress fracture or delamination during washing step). The washing step involved a careful 10 min soak in ethanol or deionised water.

3.2.4 Instrumentation

AFM topographic imaging was acquired with Nscriptor AFM system (Pacific Nanotechnology) or Asylum Research MFP-3D AFM system in tapping mode in air at room temperature. Conductive AFM (C-AFM) measurements were performed with the ORCA module of the Asylum system equipped with PtIr5 coated conductive probes (Nanoworld, EFM, spring constant: 2.8 N/m) in contact mode in air at room temperature. Electrical characterization of PEDOT DPN printed microwires was performed using a bipotentiostat (CH1900B, CH Instruments). Raman spectra were obtained on a Jobin Yvon Horiba HR800 Raman spectrometer with LabSpec software using a wavelength of 632.8 nm and a 300 mm-1 grating.

3.3 Results and Discussion

3.3.1 Ink Formulation and Patterning

We first discuss the formulation of the oxidant ink for DPN writing and the subsequent calibration of feature size using dwell-time and write-speed parameters demonstrating attolitre control of deposited volumes. Oxidant formulations incorporating iron(III) para-toluenesulfonate (Fe(III) tosylate) and poly(ethylene glycol)-ran-poly(propylene glycol) (PEG-PPG) in butanol have been shown to yield PEDOT thin-films exhibiting very high conductivity.[10-12,32] The polymerization route has been previously described.[10] Fe(III) tosylate rapidly absorbs water from the atmosphere to form crystals and this crystallization inactivates the oxidant. PEG-PPG is an amphiphilic block-copolymer which acts as a stabilizer of the oxidant, slowing the water absorption process. Incorporation of polyethylene glycol into VPP-PEDOT is also reported to increase film conductivity in a structure inducing mechanism.[33] Ink transport in DPN can be facilitated via incorporation of a high-viscosity, high boiling point liquid in the ink.[34,35] The PEG-PPG stabilized Fe(III) tosylate spin-coating solution was therefore a good candidate for developing a DPN writeable ink with the PEG-PPG exhibiting tri-functionality, namely; Fe(III) tosylate stabilization, conductivity enhancement and ink-thickening.

A previously reported formulation optimized for conductivity of spin-coated thin films[11] (16 wt % Fe(III) tosylate in butanol plus 4 wt % PEG-PPG) was not amenable to efficient patterning by DPN due to water absorption and the formation of oxidant crystals on the DPN-tip. This was found to be the case for all humidities ranging 5-75%. Hence ink formulations containing increased PEG-PPG content (6%, 12% and 20%) were investiaged for DPN patterning.

None of the formulations were printable at high humidities (>70%) due to rapid oxidant crystallization. None of the formulations were printable at

low relative humidities (<40%), possibly due to a reduction in the water meniscus between tip and substrate (which facilitates molecular ink transport in classic DPN)[36] or a modification in ink properties due to absorbed water. The necessity for high a water-meniscus to effect ink transport and yet low humidity to prevent crystallization represents a challenge to the technique. However, environmental conditions were determined (namely 25 C at 60% relative humidity) which allowed printing with each of the formulations of 6, 12, and 20 wt % PEG-PPG for the duration of a typical patterning experiment (~30 min) without the onset of crystallization. A comprehensive table illustrating the range of parameters investigated is included in the appendix (Table 3-4). The 6 wt % PEG-PPG solution was chosen for continued investigation as its patterning was facile, reproducible, and it was the formulation closest to that previously optimized for high conductivity. The 6 wt % PEG-PPG solution is the formulation used henceforth, unless otherwise stated. Contact angle measurements of this ink formulation on the various substrates employed in this study are shown in Table 3-2. Liquid properties of the ink formulation are outlined in Table 3-3.

	Silicon		**glass**		**gold**	
	*	**	*	**	*	**
H_2O	49.1° (3.5°)	<5°	34.2° (3.0°)	<5°	86.0° (2.6°)	24.5 (3.1)
Butanol	12.0° (1.8°)	<5°	16.9 (3.5)	6.4 (2.0)	<5°	<5°
Oxidant ink	15.5° (2.5°)	13.9 ° (2.0°)	15.3° (1.5°)	16.6° (2.0°)	12.9° (1.9°)	11.3 ° (2.2°)

Table 3-2: Contact angles of the ink formulation on relevant substrates obtained by goniometery. Parentheses represent standard deviation. Note: contact angles < 5° indicate complete or almost complete wetting.

*** Substrate prepared by bath sonication in methanol and H2O followed by N2 blow dry.**

**** Substrates prepared as above plus additional treatment with O2 plasma (5 minutes, 1100 mTorr).**

	Density ($kg\ m^{-3}$)	*Surface tension* ($N\ m^{-1}$)	*Viscosity* ($Pa \cdot s$)
Butanol	0.8057	0.0254 (0.0003)	0.0026
Oxidant Ink	0.87 (0.02)	0.0263 (0.0002)	0.0134 (0.0002)

Table 3-3: Liquid properties of the oxidant ink formulation and its solvent.

Arrays of oxidant dots were generated on silicon oxide by depositing at a range of dwell times (Figure 3-1). Dot diameters of 1.2-5 μm could be deposited utilizing dwell-time control of feature size. At extremely short dwell-times (0.01-0.1s) dot size reached a minimum of 1.2 μm. This minimum size is comparable to that reported by other liquid-ink DPN studies.[34] Above 0.1s, both dot diameter and dot height follow power law relationships with dwell time (Figure 3-1 (C)). The ink calibration curves quoted here refer to silicon oxide substrates only. We have also calibrated the ink according to deposition volume (Figure 3-1 (D)), where volume is calculated from dot radius and dot height values by assuming each dot as a spherical cap. Conventional micro-printing techniques, such as ink-jet printing, measure drop deposition in picolitres (10^{-12} L). Ink droplets deposited by DPN, however, are on the order of a million times less voluminous. We have adopted the attolitre (1 aL = 10^{-18} L = 10^{6} nm^3) as a convenient unit. Drop volume exhibits $t^{1/2}$ dependence, suggesting a dynamics describable in terms of spontaneous capillarity mechanisms under laminar conditions. Modelling of the ink-substrate interactions in a similar system has been performed by others.[21] These dimensions of feature-size control highlight the ability of DPN, not only for high-resolution lithographic patterning, but also for the precise delivery of attolitre volumes of liquid reagent.

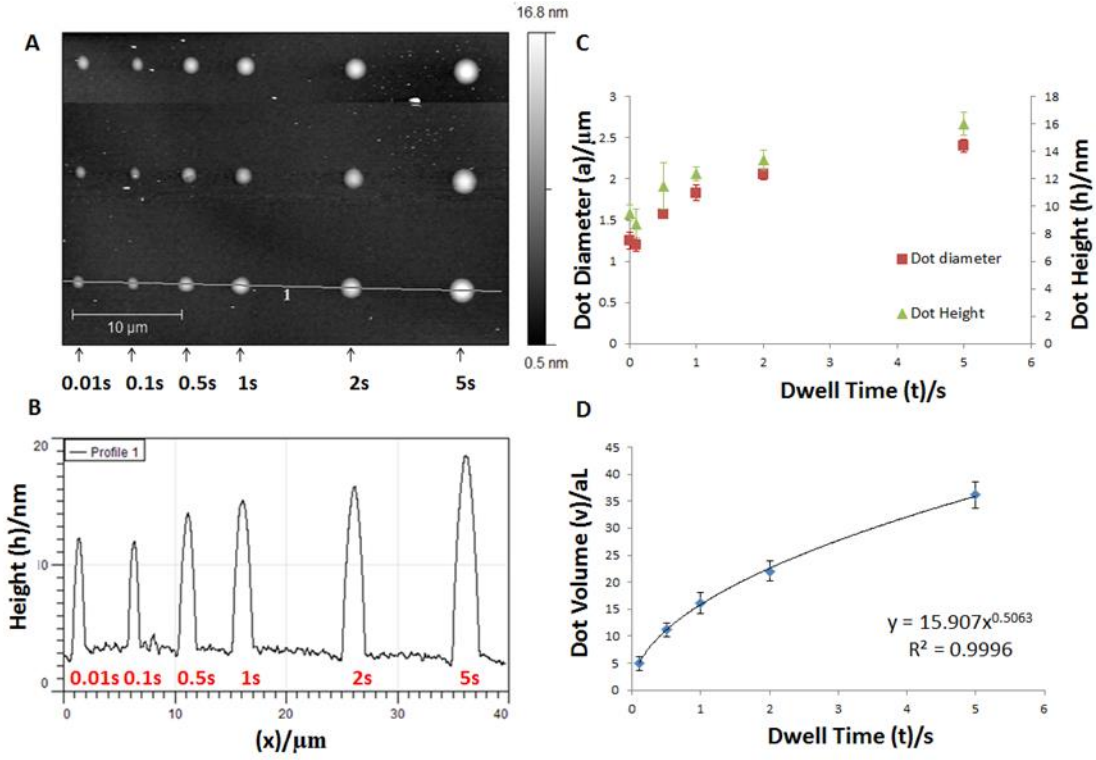

Figure 3-1: A) AFM a/c mode topography image of an array of PEDOT dots deposited on silicon with various dwell times. Vertical columns, from left to right, are 0.01s, 0.1s, 0.5s, 1s, 2s, and 5s respectively; B) Topographical data through horizontal line profile in (A); C) Relationship between dot diameter and dot height with dwell time. Both parameters exhibit power-law dependence with time; D) Dot volume vs. dwell time exhibits $t^{1/2}$ dependence for this dot pattern. Note, the data for 0.01s dwell time has been omitted from this graph as dot size at very short dwell times is time-independent (see discussion).

Line writing was also performed by laterally moving an inked tip while in contact with the substrate (Figure 3-2). At high write-speeds (>50 µm s^{-1}) discontinuous lines are deposited, while at slower write speeds the lines are continuous and control of line width is afforded by the write speed parameter. As can be seen in Figure 3-2 (B), line writing can achieve considerably improved resolution over dot-deposition. Line-widths of 250-300 nm could be routinely achieved, whereas the minimum dot diameter was 1.2 µm. The difference in achievable feature size may be related to the differing deposition mechanisms. Studies which have examined the capillary forces at play during liquid ink nanodispensing suggest that the

dot-deposition event occurs, not when the tip first contacts the surface, but when it retracts (i.e. as the tip retracts, it distends a 'meniscus bridge' of ink between itself and the surface; it the breaking of this meniscus that effects deposition).[21] In line writing, on the other hand, deposition does occur during tip-substrate contact. In this case it is capillary forces that pull ink from the moving tip to the substrate. As such, writing of continuous lines requires extremely fine adjustment of the write-speed to balance the ink substrate adhesion and ink-ink cohesion forces during writing.

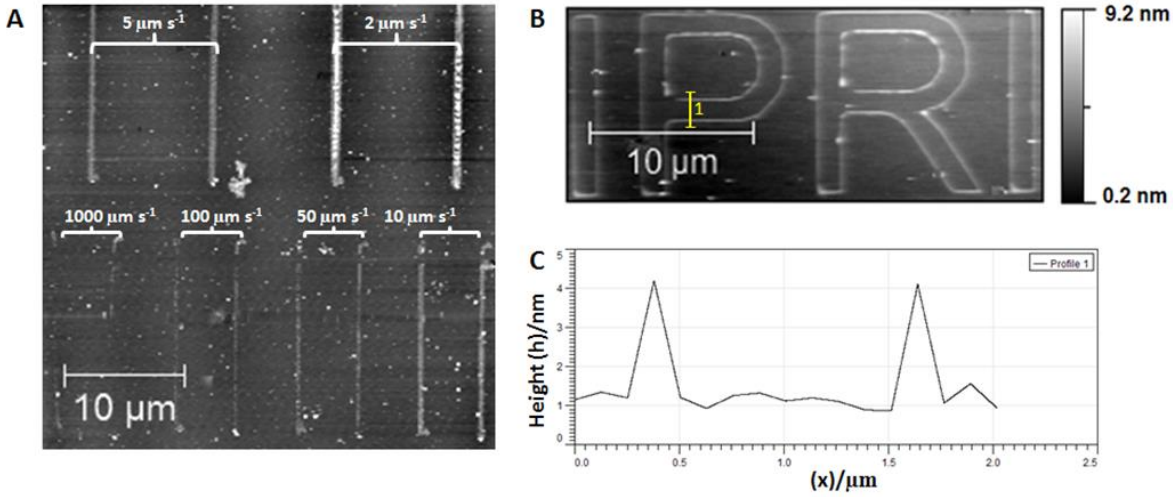

Figure 3-2: A) AFM a/c mode phase image of oxidant lines (15 µm long) patterned on a Si/SiO_2 substrate. The lines drawn at write-speeds of 50 µm s^{-1}, 10 µm s^{-1}, 5 µm s^{-1} and 2 µm s^{-1} correspond to line-widths of 400 nm, 600 nm, 700 nm and 1000 nm respectively; B) AFM a/c mode topographical image of an oxidant pattern (IPRI = Intelligent Polymer Research Institute) on Si/SiO_2 patterned at a line speed of 10 µm s^{-1}. C) Topographical data through vertical line profile in (B). Line heights are 4-5nm and line widths are 250-300 nm.

Although line-writing can achieve higher resolution than dot-deposition, line writing is more problematic in practice. The line-width/write-speed relationship is generally less reproducible than dot-width/dwell-time relationship between experiments. Thus, it is difficult to generate line features of a pre-calculated resolution. For this reason we do not include line-width/write-speed calibration curves as would correspond to Figure 3-1(C). It may be that line-writing is more sensitive to the precise volume

of ink in the cantilever reservoir and that the corresponding variations in Laplace pressure may alter the conditions of deposition via capillary action. Achieving line continuity over >10μm line-length is also difficult. The problem of writing continuous lines of liquid at the sub-micron to nanoscale is a very complex one, involving a delicate balance between the forces of liquid cohesion and substrate adhesion. Nanoscale variations in surface energy, nanometre scale roughness variations as well as surface defects and agglomerations within the ink can all contribute to a line's continuity. Furthermore the writing process is taking place at characteristic liquid thicknesses of a few tens of nanometres or less, well within the regime where dispersive forces tend to dominate and for which contact angles are not well defined.[37] The quality of patterned lines was also found to vary between different substrates. Gold substrates resulted in more continous lines compared to SiO2, possibly due to a slightly greater ink-substrate adhesion as evidenced by macro-scale contact angle studies (see Table 3-2). Despite this variability in line deposition rate, lines could be patterned across interfaces of gold and silicon dioxide (see conductivity section). The prospect of drawing nanometre scale features of liquid ink using a moving pen in contact with the surface is a fascinating opportunity, but further work is needed in this area to fully understand and control the mechanism of deposition by capillary action.

3.3.2 Vapor phase polymerization

The following sections present characterisation of oxidant patterns (now PEDOT) after VPP, discussing morphology, Raman spectroscopy and electrical characteristics. The morphology of oxidant dots at different stages of the VPP process were compared using AFM a/c mode imaging (Figure 3-3). The as patterned oxidant dot, imaged one hour after patterning, exhibits a spherical cap shape with no obvious evidence of Fe(III) tosylate crystallization (Figure 3-3 A-C). This smooth morphology indicates that the incorporation of 6 wt % PEG-PPG is sufficient to stabilize

the oxidant against water absorption when kept at room temperature for one hour. A dot of oxidant ink which has been heated on a hotplate at 65 °C before imaging, however, is completely crystallized (Figure 3-3 D-F). The evaporation of residual butanol from the dot exposes the hygroscopic Fe(III) tosylate which, on cooling, absorbs water from the atmosphere to form large (400-600nm high) crystals.[11] A dot of oxidant ink which has been exposed to EDOT monomer in the VPP chamber (Figure 3-3 G-I) exhibits a nodular morphology and little, if any, crystallization. In this case the oxidant has polymerised the monomer and the tosylate anion has become incorporated in the resulting PEDOT as dopant.

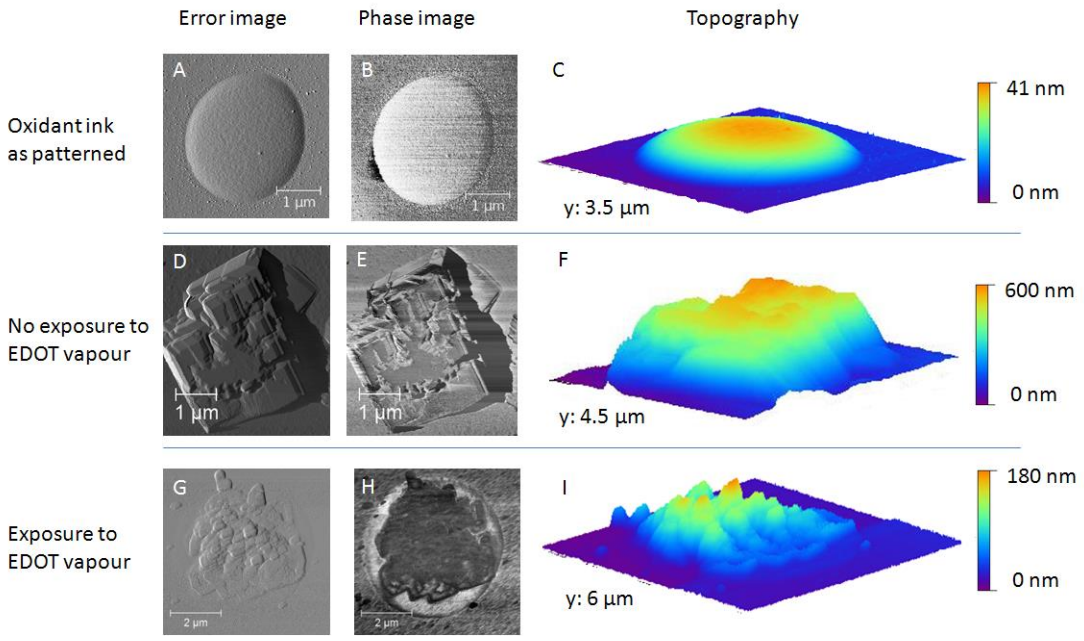

Figure 3-3: Morphological evidence of PEDOT polymerization from three representative dots after differing treatments. A) Error* image, B) phase image and C) topographical image of a single dot of oxidant ink imaged within one hour of patterning. The oxidant molecules are stabilized within a matrix of PEG-PPG and residual butanol yielding the smooth spherical cap shape of the as-printed ink: D) Error image, E) phase image and F) topographical image of a single dot of oxidant ink which has been heated on a hotplate at 65 °C for several minutes without undergoing the VPP step. Heating removes the residual butanol and disrupts the PEG-PPG stabilization effect. The hygroscopic oxidant subsequently absorbs water from the atmosphere to form crystals of several hundred nanometre height: G) Error image, H) phase image and I) topographical image of a single dot of oxidant ink which has been exposed to EDOT

monomer in the vapor phase polymerization chamber prior to heating at 65°C for several minutes. The morphology of the VPP dot is nodular, contrasting with the smooth as-patterned dot (A-C) and the crystallized non-VPP dot (D-F) above. The phase image (H) reveals the outline of as-patterned ink upon which this polymerization is localised. [Note: The AFM error image is generated from the vertical displacement of the laser spot on the AFM photodetector and can be useful for highlighting topographical steps or boundaries. The phase image is generated from the phase lag between the AC input signal (which drives the cantilever) and the photodetector output signal (a function of cantilever resonance). Variations in sample composition and mechanical properties can be highlighted in the phase image.]

The post polymerisation washing step resulted in a decrease of feature volume to about 13% of the original (see Figure 3-4). Dramatic shrinking of VPP-PEDOT thickness post-washing occurs due to the removal of Fe(II) and excess counter ion. Previous groups synthesizing VPP-PEDOT (without using PEG-PPG as stabilizer) have reported a shrinkage to 5% of the original volume, and the washing step has even been used as a method to entrap active molecules into the CP matrix.[38] The assertion that all spent oxidant is washed out is supported by several studies which used XPS evidence to conclude that a simple methanol or ethanol washing steps were sufficient to remove all traces of Fe(II) from similar VPP-PEDOT systems.[14,32,39] The removal of PEG-PPG is also likely, although a recent study has used XPS and other evidence to suggest the incorporation of a PEG-PPG copolymer into the VPP-PEDOT matrix itself.[32] A theoretical value for the volume reduction can be estimated using the assumptions that 2.5 mol iron(III)tosylate is used to oxidise 1 mol EDOT, that 0.3 mol tosylate remains as dopant in the VPP:PEDOT after washing, that the mass ratio of PEG-PPG to iron(III)tosylate is 0.325 (ink formulation 16% wt Fe(III) tosylate + 6% wt PEG-PPG in butanol), that all solvent is removed prior to VPP, and that the density of the reactants is unity.36 If all PEG-PPG is washed out, the volume of VPP-PEDOT remaining should be 10% of the original. The reason we see a shrinkage to 13% of the original, and not 10%, may be the result of incorporation of PEG-PPG into the VPP-PEDOT matrix. If this is the case, about 20% of the final VPP-PEDOT volume is composed of PEG-PPG.

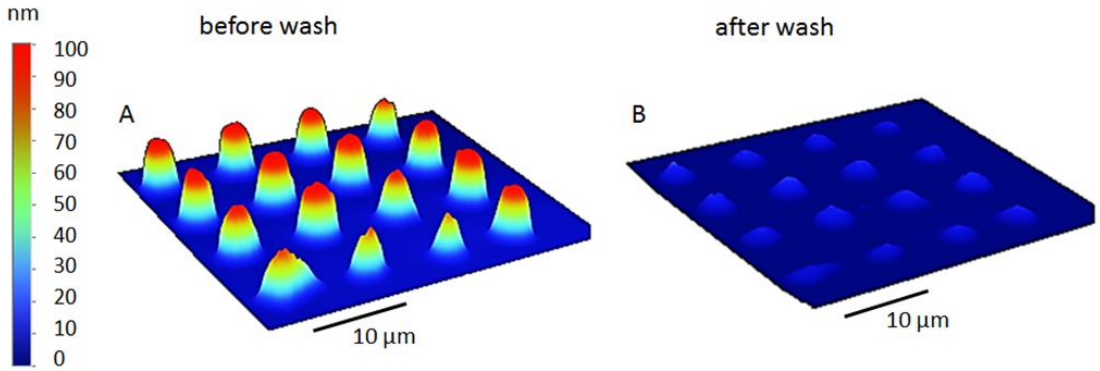

Figure 3-4: 3D image rendered from optical profilometry of an array of VPP-PEDOT features A) before and B) after H2O washing step. The features shrink ~85% from a feature height of ~100nm to ~15 nm.

3.3.3 Raman Spectroscopy

The synthesis of PEDOT during vapor phase polymerization was confirmed by Raman spectroscopy of a single 2 µm dot (Figure 3-5). The Raman spectrum exhibits the characteristic peaks of PEDOT,[40,41] including the C-S-C deflection at 706 cm-1, the oxyethylene ring deformation at 985 cm-1, the Cα-Cα' (inter ring) stretch at 1254, the Cβ-Cβ stretch at 1366 cm-1, the symmetric Cα=Cβ(-O) stretch at 1424 cm 1 and the asymmetric Cα=Cβ stretch at 1531 cm-1. The position of the symmetric Cα=Cβ(-O) stretch at 1424 cm-1 is indicative of an oxidised PEDOT structure,[41] confirming that the VPP process can initiate PEDOT formation at such small volumes. Calculating from the AFM morphology and known values for the density of vapor phase polymerised PEDOT:tosylate (2.01 g/cm3), this single dot contains at most 2.5 pg (1pg = 10 12 g) of PEDOT. To our knowledge this represents the in-situ vapor phase synthesis of a conducting polymer on the smallest (picogram) scale to date.

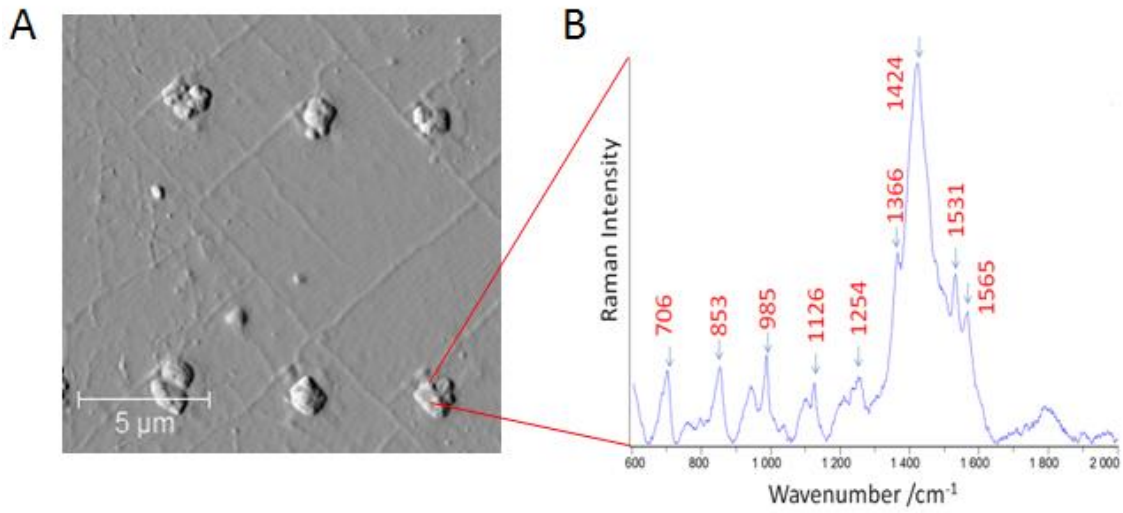

Figure 3-5: A) AFM A/C mode error signal image of 6 DPN deposited PEDOT dots after VPP; B) Typical Raman spectrograph obtained from the PEDOT dot at the bottom left of (A). Characteristic peaks for PEDOT include the C-S-C deflection at 706 cm^{-1}, the oxyethylene ring deformation at 985 cm^{-1}, the C_{α}-$C_{\alpha'}$ (inter ring) stretch at 1254, the C_{β}-C_{β} stretch at 1366 cm^{-1}, the symmetric C_{α}=C_{β}(-O) stretch at 1424 cm^{-1} and the asymmetric C_{α}=C_{β} stretch at 1531 cm^{-1}.

3.3.4 Electrical conductivity

Assessing the conductivity of conducting polymer patterns at submicrometer scales represents a significant technical challenge. Conductive-atomic force microscopy (C-AFM, also known as current-sensing AFM) was used to qualitatively confirm the conductivity of printed PEDOT wires. C-AFM involves placing an electrical bias on the sample and measuring local conductivity via the current passing through a conductive AFM tip.[42] As direct electrical contact between the sample and tip must be maintained, contact mode imaging is used while simultaneously recording topography and current channels. Figure 3-6 shows (A) an AFM phase image and (B) show a C-AFM image of a PEDOT microwire patterned across a gold-glass substrate interface. A current signal is clearly measured from the gold substrate and from along the PEDOT wire. Measurement of current indicates conductive areas of the scanned surface and confirms the

electrical conductivity of the PEDOT microwire. No current is measured from the glass (insulating) substrate.

Higher loading forces can be used to decrease contact resistance and increase stability but in our case a high force had the effect of smearing the PEDOT patterns. The high contact resistance, coupled with the necessity to apply very low loading forces (0.05 nN) necessitated a high surface bias (9V), although a current signal was measured from PEDOT at voltages as low as 3V. The large contact resistance between tip and sample made quantitative measurements prohibitively difficult for this system.

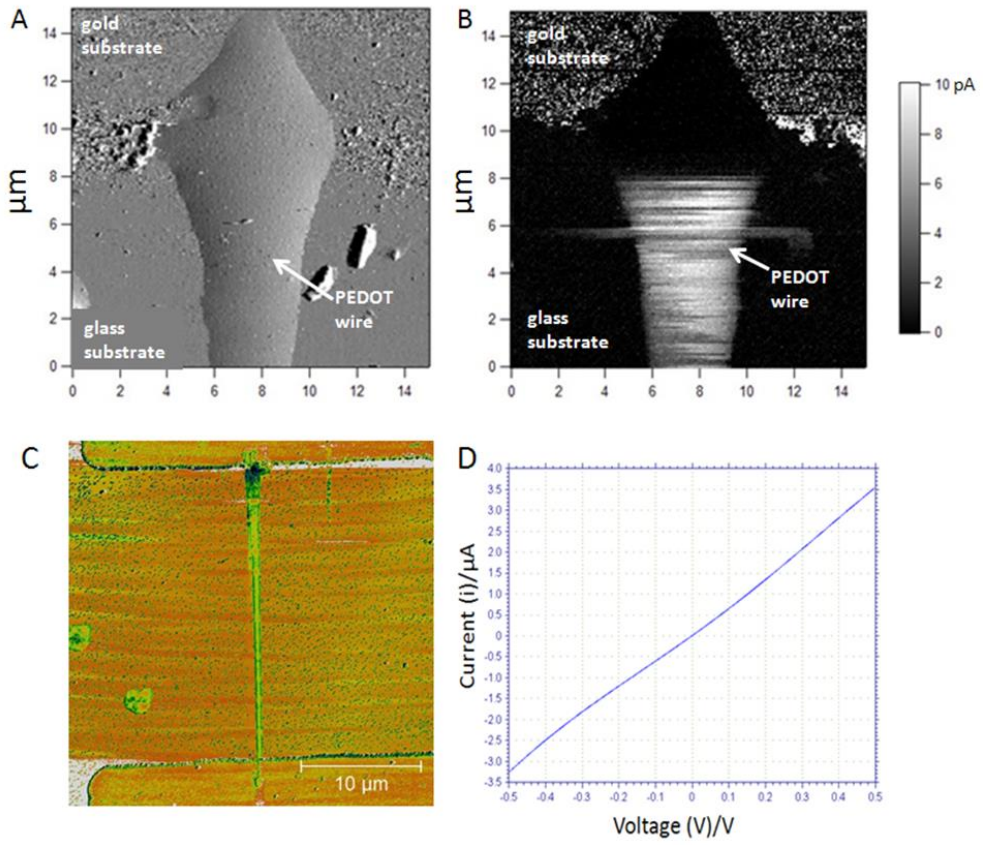

Figure 3-6: A) Contact mode deflection image of a line of vapour phase polymerised PEDOT. The patterned line crosses the interface of glass and a 24 nm layer of evaporated gold. B) Current image at 9V substrate bias. Light colouring indicates current flow (conducting material), dark colouring indicates no current flow (insulating material). Local current is recorded from the gold substrate but not the glass

substrate. Current is measured travelling along the PEDOT wire and across the glass insulator. Note: the inability to measure current in the PEDOT on gold portion is an artefact due to saturation of the current signal by gold on the same (horizontal) scan-line. C) PEDOT microwire connecting two planar gold electrodes as used for electrical measurements; D) Current-voltage characteristic of a PEDOT microwire (10 µm width) deposited across a 45 µm insulating gap between planar gold electrodes. The microwire has a resistance of 167 kΩ and a conductivity of 0.7 S cm^{-1}.

Quantitative electrical conductivity measurements were performed by measuring the current-voltage characteristics of PEDOT microwires bridging an insulating gap (25 or 45µm) between planar electrodes (Figure 3-6 (C) and (D)). Larger microwires (~10 µm width) were used for ease of measurement. Measurements were undertaken on unwashed samples as the washing step had the effect of breaking microwire connectivity. Conductivity of these microwires was calculated to be 1 +/ 0.5 S cm^{-1}. This value, while being comparable to that of commercially available PEDOT:poly(styrene sulphate) dispersions previously patterned by DPN,[30] is still far below the highest reported conductivity values of PEDOT thin films synthesized by VPP. The measured conductivity of a conducting polymer sample can vary significantly depending on the particular system geometry, and depending upon subtleties of the measurement performed.[43] Therefore the direct comparison of PEDOT microwire conductivity with that of the equivalent spin-coated thin film probably has limited meaning. Nevertheless we suggest three possible reasons for the discrepancy between our VPP-PEDOT microwire properties and that of the literature record spin-coated VPP-PEDOT: 1) The strongest effect is most likely the large volume percentage of spent oxidant which must persist in the unwashed microwires. The disruptive effect of the washing step on microwire connectivity highlights the increased difficulty of achieving adequate adhesion at reduced scales (thin films submitted to the same treatment exhibit no observable delamination). We are currently investigating methods, such as the utilization of adhesion promoting substrate treatements, which may effect covalent attachment of the VPP-PEDOT to the substrate. 2) The contact resistance of the microwire-Au

contacts is likely very high, due to the tiny area of contact (~5 μm2) and the weak, physioadsorbed nature of the connection. This extra resistance is included twice-over in the measured resistance value and its subtraction would result in a more realistic, and certainly higher, conductivity value for the PEDOT microwire. 3) Vapor phase chamber conditions. The optimisation of the vapor phase parameters were outside the scope of this study and hence humidity, temperature and pressure were not precisely controlled. In our laboratory, the PEDOT thin-films generated from spin-coated films of our ink formulation had conductivities of ~100 S cm-1, already an order of magnitude lower than some literature values. No doubt significant improvements in microwire conductivities would follow a more directed optimisation of vapor phase conditions.

3.4 Conclusions

To our knowledge this is the first demonstration of patterning conducting polymer by DPN via VPP. Furthermore, the use of DPN allowed us to demonstrate that the in-situ polymerization of a conducting polymer by the vapor phase could proceed within attolitre volumes of an oxidant ink. As proof of concept, we have confirmed the polymerization of picogram scale individual PEDOT features by Raman spectroscopy and confirmed the conductivity of patterned PEDOT microwires. Although this concept aims to take advantage of the VPP process, we have shown that further optimization (e.g. ink properties, conductivity) at the nanoscale are required. The downscaling of the VPP process towards a micron to sub-micron scale presents new challenges not encountered in thin film studies, in particular; 1) the relatively increased rate of water induced crystallization due to the greater surface area to volume ratio; 2) the change of ink properties over time due to solvent evaporation from the cantilever and 3) the challenge of effecting strong adhesion between the VPP-PEDOT pattern and the substrate. We have found that challenge 1 could be overcome by increasing the PEG-PPG content of the ink. The

utilization of a solvent carrier system with lower vapour pressure may alleviate the curtailing of patterning time due to change in ink properties with time. In addition, functionalization of the surface with adhesion promoters such as γ-glycidoxypropyltrimethoxysilane may improve the stability of microwires during the washing step. With a greater fundamental understanding of the ink deposition, VPP process (e.g. diffusion and nucleation kinetics of monomer) and suitable means for quantifying the conductive properties of nanoelectromaterials, the controlled deposition of attolitre volumes of liquid reagent has potential to introduce a unique strategy for in-situ synthesis in predefined architectures.

3.5 References

1. Forrest, S. R. The path to ubiquitous and low-cost organic electronic appliances on plastic. *Nature* **428**, 911–8 (2004).

2. Pron, A., Gawrys, P., Zagorska, M., Djurado, D. & Demadrille, R. Electroactive materials for organic electronics: preparation strategies, structural aspects and characterization techniques. *Chemical Society reviews* **39**, 2577–632 (2010).

3. Wallace, G. G., Spinks, G. M., Kane-maguire, L. A. P. & Teasdale, P. R. *Conductive Electroactive Polymers: intelligent polymer systems*. (CRC Press: 2008).

4. Mele, E. *et al*. Sub-50-nm conjugated polymer dots by nanoprinting. *Small (Weinheim an der Bergstrasse, Germany)* **4**, 1894–9 (2008).

5. Sirringhaus, H. High-Resolution Inkjet Printing of All-Polymer Transistor Circuits. *Science* **290**, 2123–2126 (2000).

6. Wang, J. Z., Zheng, Z. H., Li, H. W., Huck, W. T. S. & Sirringhaus, H. Dewetting of conducting polymer inkjet droplets on patterned surfaces. *Nature materials* **3**, 171–6 (2004).

7. Elschner, A., Kirchmeyer, S., Lövenich, W., Merker, U. & Reuter, K. *PEDOT: Principles and Apllications of an Intrisically Conductive Polymer*. *Advanced Materials* 353 (CRC Press: 2002).doi:10.1002/1521-4095(20020503)

8. Kirchmeyer, S. & Reuter, K. Scientific importance, properties and growing applications of poly(3,4-ethylenedioxythiophene). *Journal of Materials Chemistry* **15**, 2077 (2005).

9. Winther-Jensen, B., Winther-Jensen, O., Forsyth, M. & Macfarlane, D. R. High rates of oxygen reduction over a vapor phase-polymerized PEDOT electrode. *Science (New York, N.Y.)* **321**, 671–4 (2008).

10. Fabretto, M., Zuber, K., Hall, C. & Murphy, P. High Conductivity PEDOT Using Humidity Facilitated Vacuum Vapour Phase Polymerisation. *Macromol. Rap. Comm.* 1403–1409 (2008).doi:10.1002/marc.200800270

11. Zuber, K., Fabretto, M., Hall, C. & Murphy, P. Improved PEDOT Conductivity via Suppression of Crystallite Formation in Fe(III) Tosylate During Vapor Phase Polymerization. *Macromolecular Rapid Communications* **26**, 1503–1508 (2008).

12. Fabretto, M., Müller, M., Zuber, K. & Murphy, P. Influence of PEG-ran-PPG Surfactant on Vapour Phase Polymerised PEDOT Thin Films. *Macromolecular rapid communications* **30**, 1846–51 (2009).

13. Fabretto, M. *et al.* In-situ QCM-D analysis reveals four distinct stages during vapour phase polymerisation of PEDOT thin films. *Polymer* **51**, 1737–1743 (2010).

14. Fabretto, M., Autere, J., Hoglinger, D., Field, S. & Murphy, P. Vacuum vapour phase polymerised poly(3,4-ethyelendioxythiophene) thin films for use in large-scale electrochromic devices. *Thin Solid Films* **519**, 2544–2549 (2011).

15. Mueller, M. *et al.* Vacuum vapour phase polymerization of high conductivity PEDOT: Role of PEG-PPG-PEG, the origin of water, and choice of oxidant. *Polymer* **53**, 2146–2151 (2012).

16. Fabretto, M. V. *et al.* Polymeric Material with Metal-Like Conductivity for Next Generation Organic Electronic Devices. *Chemistry of Materials* **24**, 3998–4003 (2012).

17. Brooke, R. *et al.* Inkjet printing and vapor phase polymerization: patterned conductive PEDOT for electronic applications. *Journal of Materials Chemistry C* 18–20 (2013).doi:10.1039/c3tc30356j

18. Kim, Y. H. *et al.* Highly Conductive PEDOT:PSS Electrode with Optimized Solvent and Thermal Post-Treatment for ITO-Free Organic Solar Cells. *Advanced Functional Materials* **21**, 1076–1081 (2011).

19. Winther-jensen, B. *et al*. Application of Polypyrrole to Flexible Substrates. *Journal of Applied Polymer Science* **104**, 3938–3947 (2007).

20. Choi, J. S., Cho, K. Y. & Yim, J. Micro-patterning of vapor-phase polymerized poly(3,4-ethylenedioxythiophene) (PEDOT) using ink-jet printing/soft lithography. *European Polymer Journal* **46**, 389–396 (2010).

21. Fang, A., Dujardin, E. & Ondarçuhu, T. Control of droplet size in liquid nanodispensing. *Nano letters* **6**, 2368–74 (2006).

22. Hwang, K., Shin, C., Mingwu, R., Lee, S.-H. & Kim, H. Design of a nanoprinter based on AFPN (Active Fountain Pen Nanolithography) using switch control. *Journal of Mechanical Science and Technology* **25**, 977–985 (2011).

23. Liu, X., Guo, S. & Mirkin, C. a Surface and site-specific ring-opening metathesis polymerization initiated by dip-pen nanolithography. *Angewandte Chemie (International ed. in English)* **42**, 4785–9 (2003).

24. Hong, S. Multiple Ink Nanolithography: Toward a Multiple-Pen NanoPlotter. *Science* **286**, 523–525 (1999).

25. Huo, F. *et al*. Polymer pen lithography. *Science (New York, N.Y.)* **321**, 1658–60 (2008).

26. Sistiabudi, R. & Ivanisevic, A. Dip-Pen Nanolithography of Bioactive Peptides on Collagen-Terminated Retinal Membrane. *Advanced Materials* **20**, 3678–3681 (2008).

27. Lim, J.-H. & Mirkin, C. A. Electrostatically Driven Dip-Pen Nanolithography of Conducting Polymers. *Advanced Materials* **14**, 1474–1477 (2002).

28. Maynor, B. W., Filocamo, S. F., Grinstaff, M. W. & Liu, J. Direct-Writing of Polymer Nanostructures: Poly(thiophene) Nanowires on Semiconducting and Insulating Surfaces. *Journal of the American Chemical Society* **124**, 522–523 (2002).

29. Su, M., Aslam, M., Fu, L., Wu, N. & Dravid, V. P. Dip-pen nanopatterning of photosensitive conducting polymer using a monomer ink. *Applied Physics Letters* **84**, 4200 (2004).

30. Lu, H.-H. *et al*. Electrical properties of single and multiple poly(3,4-ethylenedioxythiophene) nanowires for sensing nitric oxide gas. *Analytica chimica acta* **640**, 68–74 (2009).

31. Nakashima, H., Higgins, M. J., O'Connell, C., Torimitsu, K. & Wallace, G. G. Liquid deposition patterning of conducting polymer ink onto hard and soft flexible substrates via dip-pen nanolithography. *Langmuir : the ACS journal of surfaces and colloids* **28**, 804–11 (2012).

32. Fabretto, M. *et al*. High conductivity PEDOT resulting from glycol/oxidant complex and glycol/polymer intercalation during vacuum vapour phase polymerisation. *Polymer* **52**, 1725–1730 (2011).

33. Winther-Jensen, B., Knecht, T., Ong, C., Vongsvivut, J. & Clark, N. Inhomogeneity Effects in Vapor Phase Polymerized PEDOT: A Tool to Influence Conductivity. *Macromolecular Materials and Engineering* **296**, 185–189 (2011).

34. Wang, H. *et al*. Toward conductive traces : Dip Pen Nanolithography ® of silver nanoparticle-based inks. *Applied Physics Letters* 143105 (2008).doi:10.1063/1.2995859

35. Hung, S. *et al*. Dip Pen Nanolithography of Conductive Silver Traces. *The Journal of Physical Chemistry C* 9672–9677 (2010).

36. Su, M., Pan, Z., Dravid, V. P. & Thundat, T. Locally enhanced relative humidity for scanning probe nanolithography. *Langmuir : the ACS journal of surfaces and colloids* **21**, 10902–6 (2005).

37. Ma, J., Jing, G., Chen, S. & Yu, D. Contact Angle of Glycerol Nanodroplets Under van der Waals Force. *The Journal of Physical Chemistry C* **113**, 16169–16173 (2009).

38. Winther-Jensen, B., Chen, J., West, K. & Wallace, G. "Stuffed" conducting polymers. *Polymer* **46**, 4664–4669 (2005).

39. Ali, M. A., Kim, H., Lee, C., Nam, H. & Lee, J. Effects of iron(III) p-toluenesulfonate hexahydrate oxidant on the growth of conductive poly(3,4-ethylenedioxythiophene) (PEDOT) nanofilms by vapor phase polymerization. *Synthetic Metals* **161**, 1347–1352 (2011).

40. Chiu, W. W., Travaš-Sejdić, J., Cooney, R. P. & Bowmaker, G. A. Spectroscopic and conductivity studies of doping in chemically synthesized poly(3,4-ethylenedioxythiophene). *Synthetic Metals* **155**, 80–88 (2005).

41. Cooney, R. P., Bowmaker, G. A., Chiu, W. W. & Trava, J. Studies of dopant effects in poly (3 , 4-ethylenedi- oxythiophene) using Raman spectroscopy ˇ. *J. Raman Spectrosc*. 1354–1361 (2006).doi:10.1002/jrs.1545

42. O'Neil, K. D., Shaw, B. & Semenikhin, O. a On the origin of mesoscopic inhomogeneity of conducting polymers. *The journal of physical chemistry. B* **111**, 9253–69 (2007).

43. Fabretto, M., Zuber, K., Jariego-Moncunill, C. & Murphy, P. Measurement Protocols for Reporting PEDOT Thin Film Conductivity and Optical Transmission: A Critical Survey. *Macromolecular Chemistry and Physics* n/a–n/a (2011).doi:10.1002/macp.201100303

3.6 Appendix

PEG-content wt %	*% Relative humidity*	*Substrate Temp (℃)*	*Substrate*	*Deposition?*	*Comments*
4	30	25	SiOx	No	Rapid crystallization of ink on tip. Ink transfer ceases in <10 min.
	40	25	SiOx	No	
	50	25	SiOx	Some	
	60	25	SiOx	Some	
	70	25	SiOx	Some	
6	30	25	SiOx	No	Ink sticks to tip, no deposition.
	40	25	SiOx	No	Ink sticks to tip, no deposition.
	50	25	SiOx	Some	Some deposition, but uncontrolled.
	60	**25**	**SiOx**	**Yes**	**Reliable dot deposition. Calibration.**
			Gold	Yes	Reliable dot deposition
			Gold mylar	Yes	Reliable dot deposition
			PDMS	Yes	Reliable dot deposition
			SiO_2	Yes	Reliable dot deposition
		40	SiOx	No	Ink sticks to tip, no deposition.
		50	SiOx	No	Ink sticks to tip, no deposition.
	70	25	SiOx	Yes	Some dot deposition, but short term. Crystallization onset <30 min
12	60	25	SiOx	Yes	Reliable dot deposition, limited control of dot-size
20	60	25	SiOx	Yes	Reliable dot deposition, limited control of dot-size

Table 3-4: A selection of patterning parameters investigated. The highlighted parameters were chosen as the focus of this study.

Chapter 4: Nanoscale platinum printing on insulating substrates

4.1 Introduction

The emerging field of nanobionics is borne from advances in our ability to control the structure of materials on finer and finer lengthscales, coupled with an increased appreciation of the sensitivity of living cells to nanoscale topographical, chemical and mechanical cues.[1-4] Ultimately, bionic devices may be designed which will integrate seamlessly with the body, sending and receiving chemical, mechanical and electrical signals to initiate and direct regrowth of damaged nerves,[5,6] to restore sensory perception (e.g. hearing, sight) to a natural level,[7,8] to control epileptic seizures[9] or for two-way communication of prosthetic limbs with sensory and motor neurons.[10,11] Devices have already been fabricated to interface neurons on the single-axon level.[12] As we envisage and prototype nanostructured bionic devices there is a crucial need to understand how cells feel and respond to nanoscale materials, particularly as material properties (surface energy, conductivity etc.) can be very different at the nanoscale than at bulk.[13]

Understanding cellular-nanomaterial interactions are especially important at the electrode, the functional interface of a bionic device.[8]

Platinum is the conventional material of choice for bionic electrodes due to its wide electrochemical window, high stability and inertia.[14] A range of techniques are commonly used to pattern noble metals at nanoscale resolution on rigid substrates, including electron beam lithography (EBL), photolithography, contact printing, and nanoimprint lithography (NIL).[15] Bionic devices, however, are ideally composed of material with mechanical properties which match living tissue.[16–18] Traditional techniques used to fabricate platinum electrodes may not be applicable for processing on soft and/or flexible polymeric materials. For example, these substrates are non-conducting, so electroless deposition methods must be used.[19] The polymer substrate may also be sensitive to temperature, precluding deposition via vacuum evaporation, and meaning that any curing of the metal must be performed under mild conditions.

An alternative strategy is to print the metal in the desired pattern in the form of a processable (i.e. liquid at room temperature), precursor 'ink', and to subsequently convert the ink to solid metal *in situ*. Ink deposition has the advantage of being versatile among over virtually any substrate. Liquid inks composed of metal micro- or nanoparticles have been commercially available for decades. They may contain a metal loading of 50% or more. The metal of choice is often silver due to its ease of reduction and low annealing temperatures. Commercially available metal inks may contain a cocktail of volatile organic solvents, reducing agents, nanoparticles, metal precursors, stabilisers, surfactants, thickeners, adhesives and other molecules designed to tailor the ink to a specific application, such as ink-jet printing or silver paint.[20] Clever chemistry can be used to generate ink formulations without extensive additives; for example a modified Tollen's process was recently used to synthesise a reactive silver ink which achieves high conductivity patterns at low reduction temperatures.[21] These inks have been formulated for traditional

printing methods, such as ink-jet printing, where resolution is restricted to the micro-domain. Dip-pen nanolithography (DPN) may be one avenue to extend the printing of noble metals on flexible substrates into the nanodomain.

A range of methodologies have been developed over the past decade to print metal features via DPN (see Table 4-1 for a summary). Progress in DPN fabrication of metal and semiconducting nanostructures up to the year 2009 has been previously reviewed.[22]

Many of the DPN approaches concern the patterning of metal nanoparticles, in particular functionalised Au nanoparticles, for sensing or bio-recognition applications.[23-27] Although interesting for the varied approaches used to effect ink-transfer (e.g. ink-substrate hyrophobicity, nanografting etc), the presence of insulating capping agents precludes many of these strategies from generating conductive lines. One nanoparticle based methodology did target the deposition of conductive traces by including silver nanoparticles in a glycerol thickened ink formulation.[28,29] A relatively high conductivity was achieved ($3x10^4$ S cm^{-1}) using an annealing temperature of 150 °C. Silver, however, is potentially cytotoxic *in vivo*.[14] No strategy involving the direct printing of Pt nanoparticles has so far been reported.

The surface activated *in-situ* redox approach utilises opportune surface chemistry to effect reduction of a metal precursor ink upon deposition.[31,32] *In-situ* reduction has been achieved for Au and Pd on bare Si (from which the oxide layer was removed by hydrogen fluoride) and Ge substrates. Although extending this approach to flexible materials may be possible, it would require pre-functionalising the substrate with a suitable electron donating ligand.

Metal	Sub	Method	Res (nm)		σ (S/cm)	Adhes -ion	Ref	Year
			Dot	Line				
		Direct deposition of NPs						
Au	SiOx	Au NPs; hydrophobic modified	50	-	-	vdW	23	2002
Au	Au	Nanografting on thiolated Au	-	150	-	covalent	24	2003
Au	mica	Functionalised NPs, DPN in solution	-	40	-	e-static	25	2006
Au	$-NH_2$/ SiOx	Nanofountain pen, functionalised NPs	200	-	-	e-static	26	2007
Au	-OH/ SiOx	Hydrophilic NPs, UV treated SiOx		-		e-static, covalent	27	2008
Ag	SiOx, Kapton	Ag NP ink, 150 °C cure	-	500	$3x10^4$	vdW	28,29	2008, 2010
		Thermal DPN						
In	SiOx	Heated tip, 250-500 °C	-	50	$4x10^{-5}$	vdW, mech	30	2006
		Surface activated *in situ* redox						
Au	Si (HF treat)	$HAuCl_4$ in situ redox on elemental Si	< 100	< 100	-	e-static, vdW	31	2001
Au,Pd	Ge	In situ redox on Ge	-	30	-	e-static, vdW	32	2002
		Electrochemical DPN						
Pt, Au, Ag	SiOx	H_2PtCl_6 reduction with 4V bias applied to tip	-	30	-	e-static	33	2001
Au	OTS/ SiOx	Electrograft Au NPs on OTS SAM	-	50	-	covalent	34	2005
		Chemically directed assembly (CDA) of NPs						
Au	Au	Au NPs on amine terminated patterns	-	< 100	-	covalent	35	2006
		Seeded growth						
Au	Ag/ SiOx	Thiol pattern and etch Ag, reduce $HAuCl_4$ on Ag	Rings ~1μm	-	-	metallic	36	2004
Ag	Au	Electroplate Ag on thiol patterned Au	190	170	-	Electroplate	37	2006
Au	SiOx	+12V bias, Au NPs, seed growth of $HAuCl_4$	-	250	10^5	e-static	38	2007
Au, Ag	SiOx	Print NP tagged enzyme $HAuCl_4$ growth solution	-	500	η barrier	covalent	39	2006
		Wet etching a metal coating						
Au	SiOx	DPN print ODT resist and wet etch	~50	~50	As bulk	metallic	40	2000
Au	SiOx	Polymer pen MHA resist and wet etch	~50	~50	As bulk	metallic	41	
Au	SiOx	DPN print the etchant itself			-		42	2006
		Electroless deposition						
Au, Pt	HMDS/ SiOx	Print metal precursor loaded block-copolymer micelles, O_2 or Ar plasma treat	5	-	-	Not discussed (vdW)	43	2010
Pd, Pt	SiOx	[Patent] DPN deposition of metal precursor salt, followed by reduction step	-	-	-	e-static	44	2003
Au	SiOx, Al_2O_3, polyimide	Thermal DPN deposition of $HAuCl_4$, annealing at 270°C.	50	55	-	Not discussed	45	2010

Table 4-1: Selected DPN metal printing studies.

Reduction of a metal precursor within the contact water meniscus by applying a bias between pen and substrate (i.e. electrochemical DPN) has been used to nanopattern both Pt[33] and Au[34] at line resolution down to 30 nm. This approach, however, necessitates a conducting or semi-conducting substrate. Also, significant engineering challenges (such as electrical addressability of the pens, nanofluidic ink delivery) would need to be surmounted to upscale the process.

The seeded growth approach uses the metal pattern as a seed site for the reduction of a metal precursor in a post-treatment growth step.[36–39] The idea is interesting as a augmentation to other printing methods (e.g. to improve pattern continuity),[38] but is not a printing methodology in itself.

Nanopatterning a thiol resist against the wet-etch of a metal coating is the most popular method in the literature for generating conductive metal patterns by DPN.[37,41,46] This method can achieve micro- or nanoscale resolution (<50 nm) and upscalability to millions of features over cm^2 areas (via polymer pen lithography).[41] The method also does not compromise electrical properties as the pattern will retain the conductivity of the thermally evaporated metal thin film. Most of the work thus far has focused on gold, although both Ag and Pd patterning have been demonstrated.[47] Extending this approach to Pt presents significant challenges, however. The only known etchant for Pt metal is the highly corrosive aqua regia (a mixture of concentrated nitric and hydrochloric acids in a 1:3 ratio). The effectiveness of a thiol SAM to protect against an aqua regia etch is yet to be demonstrated.

Recently, the Mirkin group adapted 'block copolymer lithography' for both DPN and PPL techniques.[43] Their ink was based on block-copolymer micelles loaded with metal ions ($AuCl_4^-$ or $HPtCl_6^-$). After printing of the micellar ink, an oxygen plasma treatment effected reduction of the metal ions by a hydrocarbon oxidation mechanism. Although a landmark study, as the features generated (~4.8 nm) were smaller than the radius of the pen used

to print them (~15 nm), this approach was limited to patterning of single dots, and not continuous lines. The micellar vehicles define the minimum proximal distance between features at about 500 nm.

A final approach is the electroless deposition of metal precursors is to DPN print a metal precursor salt and subsequently reduce the salt *in situ*. In 2003 a US patent (Crocker, US 7,005,378 B2) outlined the general approach to formulate an ink including metal precursor salts and an electron donating ligand.[44] After DPN printing, the generated ink pattern could be reduced to conductive metal by heat treatment. Several worked examples were described for different metals, including one involving the printing of an aqueous $PtCl^{4-}$ on -NH2 functionalised SiOx, followed by reduction with an aqueous dimethlyamine:boran complex. Characterisation beyond the basic proof of concept was not performed. More recently, the deposition of a precursor has been used to fabricate gold patterns using a locally heated DPN tip.[45] Both dots and lines were deposited on various substrates, however a reduction temperature of 270°C was required and the method was not demonstrated for platinum deposition.

A major advantage of the metal precursor approach is its versatility across different substrate systems, though high temperature reduction strategies would not be suitable for *in situ* reduction on soft, flexible polymers. In this chapter a strategy is developed which marries the direct deposition of metal salts with the mild plasma reduction step used by Mirkin to reduce metal precursor loaded in block copolymer micelles. As a preliminary work, this study focuses on the patterning and characterization of platinum on a model silicon oxide (SiOx) substrate, followed by demonstration of the applicability of the method to various other substrates, including PDMS.

4.2 Experimental

Materials

Ethylene glycol and the metal precursors H_2PtCl_6.x H_2O and $HAuCl_3$.xH2O were obtained from Sigma-Aldrich.

Substrate preparation

Silicon oxide and gold substrates were cleaned by water bath sonication for 10 min each in isopropanol, acetone, and Milli-Q water. Gold substrates were fabricated by depositing gold/chromium (30 nm/10 nm) on glass or silicon wafer using a laboratory-built metal evaporator.

Smooth, hydrophobic Si/SiOx substrates were prepared by chemical functionalization with octadecyltrimethoxysilane (ODTMS).[48] The procedure followed was modified from the literature.[49] Briefly; after pretreatment the substrates were plasma treated (as described in Chapter 3), then immersed in a freshly prepared solution of 0.1% ODTMS in isopropanol for 5 minutes, before a further 5 minutes on a hotplate (80 °C) for 5 minutes. The substrates were dipped in the 0.1% ODTMS/isopropanol solution and placed on the hotplate (80°C, 5 minutes) a further three times to ensure consistent levels of silanization. Hydrophobicity of the substrate was confirmed by water contact angle (~88°). This degree of hydrophobicity was maintained for several weeks as confirmed by repeated water contact angle measurements.

Patterning methodology

DPN patterning was performed using an Nscriptor system (NanoInk, Skokie, IL) in an environment controlled at 45% relative humidity and 22°C temperature (unless otherwise stated). The metal precursor ink (formulation discussed in section 4.3.1 section) was wetted onto a single tip (hereafter 'DPN-tip') of NanoInk M-Type probes (NanoInk part # PEN-0300-03, material Si3N4, length 107 µm, width 22 µm, spring constant 0.5

N/m) by dipping for five seconds into the microwell of a NanoInk Universal Inkwell (part # IWL-0009-03). The tip was bled of excess ink in a method similar to that previously reported for DPN of liquid inks by bringing it in contact with the substrate in several (typically 4-5) locations, until deposition of large ~10 μm 'bleed-spots' ceased. All patterns were generated using the InkCAD software (v 2.7.1) provided with the Nscriptor system. The dwell time dependence of the ink was calibrated by printing arrays of dots using a dwell times ranging 0.002 s, 0.01 s, 0.05 s, 0.1 s, 0.25 s, 0.5 s, 1 s, 2 s, 3 s and 5 s. After DPN printing, the substrate was removed for immediate plasma treatment unless otherwise stated. In some experiments time was allowed to elapse (from 20 minutes to 24 hours) after DPN printing before the plasma reduction step was performed.

Plasma reduction

The plasma reduction step was performed in a Harrick Expanded Plasma Cleaner at 1100 mTorr on high power setting (29.6W). The plasma species was controlled by feeding N_2, O_2 or air into the chamber at the desired pressure. A range of plasma times, 30 s to 40 minutes was investigated. 10 minutes plasma treatment was found to ensure complete reduction of the precursor and was used for all experiments unless otherwise stated.

Electrical properties

Confirmation of electrical conductivity was performed by depositing large (~10 μm) 'bleed spots' of platinum precursor ink between micron-scale planar electrodes. After plasma reduction, the resistance of the resulting platinum resistor was measured using an eDAQ (x) system (linear voltage sweep from -10 V to + 10 V).

Scanning electrochemical microscopy (SECM) was performed by raster scanning an SECM tip inset with a 10 μm diameter platinum microelectrode over printed platinum feature in aqueous 0.1M KCl with 1mM ferrocenemethanol 1mM as redox mediator. Current was measured at a z-

height of 3 μm and an 'increment time' of 0.04 s on a point by point basis over the scan area. The distance between points, determining the scan resolution, was typically 1 μm.

Instrumentation

Atomic force microscopy (AFM) topographic imaging was acquired with an Nscriptor AFM system (Pacific Nanotechnology) or Asylum Research MFP−3D AFM system in tapping mode in air at room temperature. Scanning electron microscopy was performed on a JOEL 7500FA Field Emission Scanning Electron Microscope (FESEM). Scanning electrochemical microscopy (SECM) was performed on a CHI SECM.

4.3 Results and discussion

4.3.1 Ink Development: Choosing a reduction strategy

Under ambient conditions H_2PtCl_6 thermally reduces to platinum metal at 500 °C.[50] When dissolved in a reducing agent, such as ethylene glycol, the temperature of reduction is lowered significantly. Cho et al. have shown that thin films of platinum nanoparticles could be formed by simply drop-casting of H_2PtCl_6/EG solution onto a substrate heated to 160 °C.[51] The poor thermal stability of our prospective flexible substrates, however, precludes them from such hot-plate heating.

As a first step in our ink development, the use of plasma treatment to reduce thin films dropcast from chloroplatinic acid in ethylene glycol was investigated. Ethylene glycol was chosen as solvent because; (1) it is used extensively as a reducing agent for chloroplatinic acid[51-53] and (2) it has a relatively low volatility (boiling point 197 °C), making it a promising ink for DPN.

In a typical experiment, a small volume (<5 μL) of metal precursor solution was drop cast onto a clean glass substrate. Films were dropcast from a

range of precursor concentrations (4-40% wt) in both water and ethylene glycol as outlined in Table 4-2. Plasma treatment (air, O_2 or N_2) was performed for 5 or 10 minutes. Afterwards the presence of a shiny, metallic layer, as opposed to a dried, red/brown salt, was deemed an indication of successful reduction.

Soln #	*Precursor*	*Precursor % (wt)*	*Solvent*	*Plasma type*	*Plasma time*	*Reduction?*
1	$HAuCl_3.xH_2O$	10	EG	AIR	5 min	YES
2	$HAuCl_3.xH_2O$	40	EG	AIR	5 min	YES
3	$H_2PtCl_6.xH_2O$	10	EG	AIR	5 min	YES
4	$H_2PtCl_6.xH_2O$	40	EG	AIR	5 min	YES
5	$H_2PtCl_6.xH_2O$	4	H_2O	AIR	5 min	YES
6	$H_2PtCl_6.xH_2O$	10	EG	O_2	10 min	NO
7	$H_2PtCl_6.xH_2O$	4	H_2O	O_2	10 min	NO
8	$H_2PtCl_6.xH_2O$	10	EG	N_2	10 min	YES
9	$H_2PtCl_6.xH_2O$	4	H_2O	N_2	10 min	YES

Table 4-2: Plasma treatment as a reduction strategy for dropcast metal precursor solutions.

From the series of experiments summarized in Table 4-2, we made the following principle observations:

- Both H_2PtCl_6 and $HAuCl_3$ in ethylene glycol could be reduced by air plasma treatment (Soln #1-4).
- Solutions with low (4%) and high (40%) loading of metal precursor appeared to be reduced equally well (Soln #4 and #5).
- Nitrogen plasma treatment effected reduction of the H_2PtCl_6/EG film, whereas oxygen plasma did not. (Soln #6, #7 and #8)
- Ethylene glycol was not necessary to effect reduction. The platinum precursors reduced when dissolved in water rather than EG (Soln #9).

Although it was found that EG is not necessary as a reducing agent, the high boiling point of EG is still an attractive property in the formulation of a DPN ink and so analysis proceeded with the H_2PtCl_6/EG films reduced by nitrogen plasma. Figure 4-1 shows optical microscopy images of the H_2PtCl_6/EG film after 10 minutes N_2 plasma treatment (i.e. Soln #8). The

film appears as a structure of apparently continuous platinum islands separated by micron-scale particles. The grain boundaries formed during the reduction step are evident.

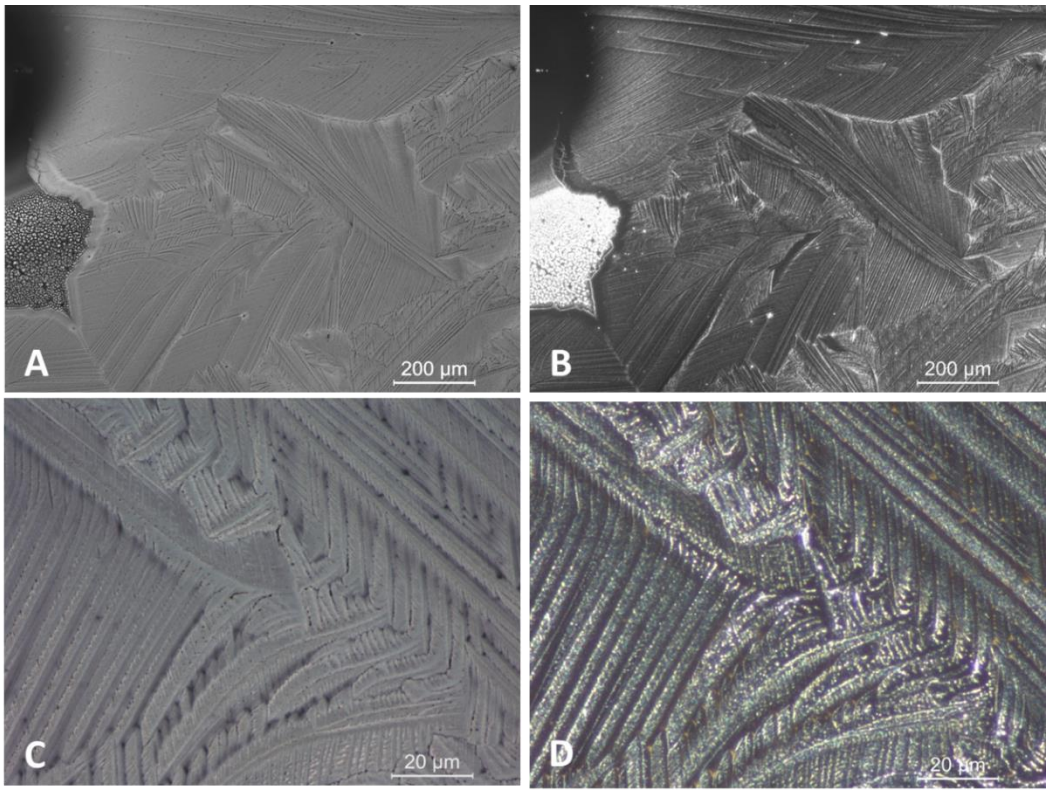

Figure 4-1: Optical microscopy of a drop-cast H_2PtCl_6/EG film after N_2 plasma treatment (i.e. reduced to platinum metal); A) Bright field optical micrographs (x10 magnification) of an area of reduced platinum film. Most of the platinum in the image appears composed of one solid metal film. The dark area at the left of the image is the film edge; B) Dark field optical micrograph (x10 magnification). The dark field images highlight the grain boundaries formed during the reduction of the precursor to platinum metal; C) bright field and; D) dark field x100 magnification of a single grain boundary.

SEM imaging of the H_2PtCl_6/EG film (10 minutes N_2 plasma treatment) revealed two principle material phases in the nanoscale structure. Most of the film was composed of large, continuous islands of conductive material (Figure 4-2 A). Energy dispersive X-ray spectroscopy (EDS) of the islands indicates the islands to be made principally of platinum metal (Figure 4-2 C). The lack of a chlorine component suggests this platinum has been

reduced to Pt^0. The conductive islands are separated by small amounts of non-conductive salt microcrystals (Figure 4-2 B). The presence of chlorine and platinum in a 6:1 ratio, as indicated by EDS (Figure 4-2D) indicates these crystals to be non-reduced H_2PtCl_6.

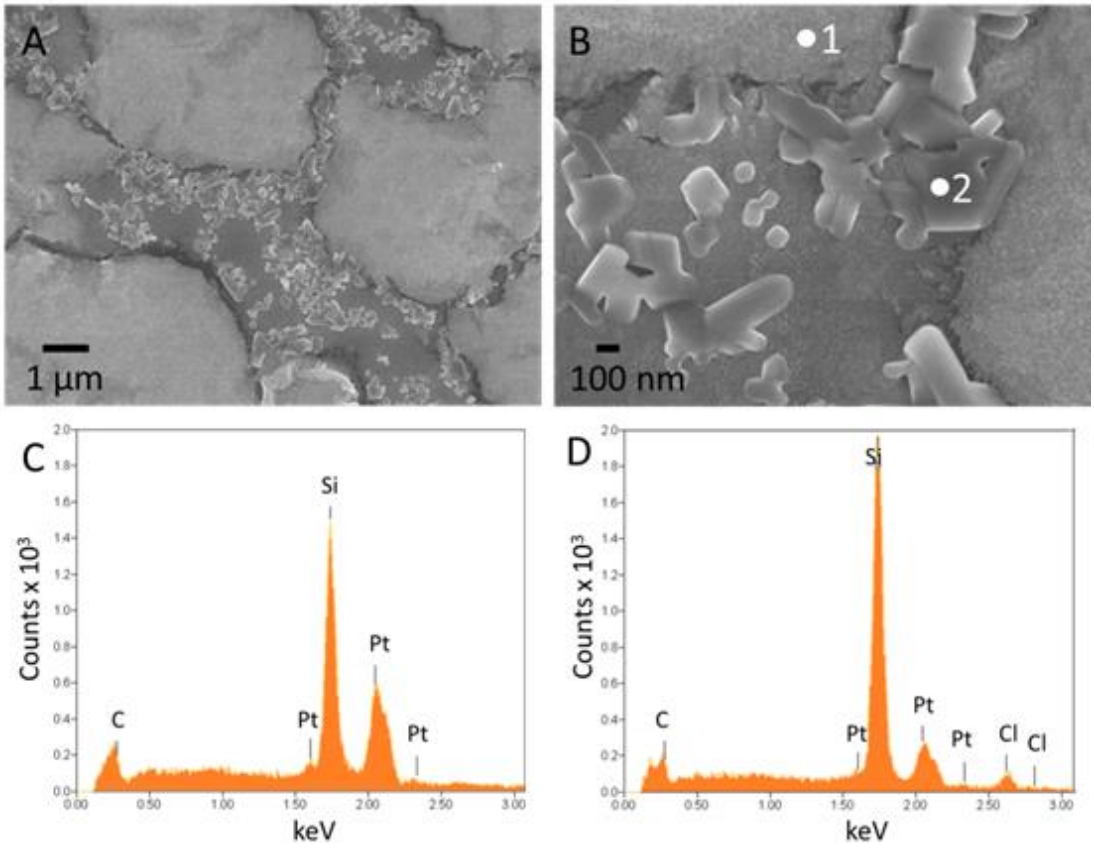

Figure 4-2: SEM imaging and EDS elemental analysis of a drop-cast H_2PtCl_6/EG film after N_2 plasma treatment: A) A low magnification SEM micrograph shows islands of platinum metal of 5-10 µm in diameter, surrounded by smaller particles; B) A higher magnification SEM micrograph shows the apparent crystalline nature of the smaller particles. The crystals are likely non-conductive and so are charging during the SEM scan; C) Energy dispersive X-ray spectroscopy (EDS) of the island structure indicated by spot 1 in image (B). The EDS spectrum indicates the composition of the island to be mostly platinum, with some carbon contamination, and no chlorine present. The large Si peak comes from the underlying substrate; D) EDS of the microcrystal indicated by spot 2 in image (B) demonstrates the presence of chlorine and platinum in a ratio of 6:1. The microcrystals are likely non-reduced H_2PtCl_6.

The reduction of the H_2PtCl_6/EG drop cast films to platinum metal was further characterised by X-Ray Diffraction (XRD) measurements on various

films drop-cast from 10% H_2PtCl_6 in ethylene glycol. As shown in Figure 4-3, the N_2 plasma treated film and the hotplate heated (300°C) film exhibit the spectra expected from platinum metal, including peaks at 40.04° associated with the Pt(111) face, 46.53° associated with the Pt(200) face and 67.86° associated with the Pt(220) face. The O_2 plasma treated film and the non-treated control film do not exhibit the platinum peaks. The N_2 plasma treated film has not undergone complete reduction, however, and small peaks associated with non-reduced precursor crystals are evident at 34°, 66° and 78°.

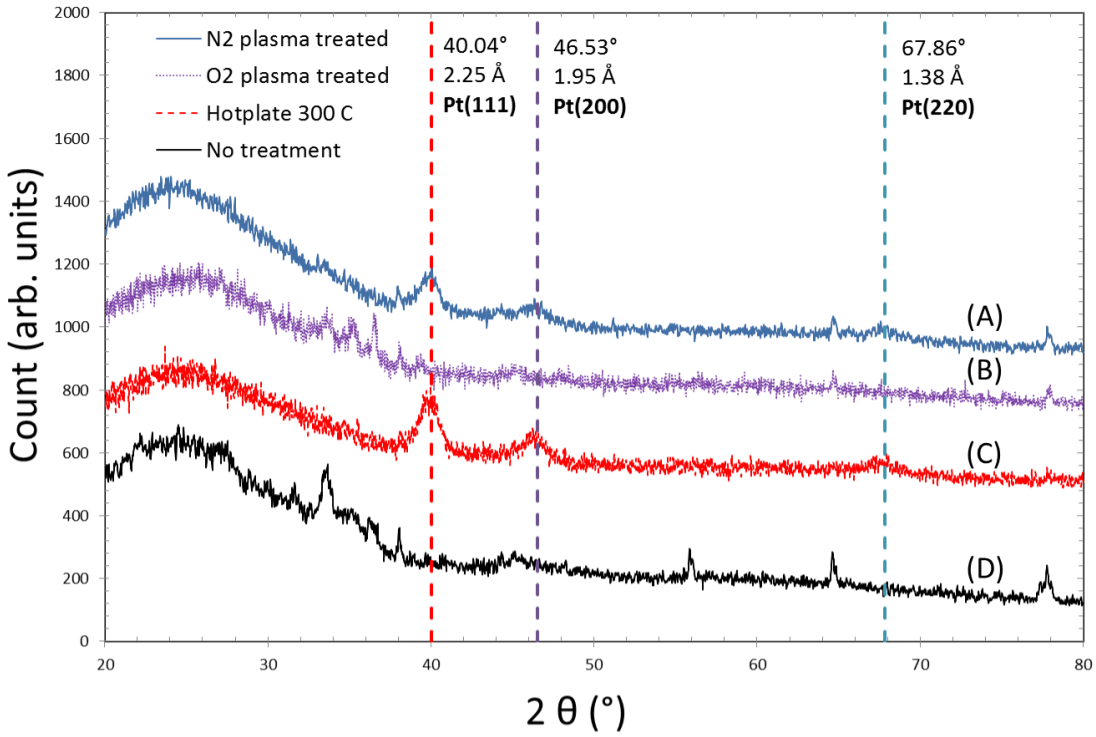

Figure 4-3: X-Ray Diffraction (XRD) of films formed by dropcasting 10% H_2PtCl_6 in EG on glass coverslips and then performing differing reduction treatments. The N_2 plasma treated film (A) and the hotplate heated (300°C) film (C) exhibit three clear peaks at scattering angles which correspond to the Pt (111), Pt(200) and Pt(220) faces. The O_2 plasma treated film and the non-treated control film do not exhibit the platinum peaks. (Note: The spectra have been off-set on the vertical axis for clarity.)

The reduction of metal precursor loaded block-copolymer micelles using oxygen plasma has been attributed to a mechanism of hydrocarbon oxidation, however no precise reduction mechanism was elaborated.[43,54] In

our case, reduction only takes place using nitrogen or air plasma, and not pure oxygen. It is unclear at present whether a nitrogen plasma species is playing a direct role in the redox or whether reduction is effected by localised heating only.

The thermal reduction of various metal precursors loaded in a poly(ethylene oxide)-block-poly(2-vinyl pyridine) (PEO-*b*-PVP) block-copolymer carrier has been probed by subjected samples to differing heating cycles.[55] Reduction of each metal precursor was found to follow one of three pathways, depending on the reduction potential of that species. High redox potential species, such as gold and silver, were reduced by the polyethylene oxide (PEO) copolymer at low annealing temperatures (~150°C). The platinum precursor (H_2PtCl_6) had to undergo a high temperature annealing step (~500°C) for reduction to take place, at which temperature the block copolymer carrier also decomposed. This high temperature corresponds to the thermal decomposition temperature of H_2PtCl_6 in the absence of a reducing agent.[50] In systems where EG is used as a reducing agent, the thermal reduction temperature of H_2PtCl_6 can be as low as 160°C.[51] The reaction is proposed to proceed via a double-oxidation of EG.[52,56] Thus, localised heating of the substrate to 160°C by plasma treatment may be enough to facilitate reduction, as long as the reducing agent is still present.

In our system, dropcast films which were dried out prior to plasma treatment were mostly not reduced to metal, suggesting that the precursor must be solvated for reduction to occur. Interestingly, reduced metal was found at the extreme peripheries of these dried films (where they were most thin). It may be that the water layer adsorbed under ambient conditions is enough to facilitate reduction of the thinner section of the dried metal precursor film, but not larger crystals. This becomes important when we consider the successful reduction of some dried DPN patterns below (4.3.4).

4.3.2 Developing a methodology for printing platinum precursor solutions by DPN

We found in section 4.3.1 above that both gold and platinum precursors could be reduced by air or nitrogen plasma treatment when drop-cast from ethylene glycol or water. Preliminary DPN experiments were next performed on silicon using both EG and water as ink solvent, and high metal precursor concentrations (~40% wt). The focus of these initial DPN experiments was on development of the platinum precursor inks, though results will be periodically included for gold precursor inks to demonstrate the versatility of the approach.

Ink #	*Precursor*	*Precursor % (wt)*	*Solvent*	*Printability on Si*
1	$HAuCl_3.xH_2O$	36	EG	YES
2	$HAuCl_3.xH_2O$	36	H_2O	NO. Rapid evaporation from tip.
3	$H_2PtCl_6.xH_2O$	40	EG	YES.
4	$H_2PtCl_6.xH_2O$	40	H_2O	NO. Rapid evaporation from tip.

Table 4-3: Preliminary DPN metal precursor ink formulations

Table 4-3 summarises our preliminary DPN experiments. It was observed that, after inking, the water based inks evaporated rapidly from the pen and so were not practical for liquid ink deposition (Ink #2 and #4 in table). DPN printing of the dried salt via meniscus transport was also investigated but was largely unsuccessful due to non-reproducible drying of the salt crystals at the tip apex—see Appendix 4.5.1.) The EG based solutions did not have the same evaporation issue and they could be successfully deposited as liquid ink features on silicon (ink #1 and #3 in table). We proceeded with developing a DPN methodology for the ethylene glycol based solutions only.

Although printing of the EG based H_2PtCl_6 ink was successful on Si, printing ceased after only 10 deposited features. Optical microscopy of the DPN

pens after printing revealed diffusive rings emerging from the inked cantilevers onto the back of the chip (see Figure 4-4 (B)). This spreading effect could be prevented rendering the pens hydrophobic with octadecyltrimethoxysilane(ODTMS), thus reducing the mobility of the ink on the cantilever. Pens functionalised with ODTMS had a much longer printing lifetime than non-functionalised pens. We characterised the improvement in inking lifetime by following the mass of ink on the cantilever using its resonant frequency. As shown in Figure 4-4 (A) the non-functionalised (hydrophilic) cantilever displayed a relative decrease of 80% of its ink mass within 10 minutes after inking. The hydrophobic cantilever showed a decrease of only 10% ink mass over the same time period. This smaller decrease was not the result of ink diffusion over the chip, but rather of EG evaporation. The rate of evaporation suggested the ink would maintain viability for a period of at least an hour. However, it must be noted that the gradual evaporation of EG from the ink would lead to a general increase in metal precursor concentration over the course of long printing experiments.

The addition of stabilizer additives (such as glycerol, trehalose, oligo (ethylene glycol), polyethylene glycol-ran-polypropylylene glycol) was investigated as a means to further increase printing lifetime (see Appendix 4.5.2). The additives had the effect of inhibiting the reduction by plasma treatment (possibly due to incomplete pyrolysis)[ref]. All experimentation continued with ink formulations of H_2PtCl_6 in ethylene glycol only.

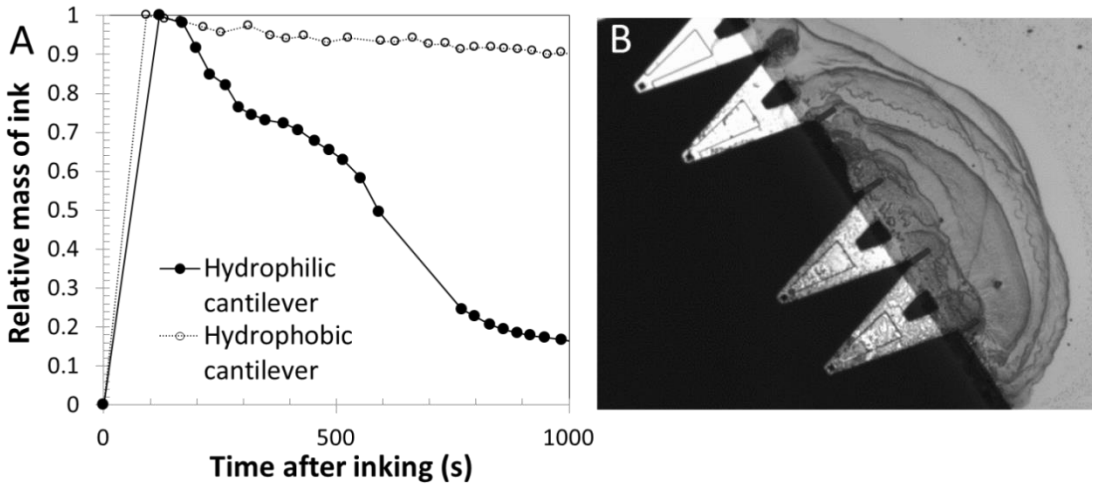

Figure 4-4: Spreading of the metal precursor ink over the cantilever chip dramatically effects printing lifetime: A) Measurements of the resonance frequency of cantilevers inked with 40% wt H_2PtCl_6 in EG over time (without printing). The change in resonant frequency has been converted to a change in ink mass following Biswas et al.[74] A non-functionalised cantilever lost 80% of ink mass whereas a cantilever functionalised to be hydrophobic (with octadecyltrimethoxysilane) lost only 10% of its ink mass over 15 minutes. B) The rapid decrease in mass of ink on the hydrophilic (non-functionalised) cantilever was caused by the spreading of the ink from the cantilever itself on to the back of the cantilever chip.

4.3.3 DPN printing on Silicon

Reduction of H_2PtCl_6/EG DPN patterns in situ using nitrogen plasma treatment

In section 4.3.1 above we demonstrated that drop-cast solutions of H_2PtCl_6 in EG could be reduced using nitrogen plasma treatment. In section 4.3.2 we developed a methodology to reliably effect ink transfer from the DPN tip to a Si substrate. The next step was to confirm that DPN printed patterns could be reduced to form platinum metal, just like the larger drop-cast films.

To investigate the effect of plasma treatment on the morphology of printed patterns, two similar DPN dot arrays of H_2PtCl_6 (50% wt) in EG were printed on different Si substrates. The first substrate was not treated, and simply

allowed to dry over a period of hours. The second substrate was treated with nitrogen plasma for 10 minutes immediately after printing. SEM images of each sample are shown in Figure 4-5.

The printed features on the non-plasma treated sample formed clusters of crystals due to the evaporation of the EG solvent. EDS of a single crystal confirmed the presence of platinum and chlorine in a ratio of 1:6, suggesting these are crystals of unreacted H_2PtCl_6. The dark circles surrounding each crystal cluster in the non-treated sample are likely an SEM contrast resulting from residual EG on the substrate, and therefore may indicate the original dimensions of each feature before drying.

The printed features on the plasma treated sample formed discrete dots. EDS confirmed that each feature was composed of platinum, with some carbon contamination and no chlorine. Each printed dot contained one small white region. Higher magnification micrographs revealed the white regions to be cubic in shape; the cube may represent a crystal of H_2PtCl_6 being formed at the onset of EG evaporation.

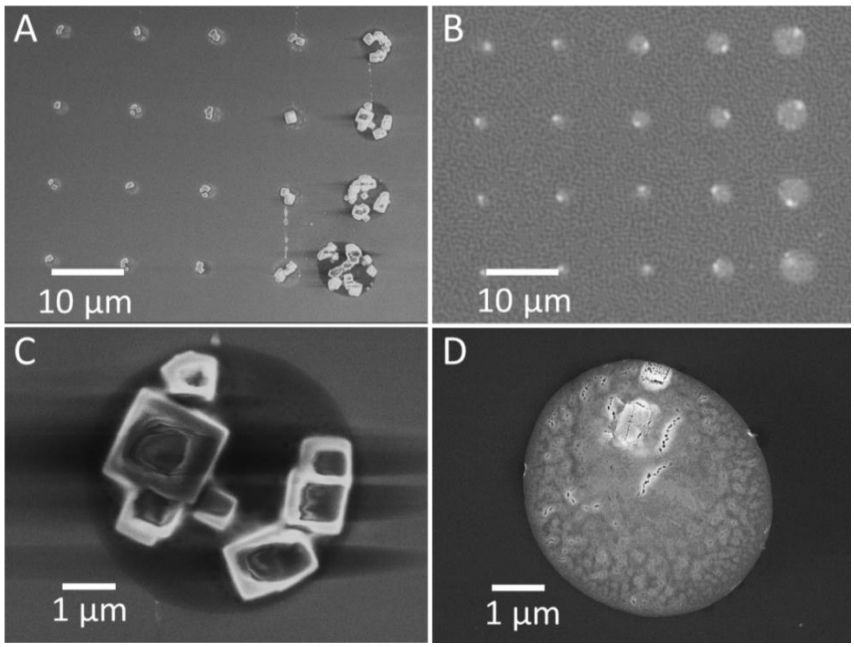

Figure 4-5: Effect of nitrogen plasma treatment on morphology of 50% wt H_2PtCl_6/EG DPN patterns: A) and C) SEM micrographs of H_2PtCl_6/EG features printed on silicon

without subsequent plasma treatment. The printed solution has dried out, forming crystals of hydrated H_2PtCl_6. The dark circles around each crystal cluster are likely an SEM contrast resulting from residual solvent on the substrate. EDS of the crystal cluster shown in (C) confirmed platinum and chlorine present in a 1:6 ratio; B) and D) H_2PtCl_6/EG features on a silicon subststrate which was treated with nitrogen plasma immediately after printing.* Each feature has reduced to form a solid platinum dot. EDS of the crystal cluster shown in (D) confirmed the feature is made of platinum with no chlorine component; [Note: all features were formed with a 5s dwell time. The gradient in feature size in both images (A) and (B) is a result of depleting ink on the cantilever as will be described in Chapter 6.]

*** The apparently high roughness of the substrate in (B) is an arteface of this low-resolution SEM image. THe higher quality SEM image of the same sample (D) shows the substrate has no detectable roughness.**

Effect of precursor concentration on DPN printing

As shown in table Table 4-4 increasing the loading of H_2PtCl_6 in the ink formulation has a significant effect on liquid properties. The surface tension increases from about 47 mN m^{-1} for pure EG, to 56 mN m^{-1} for a solution of 48 % wt $H_2PtCl_6.xH_2O$. Density increases from 1.1 g/ml for EG to 1.5 g/ml for the 48 % solution. Macroscopic contact angles, as measured by goniometry of ~1mm droplets, also increase in proportion to the precursor concentration. Variations in each of these parameters may affect the dynamics of liquid ink deposition by DPN.

Solvent	*$H_2PtCl_6.xH_2O$ loading*	*Density (g/ml)*	*Surface tension (mN m^{-1})*	*Macroscopic Contact angles*		
				Bare Si	*Si (-CH_3) X1 dip*	*Si (-CH_3) X4 dips*
EG	0	1.104	46.93	20.2	49.7	65.1
		(0.001)	(0.13)	(1.7)	(8.9)	(3.0)
EG	10.0	1.167	48.41	21.6	49	67.9
		(0.001)	(0.28)	(1.5)	(6.7)	(2.1)
EG	47.8	1.484	55.99	36.3	54.6	76.3
		(0.001)	(0.32)	(0.6)	(6)	(1.7)
H_2O	0	1.000	72.8	46	66.3	91
				(1.2)	(9.3)	(1.7)

Table 4-4: Liquid properties of various H2PtCl6 solutions and their contact angles with Si silanized to different degrees with octadecyltrimethoxysilane (ODTMS).

The images shown in Figure 4-5 above exhibit micron-scale platinum features. These dots were printed soon after inking the DPN pen, when

deposition rate is highly dependent on volume of ink on the cantilever (extensive characterisation of this effect is presented in **Chapter 6**). The following section demonstrates the reproducible printing of nanoscale Pt features which are generated when a very low loading of ink remains on the pen.

We investigated the effect of precursor concentration on DPN printing behaviour by printing a series of calibration grids using solutions of 10% wt H_2PtCl_6 and 48% wt H_2PtCl_6 on hydrophobic SiOx (i.e. SiOx fully functionalised with ODTMS). Each calibration grid consisted of a series of dots of dwell times ranging from 0.002 s to 5s. The patterns were reduced by N_2 plasma treatment and then imaged by SEM.

As can be seen in Figure 4-6, the 10% and 48% inks exhibit very similar behaviour at short dwell times. For example, the minimum feature size for each ink was 50-60 nm at 0.002 s. The 48% ink showed a linear dependence of dot-radius on the square root of dwell time. The 10% ink printed slightly larger features than the 48% ink at dwell times above 1 s. However, conclusive analysis of the effects of ink concentration were not extracted. Significant variations in printing rate of each ink were found depending on the loading of ink on the pen. In addition, inherent variations in printing performance (e.g. minimum feature size, dwell time dependence) was observed for different pens in an array, even when the pens were printing the same ink under identical environmental conditions and inking procedure. This variability between pens may be due to differences in tip sharpness, or to variability in the degree of functionalization by ODTMS.

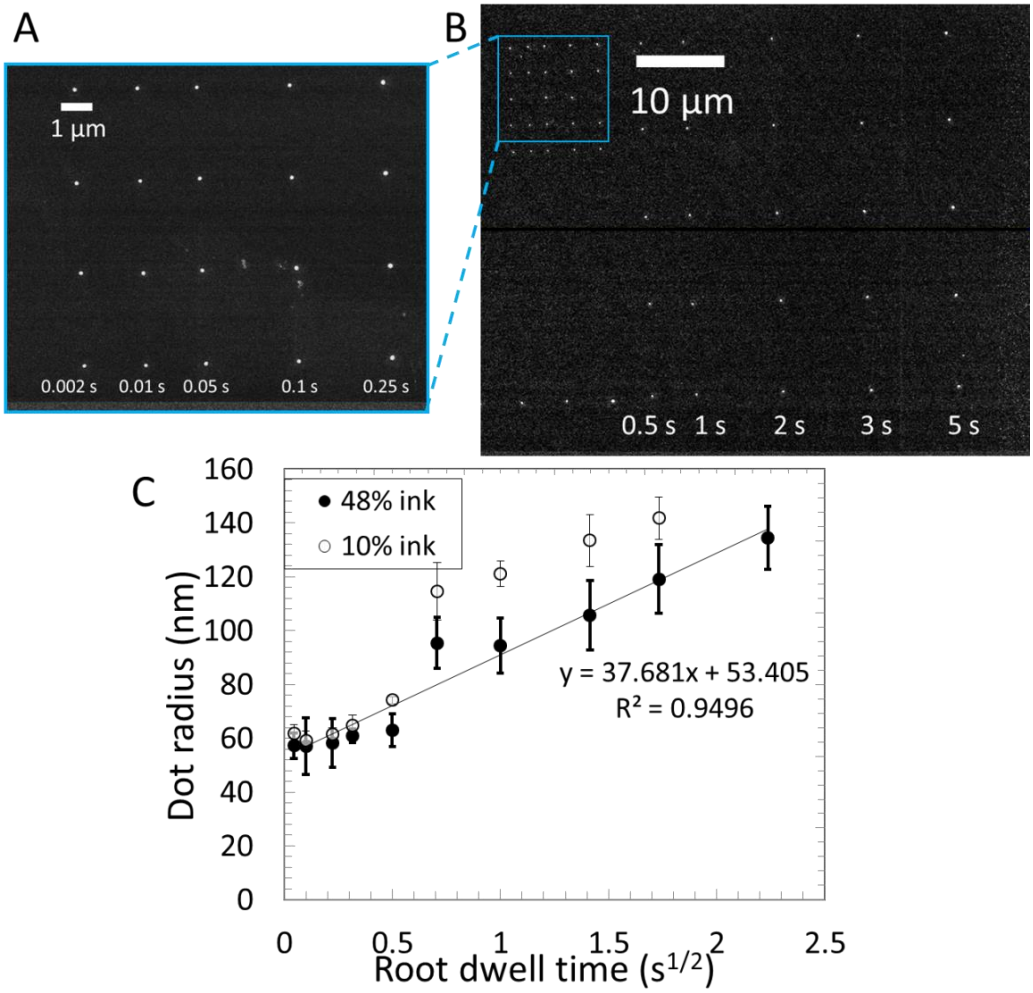

Figure 4-6: Dot-radius versus dwell time for two concentrations of H_2PtCl_6 in EG: A) SEM micrograph (magnification x8000) of the shorter dwell time array. Dots deposited with dwell times 0.002s, 0.01s, 0.05s, 0.1s and 0.25 s are indicated; B) SEM micrograph (magnification x1,500) of dots deposited with dwell times of 0.5s, 1s, 2s, 3s and 5s as indicated; C) Plot of dot radius versus square root of dwell time for two concentrations of H_2PtCl_6 in EG. Dot-size follows a $r \sim t^{1/2}$ relationship.

Proximity limit of nanoscale dot features on $-CH_3$ functionalised Si

Although a minimum feature size of 50-60 nm dots at 0.002 s dwell time was achieved, these features could not be printed arbitrarily close to one another. Figure 4-7 (A) shows the InkCAD pattern designed to investigate this effect. The pattern consists of gradient in dot density with dot-spacing decreasing from 3 µm to 250 nm. All dots were printed with a 0.002 s dwell

time. Figure 4-7 (B) shows a printed dot array generated from this gradient pattern. Consistent dot features of 50 nm diameter were printed in most programmed positions for dot-spacings of 3 µm, 2 µm, 1 µm, and 500 nm. No features were deposited at a 250 nm spacing. We suggest this lack of deposition is due to the ink transport meniscus overlapping with previously deposited features, preventing the definition of a pattern. This 'proximity limit' appears to be a limitation of the technique and arises because the deposited features are still in their precursor form, and therefore resoluble in the ink meniscus.

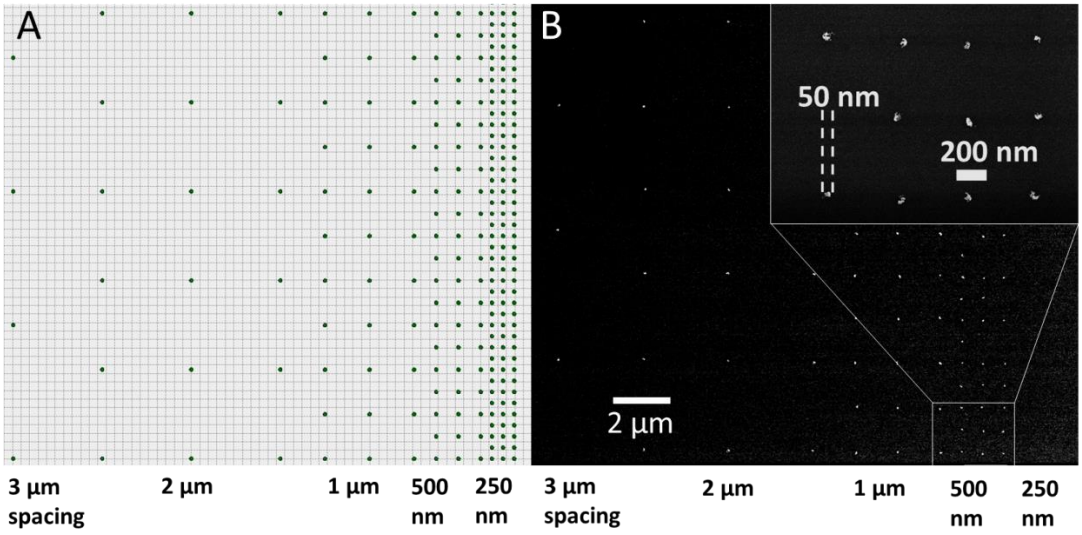

Figure 4-7: Proximity limit of nanoscale dot features at 45% humidity: A) Design of the InkCAD pattern composed of a gradient of dot density. Each dot is programmed with a 0.02 s dwell time. The dot-spacing decreases from 3 µm between dots at the left to 250 nm between dots at the right; B) A printed dot array generated from this gradient pattern. Consistent dot features of 50 nm diameter were printed in most programmed positions for dot-spacings of 3 µm, 2 µm, 1 µm, and 500 nm. No features were deposited at a 250 nm spacing. This illustrates the proximity limit below which the ink transport meniscus begin to overlap with previously deposited features, preventing the definition of any pattern.

4.3.4 Generation of direct-write platinum micro-snowflakes on Si

Effect of silicon functionalization on platinum morphology

As discussed in **Chapter 2**, a liquid ink for DPN must only partially wet the substrate. DPN printing of H_2PtCL_6/EG inks on plasma treated (hydrophilic) Si did not yield discernible features. Due to the high ink-substrate affinity (contact angle ~0°), the ink spread completely over the substrate in a rapid diffusive splash (Appendix 4.5.3). Furthermore, although DPN printing of H_2PtCL_6/EG inks on "bare" (solvent cleaned, non-plasma treated) Si/SiOx substrates was successful, we found the morphology of the features were not always uniformly circular, and that printing resolution was limited to the micron-scale regime.

We found that rendering silicon substrates hydrophobic using the surface-modifier octadecytrimethoxysilane (ODTMS) had the effect of increasing printing resolution (section below). Additionally, we found that the morphology of printed platinum structures depended dramatically on the degree of ODTMS functionalization (Figure 4-8).

By varying the number of times a silicon substrate was dip-coated in an ODTMS silanization solution (see Experimental section*: Substrate preparation*), we generated Si substrates with water contact angles of ~46°, ~66° or ~91°. The basis of increasing contact angle with number of dips is an increase in surface coverage of the ODTMS functinoalisation, though surface coverage was not quantified in this study. We quantified the ink-substrate interactions of H_2PtCL_6/EG inks containing a range of precursor loadings on these Si substrates by contact angle measurement (Figure 4-8 (A)). Contact angles of all inks increased on Si substrates with higher degrees of ODTMS functionalization. As H_2PtCl_6 loading increased, so the contact angle increased due to higher ink surface tensions.

DPN printed dots formed three distinct morphologies on substrates functionalised to different degrees. Figure 4-8 (B), (D) and (F) show the morphology of 48% wt H_2PtCl_6 ink patterns on each Si substrate as imaged by bright-field optical microscopy, 24 hours after printing, but before plasma treatment. Features printed on the untreated Si/SiOx substrate (B) formed rings of dried salt. Dried rings left by a particle laden solution after evaporation have been well documented, and the phenomenon has become known as the 'coffee-ring effect'. The effect has been explained as originating from a capillary flow mechanism causing the liquid evaporating from the edge to be replenished by liquid flow from the centre.[57] The coffee-ring effect in our printed H_2PtCl_6 ink patterns is clearly visible for the larger printed features (5-10 μm diameter). The smaller features, however (for example, the top-most dots in Figure 4-8 (B)) did not dry in ring shapes. Studies of the coffee-ring effect for micro-scale drops has revealed a threshold droplet size below which a ring does not form.[58] The threshold was shown to depend on particle size, shape and concentration. A solution of 100 nm particles, for example, had a threshold drop-diameter of about 10 μm drop diameter. The threshold drop diameter for our ink droplets appears to be about 3 μm.

Features printed on the fully functionalised Si/SiOx substrate (Figure 4-8 (F)) formed circular dots. A lack of contact line pinning on these highly hydrophobic surfaces may inhibit coffee-ring formation during drying. Nanoscale feature sizes were only achievable on fully ODTMS functionalised Si/SiOx.

Features printed on the partially functionalised Si substrate (Figure 4-8 (D)) adopted a fractal shape (herein dubbed 'platinum snowflakes'). Fractal-like growth of DPN patterned features has been previously reported for molecules with only a weak affinity for the substrate (1-dodecylamine (DDA) on mica)[59]. Analysis of the irregular geometry of the DDA patterns in that study indicated that the fractal-like shapes could not be explained by the random walk model. The mechanism for this 'anomalous surface

diffusion' was suggested to arise from the dominance of intermolecular forces (between DDA molecules) over molecule-surface interactions. After the DDA molecules were deposited, diffusing molecules preferentially attached to preferred crystalline domains. The sprouting of new crystalline domains at the edges of old domains, largely at random, led to the observed irregular patterns. The micro-snowflake structure we observe is more complicated than the DDA on mica example, as the dendritic fingers do not originate from a point source, but rather sprout from the edge of a ring shape. As can be seen in Figure 4-8 (D), and even more clearly in Figure 4-9 (A), the inside of the micro-snowflake is often empty. The platinum micro-snowflake morphology may be formed in a two-step mechanism: firstly, capillary-induced flow drives most of the solute to the edge of the drying drop (coffee-ring effect); secondly, the weak molecule-surface interaction allows for 2D diffusion of the H_2PtCl_6 molecules, and hence preferential growth from preferred crystalline domains in dendritic-like fingers. We also cannot rule out crystal growth via diffusion limited aggregation (DLA).[60] The fractal dimension of our platinum micro-snowflakes, as measured by image analysis using the method of box counting, is 1.72, which is close to the that of DLA patterns formed by non-interacting, surface bound particles in two dimensional space (1.71).[61,62]

Figure 4-8 (C), (E) and (G) show the same features (coffee ring, circular dot and micro-snowflake respectively) after N_2 plasma treatment. Plasma reduction here was performed after a 24 hour drying period, in order to ensure all samples were in a dried crystal form. The morphology of the coffee-ring structures (Figure 4-8 (C)) and the circular dot structures (Figure 4-8 (G)) did not dramatically change after treatment with N_2 plasma. The micro-snowflakes, however, transformed from a brown colour to silvery/white after treatment (Figure 4-8 (E)). This suggests that the micro-snowflakes are reduced by plasma even in the dry form, whereas the

coffee ring and dot structures are not. A proposed explanation for this behaviour is discussed in the following two sections.

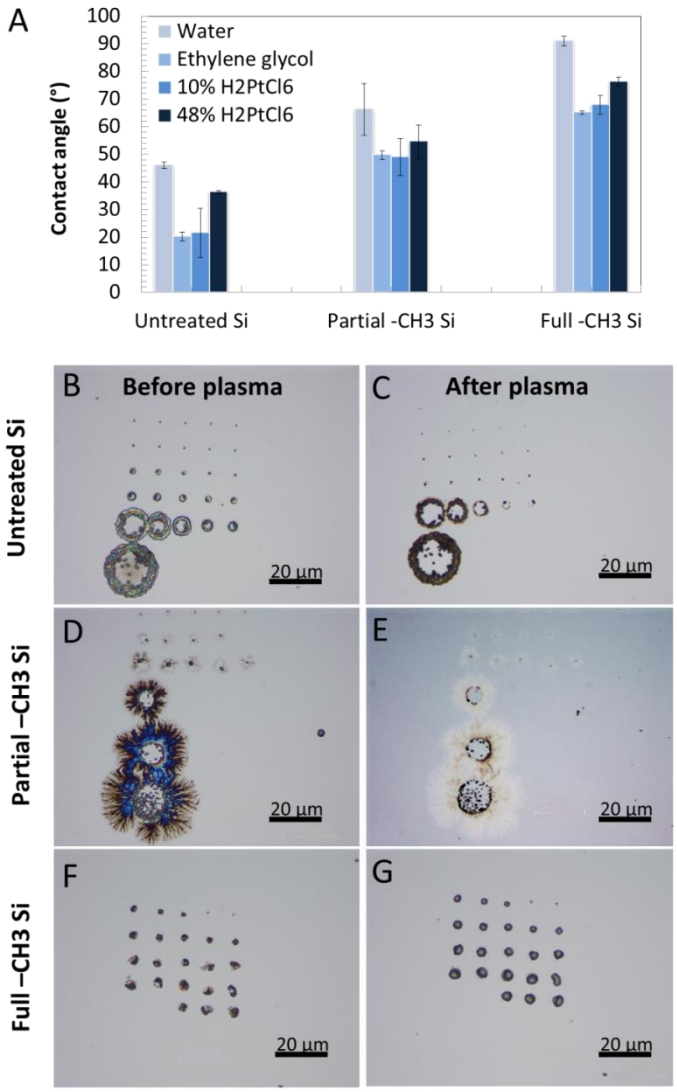

Figure 4-8: Effect of substrate hydrophobicity on morphology of DPN printed patterns: A) The contact angles* of various ink formulations and of milli-Q water on Si substrates functionalised to differing degrees. Contact angles of all liquids increase on Si substrates with higher degrees of ODTMS functionalization. On each substrate, the contact angle increases with increasing H_2PtCl_6 loading due to an increase in ink surface tension; B) to G) Optical microscopy showing the morphology of 48% wt H2PtCl6 ink patterns on each Si substrate before and after plasma treatment. [Plasma treatment in this experiment was performed 24 hours after printing]. A dwell time of 5s was deliberately chosen for all features to form structures large enough for optical microscopy; (B and C) Features printed on the untreated substrate form a ring shape

and their morphology does not visibly change after plasma treatment; (D and E) Features printed on the partially functionalised Si substrate adopt a fractal shape and the dendritic fingers visibly change from brown to platinum white after plasma treatment; (F and G) Features printed on the fully functionalised Si substrate form discrete dot structures. The morphology of these dots does not visibly change after plasma treatment.

*** All measurements taken at 22°C. The columns represent averages of 18-20 sessile drops on two substrates for each Si type. Error bars represent the standard deviation. ** Si was functionalised as described in Experimental section.**

Figure 4-9 shows SEM micrographs of a single micro-snowflake generated by printing the 48% H_2PtCl_6 ink on partially ODTMS functionalised silicon (as described above) over a range of magnification. The x3,700 magnification image shows the dendritic branching structure of the fingers extending radially from a central ring. At x11,000 magnification a diffuse cloud of disparate particles is visible at the peripheries of the fingers. The x37,000 magnification of the base of one finger shows pockmarked nanostructure, indicating that the feature is not composed of continuous metal. At x200,000 magnification it is clear that the feature is composed of a network of nanoparticles of 10-20 nm in diameter. Energy dispersive X-ray spectroscopy (EDS) of the dendritic fingers measured the presence of platinum and no chlorine. EDS analysis of the crystals in the core of the feature found chlorine and platinum in a 4:1 or 6:1 ratio, suggesting an incomplete reduction (data not shown).

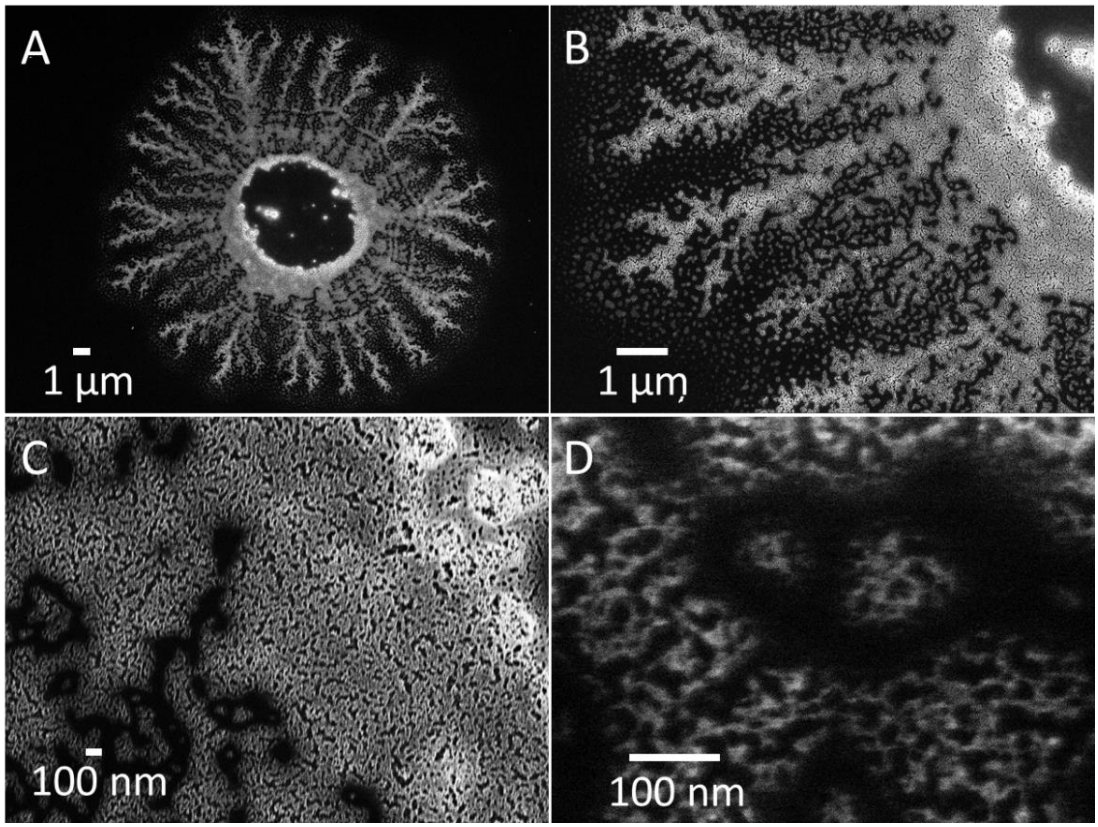

Figure 4-9: SEM imaging of platinum micro-snowflakes on partially ODTMS functionalised Si: A) SEM micrograph of a single micro-snowflake at x3,700 magnification; B) At x11,000 magnification, a diffuse cloud of disparate particles is visible at the peripheries of the dendritic fingers; C) A x37,000 magnification of the base of one finger shows pockmarked nanostructure; D) At 200,000 magnification it is clear that the feature itself is composed of a network of nanoparticles of 10-20 nm in diameter.

Elemental analysis of the micro-snowflakes (Figure 4-9) and the dramatic colour change evident in Figure 4-8 (D) and (E), suggest that the dendritic fingers of these features, at least, are being reduced to platinum metal after plasma treatment. However, the crystals present in the ring-shaped 'cores' do not completely reduce.

We suggest that this may be explained by the role of adsorbed water in the reduction mechanism. We found in section 4.3.1 above that H_2PtCl_6 drop-cast as either a water or EG solution would reduce to platinum metal when treated with nitrogen plasma. Similar drop-cast films would not be reduced if the solvent was allowed to evaporate before plasma treatment. DPN

features printed with a H_2PtCl_6/EG solution on Si could be reduced to metal if plasma treated immediately (Figure 4-5 (B) and (D)). Similar DPN patterns were not reduced when left to dry, i.e. when the plasma treatment was performed 24 hours after printing (Figure 4-8). From these results, we concluded that the solvent (EG or H_2O) is necessary to effect reduction. However, if the dry H_2PtCl_6 crystals on a substrate are sufficiently thin (such as the periphery of the drop-cast films, or the fingers of the micro-snowflake) then the adsorbed water layer present in an ambient environment is enough to effect the reduction. When the H_2PtCl_6 crystals are too large, an adsorbed water layer is insufficient and reduction is incomplete (such as the centre of the dried drop-cast film and the large crystals in the core of the micro-snowflake).

4.3.5 DPN printing on soft and flexible substrates

One of the principle advantages of the DPN liquid ink method of deposition is substrate versatility. Besides SiOx, we have successfully DPN printed the H_2PtCl_6/EG formulation on ITO, PDMS, gold, germanium, glass, parylene C and PDMS. Importantly, the N_2 plasma treatment method was effective at reducing the printed precursor inks to platinum metal without damage to the various substrates. Figure 4-10 shows an optical image of PDMS samples coated with both gold and platinum, which have been reduced by N_2 plasma treatment from dropcast films of metal precursor solutions in EG. After plasma treatment, the PDMS was undamaged and maintained its flexibility.

Figure 4-10: Optical image of two PDMS substrates coated with films of gold (left) and platinum (right). 5 µL of 10 % (wt) metal precursor solutions in ethylene glycol were dropcast on PDMS and the films were subsequently N_2 plasma treated for 5 minutes to reduce the precursor solution to metal.

An interesting advantage of the *in-situ* reduction method is the strong adhesion between the resulting platinum feature and the substrate. Figure 4-11 exhibits the durability of DPN printed platinum on several substrates after extensive sonication in both water and isopropanol. The grid of platinum dots printed on PDMS is unchanged after 1 hour bath sonication in water. The grid is still unchanged after a further 48 hour immersion and 1 hour sonication in isopropanol, though the PDMS substrate itself has begun to degrade. The grid of platinum dots on ITO remained unchanged after both sonication steps. The grid of platinum dots on silicon, however, did show some degradation with some features destroyed by each sonication step. The stronger on soft or rough substrates (PDMS and ITO) than on flat, rigid substrates (SiOx), suggests a simple interlocking mechanical adhesion is the origin of the attachment. The strong attachment of platinum nanoparticles synthesized by in-situ thermal reduction of dropcast H_2PtCl_6/EG films has previously been reported,[51,63] where the adhesion mechanism was attributed to the high surface energy of the platinum nanoparticles.

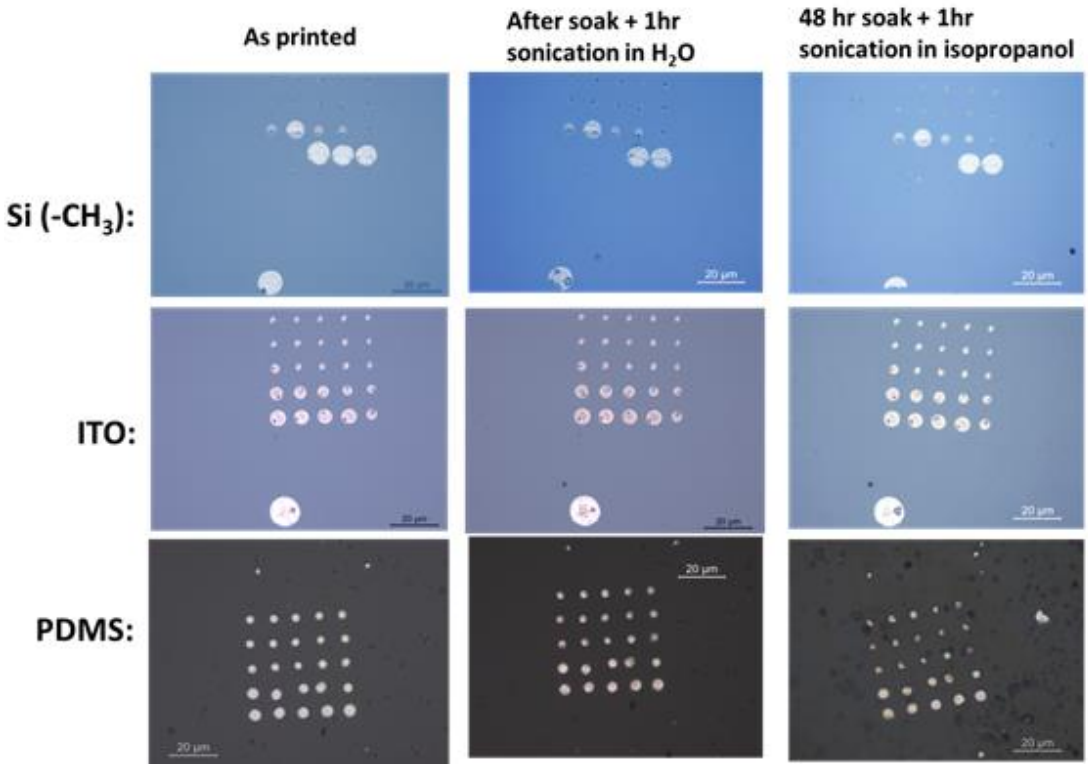

Figure 4-11: Solvent and sonication resistance of platinum features printed on various substrates. Platinum dots on ITO and PDMS all survive extensive sonication in both water and ITO. Platinum dots on ODTMS functionalised SiOx, however, begin to degrade under sonication in water. Mechanical adhesion may be stronger on rough surfaces than on the highly polished SiOx surface.

4.3.6 Line writing

Direct line writing

DPN line writing of H_2PtCl_6/EG ink was performed by bringing inked pens into contact with the substrate and moving laterally at a range of write-speeds (100 μm s^{-1} to 1 μm s^{-1}). Rather than forming continuous lines of precursor, the ink was only deposited as a final droplet punctuating the line, indicating where the tip retracted from the substrate. Figure 4-12 shows an SEM micrograph of a line pattern attempted with the 10% ink. Although faint vertical lines are visible in the image, these lines faded after a few moments of SEM imaging. This indicates the lines were most likely composed of residual solvent deposited during the DPN process. A similar

phenomenon observed during the DPN line-writing of a PEDOT:PSS has previously been described.[64]

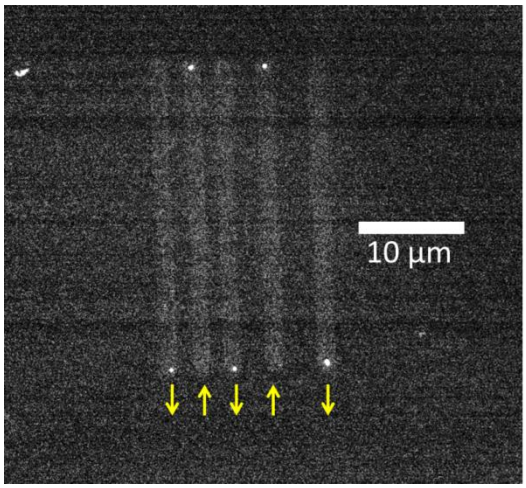

Figure 4-12: SEM micrograph of attempted DPN lines. Each line was drawn in the direction indicated by the arrow beneath it. The lines were drawn at write speeds of 100 µm s^{-1}, 10 µm s^{-1}, 5 µm s^{-1}, 2 µm s^{-1}, and 1 µm s^{-1} respectively. A single platinum dot was formed at the end of each line where the tip retracted from the substrate. The lines exhibit very poor contrast compared with the punctuating dots, and SEM imaging was only possible for several minutes before the lines faded from view entirely; this indicates the lines were most likely composed of residual solvent deposited during the DPN process and not platinum itself.

Line writing by connecting a series of dots

As discussed in section 4.3.3 above, overlap of the liquid meniscus precludes deposition of features closer together than a 'proximity limit' of about 500 nm. We conceived several experimental designs to overcome this limitation and form continuous lines by joining together a series of dots.

For example, one lithography procedure involved the deposition of a single nanoscale dot (0.002s dwell time) followed by a 'rest time' of 60 s (chosen as sufficient to allow ethylene glycol in the first dot to evaporate) before the deposition of a second dot very close (e.g. 100 nm) to the first. In this way we intended to form a line of dried H2PtCl6. The experiment was performed with a systematic range of dwell times and dot-proximities,

however line formation was never achieved. Although the first H2PtCl6 feature may indeed be dried on the substrate when the tip returns to deposit a second, the non-reduced H2PtCl6 is still soluble in water and is probably redissolved in the contact water meniscus. (A similar effect resulted in the 'proximity limit' described in section 4.3.3 above.) We performed the experiment at a range of humidities, and using several ink concentrations, but without improvement in the outcome.

Line depositing by polymer pen lithography (PPL)

We also attempted line printing of a range of H2PtCl6/EG inks using polymer pen lithography (PPL) (see Appendix 4.5.5). The PPL stamp was itself composed of lined grids. The H2PtCl6/EG ink was deposited in continuous lines (as observed by optical microscopy). However, upon retraction of the stamp the liquid ink lines rapidly beaded into disconnected dots. This beading behavior was observed on both hydrophobic and hydrophilic Si substrates, as well as Si substrates functionalized with the adhesion promoters aminopropyltrimethoxysilane (-NH_2 groups) and mercaptopropyltrimethoxysilane (-SH groups).

The particular challenge of line writing in liquid ink DPN

The surface tension of an ink provides a driving force for a partially wetting liquid ink to minimize its surface energy by forming beaded droplets, rather than continuous lines.[65] Line writing was possible with our PEDOT-VPP formulation (**Chapter 3**) as that ink contained a relatively volatile solvent and a large polymeric surfactant component. When a line was drawn, the solvent mostly diffused or evaporated away, leaving the PEG-PPG-oxidant complex as a deposited line on the substrate. In the H2PtCl6/EG case the ink only has its salt and solvent components. The surface tension of ethylene glycols is 47 mN m^{-1}, and the addition H2PtCl6 precursor increases this value up to 56 mN m^{-1} for the 48% ink (Table 4-4). The high surface tension of the ink will always work against the deposition of continuous lines as the minimum energy arrangement will be to reduce the force of

this tension by adopting circular droplet shapes. The option of including a surfactant to reduce surface tension is not open to us as even a small amount of surfactant added (e.g. 0.1% triton x-100 or 0.1% dodecylbenzenesulfonic acid) inhibits the reduction mechanism. Modifying the surface treatment to improve the ink-substrate affinity has also not been successful as too strong an affinity results in complete wetting behavior (a diffuse spreading of the ink on the substrate as visible in Appendix Figure 4-18).

One avenue we have yet to explore is to use locally defined hydrophobicity and/or chemical affinity to stabilise precursor ink in line structures. Patterns of COOH 'wetting' regions on CH_3 terminated 'nonwetting' regions have been used to generate 'nanostripes' of liquid ethanol on silicon.[66]

4.3.7 Characterisation of electrical and electrochemical properties

Electrical conductivity

The electrical conductivity of the DPN printed platinum was confirmed using a two point electrical measurement (Figure 4-13). The current voltage response of the deposited feature exhibited ohmic behaviour over a voltage range of -10 V to +10 V. The conductivity of the material is difficult to extract from this 2 point probe measurement, however, as the contact resistance is unknown. The resistance did not change after annealing at 100 °C, 200 °C and 300 °C.

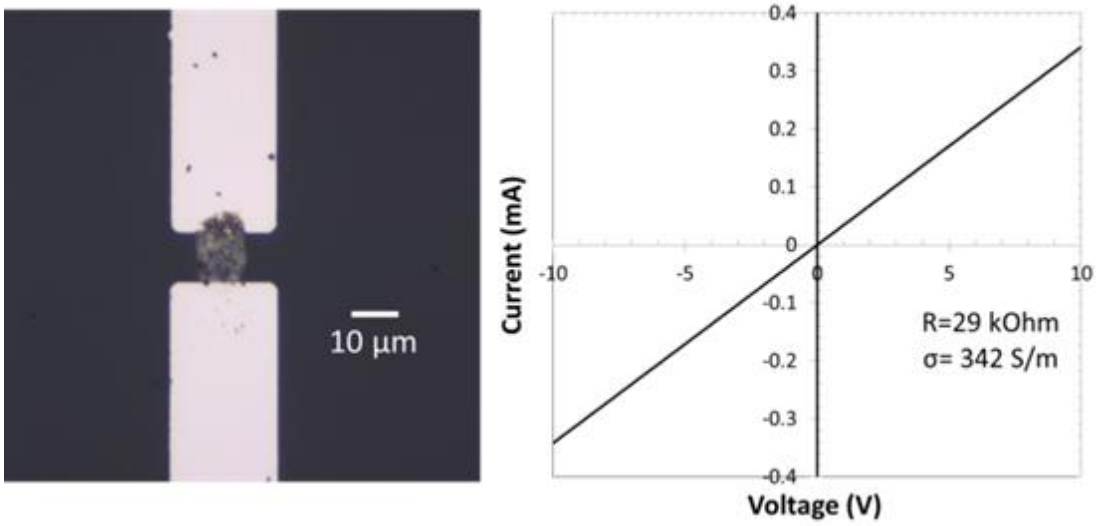

Figure 4-13: Confirming the electrical conductivity of DPN printed platinum; (Left) bright field optical micrograph of a DPN printed platinum spot connecting two planar electrodes (fabricated by photolithography); (Right) The current voltage response of the deposited feature confirms the ohmic behaviour of the platinum. The resistance of the patterned feature was measured at 342 S/m. A meaningful conductivity of the material is difficult to extract from this 2 point probe measurement, however, as the contact resistance is unknown.

Mapping electrochemical activity of platinum features by scanning electrochemical microscopy (SECM)

Scanning electrochemical microscopy (SECM) uses a scanning micro-electrode tip to measure local electrochemical activity.[67] In order to confirm the electrochemical activity of DPN printed platinum, we ran SECM scans of platinum dots on an ITO substrate. Figure 4-14 shows AFM scans of DPN printed Pt dot arrays (i.e. after plasma reduction) and the corresponding SECM current maps. Electrochemical activity is generally much higher around the printed platinum features than on the surrounding ITO substrate.

When two microelectrodes are placed close enough together (i.e. closer than the Debye length—about ten times the electrode diameter), their electric double layers can overlap, causing them to act like one large electrode. The threshold for this capacitive overlap of neighbouring Pt

features can be visualized by SECM. The dot arrays printed at a pitch of 5 µm and 10 µm (Figure 4-14 (B) and (C) respectively) act as single, square shaped electrodes of dimension 50 x 50 µm, despite being composed of much smaller individual Pt features. The SECM scan of the 20 µm pitch Pt dot array, however, shows nine current peaks, each corresponding to a single DPN printed dot (Figure 4-14 (D)).

The magnitude of the local SECM measured current has some correlation with the size of the Pt dot. Figure 4-15 plots both the dot surface area and dot volume (as measured by AFM) vs the local peak SECM current. A quantitative correlation between these parameters is difficult to extract empirically, however, as there is still some overlap of electrochemical activity between neighbouring features. This overlap in activity makes the local current measured for the middle dot in the 3x3 array, for example, exhibit an artificially large SECM current due to the influence of neighbouring dots.

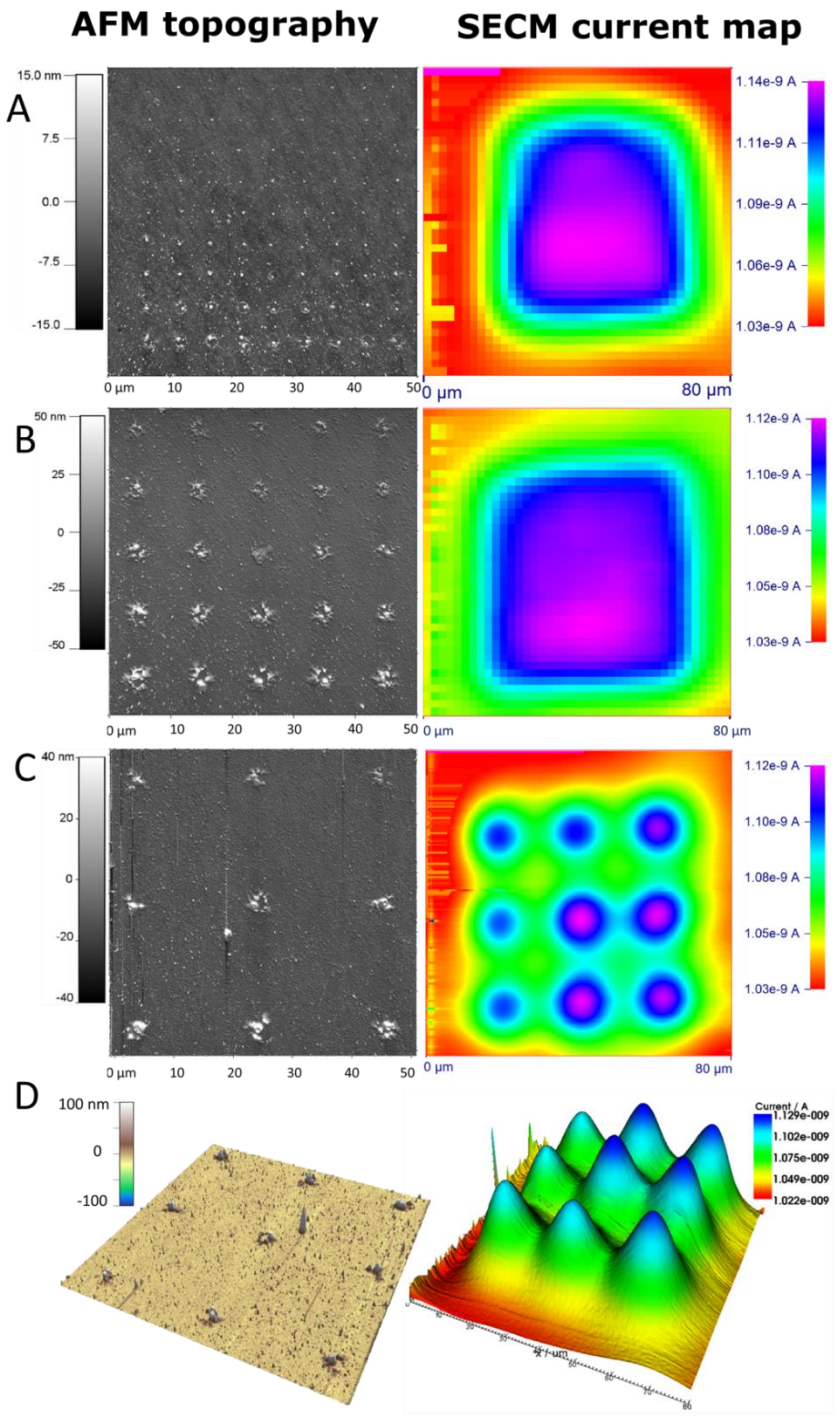

Figure 4-14: AFM topography and SECM current maps of Pt metal dot arrays on ITO glass. (Note: AFM images are 50 x 50 µm scans, while SECM images are 80 x 80 µm scans): A) AFM topography (left hand image) and SECM current maps (right hand image) for 81 Pt features of 2 µm diameter at a 5 µm pitch. The SECM current map shows the square-shaped outline of the whole array as the current signals overlap. B) AFM topography (left hand image) and SECM current map (right hand image) for 25 Pt features of ~5 µm diameter at a 10 µm pitch. Again, the ratio of pitch to feature

diameter is small and so the electrodes appear as on large electrode in the SECM scan; C) AFM topography (left hand image) and SECM current map (right hand image) for 9 Pt features of ~5 µm diameter at a 20 µm pitch. In this case the SECM detects distinct peaks corresponding to each printed platinum feature. D) 3D rendered AFM topography and SECM current map for the dot array shown in (C). [SECM experiment was performed in aqueous 0.1M KCl with 1mM ferrocenemethanol 1mM as redox mediator.]

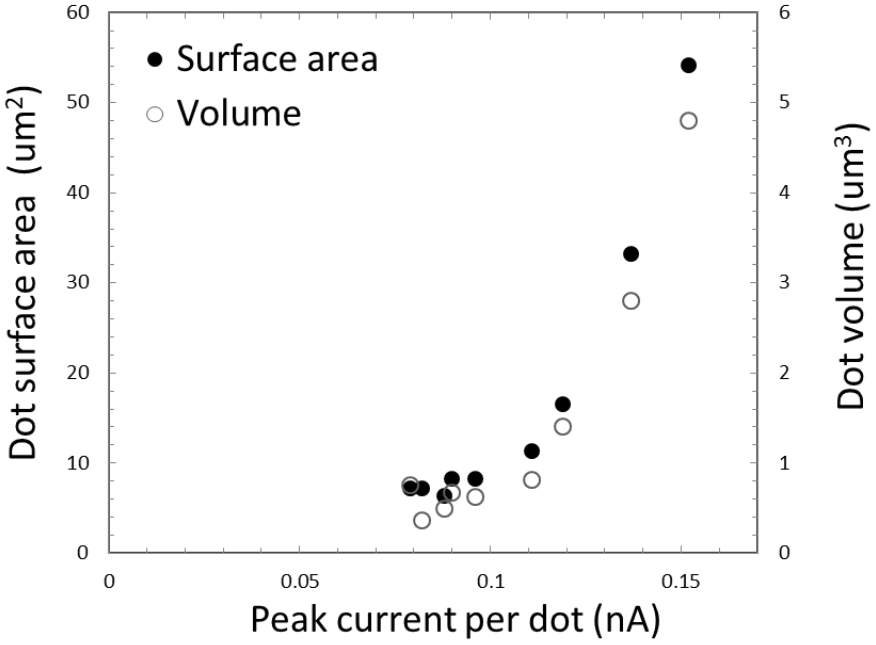

Figure 4-15: Relationship between Pt feature size and corresponding local maximum SECM current (i.e. current measured above each individual platinum feature), taken from a similar 3x3 dot array as shown in Figure 4-14 (D). The plot reveals a correlation between Pt feature-size and the corresponding current generated.

4.4 Conclusions

A liquid ink formulation has been developed to DPN print platinum features by deposition of the precursor H_2PtCl_6 in ethylene glycol, which acts as both ink carrier and reducing agent. Reduction of the precursor to metal was facilitated under mild, non-destructive conditions via a novel nitrogen plasma treatment, as supported by EDS and XRD measurements. The methodology was versatile enough to print on a range of flexible substrates

including PDMS and Parylene C with strong attachment of the platinum patterns. Ohmic conductivity of the printed platinum features was confirmed by two point measurement, and electrochemical activity by SECM. However, conductive lines could not be fabricated by this approach, limiting its application in the printing of wires and circuits. Further work could investigate the selective functionalization of a substrate to control wetting, and thus confine the ink to stable line patterns. The deposition rate of the ink was strongly dependent on the volume of ink on the cantilever, with minimum feature size of ~50 nm diameter. Several DPN strategies for printing gold features on insulating substrates have been developed, however strategies for printing platinum are lacking (Table 4-1). Although DPN printing of a platinum precursor was reported by Crocker et al., the reduction step required high temperature annealing and limited characterisation of the resulting features was performed.[44] In particular, the simplicity of our approach and the mild nature of the reduction strategy allow for the versatility to pattern on a wide variety of substrates. To demonstrate this, the 48% H_2PtCl_6/EG ink was also DPN printed on a strand of human hair (Appendix 4.5.4). Nitrogen plasma treatment reduced the printed features to platinum *in situ*, without damaging the hair.

In addition, we also developed a unique strategy to direct-write platinum micro-snowflake structures. There has been considerable interest in the synthesis of novel, high surface area noble metal nanoparticles and assemblies for catalytic and other applications.[68,69] Fractal-like electrodes are also being explored as cell-stimulation electrodes for retinal implants, as pioneered by the Taylor group at the University of Oregon.[70,71] The group argue that, by using electrodes which mimic the fractal dimension of retinal neurons (~1.7), the electrode-cell interface can be maximised. The fractal shape also allows for a high transmission of light while still achieving the charge injection capacity of a larger electrode, particularly when the branches of the fractal are <100 nm in width.[70]

The methods used to synthesise dendritic assemblies range from nanocluster deposition,[72] electrodeposition on macro-electrodes[73] and wet-chemistry using surfactants or capping agents.[68,74,75] Our approach is fundamentally different from previous methods as it is electroless, allowing deposition on insulating substrates, and also site-specific. DPN deposition determines the position of the ink droplet with nanometre registry, where ink spreading and precursor diffusion lead to the formation of a micro-snowflake. Thus patterns are formed by a method which is simultaneously top-down (direct write) and bottom-up (self assembly). This unique capability may enabling, for example, the individual placement of platinum micro-snowflakes as elements within prefabricated circuitry.

4.5 Appendix

4.5.1 Meniscus method printing of H2PtCl6

DPN printing was also attempted by direct meniscus transport of the dried H_2PtCl_6 salt. Confinement of the dried salt to the DPN tip was difficult to achieve, however. Figure 4-16 shows SEM micrographs of several DPN tips inked with aqueous H_2PtCl_6 then allowed to dry. In all cases the salt crystals formed predominantly towards the back of the cantilever, rather than at the tip.

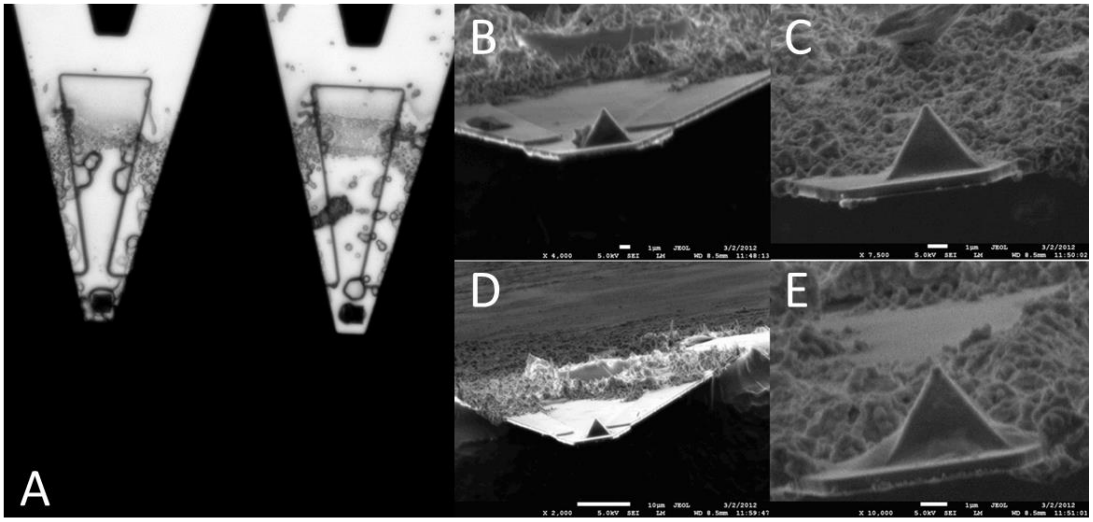

Figure 4-16: Drying of H_2PtCl_6 crystals on DPN pens after inking in water based ink: A) Optical micrograph of two pens which have been inked in H_2PtCl_6 40% wt solution in water using Nanoink inkwells. The H_2PtCl_6 crystals have dried predominantly at the back of the cantilever, with some located around the base of the tip itself; B) to E) SEM micrographs of four different DPN pens all inked with the same solution in the same way. In all cases the crystals predominantly form at the back of the cantilever. In no case do salt crystals form at the apex of the tip (where the water meniscus forms at contact with a surface).

4.5.2 Addition of ink stabilizers to improve DPN printing lifetime

We saw above that the addition of even a small percentage of longer chain polymers (e.g. PEG) to the H2PtCl6/EG solution had the effect of inhibiting the N_2 plasma reduction of the drop-cast solution to Pt metal (see Table 4-5). The relevant literature cites an 'incomplete pyrolysis' of the larger molecules as the likely mechanism of this inhibition [block-copolymer lit].

Dropcast films

Soln #	*Precursor*	*Precursor loading (% wt)*	*Solvent*	*Ink Stabilizer*	*Stabilizer loading (% wt)*	*Plasma Time*	*Reduction?*
1	$H_2PtCl_6.xH_2O$	10	EG	Glycerol	10	10 min	NO
2	$H_2PtCl_6.xH_2O$	10	EG	Glycerol	10	40 min	NO
3	$H_2PtCl_6.xH_2O$	10	EG	PEG-PPG	10	10 min	NO
4	$H_2PtCl_6.xH_2O$	10	EG	PEG-PPG	10	40 min	~edges
5	$H_2PtCl_6.xH_2O$	10	EG	PEG-PPG	10	10 min	NO
6	$H_2PtCl_6.xH_2O$	10	EG	PEG-PPG	10	40 min	~edges
7	$H_2PtCl_6.xH_2O$	10	EG	PEG 200	10	10 min	NO
8	$H_2PtCl_6.xH_2O$	10	EG	PEG 200	10	10 min	NO
9	$H_2PtCl_6.xH_2O$	10	EG	PVA	4	10 min	~edges
10	$H_2PtCl_6.xH_2O$	4	H_2O	Glycerol	10	10 min	NO
11	$H_2PtCl_6.xH_2O$	4	H_2O	PEG-PPG	10	10 min	NO
12	$H_2PtCl_6.xH_2O$	4	H_2O	Triton-X	10	10 min	NO

Table 4-5: Plasma treatment of drop-cast H_2PtCl_6 solutions containing various ink stabilizers.

DPN printed patterns

But does this inhibition effect hold at massively reduced scales? A DPN printed feature has a huge relative surface area compared to a dropcast film, and so the relative heating, caused by the plasma, and the relative penetration of reducing species should be vastly increased.

For this experiment, we printed 6 different inks incorporating various additives which may function as ink stabilizing agents. Glycerol and PEG are viscous and non-volatile ink additives which are extensively used as

carriers in DPN liquid ink transport. Trehalose is a well known natural antifreeze agent.

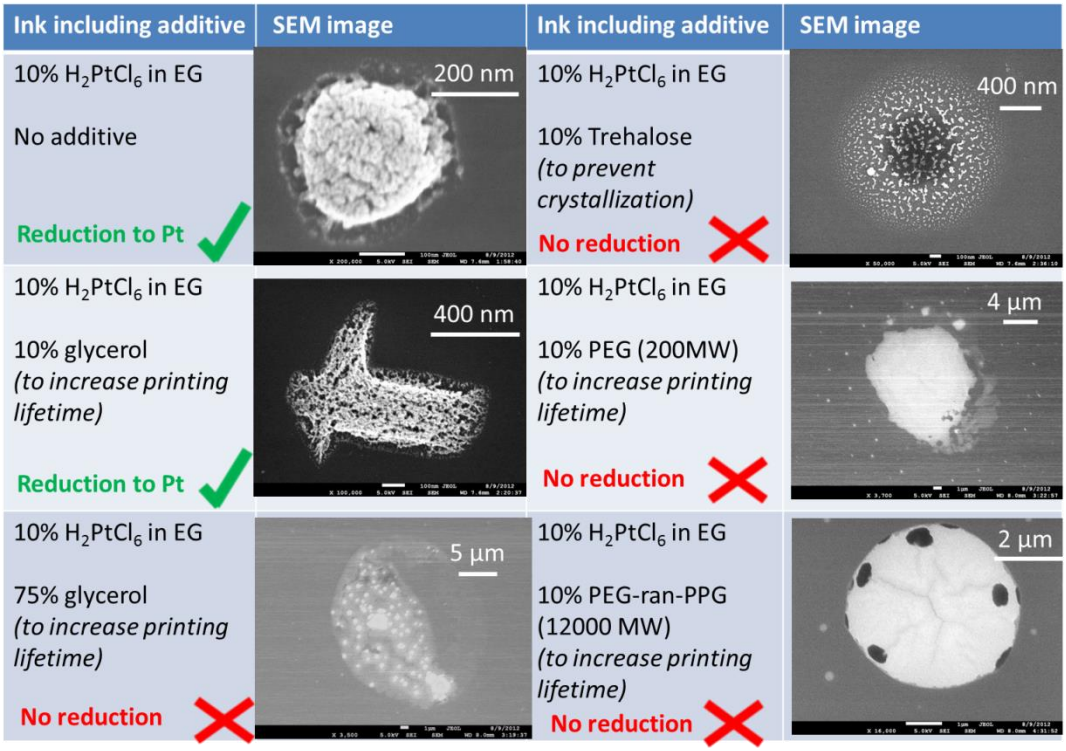

Figure 4-17: DPN printing and plasma reduction of H_2PtCl_6 EG solutions containing various stabilizing agents. Of the inks containing thickening agents, only the 10% wt glycerol ink was reduced.

Similarly to drop-cast films, most additives had the effect of inhibiting reduction of H_2PtCl_6 at the scale of single dots (as determined by EDS measurements). Besides the control solution, only the ink containing 10% wt glycerol was still reduced to Pt metal. This ink, however, did not generate uniform circular features but formed random shapes (such as the 'hammer' shown above). Even the PEG 200 additive (an oligomer composed of just three ethylene glycol units) inhibited reduction. All further work to proceed with simpler H2PtCl6 in EG system with no thickening additives.

4.5.3 DPN printing of H2PtCl6/EG ink on hydrophilic Si and glass

We attempted to print a range of H_2PtCL_6/EG formulations on hydrophilic (plasma treated) Si, however these experiments did not yield discernible features. Due to the strong affinity of the ink for the substrate (contact angle ~0°) any deposited ink wetted the substrate completely and the H_2PtCl_6 was spread diffusely over the wetted area. AFM images of the patterned area revealed a random distribution of micron scale particles (not shown). The extent of the spreading was not visible until a similar experiment was performed on plasma treated glass and then imaged with dark-field microscopy (Figure 4-18).

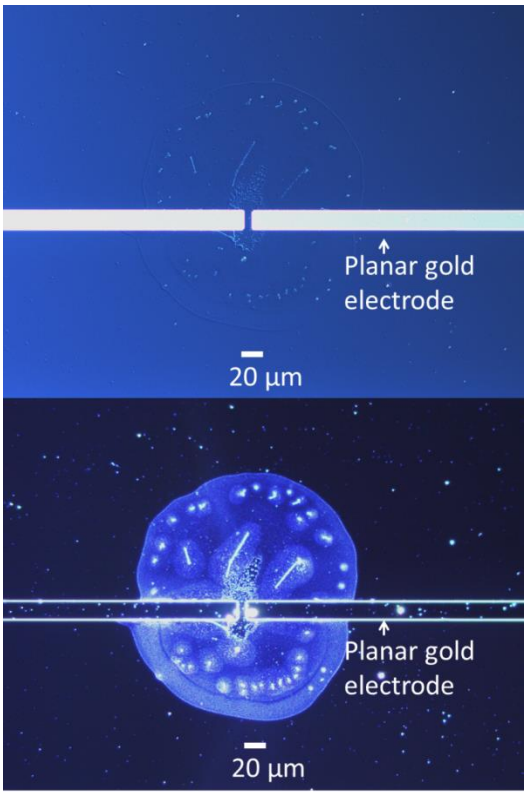

Figure 4-18: DPN printing of H_2PtCl_6/EG between planar gold electrodes on plasma treated glass. The top image shows an optical bright field micrograph of a 48% H_2PtCl_6 ink feature printed between two gold microelectrodes (dwell time 5s). The bottom image shows the corresponding dark-field micrograph. The high affinity of ink for the

substrate caused the ink on the cantilever to flood out and completely wet the substrate. H_2PtCl_6 crystals were deposited diffusely over a 100 µm radius.

4.5.4 Printing a precursor solution and reducing to platinum metal *in situ* on a human hair

In order to demonstrate the versatility of our platinum precursor ink formulation, and the mild conditions under which reduction of the printed features takes place, we DPN printed a single platinum feature on a strand of human hair.

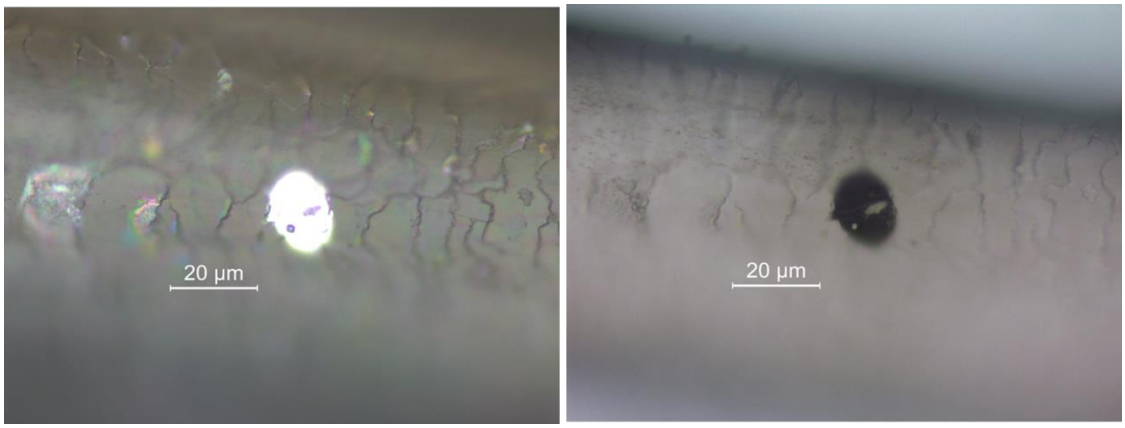

Figure 4-19: A single dot of 48% wt H_2PtCl_6 solution DPN printed onto a human hair after treatment with N_2 plasma (10 minutes). A) Bright field optical miscroscopy shows the bright silvery/white colour of the platinum feature after plasma assisted reduction; B) Transmitted light optical microscopy shows the opacity of the dense metal contrasted with the relative transparency of the hair.

4.5.5 Line printing of H_2PtCl_6/EG inks using polymer pen lithography

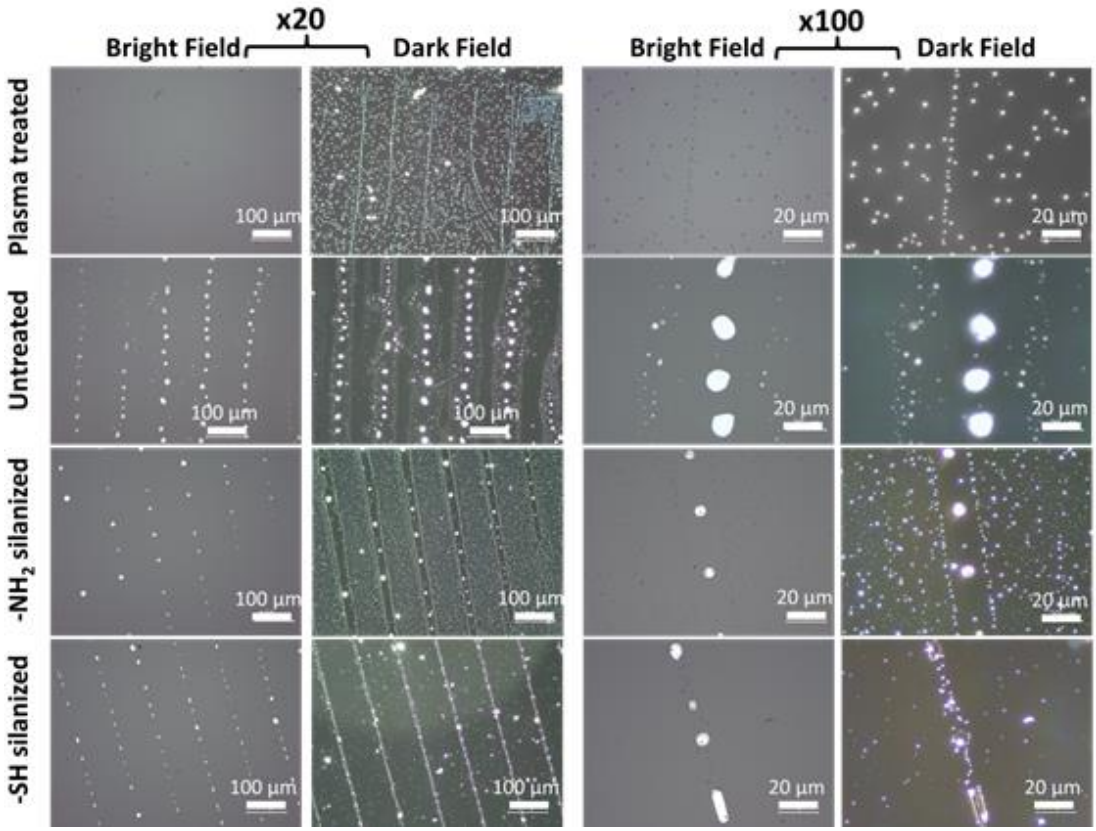

Figure 4-20: Optical micrographs of platinum line patterns printed on 4 different glass substrates (untreated glass, plasma treated glass, amine silanized glass and mercapto silanized glass). The patterns were prepared by printing a 10% wt H_2PtCl_6in EG solution using line-patterned polymer pen lithography (PPL) followed by reduction in nitrogen plasma (10 min, 1100 mTorr) within 10 minutes of printing. All printed features, regardless of substrate, beaded into dots, and so no continuous line patterns of platinum could be formed.

4.6 References

1. Moulton, S. E., Higgins, M. J., Kapsa, R. M. I. & Wallace, G. G. Organic Bionics: A New Dimension in Neural Communications. *Adv. Funct. Mater.* **22,** 2003–2014 (2012).

2. Cooper, D. R. & Nadeau, J. L. Nanotechnology for in vitro neuroscience. *Nanoscale* **1,** 183–200 (2009).

3. Dvir, T., Timko, B. P., Kohane, D. S. & Langer, R. Nanotechnological strategies for engineering complex tissues. *Nat. Nanotechnol.* **6,** 13–22 (2011).

4. Niadecki, N. A. J. S., Esai, R. A. V. I. A. D., Uiz, S. A. M. I. A. L. O. M. R. & Hen, C. H. S. C. Nanotechnology for Cell – Substrate Interactions. **34,** 59–74 (2006).

5. Brushart, T. M. *et al.* Electrical Stimulation Promotes Motoneuron Regeneration without Increasing Its Speed or Conditioning the Neuron. **22,** 6631–6638 (2002).

6. Al-majed, A. A., Neumann, C. M., Brushart, T. M. & Gordon, T. Brief Electrical Stimulation Promotes the Speed and Accuracy of Motor Axonal Regeneration. **20,** 2602–2608 (2000).

7. Clark, G. M. The multiple-channel cochlear implant: the interface between sound and the central nervous system for hearing, speech, and language in deaf people-a personal perspective. *Philos. Trans. R. Soc. Lond. B. Biol. Sci.* **361,** 791–810 (2006).

8. Wallace, G. G., Moulton, S. E. & Clark, G. M. Applied physics. Electrode-cellular interface. *Science* **324,** 185–6 (2009).

9. Velasco, A. L. *et al.* Electrical stimulation of the hippocampal epileptic foci for seizure control: a double-blind, long-term follow-up study. *Epilepsia* **48,** 1895–903 (2007).

10. Nicolelis, M. a. Actions from thoughts. *Nature* **409,** 403–7 (2001).

11. Lebedev, M. a & Nicolelis, M. a L. Brain-machine interfaces: past, present and future. *Trends Neurosci.* **29,** 536–46 (2006).

12. Patolsky, F. *et al.* Detection, stimulation, and inhibition of neuronal signals with high-density nanowire transistor arrays. *Science* **313,** 1100–4 (2006).

13. Schmid, G. in *Nanotechnology. Vol. 1 Princ. Fundam.* (Schmid, G.) **1,** 3–39 (2008).

14. Cogan, S. F. Neural stimulation and recording electrodes. *Annu. Rev. Biomed. Eng.* **10,** 275–309 (2008).

15. Gates, B. D. *et al.* New approaches to nanofabrication: molding, printing, and other techniques. *Chem. Rev.* **105,** 1171–96 (2005).

16. Rehfeldt, F., Engler, A. J., Eckhardt, A., Ahmed, F. & Discher, D. E. Cell responses to the mechanochemical microenvironment--implications for regenerative medicine and drug delivery. *Adv. Drug Deliv. Rev.* **59,** 1329–39 (2007).

17. Discher, D. E., Janmey, P. & Wang, Y. Tissue Cells Feel and Respond to the Stiffness of Their Substrate. *Science (80-.).* **1139,** (2009).

18. Rehfeldt, F., Engler, A. J. & Discher, D. E. Stem Cells and Nanomedicine : Nanomechanics of the Microenvironment. *Stem Cells* **5,** (2009).

19. Okinaka, Y. & Wolowodiuk, C. in *Electroless Plat.* 421–440 (William Andrew Publishing, 1990).

20. *The Chemistry Of Inkjet Inks*. (World Scientific Publishing Co., 2009).

21. Walker, S. B. & Lewis, J. a. Reactive silver inks for patterning high-conductivity features at mild temperatures. *J. Am. Chem. Soc.* **134,** 1419–21 (2012).

22. Basnar, B. & Willner, I. Dip-pen-nanolithographic patterning of metallic, semiconductor, and metal oxide nanostructures on surfaces. *Small* **5,** 28–44 (2009).

23. Ali, M. Ben, Ondarc, T., Brust, M. & Joachim, C. Atomic Force Microscope Tip Nanoprinting of Gold Nanoclusters. 872–876 (2002).

24. Garno, J. C. *et al.* Precise Positioning of Nanoparticles on Surfaces Using Scanning Probe Lithography. *Nano Lett.* **3,** 389–395 (2003).

25. Wiechmann, M. *et al.* Nanoscale lines of supported nanogold particles and lysozyme–nanogold conjugates generated by atomic force microscopy in aqueous solution. *Surf. Interface Anal.* **38,** 1004–1009 (2006).

26. Wu, B., Ho, A., Moldovan, N. & Espinosa, H. D. Direct deposition and assembly of gold colloidal particles using a nanofountain probe. *Langmuir* **23,** 9120–3 (2007).

27. Wang, W. M., Stoltenberg, R. M., Liu, S. & Bao, Z. Direct patterning of gold nanoparticles using dip-pen nanolithography. *ACS Nano* **2,** 2135–42 (2008).

28. Wang, H. *et al.* Toward conductive traces: Dip Pen Nanolithography® of silver nanoparticle-based inks. *Appl. Phys. Lett.* **93,** 143105 (2008).

29. Hung, S. *et al.* Dip Pen Nanolithography of Conductive Silver Traces. *J. Phys. Chem. C* **114,** 9672–9677 (2010).

30. Nelson, B. a., King, W. P., Laracuente, a. R., Sheehan, P. E. & Whitman, L. J. Direct deposition of continuous metal nanostructures by thermal dip-pen nanolithography. *Appl. Phys. Lett.* **88,** 033104 (2006).

31. Maynor, B. W., Li, Y. & Liu, J. Au “Ink” for AFM “Dip-Pen” Nanolithography. *Langmuir* **17,** 2575–2578 (2001).

32. Porter, L. a. *et al.* Electroless Nanoparticle Film Deposition Compatible with Photolithography, Microcontact Printing, and Dip-Pen Nanolithography Patterning Technologies. *Nano Lett.* **2,** 1369–1372 (2002).

33. Li, Y., Maynor, B. W. & Liu, J. Electrochemical AFM “Dip-Pen” Nanolithography. *J. Am. Chem. Soc.* **123,** 2105–2106 (2001).

34. Cai, Y. & Ocko, B. M. Electro pen nanolithography. *J. Am. Chem. Soc.* **127,** 16287–91 (2005).

35. Barsotti, Jr., R. J. & Stellacci, F. Chemically directed assembly of monolayer protected gold nanoparticles on lithographically generated patterns. *J. Mater. Chem.* **16,** 962 (2006).

36. Zhang, H., Jin, R. & Mirkin, C. A. Synthesis of Open-Ended, Cylindrical Au−Ag Alloy Nanostructures on a Si/SiO x Surface. *Nano Lett.* **4,** 1493–1495 (2004).

37. Salaita, K. S., Lee, S. W., Ginger, D. S. & Mirkin, C. a. DPN-generated nanostructures as positive resists for preparing lithographic masters or hole arrays. *Nano Lett.* **6,** 2493–8 (2006).

38. Lee, W.-K., Chen, S., Chilkoti, A. & Zauscher, S. Fabrication of gold nanowires by electric-field-induced scanning probe lithography and in situ chemical development. *Small* **3,** 249–54 (2007).

39. Basnar, B., Weizmann, Y., Cheglakov, Z. & Willner, I. Synthesis of Nanowires Using Dip-Pen Nanolithography and Biocatalytic Inks. *Adv. Mater.* **18,** 713–718 (2006).

40. Weinberger, D. A., Hong, S., Mirkin, C. A., Wessels, B. W. & Higgins, T. B. Combinatorial Generation and Analysis of Nanometer- and Micrometer-Scale Silicon Features via “Dip-Pen” Nanolithography and Wet Chemical Etching. *Adv. Mater.* **12,** 1600–1603 (2000).

41. Huo, F. *et al.* Polymer pen lithography. *Science* **321,** 1658–60 (2008).

42. Zheng, Z., Yang, M., Liu, Y. & Zhang, B. Direct patterning of negative nanostructures on self-assembled monolayers of 16-mercaptohexadecanoic acid on Au(111) substrate via dip-pen nanolithography. *Nanotechnology* **17,** 5378–5386 (2006).

43. Chai, J. *et al.* Scanning probe block copolymer lithography. *Proc. Natl. Acad. Sci. U. S. A.* **107,** 20202–6 (2010).

44. Crocker Jr, P. V., Demers, L. & Amro, N. A. Processes for fabricating conductive patterns using nanolithography as a patterning tool. **10647430,** (2006).

45. Sung, M. G., Lee, T.-Y., Kim, B., Kim, T. H. & Hong, S. Uniform patterning of sub-50-nm-scale Au nanostructures on insulating solid substrate via dip-pen nanolithography. *Langmuir* **26,** 1507–11 (2010).

46. Jang, J.-W. *et al.* Generation of metal photomasks by dip-pen nanolithography. *Small* **5,** 1850–3 (2009).

47. Zhang, H. & Mirkin, C. A. DPN-Generated Nanostructures Made of Gold, Silver, and Palladium. *Chem. Mater.* **16,** 1480–1484 (2004).

48. Sugimura, H., Hozumi, A., Kameyama, T. & Takai, O. Organosilane self-assembled monolayers formed at the vapour/solid interface. *Surf. Interface Anal.* **34,** 550–554 (2002).

49. Li, H. *et al*. Graphene oxide scrolls on hydrophobic substrates fabricated by molecular combing and their application in gas sensing. *Small* **9,** 382–6 (2013).

50. Schweizer, A. E. & Kerr, G. T. Thermal decomposition of hexachloroplatinic acid. *Inorg. Chem.* **17,** 2326–2327 (1978).

51. Cho, S. J. & Ouyang, J. Attachment of Platinum Nanoparticles to Substrates by Coating and Polyol Reduction of A Platinum Precursor. *J. Phys. Chem. C* **115,** 8519–8526 (2011).

52. Komarneni, S., Li, D., Newalkar, B., Katsuki, H. & Bhalla, A. S. Microwave−Polyol Process for Pt and Ag Nanoparticles. *Langmuir* **18,** 5959–5962 (2002).

53. Larcher, D. & Patrice, R. Preparation of Metallic Powders and Alloys in Polyol Media: A Thermodynamic Approach. *J. Solid State Chem.* **154,** 405–411 (2000).

54. Jaramillo, T. F., Baeck, S., Cuenya, B. R. & McFarland, E. W. Catalytic activity of supported Au nanoparticles deposited from block copolymer micelles. *J. Am. Chem. Soc.* **125,** 7148–9 (2003).

55. Liu, G. *et al*. Delineating the pathways for the site-directed synthesis of individual nanoparticles on surfaces. *Proc. Natl. Acad. Sci. U. S. A.* **110,** 887–91 (2013).

56. Blin, B., Fievet, F., Beaupere, D. & Figlarz, M. Double oxidation of glycol ethylene in a new process of powder metallurgy elaboration. *New J. Chem.* **13,** 67–72 (1989).

57. Deegan, R. D., Bakajin, O. & Dupont, T. F. Capillary flow as the cause of ring stains from dried liquid drops. *Nature* 827–829 (1997). doi:10.1038/39827

58. Shen, X., Ho, C.-M. & Wong, T.-S. Minimal size of coffee ring structure. *J. Phys. Chem. B* **114,** 5269–74 (2010).

59. Manandhar, P., Jang, J., Schatz, G. C., Ratner, M. A. & Hong, S. Anomalous Surface Diffusion in Nanoscale Direct Deposition Processes. **1,** 1–4 (2003).

60. Witten, T. & Sander, L. Diffusion-limited aggregation. *Phys. Rev. B* **27,** 5686–5697 (1983).

61. Halsey, T., Meakin, P. & Procaccia, I. Scaling structure of the surface layer of diffusion-limited aggregates. *Phys. Rev. Lett.* **56,** 854–857 (1986).

62. Uwaha, M. & Saito, Y. Fractal aggregation and dendritic crystal growth. *J. Cryst. Growth* **99,** 175–178 (1990).

63. Sun, K., Fan, B. & Ouyang, J. Nanostructured Platinum Films Deposited by Polyol Reduction of a Platinum Precursor and Their Application as Counter Electrode of Dye-Sensitized Solar Cells. *J. Phys. Chem. C* **114,** 4237–4244 (2010).

64. Nakashima, H., Higgins, M. J., O'Connell, C., Torimitsu, K. & Wallace, G. G. Liquid deposition patterning of conducting polymer ink onto hard and soft flexible substrates via dip-pen nanolithography. *Langmuir* **28,** 804–11 (2012).

65. De Gennes, P.-G., Brochard-Wyart, F. & Quéré, D. *Capillarity and Wetting Phenomena: drops, bubbles, pearls, waves*. (Springer, 2003).

66. Checco, A., Gang, O. & Ocko, B. Liquid Nanostripes. *Phys. Rev. Lett.* **96,** 056104 (2006).

67. Amemiya, S., Bard, A. J., Fan, F.-R. F., Mirkin, M. V & Unwin, P. R. Scanning electrochemical microscopy. *Annu. Rev. Anal. Chem. (Palo Alto. Calif).* **1,** 95–131 (2008).

68. Pang, S., Kondo, T. & Kawai, T. Formation of Dendrimer-like Gold Nanoparticle Assemblies. *Chem. Mater.* **17,** 3636–3641 (2005).

69. Song, Y. *et al.* Controlled synthesis of 2-D and 3-D dendritic platinum nanostructures. *J. Am. Chem. Soc.* **126,** 635–45 (2004).

70. Taylor, R. Vision of beauty. *Phys. World* (2011).

71. Taylor, R. Fractal interconnects for neuro-electronic interfaces, including artificial retina. (2011). at < http://icoregon.technologypublisher.com/technology/6947>

72. Zenkevich, A. *et al.* Formation of Au fractal nanoclusters during pulsed laser deposition on highly oriented pyrolitic graphite. *Phys. Rev. B* **65,** 073406 (2002).

73. Li, Y., Xian, H. & Zhou, Y. Formation of platinum nanoflowers on 3-aminopropyltriethoxysilane monolayer: Growth mechanism and electrocatalysis. *Appl. Catal. A Gen.* **401,** 226–232 (2011).

74. Sun, X. & Hagner, M. Novel preparation of snowflake-like dendritic nanostructures of Ag or Au at room temperature via a wet-chemical route. *Langmuir* **23,** 9147–50 (2007).

75. Franc, G. *et al.* Dendritic structures within dendritic structures: dendrimer-induced formation and self-assembly of nanoparticle networks. *Nanoscale* **1,** 233–7 (2009).

Chapter 5: Deposition monitoring and control of feature size in liquid ink DPN

*Part of this chapter, including figures 5-2 to 5-10, is reprinted with permission from O'Connell, C.D., Higgins, M. J., Marusic, D., Moulton, S. E. & Wallace, G. G. Liquid ink deposition from an atomic force microscope tip: deposition monitoring and control of feature size, *Langmuir doi:10.1021/la402936z*, copyright (2013) American Chemical Society.

5.1 Introduction

Confidence in any fabrication technique is built upon its ability to faithfully reproduce the user's design. Dip-pen nanolithography is unique in its ability to 'direct-write' arbitrary patterns of molecular inks at a nanometre scale.[1] Control of feature-size, and therefore pattern fidelity, arises from an empirical understanding of the rate of deposition over a range of 'dwell times' for dot printing or 'write-speeds' for line writing.[2,3] Reproducibility is garnered by understanding how deposition rate is influenced by a multitude of other critical parameters including ink loading,[4] tip sharpness,[5] relative humidity,[3] temperature,[6] surface roughness,[7] molecular diffusivity and dissolution kinetics[8] and others. The mechanism of molecular transport has been given a solid theoretical framework[9] and progress in refining the technique has become a lively conversation

involving the interplay of experiment,[4] theory,[8,10] and numerical simulation.[7,11,12]

Recently, the DPN technique has been applied to the deposition of liquid inks.[13–19] Liquid inks are seen as attractive due to their versatility in depositing on various materials.[17] They can also be used to generate 3D structures not achievable by molecular inks, such as spherical cap lenses for subwavelength optical lithography[18] or for the molded fabrication of stamps.[19] Liquid inks have also been exploited as universal 'ink-carriers' for functional materials or biological molecules.[15] Several liquid inks have been commercialized by Nanoink Inc.,[20] and the company also sell a DPN pen (the M-type probe) specifically fabricated with a reservoir etched into the underside of the cantilever to hold liquid and therefore increase printing lifetime. The stringent control of feature size, however, is challenging in liquid DPN. For example, it is necessary to 'bleed' the pen of excess ink before reproducible deposition is obtained.[13,14,17] Even after bleeding, the coefficient of variation in dot diameter is often quoted at between 10-15%.[21,22] A 10% variation in diameter would correspond to a 21% variation in feature area, and a 33% variation in feature volume (from spherical cap geometry).

Several examples extant in the published literature exhibit the relatively poor control of feature size achieved thusfar in liquid ink DPN. Figure 5-1 shows a selection of images collated from recent peer-reviewed literature of dot arrays generated by liquid ink DPN. Figure 5-1 (A) shows a fluorescence image of fluorescence-dye-labeled PEG hydrogels printed by researchers at Nanoink Inc.[23] The hydrogel dot arrays exhibit considerable variation in dot size, and this fluorescence intensity, even within the same grid of 4 x 4 dots. Figure 5-1 (B) shows AFM topographical images of PDMS droplets on SiO_2.[19] The 3D rendered image at right highlights the variation in dot height (hence dot volume) across a small area of printed features. Figure 5-1 (C) shows dot arrays of agarose gels printed by the Mirkin group.[15] The left hand image shows a fluorescence image of an array of

agarose dots incorporating Alexa Fluor 594 labeled CT. Although all features were printed using the same dwell time, a considerable variation in fluorescence (i.e. dot size) is evident. In particular, the dot size appears to vary in a row-by-row basis. The size of the dots near the bottom of the array (printed first) appear to be typically larger than those at the top. The right hand image shows the same array after probing with Alexa Fluor 488-labeled anticholera toxin. In this case, the variation in fluorescence intensity is even greater. Smaller printed dots (at left) have much lower fluorescence intensity (at right). This indicates that the variation in size of printed dots may affect the probability of antibody binding, with significant implications for the use of DPN nanoarrays as biomolecule screening assays.

In these published examples, and others, the origin of the non-uniformity exhibited by the deposited features is not discussed.

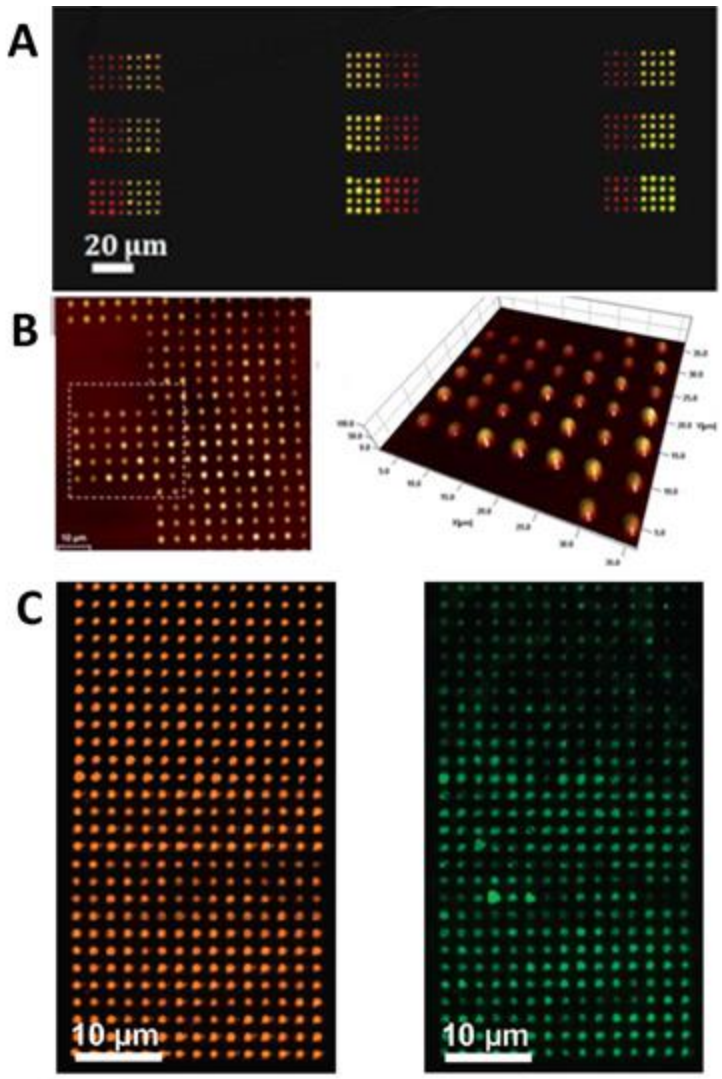

Figure 5-1: The large variation in feature size prevalent in existing literature. (A) shows a fluorescence image of arrays of fluorescence-dye-labeled PEG hydrogels printed by researchers at Nanoink Inc.[23] The hydrogel dot arrays exhibit considerable variation in dot size, even within the same grid of 4 x 4 dots. [Copyright © 2010 Wiley Periodicals, Inc. Adapted with permission.] (B) shows AFM topographical images of PDMS droplets on SiO_2.[19] The 3D rendered image at right highlights the variation in dot height (hence dot volume) across a small area of printed features. [Adapted from Ref 19 with permission of The Royal Society of Chemistry.] (C) Flourescence images DPN printed agarose gel used as a protein carrier by the Mirkin group.[15] The left hand image shows an array of agarose dots incorporating Alexa Fluor 594 labeled CT. The dots were patterned beginning with the lower left and moving right, then up to the next row and left, in a snake-like pattern. Although all features were printed with the same dwell time, a considerable variation in fluorescence (i.e. dot size) is evident. The right hand image shows the same array after probing with Alexa Fluor 488-labeled

anticholera toxin. In this case, the variation in fluorescence intensity is even greater. [Adapted with permission from ACS nano 3, 2394–402. Copyright (2009) American Chemical Society.] [15]

The explanation of such printing aberrations is made difficult because, as opposed to molecular ink DPN, a solid framework of understanding does not presently exist for DPN of liquid inks. In particular, although the driving force for deposition has been described as arising from 'physioadsorption' or 'capillarity',[13,14] this mechanism has not been quantitatively treated. The relative effects of ink properties such as viscosity and surface tension are also poorly understood. A model describing the rate of flow of ink onto the substrate (dwell-time dependence) has not been presented. When discussing liquid ink deposition, some groups have continued to use the language ('diffusion coefficient') and analysis procedures for molecular ink DPN, despite the patently different structure of resulting features (i.e. spherical caps as opposed to two-dimensional circles).[15,16]

Although explicit studies of liquid ink DPN are lacking, some groups have studied the related system of liquid deposition from a nanofountain probe (or liquid nanodispenser). The key parameters in nanofountain probe deposition were found to be the aperture diameter as well as tip and substrate hydrophobicity.[24-26] In addition, extensive studies have been performed to measure the capillary forces between a tip coated in liquid and a surface.[27,28] This system is highly pertinent to many fields as the nanoscale tip provides a 'model asperity' for studying the fundamental origins of adhesion, wear and lubrication.[29,30] A summary of the known dependent parameters for molecular ink DPN, liquid ink DPN and nanofountain pen methods is shown in Table 5-1.

	Molecular inks	*Liquid inks*	*Nano Fountain Pen*
Mechanism of transfer	Alkanethiols are dried on the outside of the AFM tip. When the tip contacts surface, the molecules diffuse through the water meniscus which condenses between the tip and substrate	Ink held in reservoir etched into the underside of the cantilever. When in contact with substrate, liquid ink 'flows' onto substrate. When the tip retracts it distends a meniscus bridge. Deposition occurs when the meniscus bridge breaks.	Ink flows from a reservoir on top of the cantilever through a nanochannel in the AFM tip and on to the substrate. When the tip retracts it distends a meniscus bridge. Deposition occurs when the meniscus bridge breaks.
Known Dependent parameters	1. Humidity 2. Temperature 3. Ink coverage on tip 4. Dwell time/write speed 5. Kinetics of deattachment from tip 6. Solubility in meniscus 7. Molecular diffusion	1. Dwell time. Ink substrate contact angle? Surface tension? Viscosity? Humidity? Tip hydrophilicity? Retract rate? Roughness?	1. Dwell time 2. Diameter of pen aperture 3. Tip hydrophilicity 4. Ink/substrate contact angle

Table 5-1: Mechanisms of ink transfer and known dependent parameters for molecular inks, liquid ink DPN and nanofountain pen methods.

In this chapter we use model ink-substrate systems (exhibiting a range of viscosities and wettabilities) to explore various methods of controlling feature size in liquid ink DPN. We begin with a description of the model systems, including measurements of relevant liquid and substrate properties. The 'printability' of 8 ink-substrate systems is investigated. The ink-substrate interaction is quantified by means of contact angle measurements at both the macro-scopic and micro-scopic scale, revealing that the dynamics of DPN deposition may play an important role in defining feature morphology. Next, the ink-transfer mechanism is probed using AFM force measurements acquired during ink deposition. We use the information as a means to elucidate the shape of the meniscus during deposition and illustrate a method to monitor the volume of deposition *in-situ*. We study the dwell-time/dot-size relationship of various ink-substrate

systems and find that dot-size generally grows with a $r \sim t^{1/2}$ dependence. However, we find the deposition rate can change dramatically over the course of an experiment, and that the volume of ink on the pen is a critical factor in determining deposition rate.

5.2 Experimental

5.2.1 Materials

Octadecyltrimethoxysilane was obtained from Sigma Aldrich. Norland Optical Adhesives are highly viscous, UV curable, acrylic based liquid adhesives. Formulations presenting a range of viscosities (NOA 65, NOA 68, NOA 68T and NOA78) were obtained from Norland Products (Cranbury NJ, USA). Appendix 5.5.1 includes a summary of the composition of each adhesive.

5.2.2 Ink properties

Viscosity

Viscosity measurements were performed on a (shear-controlled) AR-G2 Rheometer (TA Instruments) using a cone and plate geometry at 22°C, 25°C and 30°C. The values quoted throughout the chapter are for 22°C. Additional data is shown in the Appendix.

Goniometry

Surface tension measurements were made using the pendant drop technique on an OCA Contact Angle System (Dataphysics) at 22 °C. Contact angles were measured using the sessile drop method. In the case of highly viscous liquids the contact angle was measured as a function of time after deposition, and final results determined after a 24 hour equilibration period. Measurements repeated on the same drops 48 hours and several days later indicated no further change in drop morphology. The goniometer

set-up consists of a horizontal microscope focused on the drop of interest which is illuminated by a diffuse-back light for increased contrast. A snap-shot of the drop is taken and the drop-shape is fit by the software to the Young-Laplace equation.

Density

Density measurements were performed by using a 1 ml syringe and a mass balance: small volumes of ink were repeatedly dispensed from the syringe (with accuracy +/- 0.05 ml) and the mass of the syringe remeasured. The density was calculated from the slope of the resulting mass/volume plot (n>10 for each plot). R^2 values for the slope fit were typically 0.997 or better.

5.2.3 Substrate preparation

Silicon wafer pretreatment

Si/SiOx wafers were pretreated with a generic cleaning protocol consisting of bath sonication while immersed in various solvents (acetone, isopropanol, water). This was followed by a hot piranha treatment (immersion in a freshly prepared 1:3 ratio H_2O_2:H_2SO_4 mixture for 30 minutes at 80 °C) and final rinsing with copious deionized water (Milli-Q).

Preparation of hydrophilic and hydrophobic Si substrate

Smooth, hydrophilic substrates were prepared by plasma treatment of a Si/SiOx wafer (Harrick Plasma Cleaner, O_2 or air plasma at 1100 mTorr, 10 mins) immediately prior to DPN printing. Hydrophilicity of the substrate was confirmed by water contact angle (~0°).

Smooth, hydrophobic substrates were prepared by functionalization of the Si/SiOx substrate with octadecyltrimethoxysilane (ODTMS). Briefly; after pretreatment the substrates were plasma treated (as above), then immersed in a freshly prepared solution of 0.1% ODTMS in isopropanol for 5

minutes, before a further 5 minutes on a hotplate (80 °C) for 5 minutes. The substrates were dipped in the 0.1% ODTMS/isopropanol solution and placed on the hotplate (80°C, 5 minutes) a further three times to ensure consistent levels of silanization. Hydrophobicity of the substrate was confirmed by water contact angle (~88°). This degree of hydrophobicity was maintained for several weeks as confirmed by repeated water contact angle measurements.

5.2.4 DPN methodology

DPN patterning was performed using an Nscriptor system (NanoInk, Skokie, IL) in an environment controlled at 45% relative humidity and 22°C temperature. The NOA ink of interest was wetted onto a single probe on an array of NanoInk M-Type probes (NanoInk part # PEN-0300-03, material Si3N4, length 107 µm, width 22 µm, spring constant 0.5 N/m) by dipping into the filled microwell of a NanoInk Universal Inkwell (part # IWL-0009-03). The tip was bled of excess ink in a method similar to that previously reported for DPN of liquid inks by bringing it in contact with the substrate in several (typically 4-5) locations, until deposition of large ~10 µm 'bleed-spots' ceased. Patterns were generated using the InkCAD software (v 2.7.1) provided with the Nscriptor system. Thermal resonance frequencies of probes were measured using SPM Cockpit software (Pacific Nanotechnology). For long term printing studies, up to four pens were loaded with different inks and printed simultaneously.

5.2.5 AFM measurements

AFM force curve measurements were performed in air on an Asylum MFP-3D system (Asylum Research, Santa Barbara, CA). Resonance frequencies of all cantilevers were measured using the thermal noise method. The stiffness and sensitivity of each cantilever was measured prior to dipping in ink. The stiffness was typically 0.5-0.6 N/m. Force maps were processed using

Asylum Research software (based in the Igor-Pro environment, Wavemetrics). The raw data of cantilever deflection voltage versus z-piezo extension was converted to force vs tip-sample separation using the measured stiffness and sensitivity of the cantilever. In addition to block-processed force maps to calculated maximum adhesion, force curve analysis was performed manually on each force curve to extract extension length data.

Topographical images were generated on the Asylum MFP-3D instrument in intermittent contact mode. Morphologies of the printed features were analyzed using the Particle Size plug-in for the Asylum Research software.

5.3 Results and Discussion

5.3.1 The model system

A selection of 4 UV curable acrylic based liquid inks (from the family of Norland Optical Adhesives) was chosen for two main reasons; (1) they present a range of viscosities (1000 mPa.s, 5000 mPa.s, 11000 mPa.s and 25000 mPa.s), (2) they contain minimal volatile components and so their liquid properties remain stable over many hours. It should be noted that their chemical make-ups, though similar, are not identical (Appendix 5.5.1 includes a summary of the composition of each ink).

A summary of the liquid properties for each ink is presented in Table 5-2. The inks present a range in viscosity (at 22 °C) from 1.33 Pa.s to 24.86 Pa.s. For the sake of clarity, we use ink viscosity as a means to distinguish between inks throughout this chapter. The data in this chapter is presented using a consistent marker label for each ink, with the viscosity rounded to the nearest thousand milliPascal: **NOA 65** (1000 mPa.s) = blue circles, **NOA 68** (5000 mPa.s) = green diamonds, **NOA78** (11000 mPa.s) = gold triangles and **NOA68T** (25000 mPa.s) = red squares.

	Density ρ (g/ml)	Viscosity (22 °C) μ (Pa.s)	Surface tension σ (mN/m)	Contact Angles (macroscopic) Si (-OH) (°)	Si (-CH_3) (°)
Water	0.998	0.001	72.7	~0	87.8 (5.5)
NOA 65	1.093 (0.001)	1.33 (0.06)	33.8 (0.5)	~0	24.2 (2.8)
NOA 68	1.136 (0.001)	5.49 (0.13)	34.2 (0.04)	4.5 (0.5)	37.0 (4.2)
NOA 78	1.1504 (0.001)	10.86 (0.13)	36.46 (0.8)	2.2 (1.2)	42.0 (4.8)
NOA 68T	1.156 (0.001)	24.86 (0.56)	26.7 (0.5)	6.6 (0.4)	38.2 (3.6)

Table 5-2: Liquid properties of all NOA inks and of water. Values in parentheses indicate the standard deviation over multiple measurements (n=2 for density measurements; n=3 for viscosity measurements; n=6 or greater for surface tension measurements; n=8 or greater for contact angle measurements).

5.3.2 Printability threshold determined by ink/substrate contact angle

Our first step was to screen the DPN printability of our 4 inks on both the hydrophilic and hydrophobic substrates (8 ink-substrate systems in total). For this purpose, we define "successful DPN printing" as the deposition of discrete ink droplets.

Figure 5-2 (A, B, C and D) show dot arrays printed using each of the four inks on hydrophobic silicon. The formation of discrete and stable droplets shows that all inks were printable on this substrate. Figure 5-2 (F, G, H and I) show dot arrays printed using each ink on hydrophilic silicon. In this case, two of the inks, NOA65 (1000 mPa.s) and NOA78 (11000 mPa.s), did not print successfully (Figure 5-2 (F) and (H) respectively). For these two systems, ink was deposited from the pen on to the substrate but then spread to such an extent that the original pattern was unrecognizable.

Figure 5-2 (E) shows the macroscopic contact angles for each of the four inks on both the hydrophilic and hydrophobic silicon substrates. The two

unsuccessful ink-substrate systems also had the lowest contact angles (~0° for NOA 65 on Si(-OH) and ~2° for NOA78 on Si(-OH)).

As described in **Chapter 2** the spreading of a liquid drop on a surface can be characterised by two regimes: (1) total and (2) partial wetting.[32] When the ink-substrate affinity is greater than the ink-ink affinity, the ink will spread completely over the substrate with no pattern definition. A basic rule of thumb for DPN ink development is to begin with an ink-substrate system which has a non-zero contact angle.

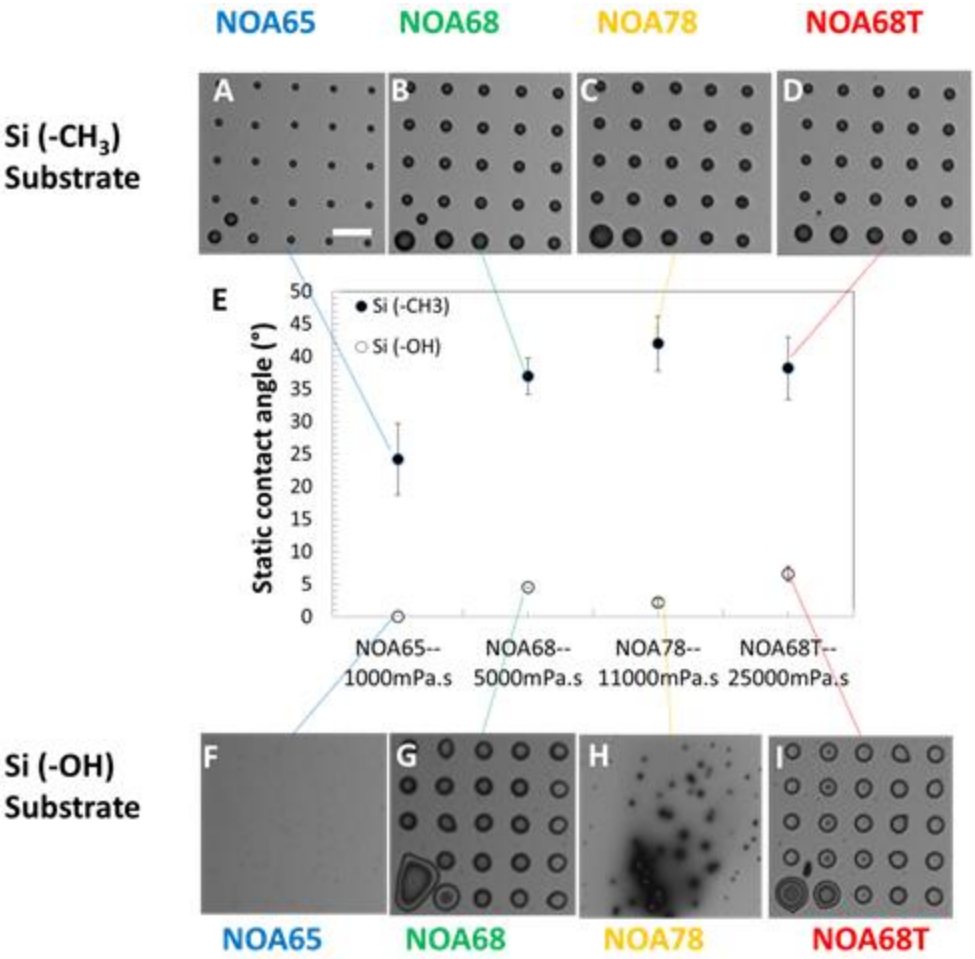

Figure 5-2: Screening the DPN printability of various NOA inks on both the hydrophilic silicon substrate, Si(-OH), and the hydrophobic silicon substrate, Si(-CH_3). (A-D) show dot arrays printed using each of the four inks on hydrophobic silicon. The formation of discrete and stable droplets shows that all inks were printable on this substrate. (F-I) show dot arrays printed using each ink on hydrophilic silicon. In this case, two of the inks, NOA65 (1000 mPa.s) and NOA78 (11000 mPa.s), did not print successfully ((F)

and (H) respectively) due to excessive spreading. The two non-printable inks (NOA 65, and NOA78 on hydrophilic Si/SiOx) had the lowest macroscopic ink/substrate contact angle (~0° and ~2° respectively). Scale bar 10 μm, shown in (A), corresponds to all images.

5.3.3 Equilibrium contact angles of ink micro-droplets

The shape of a macro-scale liquid drop on a surface is described by the equations of Young and Laplace.[32] The simple picture of a spherical cap defined by an equilibrium contact angle (CA) is complicated in real systems, however, by three principle phenomena:

1. 'Contact angle hysteresis', arising from the imperfection of the system (e.g. substrate roughness, chemical heterogeneity) and from the dynamics of deposition, means the actual contact angle can take any value between a maximum 'advancing' and a minimum 'receding' angle.[32–34]

2. The existence of a 'precursor film' (thickness typically <100 nm) at the front edge of a spreading droplet due to the influence of long range forces.[32,35]

3. When the droplet is very thin ~10 nm or less, a so called 'disjoining pressure' (Π) arises from the interaction of the liquid surface with the substrate.[36–38]

These substrate effects have much greater influence on the micro- to nanoscale, and for these reasons we cannot assume that the shape of a micron-scale DPN printed dot will scale down directly to form a miniature version of a millimetre scale droplet of the same liquid on the same substrate.[39] The contact angle of a micro- or nanoscale drop may be smaller or larger than its macro-scale counterpart depending on the nature of the long-range liquid-substrate interactions.[32]

In Figure 5-3 we examine the microscopic contact angles (θ_{micro}) of DPN printed dots (measured by AFM topographical imaging) as a function of dot-

radius. The θ_{micro} values are characteristic values for each dot calculated by fitting the measured dot volume and measured dot area to spherical cap geometry. The macro-scopic static contact angle (θ_{macro}) obtained by goniometry is also indicated for reference. In these data, it can be seen that the θ_{micro} adopted by droplets at submicron dimensions can deviate significantly from $\theta_{macro.}$ Figure 5-3 (A) shows θ_{micro} for the NOA 68 ink on each substrate. On the hydrophobic silicon substrate (filled green diamonds) the NOA68 ink assumes a θ_{micro} which is similar to θ_{macro} (~37°) for all dots. On the hydrophilic substrate (unfilled green diamonds) droplets of >1000 nm radius also adopt a θ_{micro} which is only slightly higher than the θ_{macro} value (~4.5°). However, for droplets with radius <1000 nm, the θ_{micro} value rises to ~10°. This deviation becomes especially pronounced for droplets with radius <200 nm, where θ_{micro} adopts values between 10° to 18°. Figure 5-3 (B) shows θ_{micro} versus dot radius data for the NOA68T ink on each substrate. On the hydrophobic silicon substrate (filled red squares) the larger NOA68T droplets exhibit θ_{micro} similar to θ_{macro} (~38°). Droplets with radii <250 nm have strikingly different morphology however, with θ_{micro} in a range between 15° to 25°. In the case of the hydrophilic substrate, the NOA68T ink again forms larger droplets with θ_{micro} similar to θ_{macro} (~6.6°), which increases to ~10° for droplet radius <1000 nm.

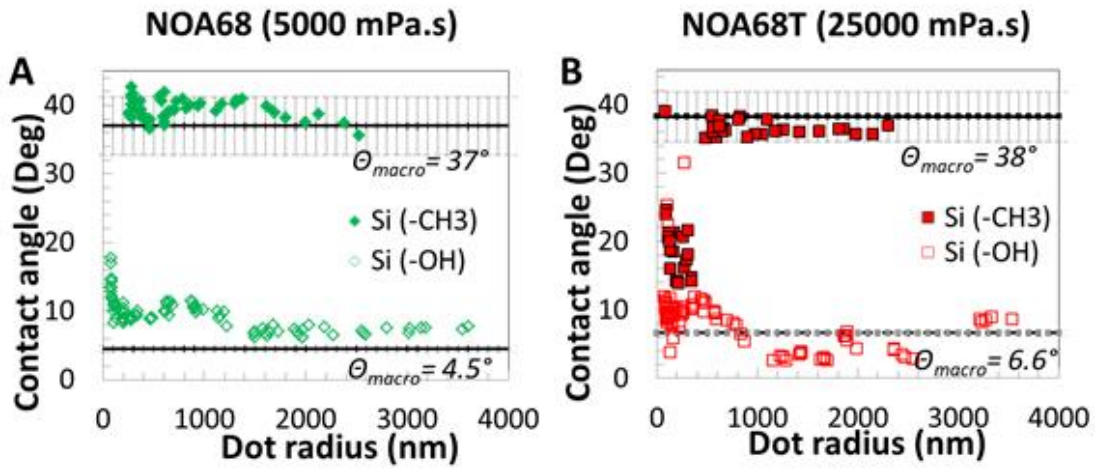

Figure 5-3: Contact angles of DPN printed dots as a function of dot radius: (A) Contact angles* for NOA68 ink micro-dots DPN printed on hydrophobic Si (filled green

diamonds) and on hydrophilic Si (unfilled green diamonds) plotted against dot radius. The horizontal lines represent the macroscopic contact angle (θ_{macro}) for NOA68 on hydrophobic Si (black line) and hydrophilic Si (grey line). The NOA68 ink droplets assume similar contact angles on the micro-scale (>1000 nm radius) as on the macro-scale (~1 mm radius) for each substrate. The contact angles of the smallest printed dots (i.e. <500 nm radius on hydrophilic Si) can deviate from this behaviour (discussion in text). (B) Contact angles* for NOA68T ink micro-dots DPN printed on hydrophobic Si (filled red squares) and on hydrophilic Si (unfilled red squares) plotted against dot radius. The horizontal lines** represent θ_{macro} for NOA68T contact angles on hydrophobic Si (black line) and hydrophilic Si (grey line). The NOA68T ink droplets again assume similar contact angles on the micro-scale (>1000 nm radius) as on the macro-scale for each substrate. The deviation from this behaviour at smaller scales (<500 nm radius) is striking on both substrates.**

***Micro-dot contact angles were calculated from the area and volume of each dot (as measured by AFM topographical scans) assuming spherical cap geometry. Data represents at least 50 individual dots for each ink-substrate system.**

****Error bars on the horizontal lines represent the standard deviation of the goniometry measurements (n~20).**

In all instances, these striking deviations correspond to instances where the height of the dot is <100 nm. Several studies have highlighted the changing dynamics of spreading for very small droplets when driven by van der Waals rather than Laplace spreading.[35,40] The dependence of contact angle on the height of nanoscale glycerol droplets due to the influence of van der Waals forces has also been measured.[39]

Conversely, the dynamics of DPN deposition may also influence the resulting contact angle of the resulting droplet. In Figure 5-4 we show the same contact angle data as above re-plotted against the dwell times used to deposit each dot. Each data point represents θ_{micro} for that dwell time averaged over 5 droplets. In this case a consistent pattern can be observed in the contact angle data at very short dwell times. Figure 5-4 (A) shows averaged θ_{micro} for the NOA68 ink. On the hydrophobic silicon substrate (filled green diamonds) θ_{micro} is relatively high (41°) at the shortest dwell time (0.002 s), then drops to a minimum of 37° at dwell time 0.1 s, before rising again to 40° at dwell time 0.5 s. On the hydrophilic substrate

(unfilled diamonds) θ_{micro} is again relatively high (14°) at 0.002 s dwell time, before dropping to a minimum of 10° at 0.1 s and rising to 10° at 0.5 s. Figure 5-4 (B) shows the averaged θ_{micro} for the NOA68 ink on each substrate. The same trends of the θ_{micro} dropping and then rising again within the range of 0.002 s to 0.5 s dwell time is evident in each case.

We suggest that the reason for this consistent trend may be related to the dynamics of droplet deposition. The effect can be conceptualized by considering how a droplet spreads with a dynamic CA approaching the maximum 'advancing' angle, and how a droplet recedes with a (lower) dynamic contact angle approaching the minimum 'receding' angle.[33] Similarly, when an inked DPN tip is in contact with the substrate, ink will spread in an 'advancing regime'. When the tip retracts, a meniscus bridge is distended, and the ink will retract in the 'receding regime'. [A similar argument has been made by the Ondarcuhu group.[26]] The specifics of the deposition event (dwell time, droplet volume, contact line pinning) may determine whether the resulting droplet assumes a contact angle closer to the advancing angle (therefore higher) or closer to the receding angle (therefore lower).

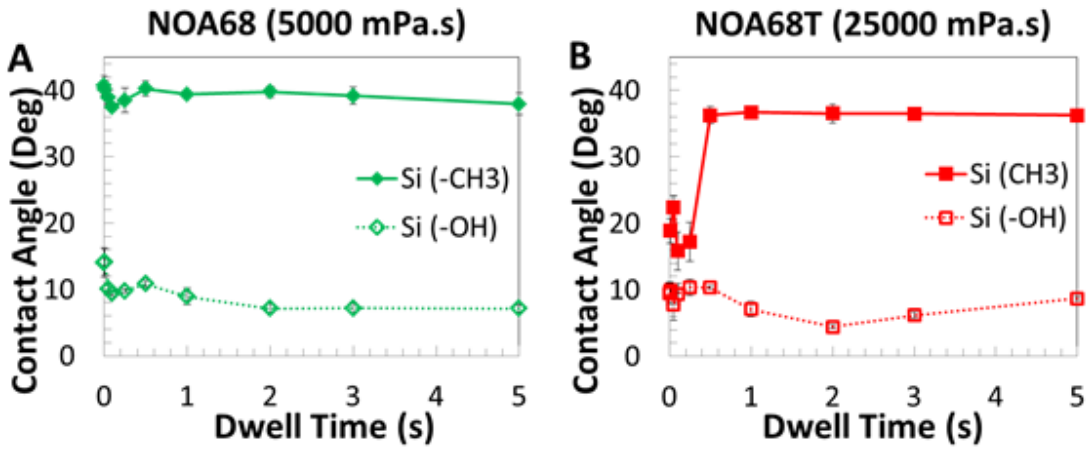

Figure 5-4: Contact angles of DPN printed dots as a function of dwell time. The dynamics of dot deposition may account for the repeating trend in contact angles observed at low dwell times. Each data point represent the mean average of 5

individual dots printed at that dwell time and error bars represent the standard deviation.

The effect of contact angle hysteresis on the nanoscale has previously been highlighted in a study of glycerol nanodroplets.[39] In that work, utmost experimental precautions were taken to ensure uniform conditions for all droplets: a pure, single component model liquid was used and the substrate used was atomically flat mica cleaved just 30 s prior to glycerol adsorption in a clean room environment. Even so, the nanodroplets exhibited a wide range of contact angles. The interesting difference in our case is that the NOA68 and NOA68T drops do not just exhibit a random variance in θ_{micro}, but follow a consistent pattern with respect to the deposition dwell time. We will discuss the effect of deposition dynamics on droplet morphology in more detail below.

5.3.4 Monitoring liquid ink deposition *in-situ* using AFM force curves

AFM force measurements have been used for two decades to model the formation of liquid meniscii at nanoscale apertures.[29] For example, the adhesion force between a tip and substrate can be used to monitor the capillary condensation of a water meniscus at various relative humidities.[41] More recently, AFM force measurements have been used to gain insight into the mechanism of liquid deposition from a nanofountain pen.[26] Besides the direct information acquired about the underlying ink-transfer mechanism, the force curves being generated may allow for a direct method to monitor feature size *in-situ* and in real time (without time-consuming AFM imaging). Such a capability, besides being useful and time-saving in an ink-development project, would also prove invaluable during a potential device manufacture; it would provide a means to instantaneous error detection (and correction).

The DPN ink-transfer mechanism was probed by monitoring the forces experienced by an AFM tip during deposition of the NOA68T (25000 mPa.s)

model ink on hydrophilic Si/SiOx substrates. Grids of dots were deposited (Figure 5-5 (A)) and the force experienced by the DPN tip was measured and used to generate a force curve (force versus tip-sample separation) corresponding to each deposition event. After AFM imaging of the printed pattern, analysis of individual force curves could proceed with respect to the dimensions of the specific dot deposited. For example, Figure 5-5 (B) shows a force map compiled by plotting the maximum adhesion force against the coordinates of each dot imaged in (A).

The data of interest is within the force retraction curve, generated when the tip is being withdrawn from the surface. Each retract curve exhibits three stages (Figure 5-5 (C)). In stage 1 (from 0 to -200 nm Zsensor height), the tip maintains contact with the surface as it is pinned down by the capillary force of ink on the substrate. When the cantilever restoring force exceeds the pinning force of the meniscus, the tip pulls away and draws a thin 'capillary bridge' of ink between itself and the substrate (stage 2). The capillary bridge "necks" (becomes thinner) as it is drawn, and hence the force on the tip decreases. When the neck of the capillary bridge breaks, the force returns to zero, and this indicates the completion of the deposition event. In the third stage of the retract curve, the tip completes its retraction at zero deflection, with no force on the tip.

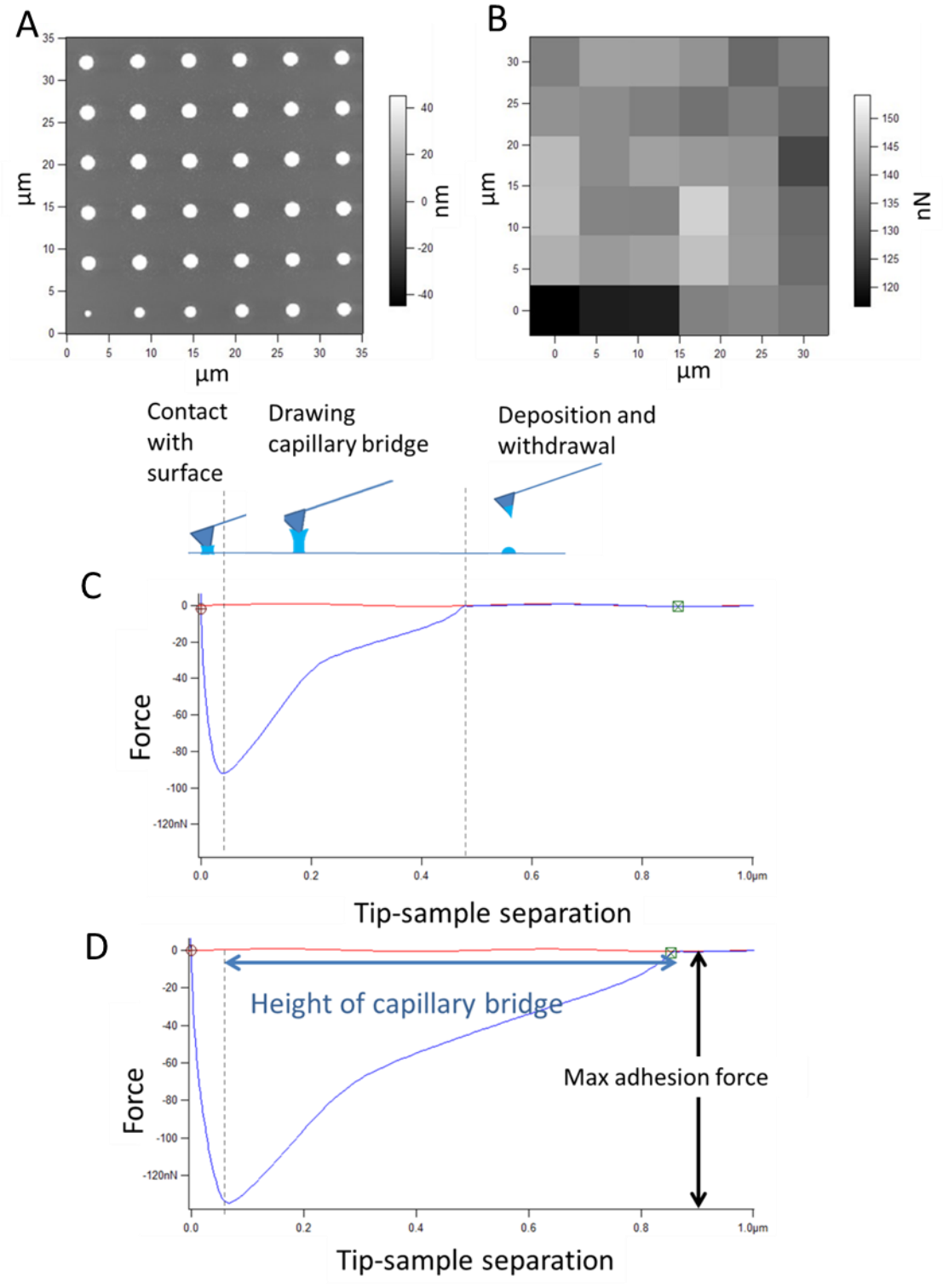

Figure 5-5: Force monitoring data: (A) AFM topography image of a 6x6 array of NOA68T dots (5s dwell time) on hydrophilic Si/SiOx; (B) Force map generated from the maximum adhesion force (retraction curve) registered during the deposition of each dot; (C) The force curve (retraction) recorded during deposition of the bottom-left dot

in the grid (radius 450 nm). Three sections of the retract curve are labelled; contact with surface, drawing of the capillary bridge, and final deposition; (D) The force curve (retraction) recorded during the deposition of bottom right dot in the grid (radius 780 nm). The DPN tip experiences larger forces and greater capillary bridge extension when larger dots are deposited.

In order to achieve reliable deposition monitoring, we must demonstrate a direct relationship between some feature of the force curve and resulting dot dimensions. Figure 5-5 (C) and (D) show force curves for two separate deposited dots; one of radius 450nm and one of radius 780 nm. It is clear that the force curve corresponding to the larger dot has a very different profile, with a stronger maximum adhesion force force (130 nN as opposed to 90nN) and a greater height of the capillary bridge (786 nm as opposed to 441 nm). In general, deposition of a larger dot generates a larger force on the tip, and a higher capillary bridge at break point.

The maximum adhesion force exhibits a direct relationship with dot radius Figure 5-6 (A) shows a plot of maximum adhesion force (black filled circles) versus deposited dot radius for 180 individual dots. The R^2 value of the fitted linear trendline is 0.951. An illustration of the meniscus geometry and the resulting forces of adhesion is given in Figure 5-6 (B). The force acting upon the cantilever during retract derives from the summation of two main components, the capillary force (F_{Cap}) and the Laplace force (F_{Lap}):

$$F = F_{Cap} + F_{Lap} \quad (1)$$

The capillary force component arises from the surface tension of the liquid (γ) acting on the ink-tip contact line (given by 2π times the radius of contact, $R_{m,tip}$), and normalized to the vertical using the angle φ_{tip}:

$$F_{Cap} = -2\pi\gamma R_{m,tip} Cos\varphi_{tip} \quad (2)$$

The Laplace force component arises from the Laplace pressure (ΔP_m, negative for negative meniscus curvature) acting on the area of contact with the tip:

$$F_{Lap} = \pi {R_{m,tip}}^2 \Delta P_m Cos\varphi_{tip} \quad (3)$$

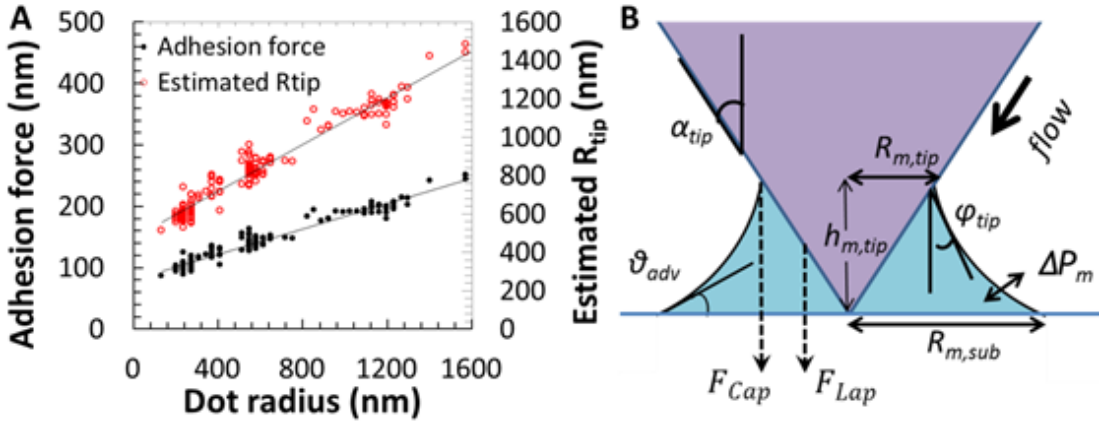

Figure 5-6: Relating maximum adhesion (or 'pull-off') force to resulting dot radius. (A) A plot of maximum adhesion force (black filled circles) versus deposited dot radius for 180 dots exhibits a linear relationship (equation of trendline: y = 0.1034x + 80.806, R^2 = 0.951). This adhesion force can be used to calculated the radius of meniscus contact on the tip, $R_{m,tip}$, (red open circles). The $R_{m,tip}$ value is typically about 60% of the resulting dot radius (equation of trendline: y = 0.6093x + 476.32). (B) The adhesion force originates from the capillary and Laplace forces defined by the geometry of the meniscus between tip and substrate.

The capillary force pulls the tip down to the substrate, and is therefore negative. The Laplace force also pulls to the substrate if the Laplace pressure is negative (true within a meniscus of negative curvature). Both forces depend critically on the radius of ink contact around the tip, $R_{m,tip}$, and not directly on the radius of the deposited feature. This crucial $R_{m,tip}$ value is difficult to independently measure, and has only previously been inferable as an adjustable parameter in simulations.[26] We can estimate $R_{m,tip}$, at the instant of pull-off, by assuming the maximum adhesion force is due entirely to the dominant capillary force acting at the angle φ_{tip} = 0 (i.e. Cos(0)=1). Our estimated $R_{m,tip}$ values, calculated using equation 2,

are plotted as the open red circles in Figure 5-6 (A); $R_{m,tip}$ is estimated to be about ~60% of the resulting dot radius.

The adhesion force can be used to estimate a reconstruction of the meniscus geometry at pull-off. As we show in Figure 5-6 (B), the geometry of the ink meniscus is defined by many parameters including; the meniscus radius at the substrate ($R_{m,sub}$), the meniscus height on the tip ($h_{m,tip}$), the ink-substrate (advancing) contact angle (θ_{adv}), the ink-tip contact angle (θ_{tip}), and the pyramidal shape of the tip itself (α_{tip}). Furthermore, if the ink-tip contact line is not pinned, the $R_{m,tip}$ value will change during retraction. The decreasing force during retraction observed in Figure 5-5 is due mainly to modification of the F_{Cap} and F_{Lap} forces by changing $R_{m,tip}$ and φ_{tip} values. The meniscus is 'pulled' down to the apex of the tip as it is distended. Detailed discussions of the changing adhesion force profile during retraction have been provided by both Chaudhury and Ondarcuhu.[26,27]

Meniscus bridge height (extension length)

The height of the meniscus bridge at break, h_m, has been suggested before as a useful parameter for monitoring deposition in a nanofountain pen approach.[26] In the nanofountain pen experiments the extension length was found to have a non-linear relationship to feature size. We have found a direct linear relationship of h_m to the radius of deposited dots (Figure 5-7 (A)). We suggest that this dependency arises from the definition of the meniscus deposition volume, and use geometrical arguments to provide a route to directly calculate the volume of deposited dots.

As we show in Figure 5-7 (A) below, the geometry is much simplified (relative to Figure 5-6 (B)) at the point of break of the meniscus bridge. If we assume that only the bottom half of the meniscus bridge is deposited on the surface, then no knowledge of the ink-tip interaction geometry is required. In order to calculate the volume of the meniscus shown in Figure 5-7 (B), we first approximate the meniscus curvature to be semi-circular (a

common assumption).[42] We also assume the receding contact angle, θ_{rec}, is near zero (likely for low contact angle systems). In this case, the height of the meniscus at break, h_m, is equal to the radius of contact with the substrate, $R_{m,sub}$ at that instant. By rotational geometry the volume of the meniscus, V_m, is given by:

$$V_m = \frac{\pi {h_m}^3}{6}(10 - 3\pi) \quad (4)$$

If we assume that V_m also constitutes the volume of the deposited dot, $V_{dot,}$ then the capillary bridge height provides direct information on the size of the deposited feature. Figure 5-7 (C) shows the volume of deposited dots (measured using Asylum Research software from AFM topographical images) plotted against the volume calculated from meniscus height according to equation 4. The volumes calculated from the meniscus height agree very well with the measured volumes (R^2=0.9899), validating equation 4. Such a level of agreement is very promising for an *in-situ* deposition monitoring system.

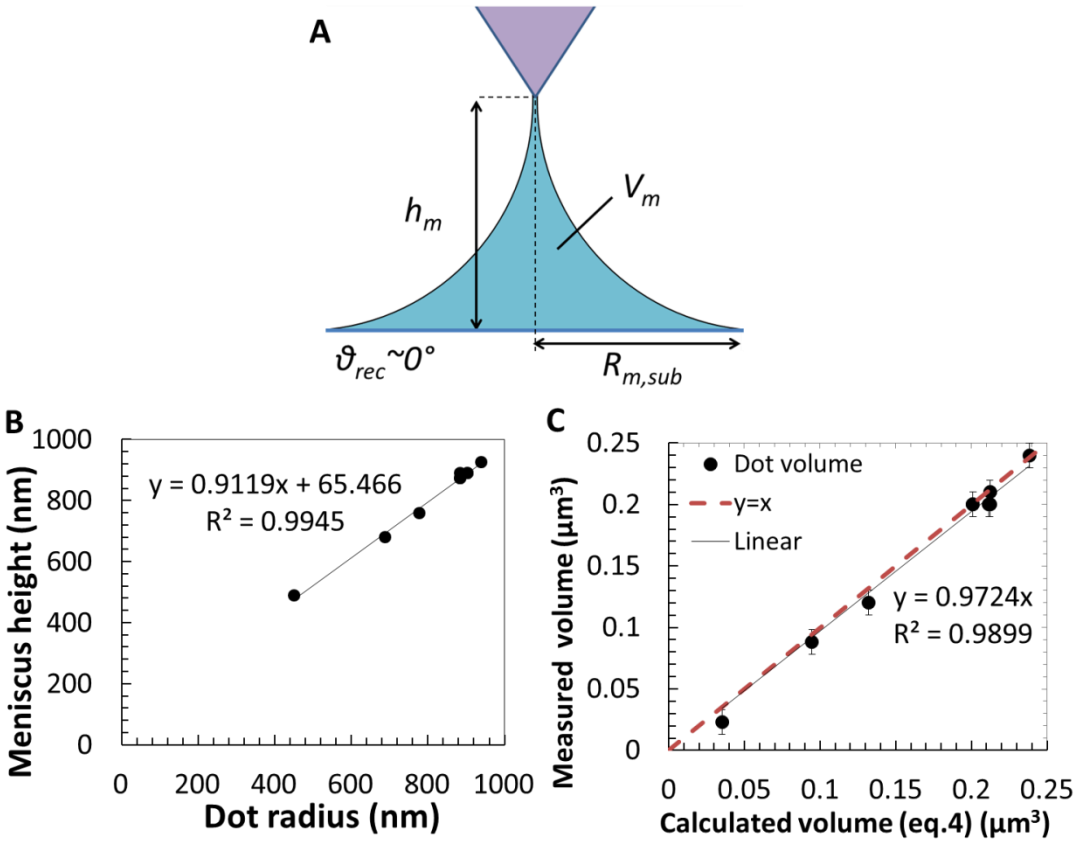

Figure 5-7: Obtaining deposited dot volume from the deposition force curve. (A) The height of the meniscus bridge (i.e. force curve 'extension length') exhibits a strong direct relationship (R^2=0.99) with dot radius. (B) Diagram of the meniscus bridge at its break point. If the receding contact angle is ~0°, then the height of the meniscus, h_m, is equal to the radius of contact with the substrate, $R_{m,sub}$. Using simple geometry, the volume of the meniscus can be calculated using the meniscus height parameter only. (C) The volume of deposited dots (as measured by AFM) plotted against the volume calculated from meniscus height according to equation 4. The measured and calculated volumes are in very good correlation, showing that our assumptions are validated. The linear trendline and line of perfect correlation, $y=x$, are plotted for comparison.

Implications for the deposition mechanism

We have assumed that the meniscus volume, V_m, equals the volume of the deposited dot, V_{dot}, and this assumption was validated by the high level of agreement between calculated and measured dot volumes in Figure 5-7 (B). We now explore the idea that the equivalence of these volumes has implications for the morphology of the resulting droplet.

The meniscus and the spherical cap are different three dimensional objects with distinct relationships between their radii and volumes (see Figure 5-8 (A)). If a droplet is constrained to the same volume as a meniscus, then the dimensions of droplet radius and/or its contact angle must change to reflect this. That is, the droplet formed from a meniscus may have to spread a little more than the meniscus, or a little less, in order to hold the same volume. This geometrical asymmetry may have implications for the morphology of deposited features under conditions of contact line pinning, and so provide an explanation for the anomalous micro-scale contact angles observed in section 5.3.3.

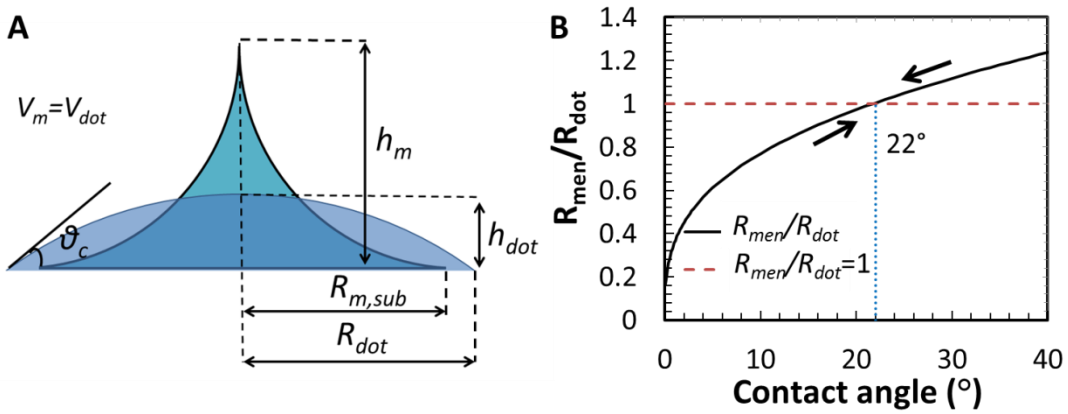

Figure 5-8: Meniscus geometry and dot geometry. (A) As the distended meniscus assumes the shape of a spherical cap, the relative geometries may dictate movement of the contact line, from $R_{m,sub}$ to its final position at R_{dot} (note: R_{dot} may be greater or smaller than $R_{m,sub}$). (B) In the case of contact line pinning during deposition, liquids will tend to assume a spherical cap with a contact angle of about 22°.

In order to quantitate this possibility, we now consider the equations of volume of both the meniscus and droplet respectively. Assuming a receding contact angle of close to 0°, h_m at the instant of break is equal to the radius of meniscus contact with the substrate, $R_{m,sub}$. In this case, equation 4 is equivalent to:

$$V_m = \frac{\pi {R_{m,sub}}^3}{6}(10 - 3\pi) \quad (5)$$

By spherical cap geometry, dot volume can be calculated from the dot radius (R_{dot}) and contact angle (θ) by:

$$V_{dot} = \frac{\pi {R_{dot}}^3}{2} tan\left(\frac{\theta}{2}\right) \quad (6)$$

Equation 5 expresses the volume of the meniscus in terms of the meniscus radius $R_{m,sub}$ and equation 6 expresses the dot volume in terms of its radius, R_{dot}. By equating equations 5 and 6, a relationship between the radius of meniscus, $R_{m,sub}$, and the radius of the deposited dot, R_{dot}, can be defined:

$$R_{m,sub} = R_{dot} \sqrt[3]{\frac{3\tan(\frac{\theta_e}{2})}{10-3\pi}} \quad (7)$$

This relationship is significant as it shows that the dot radius must be different from the meniscus radius ($R_{m,sub} \neq R_{dot}$), unless the cube root factor is unity. This suggests that the liquid substrate contact line will tend to move during the deposition event.

When the cube root factor is unity, an equilibrium geometry is achieved where both the meniscus and the dot hold the same volume at the same radius:

$$\sqrt[3]{\frac{3\tan(\frac{\theta_e}{2})}{10-3\pi}} = 1 \quad (8)$$

The solution to equation 8 is for a contact angle of 22°. The 22° contact angle is thus a special case where an equilibrium geometry is achieved. In this situation, both the meniscus and the droplet hold the same volume at the same radius. Thus, in the illustration of Figure 5-8 (A), the meniscus would fall into the spherical cap with no movement of the contact line.

The ratio $R_{m,sub}/R_{dot}$ relationship is plotted against contact angle in Figure 5-8 (B). For a liquid-substrate system with a 22° equilibrium contact angle, $R_{m,sub}/R_{dot}$=1, and so the meniscus volume will assume the shape of a spherical cap with no change in radius. Droplets with contact angle below 22° will tend to spread wider than the deposition meniscus ($R_{dot} > R_{m,sub}$) in order to hold the same volume. Droplets with contact angle higher than 22° will tend to pull up into an equilibrium shape with radius smaller than the meniscus radius ($R_{dot} < R_{m,sub}$) to hold the same volume.

Now, if the contact line is pinned during deposition, then R_{dot} will stick at the $R_{m,sub}$ value. In this case, the droplet contact angle must increase for low θ_e systems, if the droplet is to match the meniscus volume. Conversely, a nominally high θ_e droplet must decrease its contact angle. In each case, dots will tend to adopt a spherical cap with contact angle approaching 22°. We observed very similar behavior in section 5.3.3 above, where the smallest droplets (<200 nm) on hydrophilic substrates tended to have higher CA than their macroscopic values, and the dots on hydrophobic substrates tended to have smaller than equilibrium CA. In each case the tendancy was towards contact angles of about 20°.

We concede that the idealized geometry of equations 5-7 is only valid for θ_{rec}~0°, which may not be the case for higher contact angle systems. Nevertheless, we maintain that the fundamental geometrical differences between the volume contained in a meniscus and the volume contained in a spherical cap will still create a tendency towards movement of the contact line and/or contact angle hysteresis.

5.3.5 Dwell-time dot size dependence

The growth of feature-size with dwell-time is a critical parameter in DPN as it enables pattern generation from nanometre up to ~10 μm length scale. Investigations of the 'transport rate' relationship have been the basis for many studies into the ink transfer mechanisms for molecular ink DPN.[3,4,43,44]

Control of liquid ink feature-size is made more problematic by the 3 dimensional nature of the resulting features; small changes in radius can result in comparatively large increases in volume ($V_{dot} = \frac{\pi}{2} r^3 \tan\left(\frac{\theta_c}{2}\right)$ for a spherical cap). The control of deposition volume is crucial for many applications, for example those which involve monitoring of local fluorescence,[15] drug delivery targeting single cells,[45] or applications involving the fabrication of electrical components (as described in **Chapter 3** and **Chapter 4**).

We have systematically investigated the dwell time dependence of dot-size for the four NOA inks (viscosities ranging from 1000 mPa.s to 25000 mPa.s) on both hydrophilic (plasma cleaned) and hydrophobic (ODTMS functionalised) silicon substrates. However, we have found that the factor affecting transport rate most dramatically is not any intrinsic liquid or interfacial property; rather, it is the volume of ink on the cantilever at the time of printing. We illustrate this discussion with data from the NOA68 (5000 mPa.s) ink on hydrophilic silicon only for the sake of clarity.

Figure 5-9 shows the dot-size/dwell-time relationship for both radius and volume. Figure 5-9 (A) shows a 3D rendered AFM topography image of a typical dwell time calibration grid illustrating increasing dot size with dwell time. Figure 5-9 (B) shows dot radius (as measured by AFM) versus dwell time for the NOA68 (5000 mPa.s) ink on hydrophilic Si. Data for two grids are shown, both printed during the same experiment, under the same environmental conditions, by the same pen. The 'early' grid (filled green diamonds) was printed soon after inking the pen and the 'late' grid was printed following two hours of printing when much of the ink on the pen had been expended. The deposition rate of the second grid is markedly less than that of the early grid. Figure 5-9 (C) shows the same calibration grid represented in terms of dot volume against dwell time. In this case the differing deposition rates are even more pronounced.

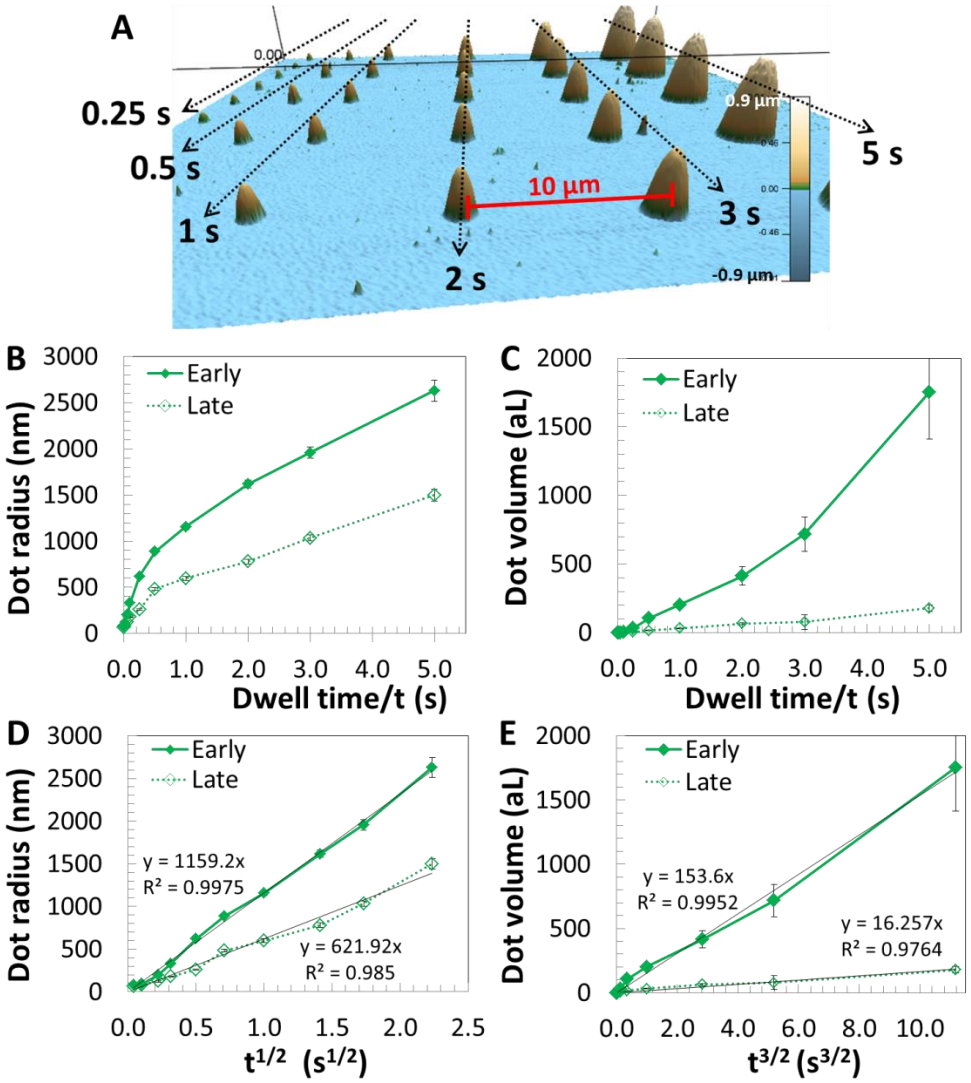

Figure 5-9: Controlling dot-size using the dwell time parameter: (A) 3D rendered AFM topography image of a typical dwell time calibration grid illustrating increasing dot size with dwell time; (B) Dot radius (as measured by AFM) versus dwell time for the NOA68 (5000 mPa.s) ink on hydrophilic Si. Data for two grids are shown, both printed during the same experiment, under the same environmental conditions, by the same pen. The 'early' grid (filled green diamonds) was printed soon after inking the pen and the 'late' grid was printed when much of the ink on the pen had been expended. The deposition rate of the second grid is markedly different from that of the early grid due to a decreased volume of ink on the cantilever. (C) The same calibration grid represented in terms of dot volume against dwell time. In this case the differing deposition rates are even more pronounced. (D) The dot radius exhibits a dependence on the square root of dwell time ($t^{1/2}$). (E) The dot volume data exhibits $t^{3/2}$ dependence following the equation for volume of a spherical cap.

Referring first to the early grid (unfilled diamonds): dot radius ranged from 80 nm for 0.002 s dwell to 2500 nm for 5 s dwell (Figure 5-9 (B)). Dot radius was found to have a direct dependence on the square root of dwell time (Figure 5-9 (D)). A similar $t^{1/2}$ dependence is often observed in microfluidics, for example in the Lucas-Washburn equation for filling of micro-channels. In the case of microfluidic channels, the $x \sim t^{1/2}$ filling rate arises from a situation of constant filling pressure acting over an increasing channel length (therefore increasing hydraulic resistance).[38,46] The possible origins of the $t^{1/2}$ dependence in liquid ink DPN will be discussed below.

Dwell time could be used to control the volume of deposited dots over four orders of magnitude. As shown in Figure 5-9 (C), dot volumes in the early grid ranged from 0.1 aL for a dwell time of 0.002 s to over 1500 aL for a 5 s dwell time. Following the equation of the spherical cap, dot volume depends on radius cubed ($V_{dot} \sim r^3$). As radius grows with the square root of time ($r \sim t^{1/2}$), dot volume is found to increase as $V_{dot} \sim t^{3/2}$ (Figure 5-9 (E)).

Deposition rate was not consistent between sequential grids. The deposition rate of the late grid is markedly less than that of the early grid over all dwell times. This is especially dramatic in terms of volume deposited. For the late grid, the range covered 0.03 aL for 0.002s dwell time to 186 aL for 5 s dwell (Figure 5-9 (C)). As shown in (Figure 5-9 (E)), the slope, k, of the linear trendline fit to $V_{dot}=kt^{3/2}$ decreased almost a factor of ten from 153 $aL/s^{3/2}$ for the early grid to 16 $aL/s^{3/2}$ for the late grid. This changing of patterning rate (which we observed for all ink-substrate systems) demonstrates that the rate of deposition depends critically on the volume of ink on the cantilever.

The driving force for deposition

According to the Young-Laplace equation, the constricting force of surface tension on a droplet-air interface results in an increased pressure inside a liquid droplet relative to outside. In general, the pressure difference

(ΔP_{Lap}, known as the Laplace pressure or overpressure) is a product of the liquid surface tension (γ) and the mean curvature of the interface (κ):

$$\Delta P_{Lap} = \gamma\kappa \quad (9)$$

The mean curvature is given by $\kappa = (\frac{1}{R_1} + \frac{1}{R_2})$, where R_1 and R_2 are the principal radii of curvature of the interface. For spherical droplets R_1=R_2=R. For menisci, we designate R_1 as positive and R_2 as negative. Thus:

$$\Delta P_{Lap} = \gamma(\frac{1}{R_1} + \frac{1}{R_2}) \quad (10)$$

In the concave shape of a meniscus, one of the radii of curvature (R_2) is negative (Figure 5-10). Thus, when the magnitude of R_1 is greater than the magnitude of R_2, the Laplace pressure will also be negative. Such negative pressures have been measured for nanoscale menisci formed by capillary condensation between an AFM tip and substrate, with the magnitude of the pressure being up to 140MPa.[47]

In Figure 5-10 we consider a liquid meniscus of micron scale where the sharpness of the tip is negligible. Due to the inclination angle of the pyramid (a_{tip}~45°), R_1~R_2 and the Laplace pressure in the meniscus is approximately zero (ΔP_{tip}~0). The Laplace pressure in the ink at the base of the tip is positive (ΔP_{tip}>0). Thus, when a DPN tip touches the substrate, a pressure gradient is set up from the top to the bottom of the tip according to the difference in Laplace pressure. According to Pascal's law the liquid must flow from the higher to the lower pressure region.[48]

If the Laplace pressure in the tip reservoir (ΔP_{tip}) is proportional to the volume of ink, then this driving pressure will decrease during an experiment as ink is depleted. Although we have not done so in this work, one method to quantify the Laplace pressure for a given volume in this geometry may be to use a simulation method based on energy minimization, such as the Surface Evolver software.[49]

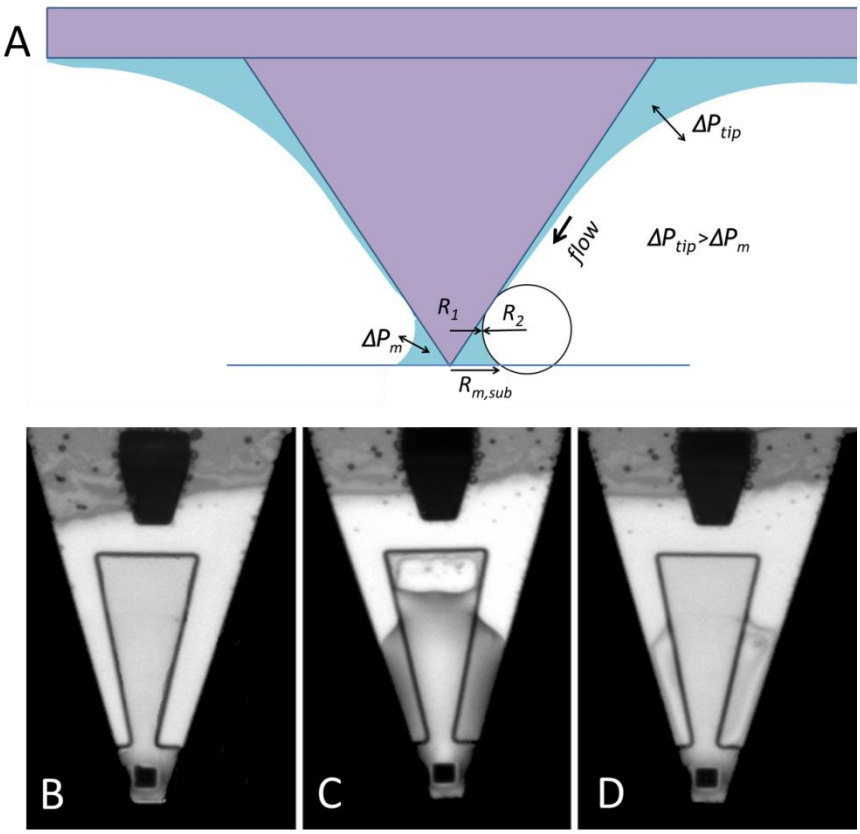

Figure 5-10: The dependence of deposition rate on volume of ink on the pen. (A) Illustration of the Laplace pressure gradient as the driving force for liquid ink deposition. (B) Optical micrograph of a dry M-type probe (as used in this study) prior to inking. (C) Optical micrograph of an M-type probe just after filling with NOA68T ink. (C) Optical micrograph of the same probe after printing for 2 hours and much of the ink has been depleted.

In molecular ink DPN, driving force and many intrinsic factors were elucidated before the effect of tip coating levels and ink depletion effects became apparent. On the contrary, we have found that 'ink loading' is the dominant factor affecting deposition rate for liquid ink DPN. Changes in ink loading can result in a ten fold decrease in deposition rate over two hours printing time (Figure 5-9 (E)). The volume dependence was so strong that no inherent effects resulting from the differences in ink properties (i.e. the range of viscosity presented by the four NOA inks) could be identified from our data.

Any understanding of liquid ink deposition must begin with an understanding of the effect of changing ink volume on the tip.

It must be noted that although our discussion treats the NOA inks as simple liquids defined by surface tension and viscosity, in reality they are complicated formulations incorporating various adhesion promoters and wetting agents. The differing adsorption times of these components may influence the growth of nanoscale droplets in particular, thus making comparison between systems difficult at the nanoscale. Deposition in the first milliseconds of contact may proceed in a manner describable by diffusive transport, as in dip-pen nanolithography of molecular inks, rather than any Laplace pressure driven transport.

5.4 Conclusions

A set of model ink-substrate systems were used to develop an understanding of the deposition of liquids by DPN. We began by characterising the ink-substrate interaction, finding that the micro-scale droplets assume a similar morphology as millimetre scale droplets, as long as the droplet radius was above a critical threshold (>500 nm). Below this threshold, contact line pinning and the dynamics of DPN deposition may play an important role in defining feature morphology.

The forces acting upon the DPN cantilever during ink deposition were measured in order to gain insight into the underlying ink-transfer mechanism. The force curve data and simple geometrical arguments were used to elucidate the shape of the ink meniscus at the instant of deposition, a methodology which may be used as an accurate and real-time means of monitoring the volume of deposited dots. Such *in-situ* monitoring could be an important capability for future autonomous fabrication systems. For example, an algorithm could be incorporated using dynamic information from force curves to adapt to specific deposition conditions (level of ink on pen, humidity, local substrate hydrophilicity etc). Ideally,

such a system would utilise optical feedback, and individual actuation, on every pen in a DPN array. Although this would necessitate a vastly more complex instrumentation, feedback systems for 2 dimensional arrays of cantilevers were demonstrated over a decade ago.[50] We encountered limitations to the deposition monitoring technique due to the relatively low stiffness (k~0.5 N/m) of the M-type probes. For example, the large adhesion forces generated during deposition of very large dots resulted in bending of the cantilever beyond the limit of detection. This put an upper limit on the magnitude of adhesion forces which could be measured. On the other hand, the meniscus bridge height of very small dots could not be measured as this information was washed out by the cantilever restoring force. Higher sensitivity of detection (and greater control of overcoming the pinning meniscus force) could be achieved with the use of higher stiffness cantilevers.

We studied growth of dot-size with increasing dwell-time and found that dot-size generally grows with a $r \sim t^{1/2}$ dependence, and dot-volume grows with $r \sim t^{3/2}$ dependence. However, the dramatic change in deposition rate over the course of an experiment limited our ability to quantify the deposition dynamics in terms of liquid properties and substrate wettability; we found that the most critical parameter affecting deposition rate was the volume of ink on the pen. The following chapter, **Chapter 6,** is devoted to understanding the effects of changing ink volume on the deposition rate. Therein, we show that deposition rate depends not just on the volume of ink on the cantilever, but on the relative location of the ink on the cantilever (and on the tip itself) and that this ink distribution is subject to dynamic reorganisation.

5.5 Appendix

5.5.1 NOA ink composition

	Norland Optical Adhesive 65 (NOA 65)	Norland Optical Adhesive 68 (NOA 68)	Norland Optical Adhesive 68T (NOA 68T)	Norland Optical Adhesive 78 (NOA 78)
Mercapto-ester	20-50%	45-65 %	45-65 %	X
Tetrahydrofurfuryl Methacrylate	X	5-20%	5-20%	X
Acrylic Urethane esters	X	X	X	40-60%
Isobornyl Acrylate	X	X	X	28-43%
1.6 Hexanediol Diacrylate	X	X	X	2-15%

Table 5-3: Components of the NOA inks as defined by the manufacturer's documentation.

5.5.2 Ink viscosity

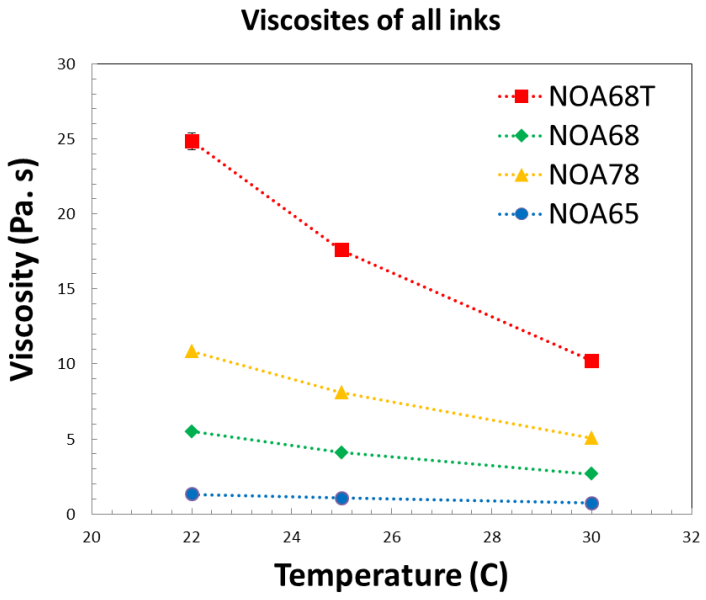

Figure 5-11: Viscosities of each NOA ink at 22°C, 25°C and 30 °C.

5.5.3 Satellite deposition

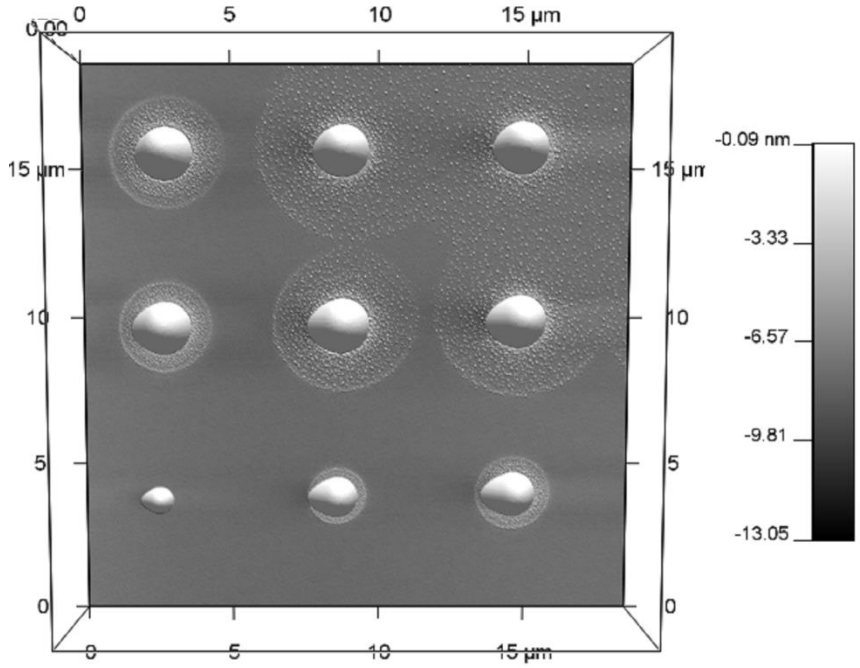

Figure 5-12: The radial extent of satellite deposits grows with deposition volume. The satellites may represent the vestiges of the deposition meniscus formed during contact, prior to the retraction of the tip and final dot deposition.

5.6 References

1. Piner, R. D., Zhu, J., Xu, F., Hong, S. & Mirkin, C. A. “Dip-Pen” Nanolithography. *Science* **283**, 661–663 (1999).

2. Sheehan, P. & Whitman, L. Thiol Diffusion and the Role of Humidity in “Dip Pen Nanolithography”. *Physical Review Letters* **88**, 156104 (2002).

3. Peterson, E. J., Weeks, B. L., Yoreo, J. J. De & Schwartz, P. V Effect of Environmental Conditions on Dip Pen Nanolithography of Mercaptohexadecanoic Acid. 15206–15210 (2004).

4. Giam, L. R., Wang, Y. & Mirkin, C. A. Nanoscale molecular transport: the case of dip-pen nanolithography. *The journal of physical chemistry. A* **113**, 3779–82 (2009).

5. Hong, S. Multiple Ink Nanolithography: Toward a Multiple-Pen NanoPlotter. *Science* **286**, 523–525 (1999).

6. Rozhok, S., Piner, R. & Mirkin, C. a. Dip-Pen Nanolithography: What Controls Ink Transport? *The Journal of Physical Chemistry B* **107**, 751–757 (2003).

7. Wu, C.-D. & Fang, T.-H. Simulation of deposition of ink molecules on rough substrates in dip-pen nanolithography. *Modelling and Simulation in Materials Science and Engineering* **19**, 065008 (2011).

8. Weeks, B., Noy, a., Miller, a. & De Yoreo, J. Effect of Dissolution Kinetics on Feature Size in Dip-Pen Nanolithography. *Physical Review Letters* **88**, 1–4 (2002).

9. Saha, S. K. & Culpepper, M. L. An Ink Transport Model for Prediction of Feature Size in Dip Pen Nanolithography. *Small* 15364–15369 (2010).

10. Chung, S., Felts, J. R., Wang, D., King, W. P. & De Yoreo, J. J. Temperature-dependence of ink transport during thermal dip-pen nanolithography. *Applied Physics Letters* **99**, 193101 (2011).

11. Ahn, Y., Hong, S. & Jang, J. Growth dynamics of self-assembled monolayers in dip-pen nanolithography. *The journal of physical chemistry. B* **110**, 4270–3 (2006).

12. Wu, C.-D., Fang, T.-H. & Lin, J.-F. Formation mechanism and mechanics of dip-pen nanolithography using molecular dynamics. *Langmuir : the ACS journal of surfaces and colloids* **26**, 3237–41 (2010).

13. Wang, H. *et al*. Toward conductive traces : Dip Pen Nanolithography ® of silver nanoparticle-based inks. *Applied Physics Letters* 143105 (2008).doi:10.1063/1.2995859

14. Hung, S. *et al*. Dip Pen Nanolithography of Conductive Silver Traces. *The Journal of Physical Chemistry C* 9672–9677 (2010).

15. Senesi, A. J., Rozkiewicz, D. I., Reinhoudt, D. N. & Mirkin, C. A. Agarose-assisted dip-pen nanolithography of oligonucleotides and proteins. *ACS nano* **3**, 2394–402 (2009).

16. Sanedrin, R. G., Huang, L., Jang, J.-W., Kakkassery, J. & Mirkin, C. A. Polyethylene Glycol as a Novel Resist and Sacrificial Material for Generating Positive and Negative Nanostructures**. 920–924 (2008).doi:10.1002/smll.200701089

17. Nakashima, H., Higgins, M. J., O'Connell, C., Torimitsu, K. & Wallace, G. G. Liquid deposition patterning of conducting polymer ink onto hard and soft flexible substrates via dip-pen nanolithography.

Langmuir : the ACS journal of surfaces and colloids **28**, 804–11 (2012).

18. Jang, J.-W. *et al*. Arrays of nanoscale lenses for subwavelength optical lithography. *Nano letters* **10**, 4399–404 (2010).

19. Hernandez-Santana, A., Irvine, E., Faulds, K. & Graham, D. Rapid prototyping of poly(dimethoxysiloxane) dot arrays by dip-pen nanolithography. *Chemical Science* **2**, 211 (2011).

20. Stiles, P. L. Direct deposition of micro- and nanoscale hydrogels using Dip Pen Nanolithography (DPN). *Nature Publishing Group* **7**, i–ii (2010).

21. Nanoink inc. *Hydrogel Patterning (Tech note)*. 1–2 (2010).

22. Nanoink inc. *Patterning Functional Hydrogels (Tech note)*. 1–2 (2010).

23. Jang, J.-W., Smetana, A. & Stiles, P. Multi-ink pattern generation by dip-pen nanolithography. *Scanning* **32**, 24–9 (2010).

24. Fang, A., Dujardin, E. & Ondarçuhu, T. Control of droplet size in liquid nanodispensing. *Nano letters* **6**, 2368–74 (2006).

25. Ondarçuhu, T. *et al*. Controlled deposition of nanodroplets on a surface by liquid nanodispensing: Application to the study of the evaporation of femtoliter sessile droplets. *The European Physical Journal Special Topics* **166**, 15–20 (2009).

26. Fabié, L., Durou, H. & Ondarçuhu, T. Capillary forces during liquid nanodispensing. *Langmuir : the ACS journal of surfaces and colloids* **26**, 1870–8 (2010).

27. Malotky, D. L. & Chaudhury, M. K. Investigation of Capillary Forces Using Atomic Force Microscopy. *Langmuir* **17**, 7823–7829 (2001).

28. Men, Y., Zhang, X. & Wang, W. Capillary liquid bridges in atomic force microscopy: formation, rupture, and hysteresis. *The Journal of chemical physics* **131**, 184702 (2009).

29. Bhushan, B., Israelachvili, J. N. & Landman, U. Nanotribology: friction, wear and lubrication at the atomic scale. *Nature* **374**, 607–616 (1995).

30. Chilamakuri, S. K. & Bhushan, B. A comprehensive kinetic meniscus model for prediction of long-term static friction. *Journal of Applied Physics* **86**, 4649 (1999).

31. Hampton, J. R., Dameron, A. A. & Weiss, P. S. Double-ink dip-pen nanolithography studies elucidate molecular transport. *Journal of the American Chemical Society* **128**, 1648–53 (2006).

32. De Gennes, P. G. Wetting: statics and dynamics. *Reviews of Modern Physics* **57**, 827–863 (1985).

33. Gao, L. & McCarthy, T. J. Contact angle hysteresis explained. *Langmuir : the ACS journal of surfaces and colloids* **22**, 6234–7 (2006).

34. Ramos, S. & Tanguy, a Pinning-depinning of the contact line on nanorough surfaces. *The European physical journal. E, Soft matter* **19**, 433–40 (2006).

35. Pérez, E., Schäffer, E. & Steiner, U. Spreading Dynamics of Polydimethylsiloxane Drops: Crossover from Laplace to Van der Waals Spreading. *Journal of colloid and interface science* **234**, 178–193 (2001).

36. Gennes, D. Communications to the Editor. *Society* **37**, 10–12 (2004).

37. Mate, C. M. Application of disjoining and capillary pressure to liquid lubricant films in magnetic recording. *Journal of Applied Physics* **72**, 3084 (1992).

38. Van Honschoten, J. W., Brunets, N. & Tas, N. R. Capillarity at the nanoscale. *Chemical Society reviews* **39**, 1096–114 (2010).

39. Ma, J., Jing, G., Chen, S. & Yu, D. Contact Angle of Glycerol Nanodroplets Under van der Waals Force. *The Journal of Physical Chemistry C* **113**, 16169–16173 (2009).

40. Pismen, L. M., Rubinstein, B. Y. & Bazhlekov, I. Spreading of a wetting film under the action of van der Waals forces. *Physics of Fluids* **12**, 480 (2000).

41. Butt, H.-J. & Kappl, M. Normal capillary forces. *Advances in colloid and interface science* **146**, 48–60 (2009).

42. Cai, S. & Bhushan, B. Meniscus and viscous forces during normal separation of liquid-mediated contacts. *Nanotechnology* **18**, 465704 (2007).

43. Hampton, J. R., Dameron, A. A. & Weiss, P. S. Transport rates vary with deposition time in dip-pen nanolithography. *The journal of physical chemistry. B* **109**, 23118–20 (2005).

44. Wu, T.-H., Lu, H.-H. & Lin, C.-W. Dependence of transport rate on area of lithography and pretreatment of tip in dip-pen nanolithography. *Langmuir : the ACS journal of surfaces and colloids* **28**, 14509–13 (2012).

45. Collins, J. M. *et al*. Targeted delivery to single cells in precisely controlled microenvironments. *Lab on a chip* **12**, 2643–8 (2012).

46. Eijkel, J. C. T. & Van den Berg, A. Young 4ever--the use of capillarity for passive flow handling in lab on a chip devices. *Lab on a chip* **6**, 1405–8 (2006).

47. Yang, S. H., Nosonovsky, M., Zhang, H. & Chung, K.-H. Nanoscale water capillary bridges under deeply negative pressure. *Chemical Physics Letters* **451**, 88–92 (2008).

48. Gao, C. & Bhushan, B. Tribological performance of magnetic thin-film glass disks: its relation to surface roughness and lubricant structure and its thickness. *Wear* **190**, 60–75 (1995).

49. Brakke, K. a. The Surface Evolver and the Stability of Liquid Surfaces. *Philosophical Transactions of the Royal Society A: Mathematical, Physical and Engineering Sciences* **354**, 2143–2157 (1996).

50. Minne, S. C. *et al*. Centimeter scale atomic force microscope imaging and lithography. *Applied Physics Letters* **73**, 1742 (1998).

Chapter 6: Variation in feature size due to ink-on-probe hydrodynamics in liquid ink DPN

6.1 Introduction

In dip-pen nanolithography (DPN), an atomic force microscope (AFM) tip is used to deposit material onto a substrate with nanoscale resolution and registry.[1] The mechanism of transport of molecular inks, typically alkanethiols, from tip to substrate is a well-studied problem.[2-12] Several studies of molecular ink DPN have shown how deposition rate is dependent on the level of inking of the pen.[3,13] Adjusted models have been proposed to account for the effect of depleting ink-level on deposition rate over long term printing.[3,14]

Recently DPN has been used to print liquid ink formulations.[15-22] In contrast to molecular ink DPN, where ink depletion may constitute a minor adjustment to the prevailing model, the depletion of liquid inks causes a dramatic change in deposition rate. For example, it is accepted procedure to 'bleed' a tip of excess liquid ink before 'reproducible' dot sizes can be printed.[15,16,19] In **Chapter 5**, we found that volume of ink on the cantilever may be a critical parameter affecting deposition rate. In this chapter, we show that deposition rate depends not just on the volume of ink, but on the relative location of the ink on the cantilever (and on the tip itself) and that this ink distribution is subject to dynamic reorganisation.

The same model ink system of highly viscous Norland Optical Adhesives (NOA) inks on silicon is used as in the previous chapter. Firstly, dynamic measurements of DPN cantilever stiffness are used to quantify ink-loading, and it is shown that the inking rate of the pen using an ink-well is describable in terms of an exponential loading function. Next, the changing deposition rate over a long term printing experiment is probed by measuring dot sizes of 2000 dots comprising all four NOA inks. The deposition rate is found to change over three distinct regimes, and these are understood to arise from changes in (I) ink volume on cantilever, (II) 'rest-time' between grids and (III) travel time between individual dots. Our results indicate that a heretofore unreported phenomenon is dominant in defining dot size for liquid inks: that of ink movement and reorganisation on the probe itself. In light of our conclusions, we pose critical questions of reservoir-on-tip liquid ink DPN as a nanofabrication technique and discuss the various parameters which must be controlled in order to achieve uniformity of feature size.

6.2 Experimental

6.2.1 Materials

Octadecyltrimethoxysilane was obtained from Sigma Aldrich. Norland Optical Adhesives are highly viscous, UV curable, acrylic based liquid adhesives. Formulations presenting a range of viscosities (NOA 65, NOA 68, NOA 68T and NOA78) were obtained from Norland Products (Cranbury, N.J., USA). Characterisation of ink properties is included in **Chapter 5**.

6.2.2 Substrate preparation

Silicon wafer pretreatment

Si/SiOx wafers were pretreated with a generic cleaning protocol consisting of bath sonication while immersed in various solvents (acetone,

isopropanol, water). This was followed by a hot piranha treatment (immersion in a freshly prepared 1:3 ratio H_2O_2:H_2SO_4 mixture for 30 minutes at 80 °C) and final rinsing with copious deionized water (Milli-Q).

Preparation of hydrophilic and hydrophobic Si substrate

Smooth, hydrophilic substrates were prepared by plasma treatment of a Si/SiOx wafer (Harrick Plasma Cleaner, O_2 or air plasma at 1100 mTorr, 10 mins) immediately prior to DPN printing. Hydrophilicity of the substrate was confirmed by water contact angle (~0°).

Smooth, hydrophobic substrates were prepared by functionalization of the Si/SiOx substrate with octadecyltrimethoxysilane (ODTMS). Briefly; after pretreatment the substrates were plasma treated (as above), then immersed in a freshly prepared solution of 0.1% ODTMS in isopropanol for 5 minutes, before a further 5 minutes on a hotplate (80 °C) for 5 minutes. The substrates were dipped in the 0.1% ODTMS/isopropanol solution and placed on the hotplate (80°C, 5 minutes) a further three times to ensure consistent levels of silanization. Hydrophobicity of the substrate was confirmed by water contact angle (~88°). This degree of hydrophobicity was maintained for several weeks as confirmed by repeated water contact angle measurements.

6.2.3 DPN methodology

DPN patterning was performed using an Nscriptor system (NanoInk, Skokie, IL) in an environment controlled at 45% relative humidity and 22°C temperature. The NOA ink of interest was wetted onto a single probe on an array of NanoInk M-Type probes (NanoInk part # PEN-0300-03, material Si3N4, length 107 µm, width 22 µm, spring constant 0.5 N/m) by dipping into the filled microwell of a NanoInk Universal Inkwell (part # IWL-0009-03). The tip was bled of excess ink in a method similar to that previously reported for DPN of liquid inks by bringing it in contact with the substrate in several (typically 4-5) locations, until deposition of large ~10 µm 'bleed-

spots' ceased. Patterns were generated using the InkCAD software (v 2.7.1) provided with the Nscriptor system. Thermal resonance frequencies of probes were measured using SPM Cockpit software (Pacific Nanotechnology). For long term printing studies, up to four pens were loaded with different inks and printed simultaneously.

Line writing was also attempted with each ink-substrate system, however no continuous lines could be formed. In each case the lines beaded up into individual droplets. Droplet deposition only is discussed in this chapter.

6.2.4 AFM measurements

Topographical images were generated on the Asylum MFP-3D instrument in intermittent contact mode. Morphologies of the printed features were analysed using the Particle Size plug-in for the Asylum Research software.

6.2.5 Optical microscopy and image analysis

Optical microscopy images were taken on a Leica DM6000 microscope at x50 magnification and with a resolution of 3408 x 2592 pixels.

Image analysis was performed on Igor Pro software. Microscope images were converted to binary images using automated iterative thresholding. Particles were identified by the software, the area in pixels counted, and the number of pixels converted to a physical area (um^2). Feature radii were determined from the measured area by assuming a circular shape.

Dot volume calculation

Studies of DPN deposition rates have usually analysed 'dot-size' in terms of dot radius, dot area or feature edge length.[3,8] The assumption that DPN patterns form only two dimensional features is reasonable for molecular inks (e.g. alkanethiols on gold). These self-assembled monolayer (SAM) systems form through two-dimensional diffusion.[31] The characterisation of

liquid ink deposition is complicated, however, by the three-dimensional shape of any deposited feature. Any ink calibration or deposition dynamics data plotted in terms of radius, or dot area, tells only part of the story. A more thorough interpretation of liquid ink deposition dynamics must take account of dot volume.

In sections 6.3.2 to 6.3.5 data is analysed for a large number of dot features. Rather than measure the volume of all of the features directly (e.g. by direct AFM imaging), we convert the dot radii measured by optical microscopy to volume using the ink-substrate contact angle and the geometry of a spherical cap. We show in section 5.3.3 below that the contact angle of droplets with radius >1 μm will assume a morphology with macro-scale contact angle.

6.3 Results and discussion

6.3.1 Quantifying ink loading using cantilever resonance

The original method of loading a DPN pen with molecular inks (and the method from which the moniker "dip-pen nanolithography" originates) was to dip the whole cantilever chip into a dilute alkanethiol solution, and then to dry off excess solvent in a stream of inert gas.[1] This method suffers from an unreliability in ink loading.[2] Improved inking methods have since been used including vapour deposition and ink-jet printing.[13]

The most reliable method for loading a DPN pen with liquid ink is to dip the tip in a specifically tailored microfluidic ink-well.[23] These ink-wells also enable the multi-plexed inking of several different liquid inks on the same pen array, a capability especially interesting for patterning arrays of multiple different proteins.[24] Dipping the DPN pen in an ink-well ensures that the ink sits directly on the tip (as opposed to another equilibrium position along the base of the cantilever). Furthermore, an etched

underside reservoir (as in the Nanoink M-type probes used in this study) can increase the volume printable by an inked pen, and hold the ink in place to feed the tip during the writing step. However, as we have seen above, the deposition rate depends critically on the ink loading. A method to quantify ink loading is required.

In 2011, the Fuchs group demonstrated the possibility of using the resonance frequency of the DPN cantilever to directly quantify the mass of phospholipid deposited during writing.[25] The group calculated a theoretical mass sensitivity of 0.07 pg from the measurable change in cantilever resonance after deposition of individual dots of phospholipid.

Where M is the effective mass of the cantilever, and f is its resonant frequency, the change in mass of ink on the cantilever, Δm, can be calculated from the change in resonance frequency, Δf, by:[25]

$$\Delta m = -2\frac{M}{f}\Delta f \quad (1)$$

We have adapted this methodology in order to quantify the rate of inking of a DPN cantilever with liquid inks. Figure 6-1 (A) below shows the change in resonance frequency of a DPN cantilever as it was dipped in an inkwell for successive times and the corresponding ink volume calculated from these resonance frequencies using equation 1 and the ink density. All NOA inks appear to follow similar loading rates, regardless of viscosity (Figure 6-1 (B)). Figure 6-1 (C) and (D) show optical micrographs of an M-type probe before and after inking respectively.

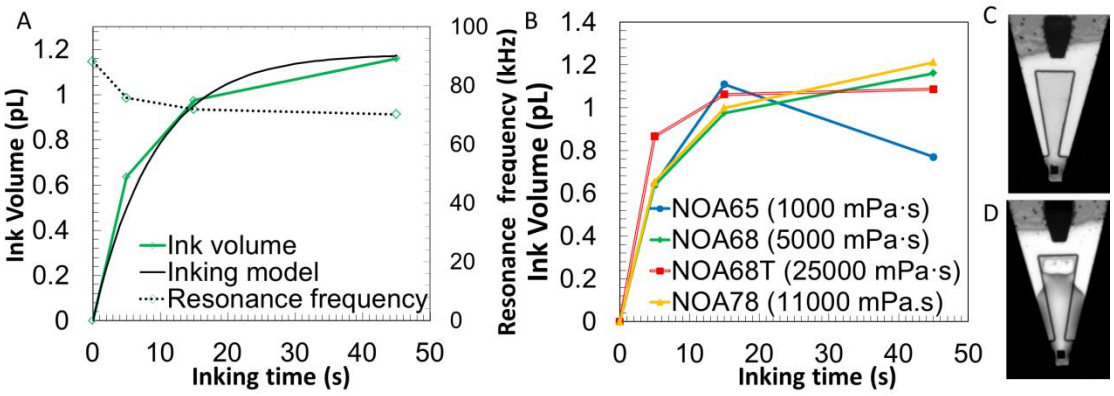

Figure 6-1: Quantifying ink loading by monitoring cantilever resonance frequency: (A) Cantilever resonance and ink volume as a function of time dipped in an ink-well filled with NOA 68 (5000 mPa.s). The dotted green line shows the change in resonance frequency (right-hand axis) of a DPN cantilever. The solid green line shows the corresponding ink volume (left-hand axis) calculated from these resonance frequencies using equation 11 and the ink density (1.137 g/ml). The solid black line represents the ink loading model (equation 2) using adjustable parameters for cantilever capacity V_C=1.18 pL and ink filling time constant λ_f=0.11 s^{-1}: (B) Ink loading as a function of dip-time for all NOA inks. All inks load according to a similar exponential functions. The decrease in ink loading of NOA65 (blue line) at 45 s loading was probably caused by poor registry of the pen with the ink-well, resulting in deposition of ink on the sides of the well, rather than loading of ink from the well. This aberration highlights the limitations of this system of inking when using instrumentation with poor registry. (C) Optical micrograph of a 'dry' M-type probe (before inking). (D) Optical micrograph of an M-type probe after inking with NOA68T ink.

The ink loading rate appears to slow as ink is loaded on the cantilever. We have found empirically that an exponential loading function (analogous to that of a charging capacitor) fits the data (Figure 6-1 (A)). The volume of ink on the cantilever as a function of time, $V(t)$, depends on the capacity of the cantilever reservoir (V_C), the time constant for ink loading (λ_f) and loading time (t) by:

$$V(t) = V_C(1 - e^{-t/\lambda_f}) \quad (2)$$

The fit of the ink loading model to the data illustrates the possibility of controlling the degree of inking of a DPN cantilever using dip-time. The similar ink-loading rates for the different NOA inks suggests the exponential

ink loading behavior may be general for all inks, and may not have a significant dependency on viscosity. As the deposition rate in liquid ink DPN is so critically dependent on ink loading, the capability to measure ink loading *in-situ* using the shift in cantilever resonance frequency may prove crucial for precise pen calibration.

6.3.2 Investigating long term printing behavior

We have investigated the change in deposition rate of all NOA inks as a function of ink loading on the hydrophobic silicon substrate. Successive grids of 25 dots (dwell time 5s) were printed simultaneously with 4 pens, each loaded with a different ink. The dot grids were then imaged by optical microscopy and analysed with image analysis software. In this way, data was obtained for the sizes of thousands of dots, comprising 4 different inks, over the course of an experiment. Dot-size data could be organised in terms of the order each dot was printed.

Figure 6-2 shows the pattern design and typical raw data for this experiment. Figure 6-2 (A) shows the programmed grid comprised of 25 dots at a pitch up 10 μm. All dots were printed using a dwell time of 5 seconds, and were printed in raster fashion, beginning with the bottom-left and finishing in the top-right (the dots in the figure are numbered in the order printed). Figure 6-2 (B) shows an optical microscopy (bright field) image of a typical printed grid on SiOx(-CH_3). Figure 6-2 (C) shows an optical microscopy image of a sequence of grids printed by 4 pens, each inked with different NOA inks.

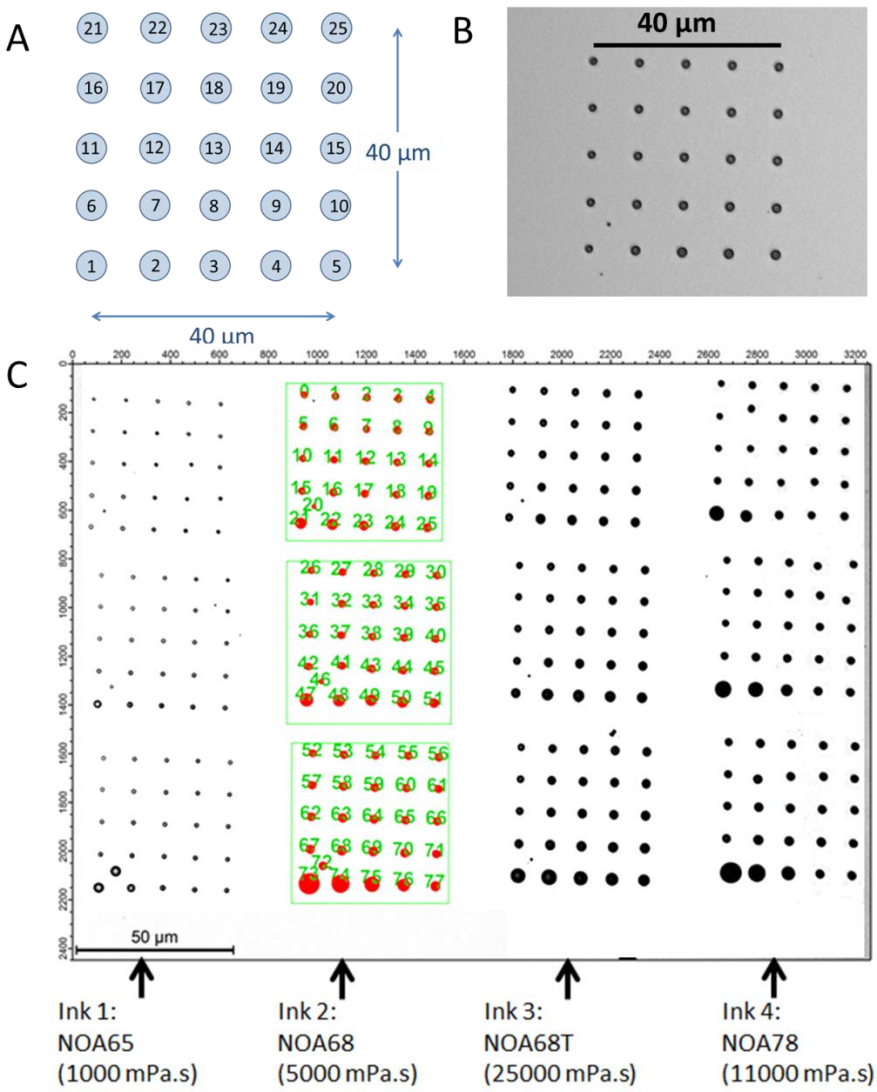

Figure 6-2: Pattern design and typical raw data. (A) A single grid was comprised of 25 dots at a pitch up 10 µm. All dots were printed using a dwell time of 5 seconds, and were printed from bottom-left to top-right as numbered; (B) Optical microscopy (bright field) image of a typical grid on SiOx(-CH_3); (C) Bright-field optical microscopy of a sequence of grids printed by 4 pens, each inked with different NOA inks. The image has been processed (using an iterative thresholding algorithm) to create a binary image of black dots on a white background. Image analysis enables high throughput measurement of feature size. The labeling of each individual feature (in this case # 0-77) enables analysis of the results in terms of the order in which they were printed. (The green boxes define the region of interest for which dot sizes are measured.) The extra dot in the bottom-left corner of some grids was deposited during the initial approach of the pen finding the surface and entering feedback mode. This extra dot is not included in the analysis.

Figure 6-3 below shows the results generated using image analysis for a typical long term printing experiment. Dot radius is plotted against dot number (i.e. order printed) for 500 dots of each of the four NOA inks. All dots were printed using the same dwell time (5 s). If the deposition rate were consistent over the experiment, one would expect each ink to form 500 sequential dots with similar radii. On the contrary, the dot radii changed significantly for all inks over the course of the experiment. In general, dots printed near the beginning (numbers 1-50) had radii between 2.5 and 4 μm, whereas near the end (numbers 500-550) dot radii decreased to between 0.5 and 1.5 μm. In addition, a periodic 'spiking' in dot radii can be observed for all inks. Each spike coincides with the beginning of a new grid (marked by an asterix in the figure), meaning that the first few dots printed in each grid were much larger than average. The optical image Figure 6-2 (C) clearly illustrates this behaviour; the NOA78 ink in particular has noticeably larger dots at the beginning of each grid.

As the four NOA inks present a range of liquid properties (e.g. viscosity), one might expect to observe intrinsic differences in deposition rate between inks. However, any intrinsic differences in deposition rate are washed out by the general decline in feature size and the spiking effect. This echoes the conclusion from **Chapter 5**, that deposition rate is more dependent on the volume of ink on the cantilever than on liquid properties.

The variation in dot radii shown in Figure 6-3 is not random fluctuation. We have identified three distinct scales of repeating structure in these data. The remainder of this chapter will elucidate a hierarchy of three regimes of printing behavior in DPN of liquid inks: (I) the long term decline in dot-size due to depletion of ink from the cantilever, (II) 'spiking' in dot-size at the beginning of each grid caused by pooling of ink around the tip during the wait-time between printing of grids, and (III) an oscillation in dot-size along lines of dots caused by the reorganization of ink on the tip between printing of individual features.

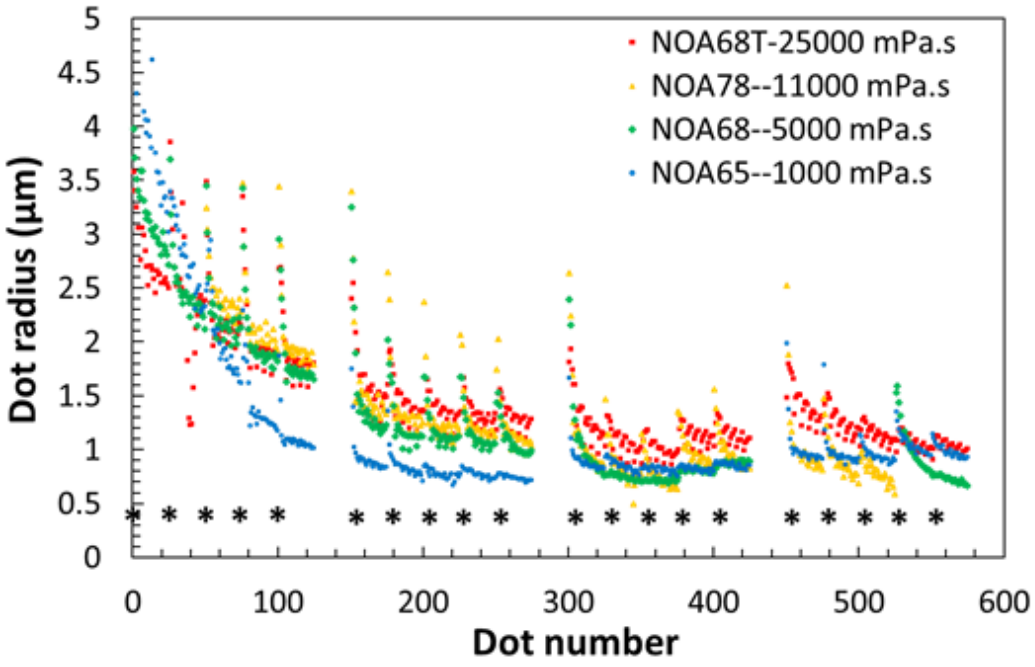

Figure 6-3: Long term printing data for all inks. Dot radii measured for 20 grids (>500 individual dots at 5s dwell time) for each of the four NOA inks printed over the course of 2 hours on hydrophobic Si (>2000 dots total). The NOA68T (25000 mPa.s) ink is represented by red squares; the NOA78 (11000 mPa.s) ink is represented by yellow triangles; the NOA68 (5000 mPa.s) ink is represented by green diamonds and the NOA65 (1000 mPa.s) ink is represented by blue circles. A gradual decline in dot-size over the course of the experiment is clear. A periodic 'spike' in dot radii coinciding with the commencement of each new 25-dot grid (each marked by an asterix) is also visible.

6.3.3 Dynamic regime I: Gradual decay in deposition rate

The requirement for depositing 'bleed spots' at the beginning of a liquid ink DPN experiment, before a 'stable regime' of printing is reached, has been well reported.[15,16,19,26] Although there has been no dedicated study of the decline in liquid ink deposition rate over a long term patterning procedure (as have been performed for molecular inks)[3,14] the exponential nature of the decay has been noted.[25]

In Figure 6-4 we show the decline in dot size over the course of a ~2hr printing experiment. (The data analysed is for the same experiment presented above in Figure 6-3, and is composed of over 500 dots for each NOA ink.) Figure 6-4 (A) shows the dot volume (see experimental section for method of calculating dot-volume from radius) for the NOA68 ink. The dot volume declines in the manner of an exponential decay, though some aberrant 'spikes' in dot-size are observed. To negate these other dynamic effects (described later) the dot-volumes are averaged for each grid (Figure 6-4 (B)).

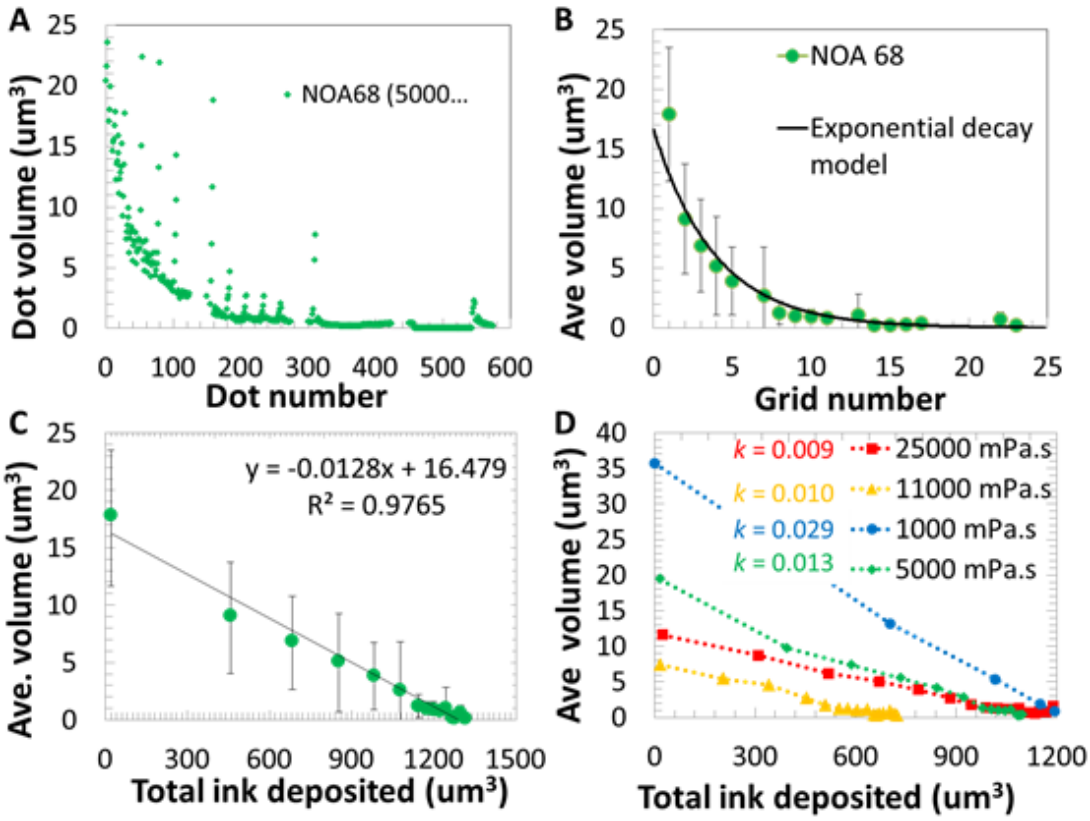

Figure 6-4: Long term decline in dot-size over consecutive 5 x 5 dot arrays: (A) Volume of >500 individual dots plotted against dot number for the NOA68 (5000 mPa.s at 22°C) ink; (B) The same data converted to dot volume and averaged per grid number (green circles). The black line represents the expected dot volumes calculated from the exponential decay model (equation (3)) with decay constant k=0.0128 and volume calculated from the cantilever resonance ($V_{res(o)}$= 1300 μm^3); (C) Plot of dot volume averaged per grid versus total ink deposited. Each green circle represents the average volume of 25 dots in one grid. The slope of the linear fit gives the decay constant used

in the exponential decay model; (D) Plot of grid averaged dot volume versus total volume of ink deposited for all NOA inks. Each ink demonstrates linear behaviour with slopes, k= 0.029 for NOA 65 (1000 mPa.s), k=0.013 for NOA 68 (5000 mPa.s), k=0.010 for NOA 78 (11000 mPa.s) and k=0.009 for NOA 68T (25000 mPa.s). We note that the decay slopes increase with decreasing ink viscosity, suggesting a role for viscosity in the printing rate.

Figure 6-4 (C) shows a plot of the grid averaged dot volume versus the total volume deposited. The plot yields a linear relationship, meaning that the decline in deposition rate is directly proportional to the total volume deposited. (Conversely, deposition rate is thus directly proportional to the volume of ink on the cantilever.) Beginning with the assumption that deposition rate is proportional to the volume of ink on the cantilever, a simple empirical model of exponential decay behaviour can be developed (detailed derivation included in Appendix 6.5.1). A similar line of argument has been followed to model the exponential decay in deposition rate for molecular ink DPN.[14] The volume of dot 'n' ($V_{dot(n)}$) is related to the decay constant (k), the initial volume in the cantilever reservoir ($V_{res(o)}$), and the deposited volume (V_{dep}) by:

$$V_{dot(n)} = -kV_{res_{(0)}}e^{-kV_{dep}} \quad (3)$$

This expression can be used to predict the decay in feature size over the course of a long term experiment. Figure 6-4 (B) shows a model of exponential decay plotted using equation (13). The decay constant, k, was taken as equal to 0.0128 from the negative slope of the dot volume vs volume deposited plot (Figure 6-4 (C)). The volume of ink in the reservoir at the beginning of the experiment, $V_{res(0)}$, was measured as 1300 μm^3 via the cantilever resonance frequency (section 6.3.1). The decay model shows a good fit to the measured dot volume data.

In Figure 6-4 (D) the grid average dot volume versus volume deposited for each of the four NOA inks. A linear relationship is found in each case, showing that the exponential decay dynamics hold for all inks. Interestingly, the decay slopes tend to increase for decreasing ink viscosity.

This may suggest a role for viscosity in the deposition rate. Lower viscosity inks will move more rapidly from the 'bleed' regime, to a regime of more stable deposition.

6.3.4 Dynamic Regime II: Time dependent reloading of tip during rest time between grids

The periodic, sharp spikes in dot-size evident in Figure 6-3 coincide with the dots printed at the start of each new grid. This spiking effect occurred at the beginning of all grids printed and for all four NOA inks. This behaviour appears superimposed on the gradual exponential decay (caused by the gradual depletion of V_{res}), and so we supposed it to have a separate origin.

In order to investigate this 'Regime II' behaviour, the long-term printing experiment was repeated with one augmentation; the elapsed 'rest time' between each printed grid was now controlled. Figure 6-5 (A) shows dot volume (for clarity, the NOA68 ink only is shown) plotted against the time of deposition (rather than dot number). A series of 5 grids is shown. Each grid is labelled with the 'rest time' elapsed before it was printed: 540 s rest time preceded the first grid, 30 s rest preceded the second grid, 60 s rest preceded the third, 120 s rest preceded the fourth and 240s rest preceded the fifth. The grids printed after longer rest times show greater increases in dot volume (i.e. an increased magnitude of the spiking effect). This indicates that the spiking effect is time dependent. The time dependency of the spiking effect is quantified in Figure 6-5 (B) (discussed below).

We suggest that the increase in deposition rate at the beginning of each grid arises from movement of ink along the DPN cantilever itself. As described in section 6.3.3 above, the deposition rate of printed features depends on the volume of ink contained in the cantilever reservoir. Any ink transferred from the reservoir to the substrate, however, must deposit via

the tip. As illustrated in Figure 6-5 (C) we consider the cantilever divided into two regions; (1) the cantilever reservoir (holding the ink volume V_{res}), and (2) the tip reservoir (holding the printable local volume V_{tip}). We suggest that when a grid is printed, the area around the tip is locally depleted of ink (V_{tip} is low). This local depletion of ink sets up a gradient in Laplace pressure along the cantilever, causing ink to flow from the cantilever reservoir (V_{res}) to replenish the tip reservoir (V_{tip}).

In order to quantify the tip reload rate, a method is first required to calculate the relative increase in ink volume on the cantilever ΔV_{tip} due to this replenishment. Briefly, the volume of the final dot of the previous grid is used to define a baseline dot-size. Any increase in dot-size above this value is attributed to the loading of excess ink onto V_{tip}. The excess volume ΔV_{tip} is then calculated by integrating the accumulative dot volume of the second grid above this baseline. (The calculation is illustrated in Appendix 6.5.2.) Figure 6-5 (B) shows a plot of the tip reload volume versus the rest time.

We model rate of tip reload by supposing that the reload rate is inversely proportional to V_{tip} (a similar argument was used to derive the ink loading function in section 6.3.1 above). The volume of ink in the tip reservoir (V_{tip}) depends on the maximum volume capacity of the ink reservoir (V_{max}), a reload time constant (λ_r) and time (t), by:

$$V_{tip} = V_{max}(1 - e^{-t/\lambda_r}) \quad (4)$$

In Figure 6-5 (B) we input the adjustable parameters of V_{max}=54 μm^3, a reasonable figure considering the tip geometry, and the reload constant (λ_r=303 s^{-1}) to achieve a good fit for the model to the experimental data. The time constant λ_r corresponds approximately to the time taken to reload V_{tip} to half its maximum volume.

The slow reload of V_{tip} by V_{res} is likely due to their separation by a thin-film, resulting in a flow bottleneck. The reload rate may be dictated

ultimately by the thickness of this film, as well as the Laplace pressure difference along the cantilever. Further work, such as the geometrical modelling of the liquid coated cantilever, is required to understand the dimensions of this film and its effect on reload rate.

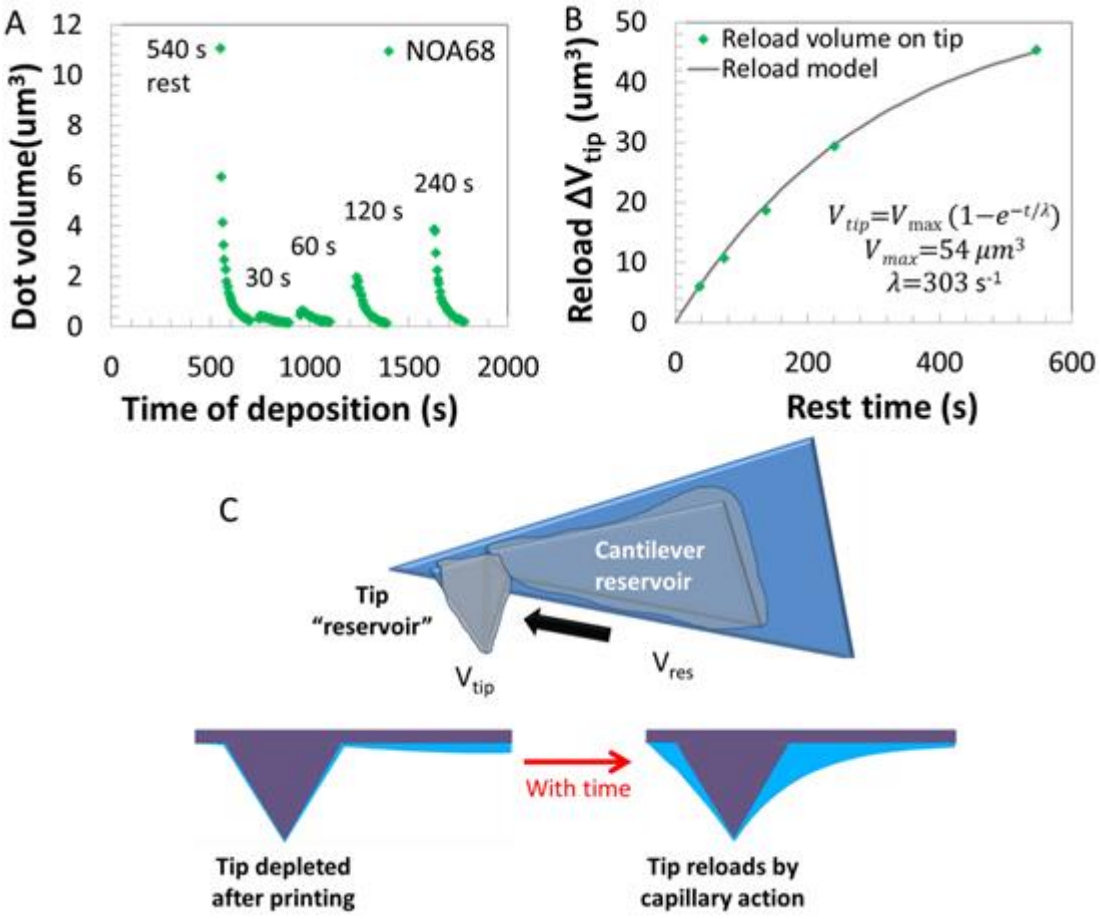

Figure 6-5: Quantifying the effect of 'rest time' between grids. (A) Dot volume versus relative time of deposition for the NOA 68 ink. A spike in dot-size occurs at the beginning of each new grid of 25 dots. The magnitude of the spike increases for longer 'rest time' between grids. We suggest the spike in deposition rate occurs due to a 'reloading' of ink from the cantilever reservoir to the DPN tip (explanation in text). Dot-volume within each grid also exhibits an exponential decay; (B) Relationship between the volume of ink reloaded onto the tip (calculation discussed in text) and the rest time. Inset is the equation of the empirical tip reload model using the adjustable parameters V_{max} = 54 μm^3 and λ= 303 s^{-1}. (C) Ink on tip dynamics. We consider the DPN cantilever as divided into two regions; the cantilever reservoir (containing ink volume V_{res}) and the tip reservoir (containing the much smaller volume V_{tip}). Ink is depleted from V_{tip} during deposition, but V_{tip} can reload in the rest time between grids.

The phenomenon of ink movement on a DPN probe itself has been discussed only rarely in the literature, and never quantified. For molecular inks, deposition of molecules must cause a localised depletion of ink at the tip. In turn, a concentration gradient must be set up along the cantilever, which may drive Fickian diffusion. It is unknown whether such ink-on-tip dynamics have a significant effect on DPN deposition rates. The Mirkin group proposed an increased migration rate of alkanethiols on the AFM tip as a possible mechanism for increased transport rate in an organic vapour environment.[27]

The introduction of 'rest time' between grids as a crucial parameter has implications for future liquid ink DPN fabrication methodologies. In addition, the identification of two distinct ink reservoirs on the cantilever may influence rational cantilever design. While cantilever resonance frequency allows a measurement of the total volume on the cantilever, it does not provide information on the relative distribution of the ink between V_{tip} and V_{res}. A greater understanding of the ink transfer dynamics could be gained by performing an experiment for which V_{tip} was exactly known. Although we have not explored this route, such an experiment may be possible by dipping a dry cantilever tip into a very small volume (for example into a pre-deposited DPN droplet sitting on a surface). By measuring the dot volume (AFM topography) before and after dipping, the exact volume of ink on the DPN tip could be inferred.

6.3.5 Dynamic regime III: the first dot effect

Upon examining the dot-sizes of individual grids and individual lines, we noticed a further substructure to the data. As illustrated in Figure 6-6 we observed a repeated oscillation in dot-size on the level of single rows of 5 dots. In general, for all four inks, the first dot in a row was smaller than the following dots. (This sequential increase in dot-size is a reversal of the behaviours we have already seen). Qualitatively the strength of this 'first

dot effect' appeared to increase with increasing ink viscosity, a relationship which is explored more explicitly below.

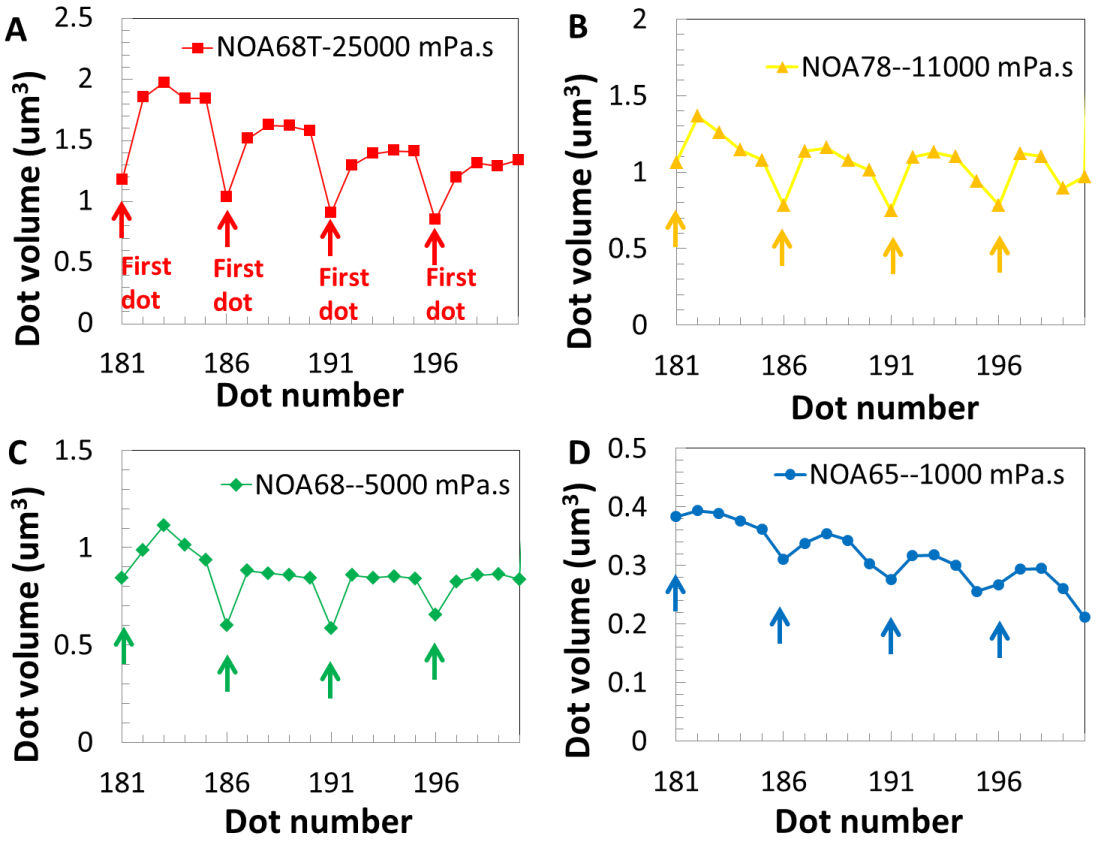

Figure 6-6: The first dot effect. Dot volumes measured from 4 lines of a typical 5 x 5 dot array for all inks (data shown is a magnified subsection of Figure 6-3). Dots printed at the beginning of new rows (as indicated by arrows) are generally smaller than those following in the same row. (A) NOA68T (viscosity 25000 mPa.s) in red; (B) NOA78 (viscosity 11000 mPa.s) in yellow; (C) NOA68 (viscosity 5000 mPa.s) in green; (D) NOA65 (viscosity 1000 mPa.s) in blue.

Origin of the first dot effect

We suggest that the first dot effect originates from ink-dynamics at a much smaller scale than described above,that is ink movement along the pyramidal DPN tip itself. To describe our suggested mechanism for this behaviour we must subdivide the pyramidal DPN tip into two regions; (1) the 'tip reservoir', located at the base of the pyramid and (2) the tip apex, the sharp point which actually contacts the surface.

When a liquid sits in contact along the intersection between two surfaces, it will form a meniscus shape with curvature as governed by the Young-Laplace equation.[28] In the case of a pyramidal DPN tip, ink tends to accumulate at the base of the pyramid where it meets the cantilever. (This comprises the 'tip reservoir' described in regime II above.) In this equilibrium arrangement, only a thin film of ink wets the tip apex (Figure 6-7 (A)). When the tip contacts the substrate, however, a Laplace pressure gradient is set up which drives the ink into the deposition meniscus (Figure 6-7 (B)). When the tip retracts, a meniscus 'bridge' is distended between the tip and substrate (**Chapter 5**). When the meniscus bridge breaks, ink is deposited on the surface. Not all of the ink contained in the meniscus is deposited, however. The non-deposited ink remains on the tip, close to the apex (Figure 6-7 (C)).

If the next dot is printed almost immediately (time between printing dots on same row ~0.2s) this ink at the apex is readily available. Again, following our general argument that the deposition rate is proportional to the volume of ink on the tip, the second dot in the row will be larger than the first (Figure 6-7 (D)). This effect repeats for the rest of the dots on the same row (Figure 6-7 (E)). At the end of the row, however, there is an additional travel time (~1 s) while the tip moves to start the next row. This is enough time for ink on the tip to retract to its equilibrium position again at the base of the pyramid (Figure 6-7 (F)). The first dot of the next row is again small, and the cycle repeats.

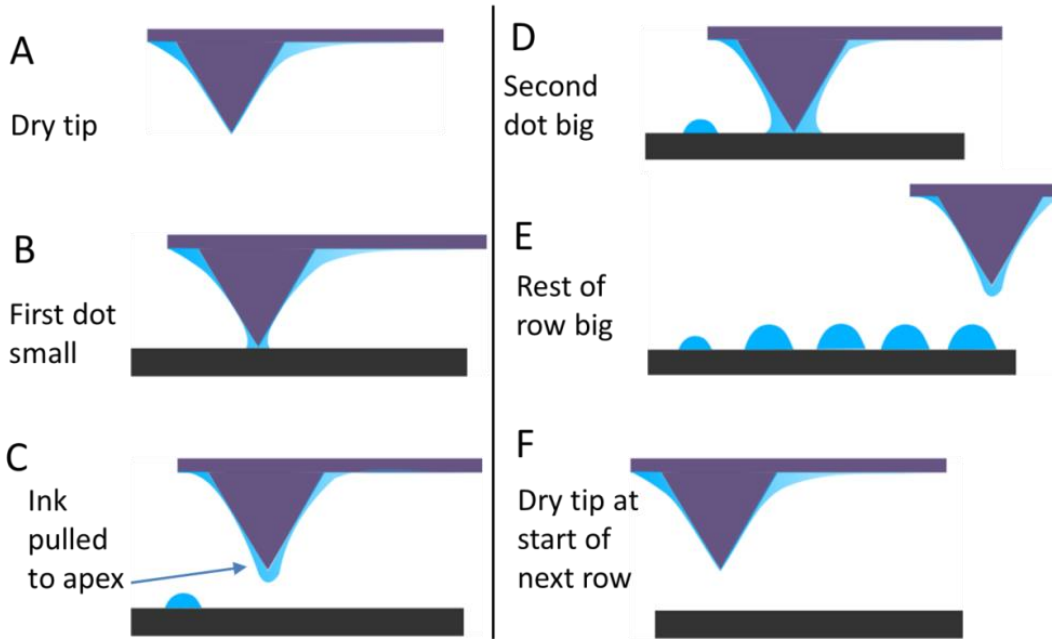

Figure 6-7: Illustration of the suggested origin of the first dot effect. (A) At the start of a new line, the ink is held in its equilibrium position at the base of the pyramid. (B) The first dot deposited is smaller than subsequent dots as there is less ink available near the tip apex. (C) The act of printing the first dot pulls ink down to the apex, and so (D) the second dot is larger than the first. (E) The following dots on the same line are also large. (F) At the end of the line the one second rest period while the pen moves to print the next line is enough for the ink to return to its equilibrium posistion away from the tip apex. The cycle repeats.

Quantifying the first dot effect

In order to quantify the first dot effect, it must be examined in the absence of other trends in deposition rate. Both the gradual exponential decay in dot size (regime 1) and the tip-reload effect at the start of each grid (regime II) must be excluded. We can isolate the first dot effect by considering only dot-size variations within each row. By dividing the size all 5 dots in a row by the size of the first dot in that row, we remove any long term or grid level trends in deposition rate. Thus the dot-size data is normalised, on a row by row basis, against the first dots printed in each that row.

Figure 6-8 (A) shows a plot of normalised dot-volume for 500 dots of each NOA ink against the order each dot was printed (the data is the same as shown in Figure 6-3 above). This figure provides a measure for the relative fluctuation in dot volume caused by the first dot effect. The magnitude of the first dot effect is not trivial. For example, dot-volumes for the NOA 68T ink (red line) often show an increase of over 1.5 times relative to the first dot volumes. Fluctuation in dot-size on a row-by-row basis is much greater for the NOA68T ink than the other inks.

The data shown in Figure 6-8 (A) bears a strong resemblance to signal noise. We quantify the degree of variance of normalised dot-volume using root mean squared (RMS) variance. Figure 6-8 (B) shows the RMS variance of the normalised data plotted against ink viscosity. As mentioned above, the highest viscosity ink (NOA68T) exhibited the greatest fluctuation in dot volume and therefore has the highest RMS variance (=0.35). For the four inks printed in this study, RMS variance shows a linear relationship with viscosity. This suggests that the intrinsic liquid properties of an ink may be an important indicator of achievable printing uniformity.

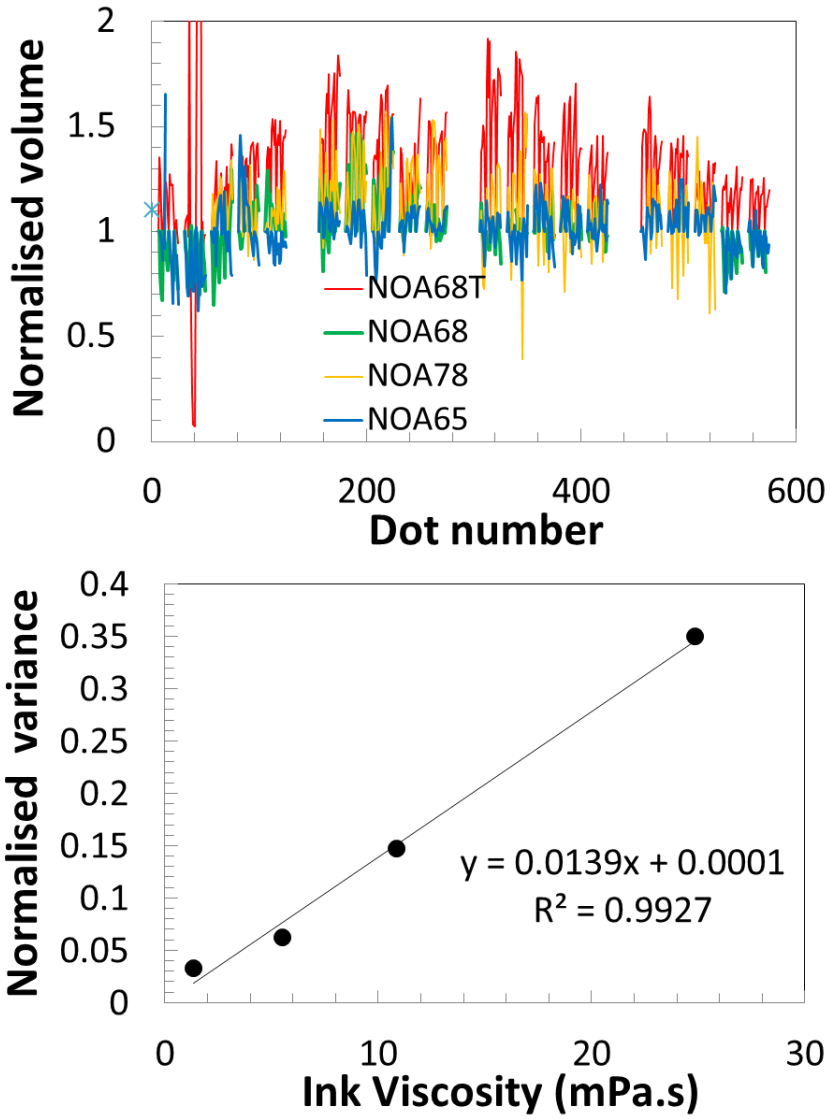

Figure 6-8: RMS mean variance data. In order to quantify the first dot effect in isolation, we normalise the size of dots in each line against the first dot of that line. (A) The plot of normalised volume versus dot number for the all 2000 dots (data same as shown in Figure 6-3) illustrates the printing 'noise' not a result of either the exponential decay (regime I) or the tip reload effect (regime II). (B) The root-mean squared variance of the normalised data shows a linear dependence on ink viscosity. This result has significant implications for the achievable feature-size uniformity when DPN printing highly viscous inks (discussed in text).

To our knowledge no behaviour like this 'first dot effect' has previously been reported in the DPN literature. In particular, the oscillatory nature of the pattern in dot-size may be unique to liquid ink DPN. (The oscillation derives from the Laplace pressure gradient which points down towards the

deposition meniscus when the tip contacts the substrate, but points up towards the base of the pyramid when the tip is not in contact.)

It is true that the first dot effect could be reduced by a simple redesign of the printing order of the 5 x 5 dot grid (for example to print in a 'snaking pattern' rather than a raster scan). Printing features uniform distances apart will not be possible for all patterns, however.

For the most highly viscous ink (NOA68T), the RMS variance is 1.35, meaning a ~35% standard deviation in dot volume, corresponding to a ~10% variance in dot radius. Although this value seems very high, a 10%-15% variance in dot radius is commonly reported in DPN of liquid inks.(Nanoink App notes) Although inhomogeneities in local substrate wettability and roughness may contribute to this variance, our results suggest that ink-on-tip dynamics, inherent to the technique, is the dominant factor. The apparent dependence of variance upon ink viscosity implies that the achievable uniformity in feature-size may depend on inherent ink properties, and not only on consistency of experimental conditions.

In this study, we have repeatedly found evidence that the printing rate is dependent on the local ink volume on the tip. The deposition of ink will, by necessity, modify this local volume and thus affect the printing rate. Lower viscosity inks will 'recover' local tip volume at a faster rate, and so print more uniform features. Lower viscosity usually means higher volatility, however, and volatile inks are unsuitable for DPN.

6.4 Conclusions

A system of model, high viscosity liquid inks were used to elucidate several distinct phenomena related to how depletion of ink volume and flow of ink on the DPN probe affects deposition rate.

Firstly, dynamic measurements of DPN cantilever stiffness were used to quantify ink-loading. It was shown that the loading of ink onto the tip from a micro-well is describable in terms of an exponential function.

Next we analysed recurrent patterns in dot-size data over long term printing experiments in terms of (I) ink volume on cantilever, (II) 'rest-time' between grids and (III) travel time between individual dots. We began in regime I by showing how deposition rate is dependent on the volume of ink on the cantilever. As the volume on the cantilever decreases during an experiment, the deposition rate decreases exponentially.

$$Dot\ Size \propto V_{res}$$

In regime II we showed that this is not the whole story. Really, the dot-size depends on the volume of ink in the tip-reservoir (a function of time between grids), which in turn depends on the volume in the cantilever reservoir.

$$Dot\ Size \propto V_{tip}(t) \propto V_{res}$$

In regime III, we described one further pattern in the data, concluding that dot size also depends on the how much ink is at the apex of the tip (a function of time between dots).

$$Dot\ Size \propto V_{apex}(t_2) \propto V_{tip}(t_1) \propto V_{res}$$

We have identified a hierarchy of effects contributing to the deposition rate of ink onto the substrate (Figure 6-9).

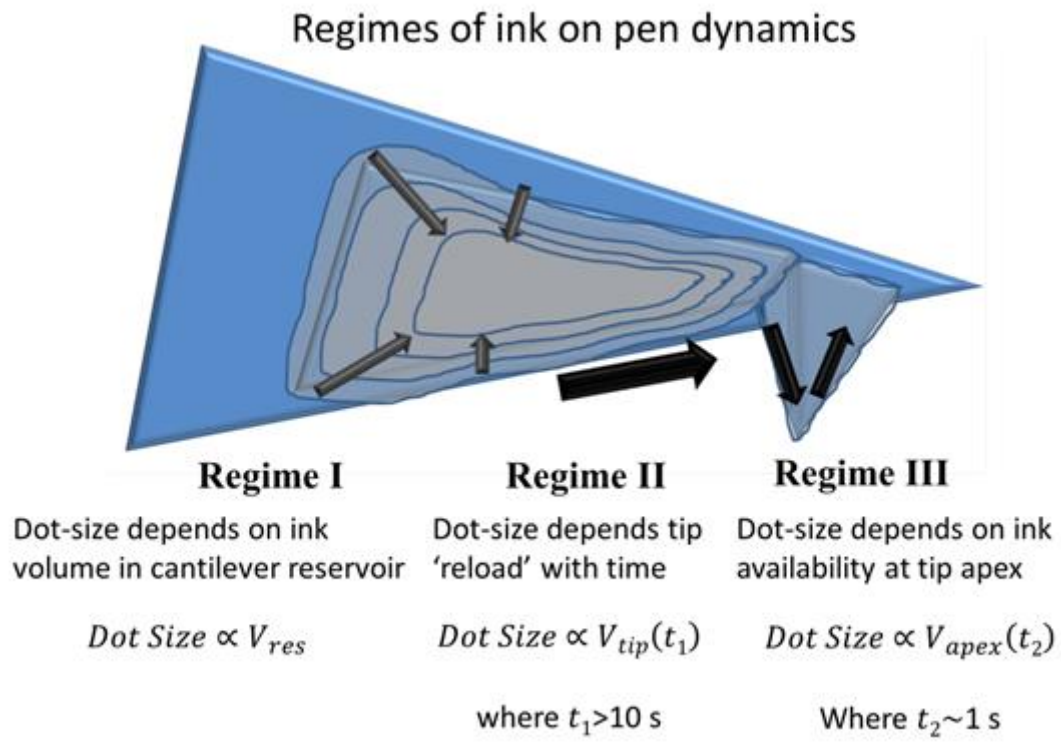

Figure 6-9: The hierarchy of ink on pen dynamics.

Deposition rate is dependent on the local volume of ink around the tip. Yet deposition necessitates the depletion of ink from this local volume. Unless the recovery of this local volume is perfect and instantaneous, the deposition rate at the next feature will differ from the first. This vastly complicates the process of pattern design, especially when a hierarchy of dynamic effects is at play.

For example, one implication is the design of dwell time calibration grids. Such grids are typically programmed using an ordered array of sequentially increasing dwell times. Since the deposition rate will depend on the order of dots printed, an ordered pattern of dwell times will exaggerate ordering effects, and introduce error. Following the ideas of the statistician R.A. Fisher,[46] random ordering of dwell times within the calibration grid could overcome this issue.

Most of the issues arise due to the design of the cantilever reservoir, and the reliance of spontaneous capillary action to feed the tip. Some methods

of nanoscale liquid ink printing provide a more direct control over ink availability at the tip apex by drilling a nanofluidic channel through the tip itself.[29,30] These nanofountain pen (NFP) approaches may circumvent many of the issues described above. However a major obstacle to the widespread uptake of NFP is the expense of drilling the channel (currently achieved by focused ion beam (FIB)) which would be highly laborious for parallel pen arrays. A purely photolithographic approach has been developed which may be more amenable to probe array fabrication.[30-33] The development of NFP ink formulations is still in its infancy, however, and it is unclear whether the nanoscale apertures impose limitations (in terms of viscosity or surface tension) on the range of liquids which are printable. A key limitation of the NFP approach in general arises from the susceptibility of nanoscale channels to clog. Other designs could be envisaged using microfluidic channels along the underside of the cantilever to control liquid flow, and thus maintain a constant driver force (Laplace pressure). Ultimately, *in-situ* monitoring of the deposition rate of (using AFM force curves), could be used to inform a feedback algorithm and so attain a desired feature size regardless of ink properties, tip volume or ink-substrate conditions.

6.5 Appendix

6.5.1 Regime I: Derivation of exponential decay model

We begin with one basic hypothesis: that the ink deposition rate, R, is proportional to the volume of ink contained in the cantilever reservoir (V_{res}):

$$R \propto V_{res} \quad (6)$$

Inserting an arbitrary proportionality constant (with units s^{-1}):

$$R = kV_{res} \quad (7)$$

Or, where R_0 is the initial deposition rate, we can substitute in the volume deposited:

$$R = R_0 - kV_{dep} \quad (8)$$

(A similar line of argument has been followed by others studying the long-term decline in deposition rate for molecular based inks).[14]

We do not attempt a rigorous derivation of an expression relating patterning rate (R), dwell time (t) and the volume of a deposited dot (V_{dot}). Nevertheless, we assume that the volume deposited is proportional to the deposition rate, at a fixed dwell time (5s).

$$V_{dot} \propto V_{res} \quad (9)$$

Thus, Where $V_{dot(0)}$ is the volume of the first dot printed.

$$V_{dot} \sim V_{dot(0)} - kV_{dep} \quad (10)$$

We can test this relationship with our data by plotting dot volume vs the total volume deposited. A linear relationship will justify equation 10 with the y-intercept value equivalent to $V_{dot(0)}$ and k the negative of the slope. We plot this in Figure 6-4 (C). The plot is linear with a y-intercept value (equivalent to $V_{dot(0)}$) of 16.5 μm^3 and a k value (the negative of the slope) of 0.0128.

By integrating equation 10, we arrive at an expression for the volume of the n^{th} dot; it depends on the initial volume within the cantilever reservoir, V_{res}, and the decay slope, k.

$$V_{dot(n)} = -kV_{res}e^{-kn} \quad (11)$$

6.5.2 Regime II: Calculation of tip reload volume

The calculation the 'reload volume, ΔV_{tip}, is illustrated in Figure 6-10. First, the volume of the final dot of the previous grid is used to define a baseline

dot-size. Any increase in dot-size above this value is attributed to the loading of ink onto V_{tip}. We then calculate the excess volume ΔV_{tip} by integrating the accumulative dot volume of the second grid above this baseline.

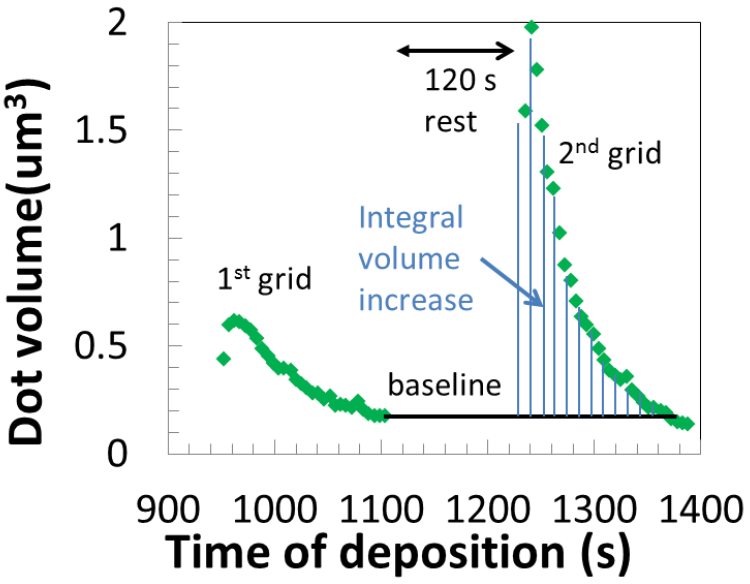

Figure 6-10: Calculating increase in V_{tip} during rest time. The excess volume ΔV_{tip} loaded in this 120 s rest time is calculated by integrating the accumulative ink volume of the second grid above a baseline value (defined by the size of the final dot in the previous grid).

6.6 References

1. Piner, R. D., Zhu, J., Xu, F., Hong, S. & Mirkin, C. A. "Dip-Pen" Nanolithography. *Science* **283**, 661–663 (1999).

2. Sheehan, P. & Whitman, L. Thiol Diffusion and the Role of Humidity in "Dip Pen Nanolithography". *Physical Review Letters* **88**, 156104 (2002).

3. Peterson, E. J., Weeks, B. L., Yoreo, J. J. De & Schwartz, P. V Effect of Environmental Conditions on Dip Pen Nanolithography of Mercaptohexadecanoic Acid. 15206–15210 (2004).

4. Schwartz, P. V Molecular Transport from an Atomic Force Microscope Tip: A Comparative Study of Dip-Pen Nanolithography. *Langmuir* **18**, 4041–4046 (2002).

5. Weeks, B., Noy, a., Miller, a. & De Yoreo, J. Effect of Dissolution Kinetics on Feature Size in Dip-Pen Nanolithography. *Physical Review Letters* **88**, 1–4 (2002).

6. Rozhok, S., Piner, R. & Mirkin, C. a. Dip-Pen Nanolithography: What Controls Ink Transport? *The Journal of Physical Chemistry B* **107**, 751–757 (2003).

7. Nafday, O. A., Vaughn, M. W. & Weeks, B. L. Evidence of meniscus interface transport in dip-pen nanolithography : An annular diffusion model Evidence of meniscus interface transport in dip-pen nanolithography : An annular diffusion model. **144703**, (2006).

8. Jang, J., Hong, S., Schatz, G. C. & Ratner, M. a. Self-assembly of ink molecules in dip-pen nanolithography: A diffusion model. *The Journal of Chemical Physics* **115**, 2721 (2001).

9. Hampton, J. R., Dameron, A. A. & Weiss, P. S. Transport rates vary with deposition time in dip-pen nanolithography. *The journal of physical chemistry. B* **109**, 23118–20 (2005).

10. Hampton, J. R., Dameron, A. A. & Weiss, P. S. Double-ink dip-pen nanolithography studies elucidate molecular transport. *Journal of the American Chemical Society* **128**, 1648–53 (2006).

11. Ahn, Y., Hong, S. & Jang, J. Growth dynamics of self-assembled monolayers in dip-pen nanolithography. *The journal of physical chemistry. B* **110**, 4270–3 (2006).

12. Saha, S. K. & Culpepper, M. L. An Ink Transport Model for Prediction of Feature Size in Dip Pen Nanolithography. *Small* 15364–15369 (2010).

13. Giam, L. R., Wang, Y. & Mirkin, C. A. Nanoscale molecular transport: the case of dip-pen nanolithography. *The journal of physical chemistry. A* **113**, 3779–82 (2009).

14. Wu, T.-H., Lu, H.-H. & Lin, C.-W. Dependence of transport rate on area of lithography and pretreatment of tip in dip-pen nanolithography. *Langmuir : the ACS journal of surfaces and colloids* **28**, 14509–13 (2012).

15. Wang, H. *et al*. Toward conductive traces : Dip Pen Nanolithography ® of silver nanoparticle-based inks. *Applied Physics Letters* 143105 (2008).doi:10.1063/1.2995859

16. Hung, S. *et al*. Dip Pen Nanolithography of Conductive Silver Traces. *The Journal of Physical Chemistry C* 9672–9677 (2010).

17. Senesi, A. J., Rozkiewicz, D. I., Reinhoudt, D. N. & Mirkin, C. A. Agarose-assisted dip-pen nanolithography of oligonucleotides and proteins. *ACS nano* **3**, 2394–402 (2009).

18. Sanedrin, R. G., Huang, L., Jang, J.-W., Kakkassery, J. & Mirkin, C. A. Polyethylene Glycol as a Novel Resist and Sacrificial Material for Generating Positive and Negative Nanostructures**. 920–924 (2008).doi:10.1002/smll.200701089

19. Nakashima, H., Higgins, M. J., O'Connell, C., Torimitsu, K. & Wallace, G. G. Liquid deposition patterning of conducting polymer ink onto hard and soft flexible substrates via dip-pen nanolithography. *Langmuir : the ACS journal of surfaces and colloids* **28**, 804–11 (2012).

20. Jang, J.-W. *et al*. Arrays of nanoscale lenses for subwavelength optical lithography. *Nano letters* **10**, 4399–404 (2010).

21. Hernandez-Santana, A., Irvine, E., Faulds, K. & Graham, D. Rapid prototyping of poly(dimethoxysiloxane) dot arrays by dip-pen nanolithography. *Chemical Science* **2**, 211 (2011).

22. Collins, J. M. *et al*. Targeted delivery to single cells in precisely controlled microenvironments. *Lab on a chip* **12**, 2643–8 (2012).

23. Ryu, K. S. *et al*. Integrated microfluidic inking chip for scanning probe nanolithography. *Applied Physics Letters* **85**, 136 (2004).

24. Jang, J.-W., Smetana, A. & Stiles, P. Multi-ink pattern generation by dip-pen nanolithography. *Scanning* **32**, 24–9 (2010).

25. Biswas, S., Hirtz, M. & Fuchs, H. Measurement of mass transfer during dip-pen nanolithography with phospholipids. *Small (Weinheim an der Bergstrasse, Germany)* **7**, 2081–6 (2011).

26. O'Connell, C. D., Higgins, M. J., Nakashima, H., Moulton, S. E. & Wallace, G. G. Vapor phase polymerization of EDOT from submicrometer scale oxidant patterned by dip-pen nanolithography. *Langmuir : the ACS journal of surfaces and colloids* **28**, 9953–60 (2012).

27. Salaita, K., Amarnath, A., Higgins, T. B. & Mirkin, C. A. The effects of organic vapor on alkanethiol deposition via dip-pen nanolithography. *Scanning* **32**, 9–14 (2010).

28. De Gennes, P. G. Wetting: statics and dynamics. *Reviews of Modern Physics* **57**, 827–863 (1985).

29. Meister, a., Liley, M., Brugger, J., Pugin, R. & Heinzelmann, H. Nanodispenser for attoliter volume deposition using atomic force microscopy probes modified by focused-ion-beam milling. *Applied Physics Letters* **85**, 6260 (2004).

30. Kim, K., Moldovan, N. & Espinosa, H. D. Patterning techniques A Nanofountain Probe with Sub-100 nm Molecular Writing Resolution**. 632–635 (2005).doi:10.1002/smll.200500027

31. Wu, B., Ho, A., Moldovan, N. & Espinosa, H. D. Direct deposition and assembly of gold colloidal particles using a nanofountain probe. *Langmuir : the ACS journal of surfaces and colloids* **23**, 9120–3 (2007).

32. Moldovan, N., Kim, K. & Espinosa, H. D. Design and Fabrication of a Novel Microfluidic Nanoprobe. **15**, 204–213 (2006).

33. Loh, O. *et al*. Nanofountain-probe-based high-resolution patterning and single-cell injection of functionalized nanodiamonds. *Small (Weinheim an der Bergstrasse, Germany)* **5**, 1667–74 (2009).

Chapter 7: Conclusions and outlook

7.1 Summary of main results

Dip pen nanolithography is a nanofabrication technique with unique capabilities in the nanoscale, multi-plexed, large-area deposition of molecules and materials. DPN printing of functional liquid inks may provide new capabilities in nanoscale fabrication, including the versatile printing electromaterials on biocompatible substrates for fundamental studies of the cellular-nanoelectrode interface.

This thesis contributes to the development of the DPN technique in two main aspects. The first aspect is the development of two novel methods of patterning electro-materials, described in chapters 3 and 4. The second is a contribution to the understanding of ink transport and the variability of feature-size in liquid ink DPN, as described in chapters 5 and 6.

Chapter 2 reviewed the development of the DPN technique in terms of instrumentation, ink development and applications. Background was provided to the theory of ink transport for both molecular and liquid inks. The deficiencies in current understanding of liquid ink DPN were also outlined.

Chapter 3 described the development of an oxidant ink for the vapour phase polymerisation of the conducting polymer poly(3,4-ethylenedioxythiophene) (PEDOT) via *in situ* vapour phase polymerisation. DPN patterning of the oxidant ink was facilitated by the incorporation of an

amphiphilic block copolymer thickener, an additive that also assisted with stabilization of the oxidant. When exposed to EDOT monomer in a VPP chamber, each deposited feature localized the synthesis of conducting PEDOT structures of several micrometres down to 250 nm in width, at a scale (picogram) which is much smaller than that previously reported. Although the process of VPP on this scale was achieved, we highlighted some of the challenges that need to be overcome to make this approach feasible in an applied setting.

Chapter 4 described the development of a platinum precursor (H_2PtCl_6) based liquid ink to DPN print onto hard and soft, flexible substrates with nanoscale resolution. The ink formulation was printable on Si, glass, ITO, Ge, PDMS, Parylene C and even a human hair. A mild plasma treatment effected reduction of the precursor patterns *in situ* without subjugating the substrate to destructively high temperatures. Feature size was controlled via dwell time and degree of ink loading, and platinum features with 50 nm dimensions could be routinely achieved on silanized Si. We confirmed the electrical conductivity of printed platinum by two point probe measurements and we characterized electrochemical activity using Scanning Electrochemical Microscopy (SECM). A modified method enabled deposition of micron scale Pt snowflakes; by tuning the substrate hydrophobicity using functionalization with a long chain alkane group we could temper spreading of the precursor solution and effect fractal-like crystal growth via a diffusion limited aggregation mechanism. Reduction of the precursor crystal by plasma treatment resulted in a 2D dendritic structure composed of an assembly of ~20 nm Pt nanoparticles.

In **Chapter 5** we used model ink-substrate systems (exhibiting a range of viscosities and wettabilities) to explore various methods of controlling feature size in liquid ink DPN. The ink-transfer mechanism was investigated using AFM force measurements acquired during ink deposition. This data was used to elucidate the shape of the meniscus during deposition and illustrate a method to monitor the volume of deposition *in-situ*. However,

the deposition rate was found to change dramatically over the course of an experiment due to a dependence of deposition rate on the changing volume of ink on the pen.

In **Chapter 6** we examined the effect of depleting ink volume on deposition rate over a long term experiment. A hierarchy of phenomena affecting the variability in feature size were uncovered, and were related to ink movement and reorganisation along the cantilever. These 'ink-on-tip hydrodynamics' were suggested to arise from (I) changes in ink volume on cantilever, (II) 'rest-time' between grids and (III) travel time between individual dots. In light of our conclusions, we posed critical questions of reservoir-on-tip liquid ink DPN as a nanofabrication technique and discuss the various parameters which need to be controlled in order to achieve uniformity of feature size.

Table 7-1 summarizes the liquid properties of the inks studied in this thesis. In particular, the macroscopic contact angle and minimum dot diameter achieved with each ink. The minimum dot diameter is taken as the average dot-size for dots printed at the shortest dwell time for our system (0.002 s).

Liquid	Density ρ (g/ml)	Viscosity (22 °C) μ (Pa.s)	Surface tension σ (mN/m)	Substrate	Contact Angles (macro.)	Min. dot diam. (nm)
NOA 65	1.093 (0.001)	1.33 (0.06)	33.8 (0.5)	Si(-OH)	~0	X
				Si(-CH_3)	24.2 (2.8)	242
NOA 68	1.136 (0.001)	5.49 (0.13)	34.2 (0.04)	Si(-OH)	4.5 (0.5)	122
				Si(-CH_3)	37.0 (4.2)	278
NOA 78	1.1504 (0.001)	10.86 (0.13)	36.46 (0.8)	Si(-OH)	2 (1.2)	X
				Si(-CH_3)	42.0 (4.8)	275
NOA 68T	1.156 (0.001)	24.86 (0.56)	26.7 (0.5)	Si(-OH)	6.6 (0.4)	132
				Si(-CH_3)	38.2 (3.6)	114
Oxidant ink	0.87 (0.02)	0.0134 (0.0002)	26.3 (0.2)	Si(-OH)	13.9 (2)	1200
10% Pt	1.167 (0.001)	-	48.41 (0.28)	Si(-CH_3)	67.9 (2.1)	50
48% Pt	1.484 (0.001)	-	55.99 (0.32)	Si(-CH_3)	76.3 (1.7)	60

Table 7-1: Liquid properties of all inks printed in this thesis.

Figure 7-1 plots the minimum dot-diameter against the macro-scopic contact angle for each ink system. No general trend is evident, indicating that the macro-scale liquid-substrate interaction may not be the defining factor in determining DPN printing performance. More work is required to understand the variation in minimum achievable feature size. For example, a chemical interaction between a component of the NOA inks and the Si substrate cannot be ruled out, in which case a purely physical analysis of liquid properties is insufficient. Another factor which may have a critical impact is the wetting of the ink on the tip itself, in particular the thickness of the liquid coating the tip apex.

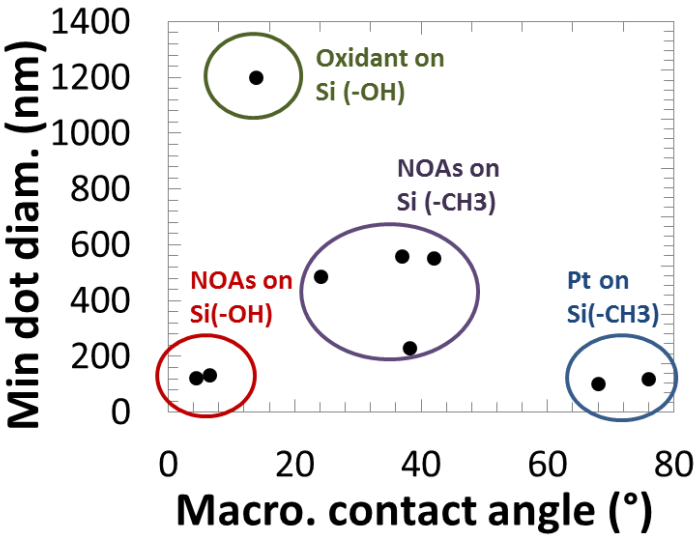

Figure 7-1: Minimum dot diameter plotted against the macro-scopic contact angle for all ink-substrate systems explored in this thesis.

Other model ink systems may be more suitable for delineating the relative effects of ink properties. For example, liquid polydimethylsiloxane (PDMS) is extensively used as a model ink as is highly inert, and its viscosity can be tuned over several orders of magnitude without changing its surface tension.[1] However, such experiments will have to be designed in such a way as to control for the dependence of deposition rate on the volume of ink on the tip, as described in the second half of this thesis.

7.2 Towards large-area high-resolution electromaterial printing using polymer pen lithography

Improving the limited 'upscalability' of DPN was a focus of much research in the first ten years of development of the technique. In 2008 this culminated in the invention of Polymer pen lithography (PPL), which has been touted as a facile and cost-effective route to expanding DPN to millions of simultaneous nanopatterns over cm^2 areas.[2]

Recently, we have utilised PPL technology to achieve large area patterning of a liquid ink incorporating the conducting polymer PEDOT:PSS. The preliminary results shown in Figure 7-2 highlight the potential of PPL for printing liquid inks over large areas. Figure 7-2 (A) shows a photograph of the PPL stamp on a 3" glass wafer backing. The PPL features (pyramids or lines) are molded into a 100 μm 'hard' PDMS layer on top of the glass wafer. Figure 7-2 (B) shows an SEM micrograph individual PDMS pyramids with nanoscale (~50 nm) sharpness. Figure 7-2 (C) and (E) show optical micrographs of the array of pyramidal tips and line features respectively. Figure 7-2 (D) and (E) show optical profilometry images of dots and line features respectively of PEDOT:PSS printed using PPL.

The more than ten thousand PEDOT:PSS features shown in Figure 7-2 (D) were printed in a single stamp of 1 s dwell time. The generation of equivalent features using DPN, although possible using the typical array of 12 probes, would require a laborious series of print runs. Furthermore, the deposition rate over long term printing would be subject to change due to the gradual depletion of ink as described in this thesis. Achieving uniform feature size with DPN over all ten thousand features as required, for example, to assay the response of statistically meaningful populations of living cells, would be highly challenging. PPL, therefore, represents a significant forward step towards the fabrication of applied devices.

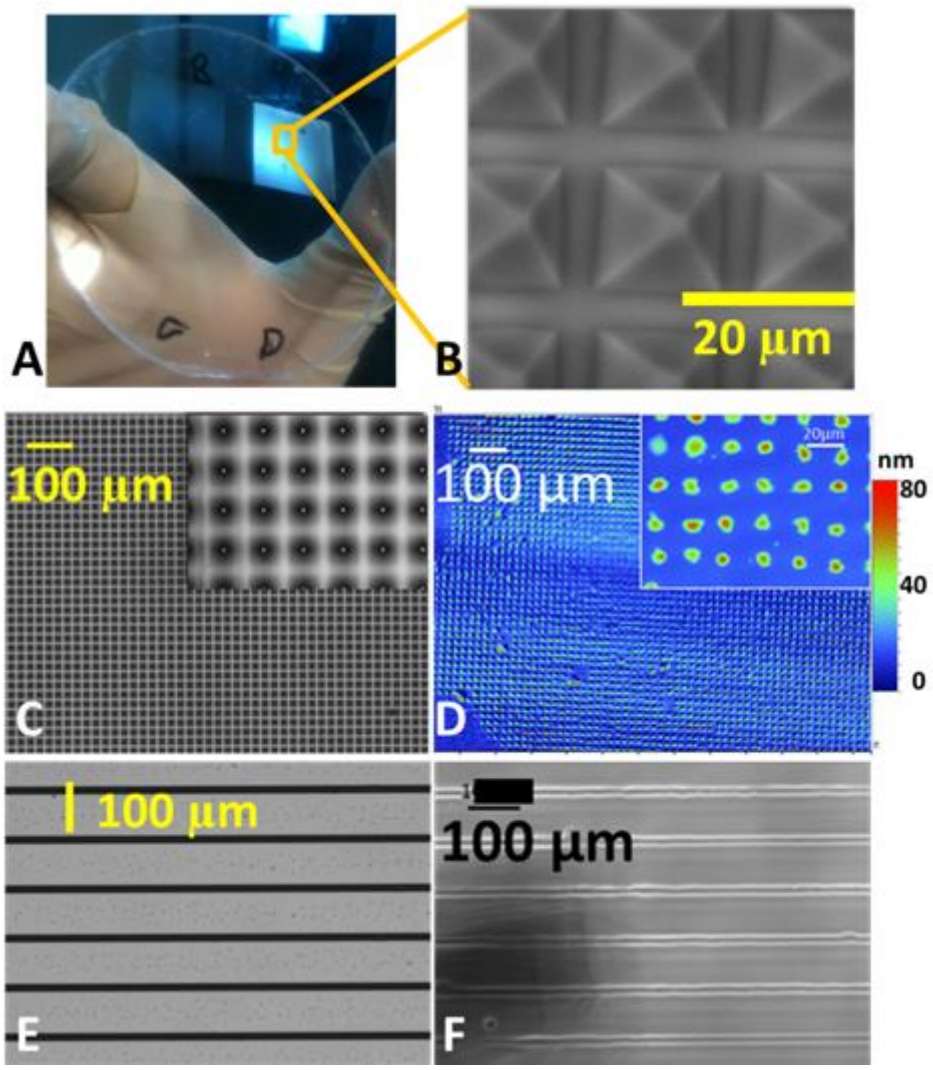

Figure 7-2: Polymer pen lithography for large area, high resolution conducting polymer patterning. (A) Photograph of the PPL stamp on a 3" glass wafer backing. (B) SEM micrograph showing individual pyramids with nanoscale (~50 nm) sharpness on the PPL array. (C) Optical micrographs of the array of pyramidal tips. (D) Optical profilometry generated images of an array of over 10000 PEDOT:PSS features printed by the pyramidal tip array. Inset shows higher magnification image of individual PEDOT:PSS dots with 20 µm spacing. (E) Optical micrograph of the PPL line stamp. Each line has a sharpness equivalent to that of an individual pyramid (~50 nm). (F) Optical micrograph of continuous PEDOT:PSS lines printed using the PPL line stamp.

7.3 DPN beyond Nanoink

In February 2013, it was announced that Nanoink Inc. was to shut down with immediate effect due to the withdrawal of funds by its primary investor, Ann Lurie.[3] The failure of the company has been attributed to its failure to commercialize a substantive development from its platform, despite an investment of $150 million over 10 years. Whether the end of Nanoink is commensurate with the end of dip-pen nanolithography remains to be seen.

Although an NScriptor instrument was used in this thesis, DPN experiments can be performed on virtually any AFM and many of the groups actively researching the DPN technique do so on without a Nanoink instrument. The loss of the company will have the immediate impact on the availability of consumables tailored to DPN (such as pen arrays and microfluidic ink-wells). However, the advent of PPL is enabling scanning probe based nanofabrication utilising stamps which can be produced in-house by most research institutions at little cost. Certainly, much of the knowledge generated during the development of the DPN technique, in terms of ink formulations, understanding of ink transport mechanisms, will feed directly into these and other massively parallel, scanning probe based lithography techniques yet to be developed.

A DPN researcher might anticipate a cool reception from nanotechnology editors to article submissions in the short term. However, it is highly unlikely that the closure of Nanoink will have a significant impact on research in the field in the longer term. DPN, like other SPM based lithography tools, is in its element in a research setting. The technology provides a means to fabricate novel structures. Capabilities such as the arbitrary patterning of individual 5 nm nanoparticles,[4] or individual proteins,[5] and the patterning of multiple different proteins within subcellular areas[6] are not achievable by other means. These tailored nanoenvironments, and others, will continue to justify DPN and PPL as

enabling tools; using these techniques researchers can design new experiments and answer fundamental questions in nanoscience and fundamental cell biology which were previously unanswerable.

7.4 References

1. De Gennes, P.-G., Brochard-Wyart, F. & Quéré, D. *Capillarity and Wetting Phenomena: drops, bubbles, pearls, waves*. (Springer: 2003).

2. Huo, F. *et al*. Polymer pen lithography. *Science (New York, N.Y.)* **321**, 1658–60 (2008).

3. Pletz, J. Nanoink folds as Ann Luries Investment Runs Out. *Chicago Business* (2013).at <http://www.chicagobusiness.com/article/20130222/BLOGS11/130229924/nanoink-folds-as-ann-luries-investment-runs-out>

4. Chai, J. *et al*. Scanning probe block copolymer lithography. *Proceedings of the National Academy of Sciences of the United States of America* **107**, 20202–6 (2010).

5. Chai, J., Wong, L. S., Giam, L. & Mirkin, C. a Single-molecule protein arrays enabled by scanning probe block copolymer lithography. *Proceedings of the National Academy of Sciences of the United States of America* **108**, 19521–5 (2011).

6. Collins, J. M. & Nettikadan, S. Subcellular scaled multiplexed protein patterns for single cell cocultures. *Analytical biochemistry* **419**, 339–41 (2011).